

# Spectroscopic Studies on Photosensitive Probes

Molecular Dynamics of RNA-Protein Complexes,  
Caged and Photoswitchable Compounds

---

Dissertation  
zur Erlangung des Doktorgrades  
der Naturwissenschaften

vorgelegt beim Fachbereich 14  
der Goethe-Universität  
in Frankfurt am Main

von  
Dinh Du TRAN  
aus Frankfurt am Main

Frankfurt am Main 2019  
(D30)

Vom Fachbereich 14 der  
Goethe-Universität Frankfurt am Main als Dissertation angenommen.

Dekan            Prof. Dr. Clemens Glaubitz  
1. Gutachter   Prof. Dr. Josef Wachtveitl  
2. Gutachter   Prof. Dr. Alexander Heckel

Datum der Disputation:        01. Februar 2019

*For my family -  
related by blood or by water ...*



# Spectroscopic Studies on Photosensitive Probes - Molecular Dynamics of RNA-Protein Complexes, Caged and Photoswitchable Compounds

— von Dinh Du TRAN

Die Steuerung biochemischer Prozesse oder die Verbesserung von Materialien erfordert zunächst ein tiefgründiges Verständnis über die zugrundeliegenden Systeme. Zur Untersuchung eignet sich Licht als ideales Werkzeug, da hiermit nützliche Informationen über die chemische Struktur, ihre Eigenschaften sowie den zusammenhängenden, schnellen Reaktionsabläufen erhalten werden können. Um die Aufklärung zu erleichtern können kleine, chemische Verbindungen eingeführt werden, welche beispielsweise ein Fluoreszenzmarker, eine photolabile Schutzgruppe oder eine photoschaltbare Verbindung sein können. Von jeweils einem Vertreter dieser Moleküle wurden unterschiedliche Studien durchgeführt, dessen Ergebnisse in dieser Arbeit in insgesamt drei Projekten zusammengefasst werden.

Zunächst wurde die Funktionalität der Helikase RhIB untersucht, die der Familie der DEAD-Box Proteine zugeordnet wird, und RNA-Duplexe in ihre Einzelstränge entwindet. Als RNA-Modellduplex diente JM2h, an dem ein RNA-Einzelstrang fluoreszenzmarkiert war (M2AP6). Die Einführung dieses Markers ermöglichte die Durchführung von statischen Fluoreszenzmessungen sowie von Mischexperimenten, die mit Hilfe der *stopped-flow*-Technik durchgeführt wurden. In den einleitenden Studien wurde die Helikase weggelassen, wodurch der Fokus auf den Fluoreszenzeigenschaften der RNA gelegt wurde. Die Ergebnisse hierzu zeigten, dass die Fluoreszenzintensität des Einzelstrangs durch Zugabe des komplementären Strangs deutlich abnimmt, wobei das Minimum bei einem äquimolaren Verhältnis erreicht wird. Die dazugehörigen *stopped-flow*-Messungen zeigten eine Beschleunigung der Hybridisierungsreaktion, wenn höhere Konzentrationen des Gegenstrangs in der Lösung vorhanden waren. Nach anschließender Zugabe der Helikase zur Lösung wurde ein Anstieg der Fluoreszenzintensität erwartet, der vom separierten Einzelstrang M2AP6 herrühren sollte. Dieser Anstieg wurde jedoch erst nach weiterer Zugabe von ATP beobachtet, der auf eine ATP-Abhängigkeit der Entwindungsreaktion von RhIB hindeutet. Diese Abhängigkeit wurde auch bereits für andere Helikasen der DEAD-Box Familie entdeckt. Die korrekte Funktionalität sowie die ATP-Abhängigkeit wurden in *stopped-flow*-Messungen verifiziert, bei denen der Fluoreszenzanstieg auch zeitaufgelöst betrachtet werden konnte. Für die spektralen Korrekturen der Fluoreszenzspektren wurde ein selbstgeschriebenes MATLAB-Programm namens FluCY verwendet (engl.: *Fluorescence Correction & Quantum yield*), welches eine schnelle und fehlerfreie Verarbeitung des Datensatzes ermöglichte.

Die zwei im folgenden beschriebenen Projekte handeln von photoaktivierbaren Molekülen. Zum einen photolabile Verbindungen, welche die Funktion z.B. eines

Biomoleküls durch eine chemische Modifikation deaktivieren können. Durch eine lichtinduzierte Reaktion kommt es zur Abspaltung der Modifikation und die Funktion ist wiederhergestellt. In dieser Arbeit wurden verschiedene photolabile Schutzgruppen untersucht, die denselben Chromophor BIST (bisstyryl-thiophen) tragen. Durch die Einführung dieses Chromophors absorbierten sämtliche untersuchte Verbindungen sehr effizient sichtbares Licht ( $\epsilon_{445} = 55.700 \text{ M}^{-1} \text{ cm}^{-1}$ ), wodurch der photoinduzierte Bindungsbruch mit Wellenlängen durchgeführt werden, die bei einer biologischen Anwendungen keinen Schaden an der Zelle anrichten würden. Hieraufhin wurden in statischen und zeitaufgelösten Absorptionmessungen Teilschritte der Freisetzungsreaktion untersucht, indem nach Photoanregung die Absorptionsänderungen auf verschiedenen Zeitskalen analysiert wurden. Die ultraschnelle Dynamik im Piko- bis Nanosekundenbereich ( $10^{-12} - 10^{-9} \text{ s}$ ) wird durch eine spektral breite, positive Absorptionsänderung dominiert. Diese impliziert, dass die Deaktivierung über den Triplettpfad abläuft, der die vergleichsweise niedrigen Freisetzungsausbeuten erklärt ( $\phi_u \leq 5$ ). Aufgrund des hohen Extinktionskoeffizienten reichen dennoch bereits niedrige Strahlungsdosen aus, um eine Freisetzung zu initiieren. Der geschwindigkeitsbestimmende Schritt dieser Reaktion ist dem Zerfall des *aci*-nitro Intermediats zugeordnet. Für ein sekundäres Amin, welches mit BIST geschützt wurde, ist eine Lebensdauer des Intermediats von 71  $\mu\text{s}$  gefunden worden.

In einigen Fällen ist es erwünscht, eine vorliegende Aktivität nicht nur ein-, sondern auch ausschalten zu können, wofür photochrome Verbindungen (oder Photoschalter) verwendet werden. Die in dieser Arbeit untersuchte Verbindung ceCAM ist ein Alken-Photoschalter und vollführt bei Bestrahlung mit Licht eine *cis/trans*-Isomerisierung. ceCAM ist das Cyanoester-Derivat (ce) von Cumarin-substituierten Allylidenmalonat, von denen beide Konformere sehr effizient sichtbares Licht absorbieren (*trans*:  $\epsilon_{489} = 50.300 \text{ M}^{-1} \text{ cm}^{-1}$ ; *cis*:  $\epsilon_{437} = 18.600 \text{ M}^{-1} \text{ cm}^{-1}$ ). Andere photophysikalische Eigenschaften umfassen u.a. hohe thermische und photochemische Stabilität. Letztere wurde über ein Experiment nachgewiesen, bei dem die lichtinduzierte Isomerisierung alternierend durchgeführt wurde und selbst bei über 250 Zyklen keine signifikante Abnahme der Absorption beobachtet werden konnte. Des Weiteren konnte die Reaktion mit Quantenausbeuten von 39% (*trans*) und 42% (*cis*) induziert werden, wobei im photostationären Gleichgewicht auch hohe Isomerenverhältnisse mit bis zu 80% (*trans*) und 96% (*cis*) akkumuliert werden konnten. Die Geschwindigkeit der Reaktion wurde mit Hilfe der Ultrakurzzeit-Spektroskopie untersucht. Die Dynamik im Zeitbereich von ps-ns zeigte, dass die *trans/cis*-Isomerisierung unterhalb von 0,5 ns und die umgekehrte Reaktion noch viel schneller (wenige ps) abgeschlossen ist. Durch die Untersuchungen in dieser Arbeit an den BIST-Verbindungen und ceCAM sind viele vorteilhafte, photophysikalische Eigenschaften charakterisiert worden, wodurch sie als verbesserte Alternative zu den bisher bekannten photolabilen Schutzgruppen oder Photoschaltern anzusehen sind.

## CONTENTS

---

ZUSAMMENFASSUNG	i
LIST OF FIGURES	vi
LIST OF TABLES	viii
LIST OF ABBREVIATIONS	ix
<b>1 INTRODUCTION</b>	<b>1</b>
<b>I THEORETICAL FRAMEWORK</b>	
<b>2 THEORETICAL BACKGROUND - EXPERIMENTAL</b>	<b>7</b>
2.1 Spectroscopic Background . . . . .	7
2.1.1 UV-vis absorption spectroscopy . . . . .	8
2.1.2 Infrared absorption spectroscopy . . . . .	10
2.1.3 Relaxation Processes . . . . .	11
2.2 Nonlinear optics . . . . .	13
2.2.1 Nonlinear effects . . . . .	13
2.2.2 Supercontinuum generation . . . . .	15
2.2.3 Optical parametric amplifier . . . . .	16
2.3 Time-resolved pump/probe spectroscopy . . . . .	17
2.3.1 The pump-probe Experiment . . . . .	17
2.3.2 Functionality of a laser . . . . .	18
2.3.3 Generation of ultrashort laser pulses . . . . .	18
2.3.4 Occurring signals . . . . .	19
2.3.5 Kinetic analysis . . . . .	20
<b>3 THEORETICAL BACKGROUND - SAMPLES</b>	<b>23</b>
3.1 Ribonucleic acids and helicases . . . . .	23
3.1.1 RNA . . . . .	23
3.1.2 Helicases . . . . .	25
3.2 Photocages . . . . .	26
3.2.1 General information on photocages . . . . .	26
3.2.2 Photochemistry of <i>o</i> -NB cages . . . . .	27
3.2.3 Research and applications of photocages . . . . .	29
3.3 Photoswitches . . . . .	30
3.3.1 General information on photoswitches . . . . .	30
3.3.2 Classes of photoswitches . . . . .	31
<b>II EXPERIMENTAL METHODS</b>	
<b>4 MATERIALS AND EXPERIMENTAL PROCEDURES</b>	<b>35</b>

4.1	Materials . . . . .	35
4.1.1	RNA and Protein compounds . . . . .	35
4.1.2	Photoactivatable compounds . . . . .	36
4.1.3	Photoswitchable Compounds . . . . .	36
4.1.4	solvents . . . . .	36
4.2	Steady-state Experiments . . . . .	37
4.2.1	UV/vis-absorption spectroscopy . . . . .	37
4.2.2	FTIR spectroscopy . . . . .	38
4.2.3	Fluorescence spectroscopy . . . . .	39
4.2.4	Stopped-Flow Fluorescence . . . . .	43
4.3	Illumination Procedures . . . . .	44
4.4	Time-Resolved Experiments . . . . .	46
4.4.1	Transient Flash-Photolysis Setup . . . . .	46
4.4.2	Time-resolved IR-spectroscopy . . . . .	47
4.4.3	UV/vis-pump UV/vis-probe Setup . . . . .	48

### III RESULTS

5	RESULTS - HELICASE . . . . .	55
5.1	The RNA-duplex JM2h . . . . .	55
5.2	Preliminary fluorescence measurements of RNA single-strands J2h and M2AP6 . . . . .	58
5.2.1	Steady-state fluorescence . . . . .	58
5.2.2	Time-resolved fluorescence . . . . .	58
5.3	FluCY - a MATLAB program . . . . .	60
5.3.1	Introducing FluCY . . . . .	60
5.3.2	Import the recorded spectra . . . . .	61
5.3.3	Offset correction . . . . .	63
5.3.4	Excitation correction . . . . .	64
5.3.5	Emission correction . . . . .	66
5.3.6	Saving the corrected data . . . . .	68
5.4	Steady-state and stopped-flow fluorescence measurements of JM2AP . . . . .	71
5.4.1	Concentration-dependent steady-state fluorescence of JM2AP . . . . .	71
5.4.2	Concentration-dependent stopped-flow fluorescence of JM2AP . . . . .	72
5.5	Fluorescence measurements involving JM2AP and Rh1B . . . . .	73
5.6	Rapid-Scan measurements on NPE-caged ATP . . . . .	76
5.7	Concluding Remarks . . . . .	78
6	RESULTS - BIST-CAGES . . . . .	81
6.1	The BIST-chromophore . . . . .	81
6.2	Steady-state characterization . . . . .	83
6.2.1	Steady-state absorbance . . . . .	83
6.2.2	Steady-state fluorescence . . . . .	84
6.2.3	DFT-calculations of BIST-NHnBu . . . . .	85
6.2.4	Illumination of BIST-cages . . . . .	86



6.2.5	FTIR spectroscopy on illuminated BIST-NHnBu . . . . .	90
6.3	Ultrafast dynamics in the ps-ns range . . . . .	92
6.4	Influence of water on the excited dynamics of BIST-NHnBu . . . . .	97
6.4.1	Reaction dynamics in the $\mu$ s-ms range . . . . .	101
6.5	Concluding remarks . . . . .	102
<b>7</b>	<b>RESULTS - CECAM</b> . . . . .	<b>105</b>
7.1	General steady-state properties of ceCAM . . . . .	105
7.1.1	DFT-calculations of ceCAM . . . . .	107
7.1.2	Actinic effect of the spectrometer . . . . .	109
7.2	Determination of the photophysical parameters . . . . .	110
7.2.1	Photoconversion efficiency . . . . .	110
7.2.2	Thermal stability . . . . .	114
7.2.3	Fatigue-resistance . . . . .	115
7.2.4	Determination of the reaction quantum yields of ceCAM . . . . .	117
7.2.5	Fluorescence spectra and quantum yields of ceCAM . . . . .	122
7.2.6	Characterization of the ultrafast isomerization reaction dynamics in the ps-ns range . . . . .	128
7.3	Concluding remarks . . . . .	133
<b>IV CONCLUSION</b>		
<b>8</b>	<b>CONCLUSION AND OUTLOOK</b> . . . . .	<b>137</b>
<b>9</b>	<b>ZUSAMMENFASSUNG UND AUSBLICK</b> . . . . .	<b>141</b>
<b>V APPENDIX</b>		
<b>A</b>	<b>APPENDIX</b> . . . . .	<b>149</b>
A.1	FluCY - Version history and saving location . . . . .	149
A.1.1	Location of files and folders . . . . .	149
A.1.2	Version history . . . . .	149
A.2	Amino acid sequence of Rh1B . . . . .	150
<b>BIBLIOGRAPHY</b> . . . . .		
<b>151</b>		
<b>SCIENTIFIC CONTRIBUTIONS</b> . . . . .		
<b>171</b>		
<b>ACKNOWLEDGEMENTS</b> . . . . .		
<b>173</b>		
<b>EIDESSTATTLICHE ERKLÄRUNG</b> . . . . .		
<b>175</b>		

## LIST OF FIGURES

---

Figure 2.1	The Jabłoński diagram summarizes the deactivation processes after photoexcitation. . . . .	12
Figure 2.2	Principle of pump-probe-spectroscopy . . . . .	17
Figure 3.1	Nucleotides . . . . .	24
Figure 3.2	General reaction mechanism of <i>o</i> -NB cages, including the presumed intermediates after photoexcitation. . . . .	28
Figure 3.3	General chemical structure of prominent photocages . . . . .	29
Figure 3.4	Metaphorical comparison between a photocage and a photoswitch. . . . .	30
Figure 3.5	Exemplary classes of photoswitches. . . . .	32
Figure 4.1	Schematical depiction of the used CLARK laser system . . . . .	49
Figure 5.1	Sequence of the investigated RNA duplex JM2h. . . . .	56
Figure 5.2	Chemical structure of ATP and differential modifications, which were used in this work. . . . .	57
Figure 5.3	Steady-state and time-resolved fluorescence measurements of 2AP-labeled M2 and its duplexed form. . . . .	59
Figure 5.4	Full view of the self-written MATLAB-program FluCY. . . . .	61
Figure 5.5	FluCY - Importing the data. . . . .	62
Figure 5.6	FluCY - Offset and excitation correction of the recorded spectra . . . . .	64
Figure 5.7	FluCY - Emission correction . . . . .	66
Figure 5.8	FluCY - Saving the data. . . . .	68
Figure 5.9	Effect of the conducted fluorescence corrections on the steady-state fluorescence spectrum of the photoswitch ceCAM. . . . .	69
Figure 5.10	Fluorescence intensity of titration of J2h to M2AP. . . . .	71
Figure 5.11	Stopped-flow measurements of JM2AP with varying concentrations of non-labeled ss-JM2h. . . . .	73
Figure 5.12	Unwinding of the duplexed RNA by the helicase RhlB is detected in both steady-state and stopped-flow fluorescence measurements. . . . .	75
Figure 5.13	Rapid-scan measurement of NPE-caged ATP after LED illumination at 365 nm. . . . .	77
Figure 6.1	Lewis-Structure of investigated BIST-cages . . . . .	82
Figure 6.2	Molar extinction coefficients and scaled fluorescence spectra of the BIST-amine, -ether and -ester in DMSO. . . . .	83

Figure 6.3	Electronic transitions and associated molecular orbitals for BIST-NHnBu found in DFT-calculations. . . . .	85
Figure 6.4	LED illumination experiments of the investigated BIST-cages in DMSO. . . . .	87
Figure 6.5	Absorption spectra of BIST-NHnBu in DMSO with 20% H <sub>2</sub> O after LED illumination at 455 nm. . . . .	89
Figure 6.6	Difference FTIR-absorbance spectra of BIST-NHnBu in 20% D <sub>2</sub> O after LED illumination, overlaid with calculated vibrations of the reactant and photoproduct. . . . .	91
Figure 6.7	Transient maps and corresponding decay-associated spectra of various BIST-cages. . . . .	92
Figure 6.8	Suggested mechanism of the first steps for the BIST-uncaging reaction. . . . .	97
Figure 6.9	Transient maps of BIST-NHnBu without and with water after photoexcitation at 440 nm. . . . .	99
Figure 6.10	Influence of water to the ultrafast dynamics of (selected transients) BIST-NHnBu after excitation at $\lambda_{exc} = 440 \text{ nm}$ . The depicted transients correspond to a water content of 0/10/20/30% (blue/red/yellow/purple) in DMSO solution and were normalized to the difference absorbance at 1 ps. . . . .	100
Figure 6.11	Flash-photolysis experiments of BIST-NHnBu after photoexcitation at ( $\lambda_{exc} = 455 \text{ nm}$ ). . . . .	102
Figure 6.12	Proposed mechanism for the uncaging reaction of BIST-cages. . . . .	103
Figure 7.1	Photochromism of the investigated photoswitch ceCAM. . . . .	106
Figure 7.2	The absorbance spectra of pure ceCAM-isomers in MeCN. . . . .	107
Figure 7.3	DFT calculations for the ground-state geometry and MOs involved in photoexcitation of <i>trans</i> -ceCAM. . . . .	108
Figure 7.4	DFT calculations for the ground-state geometry and MOs involved in photoexcitation of <i>cis</i> -ceCAM. . . . .	108
Figure 7.5	Actinic effect of the spectrophotometer on ceCAM isomerization. . . . .	110
Figure 7.6	UV/vis absorbance spectra of the photostationary state (pss) of ceCAM . . . . .	112
Figure 7.7	Thermal stability of ceCAM. . . . .	114
Figure 7.8	Fatigue resistance of ceCAM after alternate photoswitching at 385 and 530 nm. . . . .	116
Figure 7.9	Reaction quantum yield of the <i>cis/trans</i> -isomerization of ceCAM in MeCN after LED-illumination at 405 nm . . . . .	119
Figure 7.10	Emission spectra of selected LEDs and absorbance spectra of various optical filters which were used for the determination of the rQY of ceCAM. . . . .	120

Figure 7.11	Steady-state absorbance and normalized fluorescence spectra of ceCAM . . . . .	124
Figure 7.12	FluCY - GUI for the determination of the fQY. . . . .	125
Figure 7.13	Transient maps and corresponding DAS of either ultrafast isomerization of ceCAM. . . . .	129
Figure 7.14	Transient courses of the SE for the <i>trans/cis</i> - and <i>cis/trans</i> -isomerization. . . . .	132
Figure 7.15	Summary of the steady-state and kinetic parameters found for the photophysical characterization of ceCAM. . . . .	134

## LIST OF TABLES

---

Table 4.1	Solvents used in this work . . . . .	37
Table 4.2	Composition of the steady-state fluorescence measurements involving the helicase Rh1B . . . . .	40
Table 4.3	Composition of the stopped-flow fluorescence measurements involving the helicase Rh1B . . . . .	44
Table 6.1	Absorption maxima and molar extinction coefficients of the investigated BIST-cages . . . . .	84
Table 6.2	Fitted lifetimes after global lifetime analysis of the BIST-cages after photoexcitation at 430 and 470 nm . . . . .	96
Table 6.3	Global lifetime analysis of BIST-NHnBu with different contents of water after photoexcitation at 440 nm . . . . .	99
Table 7.1	Photoconversion efficiency for the isomerization of ceCAM after LED- and laser illumination at different wavelengths. . . . .	113
Table 7.2	Reaction quantum yields for isomerization of ceCAM at different excitation wavelengths and with various optical filters. . . . .	121
Table 7.3	Fluorescence quantum yield of <i>cis</i> - and <i>trans</i> - ceCAM. . . . .	127
Table 7.4	Fitted lifetimes of the ultrafast photodynamics of ceCAM after GLA . . . . .	130

## LIST OF ABBREVIATIONS

---

1P	one-photon
2AP	2-aminopurine
2P	two-photon
3D	three-dimensional
A	adenosine
AMP-PNP	adenylyl-imidodiphosphate
AO	atomic orbital
AOM	acousto-optic modulator
APM	additive pulse mode-locking
ASCII	American Standard Code for Information Interchange
ATP	adenosine triphosphate
B <sub>3</sub> LYP	Becke, three-parameter, Lee-Yang-Parr
BIST	<u>b</u> is <u>s</u> tyr <u>l</u> thiophene
BODIPY	boron dipyrromethene
BP86	Becke (exchange), Perdew6 (correlation)
BS	beam splitter
C	cytidine
C153	coumarin 153
CaF <sub>2</sub>	calcium fluoride
CAM	<u>c</u> oumarin <u>a</u> llylidene <u>m</u> alonate
cAMP	3',5'-cyclic adenosine monophosphate
cGMP	3',5'-cyclic guanosine monophosphate
CHCl <sub>3</sub>	chloroform
CI	conical intersection
CPA	chirped-pulse amplification

cw	continuous wave
DAS	decay-associated spectra
DEACM	7-(diethylamino)-4-(methyl)-coumarin
DFG	difference frequency generation
DFT	density functional theory
DLaTGS	deuterated L-alanine doped triglycene sulphate
DMSO	dimethyl sulfoxide
DNA	deoxyribonucleic acid
ds	double-stranded
DTE	dithienylethene
EGTA	ethylene glycol-bis( $\beta$ -aminoethyl ether)-N,N,N',N' -tetraacetic acid
ESA	excited-state absorption
ESHT	excited-state hydrogen transfer
ESIPT	excited-state intermolecular proton transfer
FluCY	<u>F</u> luorescence <u>C</u> orrection & Quantum <u>Y</u> ield
fQY	fluorescence quantum yield
fs	femtoseconds
FTIR	Fourier-transform infrared
FWHM	full width at half maximum
G	guanosine
GABA	gamma-aminobutyric acid
GLA	global lifetime analysis
GSB	ground-state bleach
GUI	graphical user interface
GVD	group velocity dispersion
HOMO	highest occupied molecular orbital
HPLC	high-performance liquid chromatography
IC	internal conversion

IR	infrared
IRF	instrument response function
ISC	intersystem crossing
IUPAC	The International Union of Pure and Applied Chemistry
IVR	intramolecular vibrational relaxation
KIE	kinetic isotope effect
KLM	KERR-lens mode locking
laser	light amplification by stimulated emission of radiation
LCAO	linear combination of atomic orbitals
LDA	lifetime density analysis
LDM	lifetime density map
LED	light-emitting diode
LUMO	lowest unoccupied molecular orbital
MCT	mercury cadmium telluride
MeCN	Acetonitrile
MO	molecular orbital
mRNA	messenger RNA
ms	milliseconds
Nd:YAG	neodymium-doped yttrium aluminum garnet
ND	neutral-density
NMR	nuclear magnetic resonance
NOPA	noncollinear optical parametric amplifier
NPE	1-(2-Nitrophenyl)ethyl
ns	nanoseconds
OD	optical density
<i>o</i> -NB	<i>ortho</i> -Nitrobenzyl
OPA	optical parametric amplifier
OPO	optical parametric oscillator

<i>o</i> -HP	<i>para</i> -Hydroxyphenacyl
PIP	phosphatidylinositol 4-phosphate
PMT	photomultiplier tube
PMT	photomultiplier tube
pss	photostationary state
PTFE	Polytetrafluor-ethylen
R6G	rhodamin 6G
RNA	ribonucleic acid
rQY	reaction quantum yield
rRNA	ribosomal RNA
RSE	radical stabilization energy
SE	stimulated emission
SFG	sum frequency generation
SFM	sum frequency mixing
SHG	second harmonic generation
SNR	signal-to-noise ratio
SPM	self-phase modulation
ss	single-stranded
T	thymidine
TCSPC	time-correlated single photon counting
Ti:Sa	titanium-doped sapphire (Al <sub>2</sub> O <sub>3</sub> )
U	uridine
uQY	uncaging quantum yield
UV	ultraviolet



## INTRODUCTION

---

*Scientists have searched for a perpetuum mobile;  
they have found it:  
it is science itself.*

— **Victor Hugo in: William Shakespeare (1864)**

Despite the vast fields of research, scientists share a common goal that has not changed over the course of time. They strive to make intriguing observations and understand underlying processes, then partly modify them and predict an outcome, which is then observed again. This inexorable venture for knowledge is the motivating force of science, and was already poetically summarized by Victor Hugo in 1864[1].

In natural sciences, it is often the biochemical processes which are examined more closely. The collected knowledge can foster the development of new materials in technology or applications in medical therapy. To obtain information about the involved (bio-)chemical compounds and their reactions, many different techniques can be applied. Light has been proven to be a very useful tool for this purpose. Depending on what spectral fragment of light (or rather the electromagnetic spectrum) is used, it can accurately reveal the chemical structure or determine other relevant photophysical properties. Moreover, these so-called spectroscopic methods allow the observation of ultrafast processes, providing insights into the complex molecular mechanisms.

The duration of chemical reactions tends to be very short. To be able to investigate these processes, ultrafast laser pulses in the femtosecond range ( $1 \cdot 10^{-15}$  s) are a prerequisite, allowing the monitoring of a chemical reaction in real time. The underlying pump/probe-technique in the visible wavelength range, which was also used within this work, can provide an extensive comprehension of the reaction mechanism and the electronic properties of its associated molecules. Since the introduction and construction of the first laser in 1960[2, 3], lasers have been used to investigate several systems, while the technique was constantly developed further. The importance of this powerful tool is further fuelled by the fact that more than 10 Nobel Prizes in Physics and Chemistry have been awarded for achievements in this discipline, the latest one in 2018 for the CPA technique (G. Mourou, D. Strickland).[4–13] Due to its wide-ranging capability, light can be used in many ways to address various scientific domains.

After having understood a (bio-)chemical reaction, it is desirable to gain control over it for a full regulation of the accompanying processes. This can be

realized by an incorporation of a small, light-sensitive molecule, as those are easier to synthesize, analyze and improve. One of the approaches is to chemically modify e.g. a biomolecule, rendering its physiological effect inactive. The resulting so-called photocage can be designed as such, that only harmless parts of light, e.g. the visible range, will initiate the uncaging reaction and release the trapped molecule. The diversity of this research field ranges from various methods to even more differing applications, where fluorophores[14], metal ions, such as  $\text{Ca}^{2+}$ [15–21] or antibiotics[22–25] are caged, which are released upon excitation with green[26], or red light,[27] or even by two-photon absorption (2PA)[28–32]. Through the initiation of the reaction with a precise dose of light, both the recovery of activity and subsequent reactions can be accurately monitored by means of ultrafast spectroscopy.

Another class of light-sensitive molecules are photochromic compounds, which comprise at least two stable conformations. Contrary to the photocages, this approach enables a photoinduced back and forth switching of an active state, entailing a higher regulation of the chemical reaction. Despite the simplicity of the reaction, an abundance of photoswitches exist. They can either undergo electrocyclization such as spiropyrans[33] or dithienylethenes[34], or *cis/trans*-isomerization, with the most prominent classes being azobenzenes[35], and stilbenes[36], of which a representative is investigated in this work.

As a result of having such a large diversity of photoswitches, the possibilities for further applications seem widely exploited. Many reports exist on fluorescent molecular switches,[37] or markers in biological applications, material sciences, or even medical therapy.[38] Additionally, the incorporation of a molecular switch into a strand of nucleic acids grants photocontrol over biological processes, such as peptide,[39] or RNA folding,[40] which usually require other approaches of characterization than optical spectroscopy.

In view of the desired applications in biological processes, there are many prerequisites for any photoregulatory interventions, some of which pose a formidable challenge for the synthesis and analysis. While some can be easily circumvented by proper prognosis, such as the water solubility or non-toxicity, the reaction's efficiency, among others, will have to be assessed in the course of the analysis. Yet, by employing light in the analysis, the application benefits from a high spatial and temporal resolution, so that it is possible to precisely steer the reaction without damaging the cellular environment in the process, as there are no interactions.

The first part of this thesis (Part I) describes the theoretical background of the methods, as well as the investigated samples. [Chapter 2](#) contains the physical background on the spectroscopic methods in the UV, visible and IR range of the electromagnetic spectrum. Different nonlinear effects and time-resolved pump/probe spectroscopy are covered therein as well. An introduction to the studied compounds is given in [Chapter 3](#), where RNA and proteins, as well

as some established representatives of the major classes of photocages and photoswitches are briefly summarized.

Part II describes the preparation and origin of the investigated samples and the associated solvents together with the applied experimental methods. The used setups, illumination procedures and details on the different (time-resolved) techniques are introduced in [Chapter 4](#).

The results on the three different projects are comprised in the main part of this work (Part III). The fluorescence measurements on a 2AP-labeled RNA strand and an RNA helicase are summarized in [Chapter 5](#), in which the sequence of events during unwinding will be clarified.. In [Chapter 6](#), a promising new photolabile protecting group is characterized. The extensive studies comprise the steady-state investigations of four compounds and the underlying uncaging dynamics. The photophysical properties of the photoswitch ceCAM are determined in [Chapter 7](#), which includes the steady-state features as well as the ultrafast isomerization dynamics.

A brief summary of the work, as well as an outlook on possible further studies are given at the end (Part IV).



Part I

THEORETICAL FRAMEWORK



## THEORETICAL BACKGROUND - EXPERIMENTAL

---

Optical spectroscopy is a powerful tool and plays a key role, when investigating the structure of a molecules, its properties, or even its dynamics in chemical reactions. Depending on which part of the electromagnetic spectrum is used, spectroscopy enables the possibility to actually shed light onto unknown structures and functions of a molecule.

This chapter sets the basic knowledge, which is required to understand the results of this chapter. First, the spectroscopic background is briefly summarized, starting by UV/vis-absorption spectroscopy, which allows the investigation of the electronic structure of molecules and the transitions thereof (see [Section 2.1.1](#)). This is followed by IR-spectroscopy, which examines the vibrational structure of the chemical bonds ([Section 2.1.2](#)) and then the relaxation processes which can occur after transition from the ground to an excited state.

In order to follow a chemical reaction, time-resolved spectroscopy must be performed, which is typically achieved by laser light. Therefore, the subsequent part describes the nonlinear effects, which occur when working with light of high intensity. This includes the emerging effects ([Section 2.2.1](#)), the generation of a supercontinuum ([Section 2.2.2](#)) and the parametric processes which are necessary to tune the frequency of light ([Section 2.2.3](#)).

These processes set the foundation for the last part of this chapter, which revolves around time-resolved spectroscopy. After the general scheme of a pump-probe experiment is illustrated ([Section 2.3.1](#)), the functionality of a laser and the generation of ultrashort pulses are explained ([Section 2.3.2](#) and [2.3.3](#)). When doing transient absorption spectroscopy to investigate the photodynamics, the occurring signals in a transient map are relatively complex, which is why it is necessary to introduce the occurring signals ([Section 2.3.4](#)) and explain how the data set can be analyzed ([Section 2.3.5](#)).

### 2.1 SPECTROSCOPIC BACKGROUND

When a photon interacts with the sample, different types of processes can occur. Spectroscopy is the investigation of this interplay and can be divided into different parts, depending on the energy of the photon. To be able to understand the general principle, this section briefly summarizes the underlying theoretical background.

The electromagnetic spectrum of light consists of a wide variety of smaller spectral ranges. Depending on the wavelength range of this spectrum, the

photon can initiate different types of processes within the molecule, which in turn require different spectroscopic techniques for an investigation. Moreover, different types of radiation have found an application, with well-known representatives being the microwaves (wavelengths of 0.3-1 m), which are used for telecommunication, or X-rays (below 10 nm =  $10 \cdot 10^{-9}$  m), which are used for medical purposes.[41]

In general, when a molecule is investigated by light, four different energies can be observed, which are distinguished as follows: electronic states and the energy in vibration, rotation and translation, whereas only the latter cannot be actively addressed by light. The energy of a photon, however, is always quantized and can be determined from its wavelength  $\lambda$  or wavenumber  $\tilde{\nu}$ , according to the PLANCK-EINSTEIN relation, which is described in Eq. (2.1), with the PLANCK constant  $h$  and the speed of light  $c$ . If a given energy difference between two states  $E_j$  and  $E_i$  is in resonance with the energy of a photon, the absorption of such can initiate a transition from one state to the other (Eq. (2.2)). This leads to the population of a previously unoccupied state, which is then also called the excited state.

$$E = h\nu = \frac{hc}{\lambda} = hc\tilde{\nu} \quad (2.1)$$

$$\Delta E = E_j - E_i \quad (2.2)$$

### 2.1.1 UV-VIS ABSORPTION SPECTROSCOPY

The wavelength range from ca. 100 to 400 nm in the electromagnetic is called the ultraviolet (UV) range and can be subdivided into the middle to near ultraviolet, covering an energy range of 12.4-3.1 eV. At higher wavelengths, the *visible* light covers a spectral range of 400-750 nm which corresponds to an energy of 3.1-1.7 eV. The photon energy from these two spectral ranges coincide with the energy difference typically required for a transition between two electronic states. Therefore, they are typically grouped together. UV/vis-spectroscopy is normally used not only to study the electronic structure of molecules, but also reactions in which chemical bonds are formed, broken or rearranged in general. The electrons are located in a space around the nucleus, which is called orbital. These atomic orbitals (AOs) represent the probability density of the electrons and can be further characterized. This is described elsewhere. To sufficiently describe the orbitals of a molecule, a so-called linear combination of atomic orbitals (LCAO) is done which can result in a formation of a molecular bond and thus, a molecular orbital (MO). These MOs can be further divided into binding, nonbinding and anti-binding orbitals, which will not be described in detail here.[42]

To study the electronic transitions, the energy difference between two MOs is looked upon. However, if the energy of a photon matches that energy difference between two MOs, this will not necessarily lead to a photoexcitation, as a variety of additional selection rules must be obeyed, nevertheless. At first, the



multiplicity of the system must be conserved. The multiplicity describes the total number of spins  $M$ , which can be calculated from the total spin angular momentum  $S$  ( $M=2S+1$ ) and can formally not change from e.g. a singlet ( $S=1$ ) to a triplet ( $S=3$ ). Then, the LAPORTE rule must be given, which states that the parity of a system must change for any electronic transition, e.g. from  $g$  (german: *gerade* (even)) to  $u$  (german: *ungerade* (uneven)) or *vice versa*.<sup>[43]</sup> However, this rule only applies to centrosymmetric molecules, which are rarely observed, as the symmetry is often disrupted upon excitation.

In case of a transition from the ground state (i) to an excited state (j) of a system, the charge density is shifted or displaced, which can be theoretically described by the transition dipole moment  $\mu_{ji}$  in Eq. (2.3), with the dipole operator  $\mu$  and the wave functions of the ground and excited state  $\Psi_i$  and  $\Psi_j$ , respectively.

$$\mu_{ij} = \int \Psi_j^* \mu \Psi_i dt \neq 0 \quad (2.3)$$

Due to the fact that the mass of the atoms and electrons are considerably different, the wave functions of those can be analyzed separately, which is also called the BORN-OPPENHEIMER-approximation.<sup>[44]</sup> Moreover, as the electronic transitions are faster than the nuclear motions, photoexcitation will always occur vertically (without a change of nuclear coordinates) and more likely into a higher vibrational state, which is also known as the FRANCK-CONDON-principle. The actual probability of a transition is then determined via the squared transition dipole moment  $|\mu|^2$ , which itself is connected to the oscillator strength  $f$ , given in Eq. (2.4). This equation comprises the mass of an electron  $m_e$ , the frequency of the transition  $\nu_{ji}$  and the elementary charge  $e$ .

$$f = \frac{8\pi^2 m_e \nu_{ji}}{3he^2} \quad (2.4)$$

The oscillator strength  $f$  is in turn proportional to the extinction coefficient  $\epsilon$ , which displays the strength of a transition on a macroscopic scale, as shown in Eq. (2.5), comprising the extinction coefficient at the maximum of an absorbance band  $\epsilon_{max}$  and the full-width at half maximum of the absorbance band  $\Delta\tilde{\nu}_i$ .

$$f \sim \frac{\epsilon_{max} \Delta\tilde{\nu}_i}{2.5 \cdot 10^8} \quad (2.5)$$

This equation connects the theoretical description with experimental values, as the molar extinction coefficient  $\epsilon$  is a quantity in the BEER-LAMBERT-law, which correlates the extinction  $A$  to the sample concentration  $c$  and the sample thickness  $d$ , as given in Eq. (2.6).

$$A = \epsilon(\lambda) \cdot c \cdot d = -\log_{10} T = -\log_{10} \frac{I}{I_0} \quad (2.6)$$

In practice, the extinction is determined via the transmission  $T$ , which is defined as the ratio of the intensity of the transmitted light ( $I$ ) to that prior to the

absorption ( $I_0$ ). However, the law is only valid in a distinct concentration range, due to effects of e.g. aggregation. Nevertheless, it is one of the basic equations in spectroscopy and is not only valid for electronic, but other forms of transitions as well.

### 2.1.2 INFRARED ABSORPTION SPECTROSCOPY

The wavelengths from 3-50  $\mu\text{m}$  are assigned to the mid-infrared (IR) range, which corresponds to a wavenumber range from 3333-200  $\text{cm}^{-1}$ , which is the typical unit for this part of the electromagnetic spectrum. The corresponding energies of 0.413-0.025 eV can induce transitions between vibrational states. Provided that the molecules undergo changes in the dipole and hence become IR-active, IR-spectroscopy can be used to investigate the vibrational changes.[45]

In a simplified diatomic model, the vibrations can be described by a displacement of atoms from its resting position and the chemical bond as an elastic spring. A harmonic potential can then be applied, which would allow the system to be described by HOOKE'S law Eq. (2.7), with the force constant  $k$ , the distance  $r$  and the distance in the resting position  $r_0$ .

$$V(r) = \frac{1}{2}k(r - r_0)^2 \quad (2.7)$$

The frequency  $\nu$  of the harmonic oscillator is described by Eq. (2.8), in which the masses of the two atoms are combined into the reduced mass  $\mu = \frac{m_1 \cdot m_2}{m_1 + m_2}$ . After quantum mechanical consideration, equidistant and quantized energy levels are found which is described by Eq. (2.9), with vibrational quantum numbers  $v \in \mathbb{N}^0$ .

$$\nu = \frac{1}{2\pi} \sqrt{\frac{k}{\mu}} \quad (2.8)$$

$$E_v = \left(v + \frac{1}{2}\right) h\nu \quad (2.9)$$

With this, the zero-point energy of the system is located at  $E_0 = \frac{1}{2}h\nu$ . Only vibrational transitions complying with the selection rule of  $\Delta v = \pm 1$  are allowed for the harmonic oscillator. This representation, however, insufficiently describes the critical states at very low or large distances, e.g. the possibility for a dissociation after a bond breaking,[46] which is why an anharmonic oscillator or so-called MORSE-potential is used for a more realistic description (see Eq. (2.10)).

$$V(r) = D_{eq} \left[1 - e^{\beta(r_{eq}-r)}\right]^2 \quad (2.10)$$

This equation contains the newly introduced parameters  $D_{eq}$  as the dissociation energy and  $\beta = \sqrt{\frac{k}{2D_{eq}}}$  for the stiffness, furtherly introducing  $k_e$  as the force

constant at the minimum of the well. Again, after quantum mechanical consideration the energy levels are no longer equidistant, as shown in Eq. (2.11) with the anharmonic constant  $\chi_e = \frac{h\nu}{4D_e}$ .

$$E(v) = \left(v + \frac{1}{2}\right) h\nu - \left(v + \frac{1}{2}\right)^2 \chi_e h\nu \quad (2.11)$$

The selection rule for a vibrational transition in the anharmonic case is expanded to  $\Delta v = \pm 1, \pm 2, \pm 3, \dots$ [47, 48]

Due to the large number of possible vibrations, which a molecule can exhibit, several subdivisions are made. Valence or stretching vibrations classify the change of distance along the atoms, whereas deformation vibrations are used to describe whether the molecule changes its shape. Further categorization is done by evaluation into an anti-/symmetric stretching, depending on the general change of the molecule's symmetry. In total, if a molecule consists of N atoms, then  $3N-6$  (for nonlinear molecules) or  $3N-5$  (linear molecules) vibrations can be found, which are also called normal modes.

### 2.1.3 RELAXATION PROCESSES

Absorption of a photon leads to a transition from the ground state to an energetically higher electronic and/or vibronic state. The electronic structure of this excited state usually differs from the ground state, caused by the large difference of masses, which is in agreement with the BORN-OPPENHEIMER-approximation. Based on that is the FRANCK-CONDON-principle, which neglects the atomic movement during the electronic transitions, resulting in a vertical excitation. The homonym FRANCK-CONDON-region denotes the resulting higher vibrationally excited states.

Consequently after photoexcitation, the system will relax back into the ground state, which can happen either radiationless or by emission of photons (radiative deactivation). Firstly, the non-radiative deactivation processes, which are usually more likely to happen, are shortly summarized in the following: After photoexcitation into the FRANCK-CONDON-region, intramolecular vibrational relaxation (IVR) into an energetically lower (or lowest) state occurs. The energy is locally absorbed by a molecular orbital and distributed intramolecularly to the neighboring atoms and then subsequently the whole molecule and the surrounding solvent molecules. The latter could result in an increased temperature, which is why this process is also called vibrational cooling.[49, 50] Hereafter, internal conversion (IC) can occur, in which the system can further relax to a vibrationally isoenergetic state of an energetically lower electronic state. This can occur via a conical intersection (CI) of two electronic potential surfaces, whereas one of these surfaces could belong to a subsequent reaction intermediate or product. IVR, vibrational cooling or IC are processes which typically occur on time scales

of picoseconds to nanoseconds. Despite the rule that the multiplicity must be conserved, singlet-triplet-transitions (or *vice versa*) can occur also. This so-called intersystem crossing (ISC) requires a spin-flip of an electron and therefore is a slower process, compared to transitions, in which the multiplicity is unchanged. Subsequent IVR or IC can repeatedly take place, until the electronic ground state  $S_0$  is reached, without any emission of photons.

Radiative deactivation processes, however, include the fluorescence and phosphorescence, which describe the singlet-singlet or triplet-singlet transition from an electronically excited state to the ground state, respectively. Fluorescence is very fast and the lifetimes are typically found on a time scale of  $10^{-12}$ – $10^{-9}$  s. Phosphorescence is longer-lived, because an ISC must occur and can therefore range from microseconds to several seconds or even longer. Given the fact that IVR is even faster than the fluorescence, the latter will typically occur from the  $S_1$ -state, which is described by KASHA'S rule. An extension of this rule is the KASHA-VASILOV-rule, which states that the fluorescence, as well as the reaction quantum yields for a subsequent photoreaction always occur from the lowest excited state. Therefore, these processes are independent of the excitation wavelength. However, several exceptions are already known to this rule.[51–53]

Thus, the energy of the emitted photons is still lowered in most of the cases due to the described preceding processes. The corresponding red-shift of the emission wavelength compared to the excitation is described by the STOKES-shift.[54]

In the Jabłoński-diagram (Figure 2.1), most of the previously described processes are summarized, such as the UV/vis-absorption, as well as the different relaxation processes.

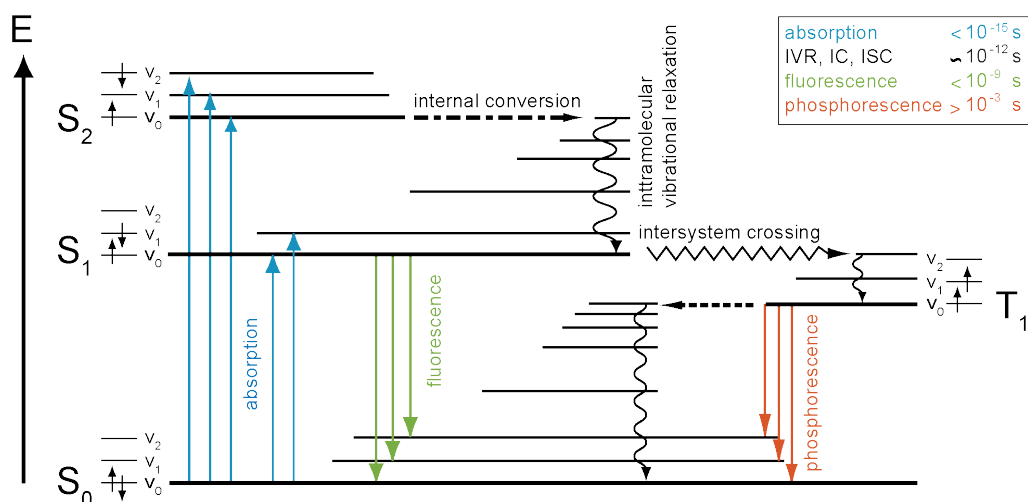


Figure 2.1: The Jabłoński diagram summarizes the deactivation processes after photoexcitation. The diagram is adapted from reference [55]

## 2.2 NONLINEAR OPTICS

The fundamental wavelength of the laser system used in this work is located at 775 nm. The spectroscopic investigations of the samples require the ability to change this wavelength and moreover be able to record spectrally broad absorbance spectra, however, the laser is not tunable. Therefore, nonlinear mixing processes are used, which are only accessible at high intensities of light, which can be achieved with lasers. These mixing processes are based on the fact, that the the polarization of a medium is not anymore linearly dependent on the the light intensity.

### 2.2.1 NONLINEAR EFFECTS

At low light intensities, the polarization vector  $\vec{P}(t)$  is proportional to the induced electric field, the field constant  $\epsilon_0$  and the first-order molar susceptibility of the medium  $\chi$ , as shown in Eq. (2.12).

$$\vec{P} = \chi^{(1)} \cdot \vec{E} \cdot \epsilon_0 \quad (2.12)$$

In nonlinear media, this equation becomes more complex, as the dielectric polarization vector does not respond linearly to the electric field.[56] A Taylor-series can then be used for an approximate understanding, which is given in Eq. (2.13), in which each term is described by a corresponding  $\chi^{(n)}$ , which is the  $n^{\text{th}}$ -order susceptibility, or  $(n+1)^{\text{th}}$ -rank tensor.

$$\begin{aligned} \vec{P}(\vec{E}) &= \vec{P}^{(1)} + \vec{P}^{(2)} + \vec{P}^{(3)} + \dots \\ \vec{P}(\vec{E}) &= \left[ \chi^{(1)} \vec{E} + \chi^{(2)} \vec{E} \vec{E} + \chi^{(3)} \vec{E} \vec{E} \vec{E} + \dots \right] \cdot \epsilon_0 \end{aligned} \quad (2.13)$$

The electric field vector for a plane wave, which is shown in Eq. (2.14), can then be inserted. This vector consists of two components, each with their own frequency  $\omega_i$  and propagation direction  $\vec{k}_i$ , which is omitted here for the sake of simplicity.

$$\vec{E} = \vec{E}_1 \cos(\omega_1 t) + \vec{E}_2 \cos(\omega_2 t) \quad (2.14)$$

The higher-order processes can only be observed at high electric fields, whereas most of the ones observed in laser spectroscopy are second-order effects. Insertion of Eq. (2.14) into the corresponding term gives Eq. (2.15), which can be subdivided into further terms of the sum.

$$\Rightarrow P^{(2)}(\omega) = \epsilon_0 \chi^{(2)} [E_1 \cos(\omega_1 t) + E_2 \cos(\omega_2 t)]^2 \quad (2.15)$$

$$= \frac{\epsilon_0 \chi^{(2)}}{2} (E_1^2 + E_2^2) \quad (2.16a)$$

$$+ \frac{\epsilon_0 \chi^{(2)}}{2} [E_1^2 \cos(2\omega_1 t) + E_2^2 \cos(2\omega_2 t)] \quad (2.16b)$$

$$+ \epsilon_0 \chi^{(2)} [E_1 E_2 \cos((\omega_1 + \omega_2)t)] \quad (2.16c)$$

$$+ \epsilon_0 \chi^{(2)} [E_1 E_2 \cos((\omega_1 - \omega_2)t)] \quad (2.16d)$$

Equation (2.15) shows that the superposition of two waves leads to the generation of new frequencies. The term Eq. (2.16)a describes the optical rectification, which causes a constant quasi-direct-current polarisation within the material[57], whereas Eq. (2.16)b consists of double the frequency of the initial frequency, which is called second harmonic generation (SHG).[58] Eq. (2.16)c and Eq. (2.16)d describe the frequency which is created when the sum or the difference of the initial frequencies are taken, denoted as sum frequency generation (SFG) and difference frequency generation (DFG), respectively.

Effects of higher-order, such as the  $\chi^{(3)}$ -process, require higher energy to be observed. The most prominent applications include self-focusing and self-phase modulation (SPM), which are part of the optical KERR-effect.[59]

**PHASE-MATCHING CONDITIONS** Apart from the high-intensity, nonlinear effects can only be induced if the two waves are able to constructively interfere with each other. To decide whether and which one of the previously mentioned conversion effects will occur, energy and momentum must be conserved. In case of the latter, the phase-matching conditions must be fulfilled, which is dependent on the wavelength and the refractive indices of the medium. Typically for  $\chi^{(2)}$ -effects, three waves are considered, where  $\vec{k}_1$  and  $\vec{k}_2$  are the vectors of the initial wave and  $\vec{k}_3$  that from the resulting wave. In case of a fulfilled phase-matching condition, Eq. (2.17) must be fulfilled. A mismatch of the phases is described as the difference of both sides of the equations and should ideally be  $\Delta\vec{k} = 0$ .

$$n_3 \vec{k}_3 = n_1 \vec{k}_1 + n_2 \vec{k}_2 \quad (2.17)$$

An ideal phase-matching cannot always be found for any kind of medium, due to the frequency-dependence of the refractive index of the medium  $n(\omega)$ , the dispersion and the resulting different phase velocity  $v_{ph}$ , which is defined by Eq. (2.18).

$$v_{ph} = \frac{c_0}{n(\omega)} = \frac{\omega}{\vec{k}} \quad (2.18)$$

The different waves will pass through the medium with different velocities, which will subsequently lead to a destructive interference. To circumvent this effect, birefringent crystals are used. The change of their refractive indices depends on the polarization of the electric field of the incoming wave, which is why they are called anisotropic media. An appropriate positioning of such an anisotropic medium to the initial waves, the wave vectors and refractive indices can be aligned to each other, and phase matching can be achieved.

**GROUP VELOCITY DISPERSION** When considering the frequency conversion for light pulses, not only phase-matching conditions, but also the group velocity needs to be taken into account as well. The group velocity  $v_g$  of a wave describes the velocity of the wave package travelling through a medium. It is described by the first derivative of the wave vector, which is given in Eq. (2.19).

$$v_g = \frac{\delta\omega}{\delta\vec{k}} \quad (2.19)$$

This equation implies that the group velocities, with which the signal travels, is dependent on the frequency, leading to a dispersion over time of the components of the laser pulse. The group velocity dispersion (**GVD**) describes the frequency-dependent delay of the different spectral components of the laser pulse and is shown in Eq. (2.20). It is defined as the first derivative of the reciproke of the group velocity  $v_g$ .

$$GVD(\omega_0) = \frac{\delta}{\delta\omega} \left( \frac{1}{v_g(\omega)} \right) = \frac{\delta}{\delta\omega} \left( \frac{\delta\vec{k}}{\delta\omega} \right) = \frac{\delta^2\vec{k}}{\delta\omega^2} \quad (2.20)$$

Within a normally dispersive medium, the components with the higher frequencies travel slower than those with lower frequencies, which results in a positively chirped pulse. Analogous to this, a negatively chirped pulse describes the reverse case, where components with higher frequencies travel faster than those with lower frequencies.

### 2.2.2 SUPERCONTINUUM GENERATION

Supercontinuum describes a spectrally broad laser pulse.[60] The generation of such is theoretically a rather complex process and requires a high-intensity, ultrashort laser pulse. For an isotropic medium, the laser pulse induces a change of the refractive index, which relies on the **KERR**-effect as a third-order nonlinear process, as shown in Eq. (2.21).

$$\begin{aligned} \vec{P} [\vec{E}(\omega)] &= \vec{P}^{(1)} [\vec{E}(\omega)] + \vec{P}^{(3)} [\vec{E}(\omega)] \\ &= \epsilon_0 [\chi^{(1)} \vec{E}(\omega) + \chi^{(3)} \vec{E}(\omega) \vec{E}(\omega) \vec{E}(\omega)] \\ &= \epsilon_0 \underbrace{[\chi^{(1)} + \chi^{(2)} |\vec{E}(\omega)|^2]}_{\chi_{eff}} \vec{E}(\omega) \end{aligned} \quad (2.21)$$

The resulting effective susceptibility  $\chi_{eff}$  can be rewritten as an expression for the refractive index (Eq. (2.22)), when considering, that the relative permittivity  $\epsilon_r$  is the squared of the refractive index and can be described with the higher-order tensors. After several relations, which are omitted here,[61] an expression

for the refractive index results, which includes an intensity-dependent refractive index  $n_2$  (Eq. (2.23)).

$$n = \sqrt{1 + \chi^{(1)} + \chi^{(3)} |\vec{E}(\omega)|^2} \quad (2.22)$$

$$n(t) = n_0 + n_2 I(t) \quad (2.23)$$

Due to the fact that the time-dependent intensity of the laser pulse  $I(t)$  is considered,  $n(t)$  is now able to describe both the intensity- and time-dependent refractive index. This change in the refractive index affects the frequency and phase of the pulse, which is called *SPM*. Thus, the laser pulse will be changed, whereas the front and back part of the pulse will, in comparison to the original frequency of the laser pulse, shift to lower and higher frequencies, respectively. As a consequence, the additional frequencies lead to a broadening of the spectrum, creating the observable *white-light*.

### 2.2.3 OPTICAL PARAMETRIC AMPLIFIER

The nonlinear optical effects of second-order can be additionally used to parametrically split a frequency into two smaller ones, however, energy and momentum conservation must be given. The energy transfer between the involved waves is used in an optical parametric process. The initial wave is referred to as the *pump-wave*, whereas the desired wave and the one resulting from energy conservation are called *signal-* and *idler-wave*, respectively. The initial wave will always be split, independent from the orientation or type of the medium. If, however, an additional so-called *seed-wave* with a specific frequency is directed into the medium, an amplification depending on the wave's frequency will take place, which is then called optical parametric amplifier (*OPA*). This requires the *seed-wave* to spatially and temporally overlap with the *pump-wave*.

When the *seed-* and *pump-waves* are directed in a noncollinear way into the medium, amplification will also occur, and is then called noncollinear optical parametric amplifier (*NOPA*). This widely-used technique has the advantage that parametric amplification can be achieved over a wide spectral range, without changing the phase-matching angle of the medium. In ultrafast laser spectroscopy, the *GVD* of the *seed-wave* is utilized, by generating a supercontinuum. Due to the dispersion of the spectral components of the supercontinuum, the temporal overlap of both pulses can be adjusted to amplify a broad pulse (instead of a distinct frequency in a collinear process). By further variation of the phase-matching angle and the angle between the two pulses, the *NOPA* can be used to efficiently convert frequencies, so that wavelengths within a spectral range of 450-1200 nm are obtained.



## 2.3 TIME-RESOLVED PUMP/PROBE SPECTROSCOPY

The knowledge about the velocity of reaction is a fundamental requirement to understand (bio-)chemical processes. These chemical reactions can occur on different time scales and can range from femtoseconds ( $10^{-15}$  s) up to days. For the elucidation of the reaction paths, technical methods are necessary which are able to temporally resolve the occurring processes. In spectroscopy, the resulting time-resolved spectra will then contain information about the dynamics of a reaction.

### 2.3.1 THE PUMP-PROBE EXPERIMENT

One of the most prominent techniques to obtain time-resolved data, is the pump-probe experiment. Independent of the covered time range, the principle of this method is always the same. The sample of interest is excited with the so-called *pump*-pulse and thus put into a higher electronic or vibronic state. With this, the photoreaction is initiated and the time zero point of the measurement is defined. The previously described relaxation processes can then occur which are measured by an additional absorbance measurement of the sample, which is carried out by the *probe*-pulse. By repetitively changing the time delay between the two pulses, a large amount of information on the photodynamics can be gathered. The general scheme of a pump-probe experiment is illustrated in [Figure 2.2](#).

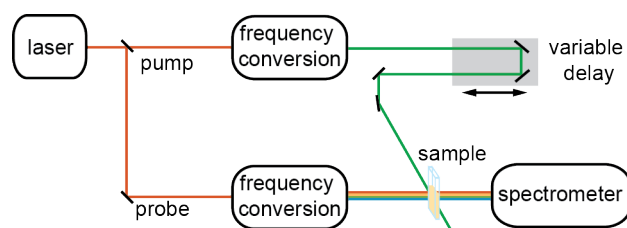


Figure 2.2: Principle of pump-probe-spectroscopy.

In the time range above nanoseconds, the delay between the pump- and probe pulse can be achieved electronically, meaning that a device will control the time difference between pumping and probing of the sample. This method is often referred to as a flash-photolysis experiment. In an alternative approach, probing of the sample is not achieved by a secondary pulse but by continuous illumination. In the first case the temporal limit is given by the duration of the probe-pulse, whereas the alternative is limited by how fast the detector is able to record the data in quick succession.

The overall time range is limited by the electronical jitter of the two pulses with respect to each other, which is why alternatives are necessary to cover the dynamics in the fs-ns time range. However, this requires even shorter laser pulses. In ultrafast spectroscopy, the pulses are manually adjusted to each other,

that they travel different distances before entering the sample. This is realized by a delay stage on which a retroreflector is mounted. Its position is changed in small steps of ca.  $2\ \mu\text{m}$  which corresponds to a time delay of 7 fs. With a maximum displacement of 60 cm (two times the length of the delay stage), delay times of up to 2 ns can be achieved. The overall time resolution of the experiment is then solely dependent on the length of the laser pulse.

### 2.3.2 FUNCTIONALITY OF A LASER

The most typical light source for ultrafast spectroscopy is a laser, which is an acronym and stands for light amplification by stimulated emission of radiation. The basic principle was introduced in the late 1950s,[2] and the first built in 1960,[3] and since then lasers have been widely used in different fields of applications since. A laser usually comprises three components, an energy (or pump) source, a gain (or laser) medium and an optical resonator (or optical cavity). Similar to spontaneous emission, the process can be induced, which is then called stimulated emission. In order to achieve stimulated emission, instead of absorbance by the laser medium, a population inversion must be realized throughout the whole process. The inversion can only be achieved when gain media with a three- or four-level system are used.

The laser process is then initiated by injecting light from the energy source (optical pumping) into the gain medium. The laser light then circulates within the resonator (e.g. two mirrors), in which the laser medium is placed for further amplification. After several round trips, the laser light gains intensity and can then be coupled out. However, a correct operation is only achieved, when the gain is larger than the losses, otherwise the laser threshold is not overcome, which would result in emission of fluorescence.

The described process will then lead to continuous wave (*cw*) laser emission with a distinct frequency and high intensity.

### 2.3.3 GENERATION OF ULTRASHORT LASER PULSES

In order to achieve pulsed lasers, additional procedures are necessary. Having ultrashort laser pulses is inevitable, if one wants to investigate ultrafast dynamics of processes. The limit of achieving high temporal resolution is only given by HEISENBERG'S uncertainty principle,[62] which therefore requires pulses with a large bandwidth. Generation of such pulses are typically achieved by Q-switching or mode locking, whereas the later is usually divided into active or passive mode locking.

**Q-SWITCHING** At the beginning of the generation of a Q-switched pulse (sometimes: giant pulse), the laser light is kept in the optical cavity. A turned off Q-switch (e.g. **POCKELS** cell or acousto-optic modulator (**AOM**)) ensures, that the laser light stays within that resonator. The associated Q-factor is defined

via the energy storage and is proportional to the ratio of the energy within the resonator and the dissipation per oscillation cycle (Eq. (2.24)).

$$Q = 2\pi \frac{E_{\text{resonator}}}{E_{\text{loss/cycle}}} \quad (2.24)$$

Once the Q-switch is activated, the losses become very low, resulting in a high-intensity pulse and a large Q-factor. The length of the pulse is then determined by the time with which  $Q \leq 1$  is reached again, and typically in the range of a few nanoseconds with a repetition rate of 1 Hz-1 kHz.

**ACTIVE MODE LOCKING** By using mode locking, ultrashort laser pulses can be generated with pulse widths of 30 fs to 30 ps and repetition rates in the MHz-GHz range. In the case of active mode locking, an active element (e.g. an optical modulator) is used to periodically modulate the resonator losses or the round-trip phase change. Synchronization of the modulation rate to the round-trip time of the resonator will generate ultrashort pulses.[63]

**PASSIVE MODE LOCKING** In the case of passive mode locking, e.g. a saturable absorber is used.[64] This is an optical component with a certain optical loss, which will be reduced when high laser intensities are applied. Whenever a pulse hits the component, it saturates the absorption, thus reducing the losses. Moreover, it can modulate the resonator loss much faster than an electrical one, resulting in even shorter pulses.

In our case, KERR-lens mode locking (KLM) (or self mode locking) is used, which causes a reduction of the beam size for high optical intensities and therefore leads to a preference of the pulsed operation.

**CHIRPED-PULSE AMPLIFICATION** The short pulses can then be further amplified, which is often realized by chirped-pulse amplification (CPA).[65] The pulses are chirped and temporally stretched by a dispersive element and then directed through the amplifier medium, which is also a gain medium. The stretching is done to reduce the laser intensity to avoid damage on the optical cavity and the gain medium. After amplification, the pulse is then compressed by another dispersive element.

The importance of having ultrashort pulses for applications is further highlighted by the recent Nobel Prize in 2018 in Physics, which was awarded to A. Ashkin, G. Mourou and D. Strickland for their contribution on the generation of high-intensity, ultra-short laser pulses.[13]

#### 2.3.4 OCCURRING SIGNALS

The resulting transient signals contain information about the absorbance, the wavelength and the delay time, which is the difference between the pump and

probe pulse. Typically, only difference signals are recorded, with respect to the non-excited sample. This results in either a positive or negative absorbance change, which can then be divided into three types of signals. Photoexcitation of the sample will lead to a transition into an electronic excited-state, which causes a loss of ground-state population. This is also called ground-state bleach (GSB) and is observed as a negative signal around the wavelength of the ground-state absorbance. The populated excited-state is then able to absorb photons, which leads to an increase of absorbance in that wavelength range. This effect is called excited-state absorption (ESA). Lastly, stimulated emission (SE) can occur, which would appear as a negative signal in the transient map, as the emitted photons suggest a decrease of the absorbance.

### 2.3.5 KINETIC ANALYSIS

The evaluation of the transient data was done by the program OPTIMUS[66], which is able to do two kinds of analytical methods, lifetime density analysis (LDA) and global lifetime analysis (GLA), whereas only the latter was applied within this work. Prior to the assessment, the data set was corrected by the time zero, which is caused by the chirp of the supercontinuum. This is done by fitting the time zero to a polynomial function of the order  $n \leq 4$ . Moreover, the coherent artifact was identified to be able to distinguish it from the data set of the investigated sample. This artifact occurs around the time zero, when the *pump*- and *probe*-pulse overlap, and leads to cross-phase modulation due to the high intensity of the pulses. This effect is compensated by measuring the solvent under ideal conditions, so that the photodynamics cannot be induced, and fitting a model of Gaussian functions including its first and second derivative to the data. The found parameters are then applied to the measurement containing the sample of interest. All transient maps shown in this work are corrected by both the chirp and the coherent artifact.

**GLOBAL LIFETIME ANALYSIS** This analytic method was applied to all transient absorption measurements in this work. It is a model-dependent procedure that simplifies the transient data set  $S(\lambda, t)$  by describing it with a distinct sum of exponential terms, as shown in Eq. (2.25). The fit parameters are entered by the user via a number  $n$  of lifetimes  $\tau$ .

$$S(\lambda, t) = \sum_j^n A_j(\lambda, \tau_j) \exp(-t/\tau_j) \quad (2.25)$$

The pre-exponential factors  $A(\lambda, t)$  are adapted by the program during the fit and give the decay-associated spectra (DAS). Due to this simplified approach, the fitting of the data is much faster and requires less computational resources. Moreover, many reactions indeed follow an exponential decay and therefore this approach is sufficient in most cases.

**LIFETIME DENSITY ANALYSIS** Compared to the the GLA, this method is model-independent and does not require a fixed number of functions. Instead, a continuous distribution of exponential terms is applied, which is shown in Eq. (2.26).

$$S(\lambda, t) = \int_0^{\infty} \Psi(\lambda, \tau) \exp(-t/\tau) d\tau \quad (2.26)$$

In mathematical terms, the measured data set  $S(\lambda, t)$  is viewed as the LAPLACE-transform of the density function  $\Psi(\lambda, t)$ . However, the integral is transformed into a quasi-continuous sum in computer-based calculations, due to numerical reasons. Then, the density function is determined by an inverse LAPLACE-transformation, which can lead to oscillations in the resulting transient map, caused by noisy data. To minimize this effect, a regularization factor for the transformation is introduced. It is then up to the user to evaluate this factor and decide which resulting lifetime density map (LDM) sufficiently describes the data set.

The main advantages of LDA is the ability to distinguish complex dynamics, which are not necessarily dependent on exponential decays.



## THEORETICAL BACKGROUND - SAMPLES

---

This chapter provides a brief introduction on the theoretical backgrounds of the investigated samples. After a short description about the types of molecules, which are investigated in this work, certain aspects and details about the system are described. Lastly, the investigated systems are put into the context of applications from different points of view.

[Section 3.1](#) introduces the background of the biochemical molecules, which were investigated in this work. A brief description of nucleic acids and their building blocks are given, followed by a short summary on helicases. Hereafter, photocages are introduced ([Section 3.2](#)), with an emphasis on the photochemistry of *o*-NB cages, of which a derivative was investigated in this thesis. Introductory remarks on photoswitches are given in the last section of this chapter ([Section 3.3](#)), in which the differences and commonalities with photocages are shortly highlighted.

### 3.1 RIBONUCLEIC ACIDS AND HELICASES

In the following section a short overview on ribonucleic acid (RNA) and a special class of proteins are given. The general structure as well as the functions are introduced briefly in the context of this work. Regarding the proteins, the emphasis is set onto the helicases. Its name already implies that they separate double helices. More information on either macromolecule can be found in the vast literature in the fields of biochemistry.[\[67, 68\]](#)

#### 3.1.1 RNA

The term *central dogma of molecular biology* was firstly used by Francis CRICK in 1958 and describes the directions of information flow in gene expression. It comprises deoxyribonucleic acid (DNA), ribonucleic acid (RNA) and proteins.[\[Crick1958, 69\]](#) Several processes are related to that dogma, describing e.g. the interaction of DNA to RNA (transcription) and RNA to protein (translation), whereas others are not possible at all, like the information transfer from protein back to both nucleic acids.

Especially the importance of RNA could be demonstrated within the last decades, showing that it is not merely a passing molecule between DNA and protein, but contributes to the translation from messenger RNA (mRNA) to protein.[\[70, 71\]](#) In fact, due to their diversity they can be subdivided into a multitude of classes,

such as transfer RNA (tRNA), micro RNA (miRNA), and smaller nuclear RNA (snRNA).[67] Another widely investigated class are the riboswitches, which are basically mRNA, carrying functional elements in the 5'-untranslated region (5'-UTR). They are known to regulate the processes described by the central dogma of molecular biology upon ligand binding.[72]

RNA is typically made of an oligomeric strand and is made up of four different nucleotides: adenosine (A), cytidine (C), guanosine (G) and uridine (U), which are shown in Figure 3.1. Those building blocks consist of the associated nucleobases (adenine, cytosine, guanine and uracil, respectively), which have a ribose ring in common, giving the nucleic acid its name. The unit is then described as a nucleoside, which in turn can additionally contain up to three phosphate residues at the 5'-end of the sugar unit (nucleoside mono-/di-/triphosphate). The phosphate at the 5'- and the 3'-end can then be chain-joined, creating a strand of different building blocks, which is then referred to as the backbone of the RNA. In a similar fashion, DNA comprises of four nucleotides as well, whereas thymidine (T) is used instead of U. Moreover, the alternative pentose 2-deoxyribose is being used.

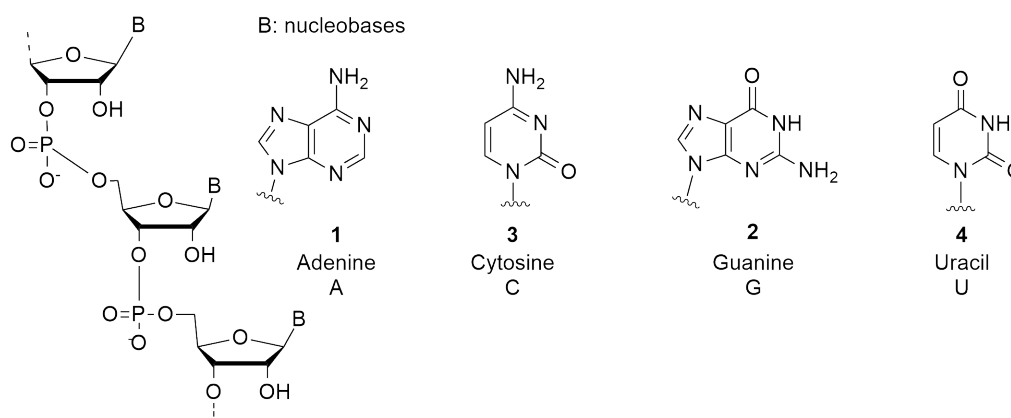


Figure 3.1: Nucleotides

While the sequence of nucleotides makes up the primary structure of the RNA, its chemical properties highly dependent on local, structural conformations. For this, the nucleobases can form so-called WATSON-CRICK base pairs, which occur between A and U (or T, in case of DNA), or G and C, and are stabilized by two or three hydrogen bonds, respectively. Two sequences of RNA oligomers can form a stable structure, provided that they are complementary to each other. If the several bases of one strand find fitting bases for base-pairing on the other, the single-stranded (ss) RNA can then become a double-stranded (ds) RNA. The pairing occurs from head to tail, meaning that the 5'-end of one strand binds to the 3'-end of the complementary counter-strand. However, the length of the strands does not necessarily have to match and an overhang at either the 5'- or 3'-end may be possible.



### 3.1.2 HELICASES

For further processing of the RNA, e.g. for translation or other RNA-protein interactions, it might be essential for the RNA to be present in a single-stranded form. However, the formed H-bonds in dsRNA are very energetic and require other means of separation. Due to the high specificity of the RNA-protein interactions, wrongly folded RNA-strands can also halt further processing. In both cases, the unwinding of the RNA duplex is realized by a specific class of proteins, namely the helicases. The name is derived from the fact that these proteins unfold double helices upon base-pair disruption, which is executed in an ATP-dependent reaction. Thus, DNA helicases also exist which can be discovered in the context of DNA replication or repair.[73–75]

By contrast, RNA unwinding is performed to either start a new effort to correctly obtain the native conformation or to linearize the strand permanently for further processing, which includes mRNA splicing, the initiation for translation, or RNA degradation.[76–78] The latter example is one of the key steps in the previously described central dogma, which makes RNA helicases indispensable to all forms of life. This leads to a vast variety of helicases, making it important to characterize the different mechanistic features, interaction partners, processivity, etc.

Regarding the processivity, two mechanisms prevail, by which RNA helicase enzymes can unwind the folded RNA: Members of the processive group often translocate along single-stranded RNA and remove paired strands (or even proteins) in their path. The translocation (or movement from one area to another) often requires a recognition feature as a starting point. On the other hand, the nonprocessive group catalyzes local strand-separation, resulting in the linearization of the strand. Both groups bind RNA differently and utilize different mechanisms for the displacements of the strands.[79] Common features are used to categorize the helicases into super families (SF), or further subgroups.

In most bacteria, the multiprotein complex degradosome plays a key role in the processing and degradation of the RNA. Among others, the RNA helicase RhlB, which is investigated in this work, is one of proteins found in the degradosome of *Escherichia coli* and is part of the DEAD-box family.[77, 80] Although four other DEAD-box helicases exist in *E. coli*, RhlB is the only one, which is part of this degradation machinery.[81] Members of DEAD-box family share the common Motif II, which contains the amino acid sequence D-E-A-D (asp-glu-ala-asp), giving the family its name.[82] The superordinate DExD-box family (where x can be any amino acid) belongs to the group of nonprocessive RNA helicases.[79]

Other proteins in the degradosome include the Polynucleotide Phosphorylase (PNPase) and Ribonuclease E (RNase E), which are both responsible for the catalysis of the degradation of the processed RNA.[83, 84] It was shown that they play a major role in the RNA degradosome, as in the absence of RhlB, the degradation process would still take place for linearized RNA. However, the reaction was obstructed, when dsRNA containing a stable stem-loop, was added.

The recovery of activity could only be recovered upon addition of Rh1B and ATP, which emphasizes the importance of the helicase as part of the degradosome.[77]

## 3.2 PHOTOCAGES

Photocages are small chemical compounds that can be activated by light, which causes a chemical cleavage of bonds, leading to the release of another molecule. They are usually used to trap a biologically active compound (acting metaphorically as a cage), whose release and subsequent reaction can be studied once activated. Detailed information on the photocages can be found in the various review articles.[85–90]

### 3.2.1 GENERAL INFORMATION ON PHOTOCAGES

The utilization of light offers many advantages, as it can be applied with a high spatial and temporal resolution. Depending on the wavelength of the applied light, it will be non-invasive and not harm the biochemical environment. Moreover it is ecological and can be exploited for various applications, e.g. in medical therapy where lasers are readily used. Often, the applicability is limited by technical restrictions (e.g. laser power, tunability of illumination wavelength), and the affordability of the necessary setups. However, certain conditions on the photocages are also necessary to be fulfilled for most kinds of biological applications.[91] These prerequisites mainly revolve around the biochemical environment, in which the photocages are to be applied in. Others can be summarized by demands on the photophysical specifications of the photocage, which will also touch some technical criteria.

First and foremost, the photocage should be non-toxic, which applies to the released photoproduct as well. Naturally, the activated bio-compound will not cause any harm to the surrounding cell, however the chemical residue of the cage after photorelease should not exhibit any signs of cytotoxicity as well.

For the cage to be used in biological conditions, they must be water-soluble. With regards to the solubility, the caged compound must be chemically stable in the aqueous environment, or else a hydrolysis reaction will preempt the release. In case an application in cell biology is desired, a minimal degree of permeability of the cell membrane is necessary.

Ideally, photodeprotection should occur at wavelengths above 300 nm. Because many biomolecules will absorb light in the ranges of 260 nm and 280 nm, the absorbance maximum of a cage should be located at higher wavelengths, or else the absorption of incoming photons will become a competitive process. Furthermore, photoexcitation at these specific wavelengths can lead to photodegradation of the biological compounds, which is why the design of new

photocages is driven to shift the absorbance maximum to higher wavelengths.[26, 92] As a result, frequencies with lower energies are utilized for the uncaging reaction, creating milder conditions within the biological environment.

However, an upper limit also exists for the excitation wavelength, as water will also absorb at wavelengths above 900 nm.[93] In order to utilize photons with higher wavelengths, nevertheless, two-photon absorption (2PA) can be initiated. This method also enables the circumvention of absorbance maxima below 300 nm. In the process of 2PA, the same electronic state will usually be populated by simultaneous absorption of two photons with double the frequency. This method was firstly predicted by Maria Göppert-Mayer in 1931,[94] and enables a precise initiation of the reaction, as only few femtoliters ( $1 \cdot 10^{-15}$  L) are excited. For a reasonable photolysis, the so-called two-photon action cross-section should be large enough, which has been the motivating force for many studies.[95–97]

The equivalent of this value for the one-photon absorption is the efficiency, which ought to be high as well. It is defined as the product of the molar extinction coefficient  $\epsilon$  of the photocage at the absorption maximum and the uncaging quantum yield  $\phi_u$ . A high value of  $\epsilon$  would only require small doses of light to be effectively absorbed by the compound. The uncaging quantum yield can be viewed as the probability of a reaction to occur and is defined as the ratio of the number of released molecules to the number of absorbed photons. Ultimately, one of the factors ( $\phi_u$  or  $\epsilon$ ) can be compensated by a larger value of the other, but preferably both factors should be high.

Lastly, the kinetic events of uncaging must be fast. In fact, for a sufficient assessment of the subsequent biological process, the release of the biomolecule should proceed on a faster time scale than the process which is studied.[98] Generally speaking, the mechanism of uncaging reaction of caged compounds can proceed in two possible ways. The faster, solvent-assisted reaction releases the caged compound in an  $S_N1$ -fashion, whereas the alternative mechanism proceeds via an intramolecular rearrangement, which is observed for *ortho*-Nitrobenzyl (*o*-NB)-cages.[99]

### 3.2.2 PHOTOCHEMISTRY OF *o*-NB CAGES

The *ortho*-Nitrobenzyl (*o*-NB) cages are the most prominent representatives of photocages. Among the firsts to discover them were Engels *et al.*, who attached this photolabile compound to the second messenger 3',5'-cyclic guanosine monophosphate (cAMP) and successfully released it after irradiation in the near-UV region.[100] Since then, various improvements on the photophysical properties were achieved, and *o*-NB-cages could be successfully attached to larger molecules in diverse biological applications.[101, 102]

The general structure of the *o*-NB-cage (**5**, Figure 3.2) comprises a nitrobenzene with an alkyl-substituent in *ortho*-position. The leaving group (LG) is attached in  $C_{\alpha}$ -position. In case an ethyl chain is substituted to the aromatic ring, the resulting cage is often alternatively referred to as a 1-(2-Nitrophenyl)ethyl (NPE)-cage.

The general reaction mechanism after photoexcitation is shown in Figure 3.2 and is presumed to be identical for both *o*-NB- and NPE-cages, however small variations regarding some of the formation rates were observed.[103] Interestingly, multiple versions of this reaction scheme exist, which have been revised, disputed and challenged, with regards to the reaction rates and subsequently the rate-limiting step of the reaction.[103, 104] Nonetheless, the general scheme of the reaction can be summarized into four steps.

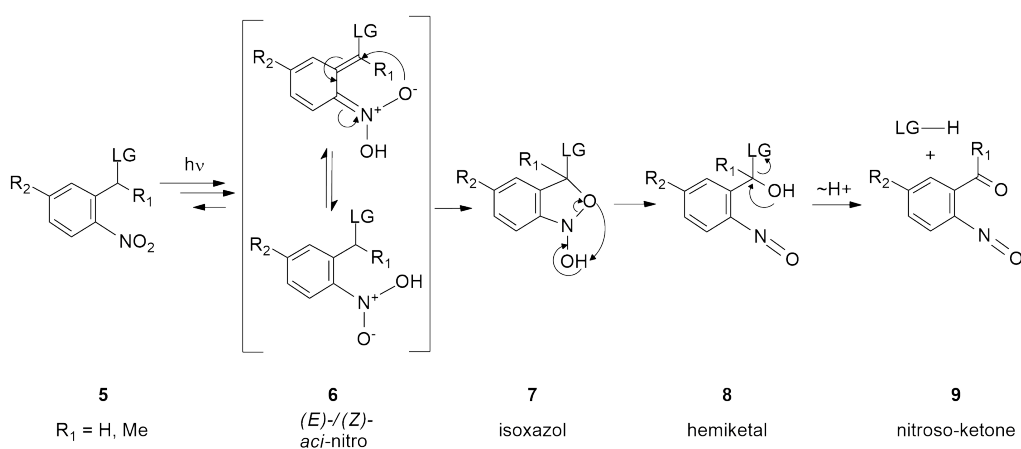


Figure 3.2: General reaction mechanism of *o*-NB cages, including the presumed intermediates after photoexcitation.

The key step and thus the most discussed part of the reaction is the formation of the *aci*-nitro intermediate **6**. After photoexcitation of the *o*-NB-cage, two possible pathways exist, with which the *aci*-nitro can be formed, namely the singlet[105] and triplet pathway[106], which is why two arrows are depicted in the reaction scheme. To identify, which of these pathways are taken, the utilization of ultrafast spectroscopical methods are required, as the *aci*-nitro intermediate is supposedly formed within the ps time range. Distinct spectral characteristics are relevant to the assignment of the pathways, which subsequently can also affect other photophysical parameters of the uncaging reaction such as the quantum yield.[107]

Hereafter, the *aci*-nitro can either react back to its former state, which is undesired, as it will not lead to the release of the leaving group, or form the isoxazol **7** in an intramolecular cyclization reaction. This step and all subsequent parts of the reaction are supposed to occur in a concerted way.[108] Hence, the decay of the *aci*-nitro intermediate is ascribed to be the rate-limiting step in most uncaging reactions of *o*-NB cages.

### 3.2.3 RESEARCH AND APPLICATIONS OF PHOTOCAGES

The focus of research within the field of photocages is mainly set onto the modifications of well-known representatives or development of new compounds, which exhibit improved photophysical properties to fulfill the requirements described earlier. The most prominent representatives of photocages within the last few years are shown in Figure 3.3 and comprise the previously described *o*-NB cages, compounds based on *para*-Hydroxyphenacyl (*p*-HP),<sup>[109, 110]</sup> boron dipyrromethene (BODIPY)<sup>[111]</sup> or derivatives of coumarin-4-ylmethyl.<sup>[112]</sup>

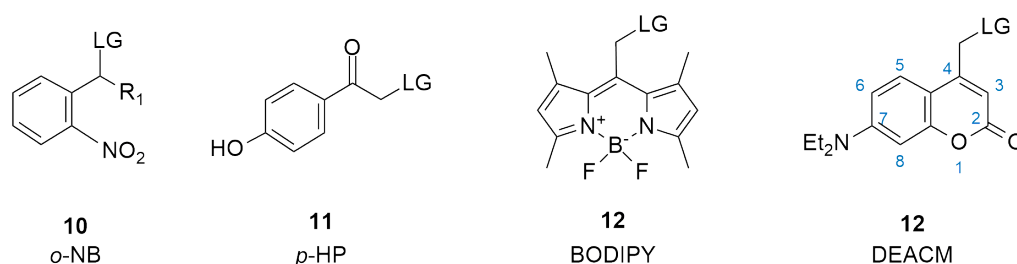


Figure 3.3: General chemical structure of prominent photocages

Chemical modifications of these compounds are often pursued to actively tune the absorbance maximum to higher wavelengths, increase the two-photon action cross-section, or for different kinds of biological applications. These compounds are often used to release small biologically active molecules, such as second messengers. These are intracellular signaling compounds, carrying encoded information<sup>[113]</sup>, with cAMP, phosphatidylinositol 4-phosphate (PIP), or  $\text{Ca}_2^+$  as its most prominent representatives. Whereas the successful caging of cAMP was described above by *o*-NB,<sup>[100]</sup> other derivatives of this cage were utilized to successfully cage calcium ions.<sup>[17, 114–117]</sup>

Another example for a small compound, which was caged successfully, is the amino acid glutamate.<sup>[118, 119]</sup> Recently a derivative of coumarin was used to cage glutamate, and the uncaging reaction monitored by means of ultra-fast time-resolved spectroscopy. Therein, the authors linked a readily available fluorophore to the coumarin moiety, which then functions as an antenna and increased the two-photon action cross-section.<sup>[120]</sup>

The large variety of possible applications for coumarins are applicable to many other fields of research as well. Due to their photophysical properties, they are often referred to as coumarin dyes and used as fluorophores.<sup>[121–123]</sup> The common core of 7-(diethylamino)-4-(methyl)-coumarin (DEACM) is shown in Figure 3.3 together with the numbering of the atoms. Depending on which position a chemical moiety is connected to, the resulting system will display different properties and can be applied differently. The attachment of an alkene photoswitch at position 3 will result in a highly efficient photoswitch with an

absorbance maximum in the visible absorption range. Such a photoswitch is investigated in this work.

### 3.3 PHOTOSWITCHES

Photochromic compounds or photoswitches are the other major class of photoactivatable compounds. When being attached to a larger biomolecule, they can be reversibly switched between two or more isomeric states,<sup>[124]</sup> possibly enabling an improved photocontrol over the underlying biochemical processes. Due to its diversification, several review articles for photoswitches exist.<sup>[125–129]</sup>

#### 3.3.1 GENERAL INFORMATION ON PHOTOSWITCHES

Common features and disparities between both photoresponsive systems are metaphorically illustrated in Figure 3.4, which also emphasizes the advantages of each system. For example, a modified biomolecule of interest, which would initiate a key reaction step, is trapped in either case of photochromic compound. This is typically achieved by a sterical hindrance of the additional modification, preventing it from being recognized by another biomolecule in a lock-and-key fashion. Photoexcitation of the cage will lead to a clean release of the biomolecule, restoring its actual bioactivity. On the contrary, excitation of a photoswitch will lead to isomerization, whereas the biomolecule is still attached to the photochromic compound. Ideally, the three-dimensional structure of the modified photoswitch in either isomeric state does not impede the subsequent initiation of the biochemical process, which highly depends on the recognition by the other biomolecule.

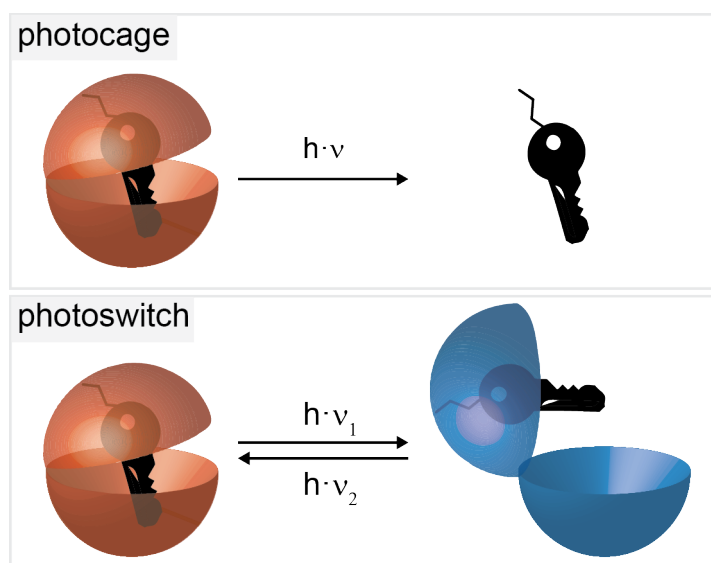


Figure 3.4: Metaphorical comparison between a photocage and a photoswitch.

However, photoswitches allow for a precise back-and-forth switching with regards to the biological activity, which is not possible at all for photocages. In general, the isomerization reaction can be induced not only photochemically, but often also thermally, which imposes another challenge onto the characterization of the photoswitch, because at least two reactions must be studied.

Apart from the prerequisite of recognition, other conditions to the design of a photoswitch apply, which are nearly identical to those described for photocages: Ideally, both states of a photoswitch are harmless to the biochemical environment, in which it is to be applied. Moreover, it should be water-soluble and non-hydrolyzable, as most of the applications demand a high stability in aqueous solutions. Here, many advances in research can be found, in which water-soluble azobenzenes or spiropyrans are presented - two of the well-known representatives of photoswitches.[130–135]

The photophysical properties of the photoswitch should be in a similar range to those of ideal photocages. A large efficiency, comprising both a high molar extinction coefficient  $\epsilon$  and the reaction quantum yield  $\phi_r$ , is desirable. Then, the absorbance maximum should be in a higher wavelength range, for the same reasons as why photocages should absorb e.g. visible light. Even though photoswitches do not have an uncaging reaction, which must be fast, analogously the two different states have to be obtained on a shorter time scale than the subsequent biochemical process.

Ideally, the photoswitch comprises of only two isomers with spectrally separated absorbance bands. This would facilitate the photophysical characterization and any form of subsequent application, as the isomers can be optimally addressed with different wavelengths, without causing any photoinduced back-reaction.

### 3.3.2 CLASSES OF PHOTOSWITCHES

The photoswitch investigated in this work is an alkene photoswitch, which was attached to DEACM, whose promising photophysical features were already briefly summarized in the previous section about photocages. However, due its novelty this photoswitch cannot be specifically allocated to one of the more well-known classes of photoswitches which are introduced in the following.

Similar to the different groups of photocages, a vast diversity of photoswitches exist. Despite the diversification, photoswitches can be subclassified into only two groups: Those who undergo a *cis/trans*-isomerization reactions and others, where a electrocyclization takes place leading to a ring-opening/closing reaction. However, photoswitches are typically grouped by the chemical structure, which provides more information on the actual isomerization reaction.

Figure 3.5 gives an overview of some classes of photoswitches, depicting (from left to right) azobenzenes[35] and stilbenes,[36] dithienylethenes (DTEs)[34] and

spiropyrans.[33] One reason for the subdivision is given exemplary on azobenzenes and stilbenes. Although both compounds undergo a *cis/trans*-isomerization and the nitrogen and the carbon atom are  $sp^2$ -hybridized, the latter lacks an additional lone pair, which in turn allows an additional reaction pathway for azobenzenes.[49, 136, 137] Furthermore, the chemical differences result in different photophysical properties, as e.g. a thermal back reaction is more commonly found in azobenzenes.[138–140] One noteworthy difference is the possibility of stilbenes to form a three-membered ring, which will react to phenantrene (not shown here) upon oxidation.[141–144]

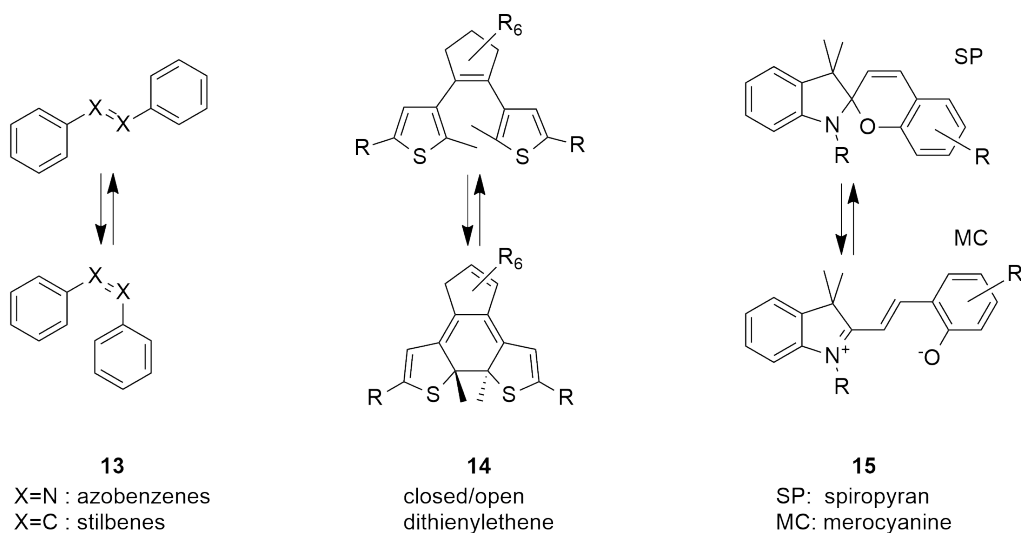


Figure 3.5: Exemplary classes of photoswitches, showing from left to right: azobenzenes and stilbenes, dithienylethenes and spiropyrans.

Countless examples for a large diversity of applications are found any class of photoswitch. Due to the high versatility of each class and the ability to chemically modify the general structure in almost any imaginable way, the number of potential applications seem endless. There have been advances in the field of material sciences,[145, 146], e.g. for a efficient on- and off-switching of a fluorescent dye,[37, 147, 148] or in the fields of energy and data storage, with photoswitches based on azobenzenes,[149–152] DTE[153, 154] or spiropyrans.[155, 156] Various examples for a biochemical or medical applications are found as well, e.g. in the fields of photopharmaceuticals, where drugs are controlled optically.[38, 157–159]



Part II

EXPERIMENTAL METHODS



## MATERIALS AND EXPERIMENTAL PROCEDURES

---

This chapter summarizes on the one hand, which chemical samples and the associated solvents were used, as well as its environment, such as the temperature, if applicable. On the other hand it describes the applied techniques, which were used to perform the spectroscopic investigations on the aforementioned sample.

At first, the biological samples, meaning the RNA strands and the helicase RhlB are described followed by the photocages and then the photoswitch ([Section 4.1.1](#), [4.1.2](#) and [4.1.3](#)). The used buffers and organic solvents are listed, hereafter ([Section 4.1.4](#)).

Subsequently, the methods and devices for the steady-state experiments are listed ([Section 4.2](#)). Their order matches their corresponding theoretical description, whereas the fluorescence Subsection is more elaborate, as few theoretical backgrounds regarding stopped-flow fluorescence and fluorescence quantum yield are briefly described here, with emphasis on the practical realization.

In the following section, the illumination procedures are described ([Section 4.3](#)). The last section concludes this chapter and provides an overview about the used setups for the time-resolved characterization. Initially the slower timescales in the  $\mu\text{s}$ -s are described for the absorption in the UV/vis ([4.4.1](#)) and IR ([4.4.2](#)) are described. Then, the technical description of the more complex setup for the investigations of ultrafast dynamics is explained ([Section 4.4.3](#)).

### 4.1 MATERIALS

The Materials section is subdivided into three smaller parts, which represent the three results chapters in this work. Firstly, the investigation on the biochemical samples involving a RNA duplex and a protein, namely the DEAD-box helicase RhlB, secondly the photoactivable compounds with the BIST-chromophore, and thirdly the photoswitch ceCAM.

#### 4.1.1 RNA AND PROTEIN COMPOUNDS

For the investigation of the RNA-protein interaction a variety of compounds were necessary. The unmodified, ssRNAs (named J2h and M2) were prepared and purified by H. Zetsche from the research group of Dr. Boris Fürtig (Goethe University, Frankfurt, Germany). The nucleic acid sequence of both strands in the duplexed form (JM2h) is shown in [Figure 5.1](#).

Additionally a modified version of M2 was investigated, where the A at the 6<sup>th</sup> position was replaced with 2-aminopurine (2AP). This so-called M2AP6 was provided by H. Zetsche.

The investigated protein RhIB is a DEAD-box helicase which was prepared and purified by H. Zetsche from the research group of Dr. Boris Fürtig (Goethe University, Frankfurt). The amino acid sequence is shown in [Section A.2](#), where the distinctive sequence DEAD is highlighted.

#### *Preparation of RNA Solutions*

The dsRNA was folded prior to performing the experiment to ensure that it is the correct conformation. For this, the dissolved RNA was heated to 95 °C for 10 minutes and then immediately stored on ice for at least another 10 minutes.

### 4.1.2 PHOTOACTIVATABLE COMPOUNDS

In this thesis four derivatives of bisstyrylthiophene (BIST)-cages are investigated. The cages are presented in [Chapter 6](#) and were synthesized and purified in the Ellis-Davies lab (Mount Sinai School of Medicine, New York, USA). The BIST-cages named BIST-amine, -ester and -ether were synthesized by Dr. H. K. Agarwal, whereas the derivative -NHnBu was synthesized by Dr. M. T. Richers. The general synthesis route is described elsewhere.[21]

### 4.1.3 PHOTOSWITCHABLE COMPOUNDS

The investigated alkene photoswitches or coumarin allylidene malonate (CAM) compounds were synthesized and purified by Dr. M. T. Richers (Ellis-Davies lab, Mount Sinai School of Medicine, New York, USA). The synthesis route is described elsewhere.[160] The cyanoester (ce)-derivative of CAM is presented and discussed in [Chapter 7](#).

### 4.1.4 SOLVENTS

**BUFFER SOLUTIONS** For the experiments involving RNA and proteins, a variety of different buffered solutions were used, which were prepared by H. Zetsche in the research group of Dr. Boris Fürtig. The used buffers differed mainly in the fact, whether the helicase was part of the experiments or not. For the steady-state and stopped-flow fluorescence measurement, as well as the time-correlated single photon counting (TCSPC)-experiments containing only RNA, the composition of the buffer was: 150 mM KCl, 25 mM  $K_xH_yPO_4$ , 1.5 mM  $MgCl_2$  at pH 6.2.

For all the measurements, where the helicase RhIB was present, the buffer contained 150 mM NaCl, 25 mM Tris, 1.5 mM  $MgCl_2$ , 5 mM DTT at pH 8.3.

**ORGANIC SOLVENTS** For the experiments described in [Chapter 6](#), dimethyl sulfoxide (DMSO) and chloroform (CHCl<sub>3</sub>) were used, which were obtained from ACROS Organics (Thermo Scientific, Waltham, MA, USA) (>99.7%, Extra Dry over Molecular Sieve, ACRO SEAL) and Fluka (Honeywell, Morristown, NJ, USA) (for UV-Spectroscopy) respectively. If water was added to the solution, doubly-distilled water from the Goethe University, Frankfurt was used. The experiments described in [Chapter 7](#) were mainly carried out in Acetonitrile (MeCN). This and all other solvents, which were used are shown in [Table 4.1](#).

Table 4.1: Solvents used in this work

solvent	grade	company
Acetone	NORMAPUR, >99.8% p.a.	
Acetonitril	CHROMANORM, >99.95%	VWR Chemicals
2-Propanol	NORMAPUR, >99.7% p.a.	(Radnor, PA, USA)
Toluene	NORMAPUR, >99.5% p.a.	
Ethanol	>99.8%, abs.	Fischer Chemicals
Methanol	Certified AR, p.a.	(Hampton, NH, USA)
Ethyl acetate	>99%, p.a.	Acros Organics (Waltham, MA, USA)

## 4.2 STEADY-STATE EXPERIMENTS

Steady-state experiments were carried out in the UV/vis- and IR-range. This section lists the used devices, technical settings and experimental details. In some cases, the experimental methods are briefly introduced, beforehand.

### 4.2.1 UV/VIS-ABSORPTION SPECTROSCOPY

Steady-state absorption spectra in the UV and visible wavelength range were measured using the diode array spectrophotometer SPECORD® S100 or S600 (Analytik Jena, Jena) and the corresponding program Aspect Plus 1.72(c) (S100) or WinAspect 2.5.0 (S600). The spectra were typically recorded from 180-900 nm, with an integration time of 70-110 ms which is mainly dependent on the stability of the lamps, but also on the spectrometer model used. Typically, 10 averages of the measurement were recorded. All recorded spectra were routinely baseline-corrected by subtracting all recorded values by the absorbance at a wavelength, where the sample does not absorb (typically: 800 nm).

Except for the experiments regarding RNA and/or protein, the procedure described hereafter is identical. The sample was prepared in a way, that the investigated absorbance band has an optical density in the range between 0.3 and 1.0. For this, usually 10x10 mm quartz glass fluorescence cuvettes were used

(Hellma Analytics, Müllheim), to enable an external, manual illumination from the side, as described in Section 4.3. The cuvettes were washed by storing them for at least one day in a solution containing 2% HELLMANEX (Hellma Analytics) in water.

In case of repetitive measurements, e.g. the procedures described in Section 4.3, the time intervals between the detection pulses were varied to optimally resolve the resulting transient course. For the illumination experiments on the BIST-cages, the full UV/vis spectrum was recorded, to enable the baseline correction. The studies on the fatigue-resistance of ceCAM were performed by cyclic measurements with alternating light-emitting diode (LED)s. When investigating less than 50 switching cycles, the full UV/vis-spectrum was recorded. Otherwise, only selected absorbances at certain wavelengths were retrieved to prevent an overload of data and the crashing of the used programs (e.g. the absorbance maximum; the absorbance at a wavelength, where the sample does not absorb, to enable the baseline correction; the absorbance at the isosbestic point to follow any photodegradation).

#### 4.2.2 FTIR SPECTROSCOPY

Investigations on the vibrational structure of the compounds, IR-spectra were recorded using a Fourier-transform infrared (FTIR)-spectrometer VERTEX 80 (Bruker, Billerika, MA, USA). The data were processed within the corresponding program OPUS 7.5. The sample chamber of the spectrometer was purged with either dry air or gaseous nitrogen prior to the experiment to exclude any contribution to the spectra from undesired IR-active compounds, such as air, or water vapor. The chamber was purged at 250 L/h, for at least 45 min to ensure a stable background signal.

Two possible detectors were used to record the IR-spectra: A deuterated L-alanine doped triglycine sulphate (DLαTGS)-detector is preferably used when recording steady-state IR-spectra over a longer time course, because they are their very high long-term stability. On the other hand, when performing time-resolved experiments, a mercury cadmium telluride (MCT)-detector was used. The downside of MCT-detectors is its limitation, that they require a cooling by liquid nitrogen ing to temperatures near that of liquid nitrogen (77 K), to reduce the noise caused by thermally excited current carriers.

Instead of the previously described cuvettes, the investigated sample was placed between two calcium fluoride windows, as these do not absorb IR-light. A TEFLON™ with a thickness of 50 μM (which corresponds to the path length in the BEER-LAMBERT law (Eq. (2.6)) was put in between the windows. A Polytetrafluor-ethylen (PTFE)-paste (Carl Roth, Karlsruhe) was used for fixation of the spacer and closure of the windows. The concentration of the sample was in the mM-range. If any illumination of the sample was performed, the optical density at the excitation wavelength was set to be in a range of 0.3-0.6. When working in

aqueous solution the IR-spectra were recorded with deuterated water instead.

The compartment lid of the spectrometer was modified and two holes were added, which allows an external illumination of the sample by e.g. a laser pulse. Within this work, illumination of samples was carried out within the sample chamber by mounting the LEDs on the designated holders. The cable from the LED was laid through the aforementioned tubes, to allow the regulation of the illumination intensity. The hardware, which was used is described in [Section 4.3](#). Unlike the absorption spectra in UV and visible range, there are two possibilities to correct the IR-spectra can be in two ways, which can also be done in a successive manner. Firstly, the measurements are performed with the purged gas as a background, which can also be used when recording a solvent spectrum. The latter can then be subtracted from the sample spectrum to yield only vibrations of the investigated compound. However, and this is done more often, double-difference spectra are obtained by measuring the IR-spectra of the samples with and without illumination. These illustration allows the exclusive visualization of vibrational changes upon illumination.

### 4.2.3 FLUORESCENCE SPECTROSCOPY

Steady-state fluorescence spectra were recorded using a FP-8500 spectrofluorometer (Jasco-Deutschland, Pfungstadt) and the corresponding program Spectra Measurement 2.4.0.1. The parameter settings were adjusted according to the investigated samples and its concentration.

The measurements were performed in either a 2·10 mm or 4·10 mm quartz-glass cuvette (Hellma Analytics) and the concentration of the samples was set as such that the optical density at the excitation wavelength was ca. 0.10 (except for the experiments where the fluorescence quantum yield was determined). Unlike the absorption spectra, the correction of the recorded fluorescence spectra was more complicated. The necessary corrections are described thoroughly in [Section 5.3.1](#), for which a MATLAB program was written and used.

Fluorescence spectra of JM2AP were recorded from 340-480 nm with a 1 nm resolution. Photoexcitation was set to 310 nm. The slit width was set of 5/5 nm and the photomultiplier tube (PMT) voltage to 500 V. For the titration experiment, in which the binding affinity was looked upon, that concentration of M2AP6 was set to 2.5  $\mu\text{M}$ . As a 1:1 ratio was assumed, the concentrations of the counter-strand J2h can be determined from the corresponding experiment in [Section 5.4.1](#).

Steady-state fluorescence with the RNA duplex and the helicase RhlB were recorded in preparation for the stopped-flow measurements. To determine possible residual fluorescence caused by any of the involved compounds and to have a reference system, different combinations of helicase RhlB, duplex JM2AP,

ATP and scavenger M2 were used. The combinations as well as the labels for the experimental data are listed in [Table 4.2](#).

Table 4.2: Composition of the steady-state fluorescence measurements involving the helicase RhlB. The legend denotes the label in the resulting plot of the measurement.

legend	RhlB 0.6 $\mu M$	JM2AP 500 mM	ATP 3 $\mu M$	scavenger M2 10 $\mu M$
RNA duplex		x	x	x
RNA reheated		x	x	x
RhlB	x		x	
full sample -ATP	x	x		x
full sample +ATP	x	x	x	x

For the BIST-cages, the fluorescence spectra were recorded from 350-800 nm with a spectral resolution of 1 nm, a slit width of 2.5/2.5 nm and a PMT voltage of 600 V. As the BIST-cages barely fluoresce, the optical density at the excitation wavelength of 455 nm was set to 0.3.

In case of ceCAM, the recording of fluorescence spectra was more complicated. Unlike the reaction quantum yield (described in [Section 7.2.4](#)) the fluorescence quantum yield ( $\phi_f$ ) is relatively low, so that either more accumulations or higher concentrations are necessary. Moreover, due to the actinic effect of the spectrometer (described in [Section 7.1.2](#)), the unavoidable excitation light for the fluorescence spectra causes a isomerization reaction of either investigated isomer. Therefore, a neutral density filter (1 OD, Schott AG, Mainz) was set in the excitation path of the compartment room to attenuate the intensity of the excitation light.

The fluorescence quantum yield ( $\phi_f$ ) of both the *cis*- and *trans*-isomer were determined in MeCN via the relative method (see below). For both the fluorescence spectra and the determination of  $\phi_f$ , the pss of the *cis*- and *trans*-isomers of ceCAM were used (described in [Section 4.3](#)). The excitation wavelength was set to 362 nm and 385 nm for the *cis*- and 530 nm for the *trans*-isomer. In either case, a dilution series was measured, in which the optical density at the excitation wavelength was below 0.25 to avoid reabsorption effects (namely ca. 0.05, 0.10, 0.15, 0.20, 0.25 OD). Each series were recorded over the course of a single day to avoid any possible external influences.

**DETERMINATION OF THE FLUORESCENCE QUANTUM YIELD** In analogy to the reaction quantum yield, the fluorescence quantum yield (fQY) is defined as the ratio of photons emitted through fluorescence to photons absorbed by the sample, as shown in [Eq. \(4.1\)](#) and gives the probability that such a process can



occur. Moreover it can also be defined as the ratio of the rate of radiation to the sum of all the rates for the deactivation processes.

$$\phi_f = \frac{n_{em}}{n_{abs}} = \frac{k_f}{k_f + k_r + k_{nr}} \quad (4.1)$$

In general, a “perfect” fluorophore cannot exist, as after photoexcitation, the molecules will quickly relax to the lowest vibrational state in the  $S_1$ . As this process contributes to the rate of non-radiation processes ( $k_{nr}$ ), the ratio of the fQY will always be smaller than 1. The experimental determination of the fQY can be achieved via two common methods, the comparative and absolute one.[161] In case of ceCAM, the fQY was determined via the comparative method.

The comparative (also called: relative) method requires the measurement of the fluorescence spectra of the sample of interest and another fluorophore with known quantum yields, whereas the latter is often called the reference sample, which should exhibit similar photophysical properties, such as the excitation and emission wavelength, and the fluorescence quantum yield. The equation which is typically used to determine the fQY is given in Eq. (4.2), in which  $F$  is the integrated area of the fluorescence spectrum of the investigated sample (index: *Sam*) and reference (index: *Ref*):

*fQY: the comparative method*

$$\phi_{f,Sam} = \phi_{fQY,Ref} \cdot \frac{f(\lambda)_{Ref}}{f(\lambda)_{Sam}} \cdot \frac{F_{Sam}}{F_{Ref}} \cdot \left( \frac{n_{Sam}}{n_{Ref}} \right)^2 \quad (4.2)$$

$$f(\lambda) = 1 - 10^{A(\lambda)} \quad (4.3)$$

The wavelength-dependent function  $f$  given in Eq. (4.3), is the amount of photons absorbed by the sample. Moreover, the refraction indices  $n$  of both the sample and reference solution are required. In this work, the determination of the relative fluorescence is based on a guide from Horiba (Middlesex, UK.[162] Therein, a slightly modified version of the typical experimental method is suggested. With a reference sample of identical absorbance, the amount of absorbed photons should be the same, thus a ratio of the integrated fluorescence intensities of both solutions will give the ratio of the quantum yield as well. To improve the accuracy of the determined value, typically a dilution series of both the sample and reference compounds is measured, usually containing five concentrations. The concentrations are set, so that at the illumination wavelength the absorbance is always  $<1$  OD (e.g, 0, 0.05, 0.10, 0.15, 0.20, 0.25 OD). This has the advantage, that reabsorption effects are minimized.

The experimental approach would be as follows: Steady-state absorbance and fluorescence spectra of the dilution series of both the sample and reference compound are recorded. The fluorescence spectra are corrected, which is thoroughly described in Section 5.3, followed by the integration of the area, for which the wavelength range must be kept the same for all measurements. Typically the stray light from the excitation is excluded, as this might vary for each measurement. Then, the integrated area is plotted against the absorbance at the

excitation wavelength, which will give a linear behaviour, if everything was done correctly. A linear fit of the data points is performed and the slope of both the sample and reference compound are inserted into Eq. (4.4). Due to the fact that a dilution series is investigated by this approach, more data points can be retrieved which will directly improve the accuracy of the determined value.

$$\phi_{f,Sam} = \phi_{f,Ref} \cdot \frac{m_{Sam}}{m_{Ref}} \cdot \left( \frac{n_{Sam}}{n_{Ref}} \right)^2 \quad (4.4)$$

It should be noted that the fit ideally passes the origin of the coordinate system, as no absorbance should be detected in the absence of the sample and solvent effects should have been eliminated in the appropriate fluorescence correction step (see Section 5.3).

With this approach for the comparative method, the error of the fQY can be easily determined via the propagation of errors and calculated from Eq. (4.5). The error of the fQY of the reference sample are known, e.g. are given in the literature ( $\Delta\phi_{fQY,Ref}$ ), the errors of the slopes are taken from the linear fits ( $\Delta m$ ) and the errors for the refractive indices are given by the manufacturer and are typically in the range of  $\Delta n = 0.005$ .

$$\Delta\phi_{f,Sam} = \sqrt{\left( \frac{\delta\phi_{Sam}}{\delta\phi_{Ref}} \right)^2 \left( \Delta\phi_{fQY,Ref} \right)^2 + \left( \frac{\delta\phi_{Sam}}{\delta m_{Sam}} \right)^2 \left( \Delta m_{Sam} \right)^2} \quad (4.5)$$

$$+ \left( \frac{\delta\phi_{Sam}}{\delta m_{Ref}} \right)^2 \left( \Delta m_{Ref} \right)^2 + \left( \frac{\delta\phi_{Sam}}{\delta n_{Sam}} \right)^2 \left( \Delta n_{Sam} \right)^2 + \left( \frac{\delta\phi_{Sam}}{\delta n_{Ref}} \right)^2 \left( \Delta n_{Ref} \right)^2$$

Altogether, this method is relatively easy to execute. Experimental errors are can be easily detected and eventually corrected, and determination does not require any additional devices. On the other hand, this approach is very time- and sample-consuming, as a total of 20 spectra are recorded, ideally within a short time frame (less than 1 day), to minimize external influences on the spectrometers and such. Often, the aforementioned errors are found during the processing of the data (and not during the measurements) with the consequence that all measurements must be repeated.

*fQY: the absolute method*

The alternative method, which is quickly executed and requires much fewer sample and spectra is the absolute determination, e.g. via a so-called integrating sphere, e.g. an ULBRICHT-sphere. In general, the determination of absolute fQY require the knowledge about device and measurement-specific parameters, which can be difficult to obtain.[163] Therefore they are more complex from an instrumental point of view, but once these parameters are obtained, the actual measurement is performed relatively quickly. The main advantage of this method is that it bypasses the necessity of fluorescence standards and therefore avoid uncertainties related to those.[161, 164]

The ULBRICHT-sphere is a hollow sphere which inside is covered with a material which scatters the excitation light (e.g. TiO<sub>2</sub> or BaSO<sub>4</sub>).[161, 165, 166] The cuvette

containing the sample is located near the center of the sphere and is excited via a small opening. After photoexcitation, the stray light and emission of the sample are reflected multiple times within the inside of the sphere before entering another small opening, where the light will be collected and sent to the detector, which records an ordinary fluorescence spectrum. For the determination of the absolute fQY this measurement is repeated with only the solvent under the exact conditions. By integrating the the whole spectra, the number emitted ( $n_{em}$ ) photons and those available for excitation ( $n_{ex}$ ) can be directly deduced from the measurement. Here it is important and necessary, to actually include the stray light of the excitation, as this predominantly represents the number of photons which undergo excitation. The ratio of both integrated areas ( $A$ ) will then give the fQY, as given in Eq. (4.6).

$$\phi_f = \frac{A_{em}}{A_{ex}} \quad (4.6)$$

The main disadvantage of this method is that it will only provide sufficiently well results, if the determined fQY is high enough (high than ca. 10%). Otherwise the signal-to-noise ratio (SNR) between both measurements too small to reliably determine the quantum yield. In general, the firstly described comparative method is the one regarded as being established, especially because of its high sensitivity, low costs and lastly its simplicity.

#### 4.2.4 STOPPED-FLOW FLUORESCENCE

The stopped-flow fluorescence measurements were carried out at a  $\pi^*$ -180 (Applied Photophysics, Leatherhead, UK) and the corresponding program PiStar 4.2.12 from the Schwalbe lab (Goethe University, Frankfurt).

The solutions were stored in a syringe prior to mixing, which was cooled at 10 °C with an external thermostat (Schwalbe lab). In preparation for the experiments, the tubes were washed with double-distilled water first and then with the buffer solution, in which the samples were stored (200 ml each). Following hereafter, 3-4 injections of the syringes containing the samples were necessary to condition the setup. Any residual fluorescence from the previous experiments could be traced. After mixing, the samples were excited at 298 nm and the fluorescence above 340 nm was recorded, for which a low-pass filter was used. For every measurement, 70  $\mu$ L from either syringe were injected into the mixing chamber.

For the measurements, in which the single-strands J2h and M2AP6 were mixed, 2000 data points were recorded linearly over a time course of 60 s. Five accumulations of mixing were performed and the transient course was averaged thereafter, to increase the signal-to-noise ratio. The concentration (regarding the final, mixed solution) of M2AP6 was constantly at 1  $\mu$ M, whereas the concentration of J2h was varied and set to 2/4/8 and 32  $\mu$ M.

In case of the measurements involving the helicase RhlB, the parameters were not changed, except for the time course, which was reduced to 30 s. The different mixtures and their respective concentrations (after mixing) are summarized in Table 4.3. It is important to prepare the solutions within the syringes accordingly, so that the reaction will not already take place before they are mixed. This would also prove, whether the functionality of the helicase RhlB is only given under the specific conditions. The used combinations as well as the names which were used in are listed in Table 4.3.

Table 4.3: Composition of the stopped-flow fluorescence measurements involving the helicase RhlB. The legend denotes the label in the resulting plot of the measurement. The measurement was carried out at a temperature of 10 °C.

legend	syringe 1		syringe 2	
	RhlB 5 $\mu$ M	JM2AP 50 $\mu$ M	ATP 3 mM	scavenger M2 50 $\mu$ M
RNA duplex		x	x	x
RhlB	x		x	x
full sample -ATP	x	x		x
full sample +ATP	x	x	x	x

**OPERATING PRINCIPLE OF STOPPED-FLOW (FLUORESCENCE) MEASUREMENTS** A stopped-flow device is used, to study fast chemical reactions which occur upon rapid mixing. Compared to the other described methods, the initiation is not achieved by absorption of a photon, but by bringing two compounds into spatial proximity. This is realized by two syringes which contain the solutions. A piston forces the solutions into a mixing chamber, which is subsequently directed into a observation cell. There, a third hard-stop syringe halts the flow and triggers the measuring device, which can either be an absorption or fluorescence spectrometer. The duration from the mixing chamber to the observation cell is called dead time and typically in the sub-ms range.[167] The time-resolution is then mainly determined by the speed of the spectrometer.

### 4.3 ILLUMINATION PROCEDURES

The experiments in this work revolve mainly around photoinduced reactions. For a distinct excitation of the samples, light sources with well-defined wavelengths are used, such as LEDs. For these illumination procedures, a Thorlabs (Newton, NJ, USA) LED driver DC4100 and DC4100-HUB was used in combination with mounted LEDs. For illumination within a steady-state UV/vis spectrometer SPECORD© S600, the LEDs were mounted onto a cubic cuvette holder (CVH100, Thorlabs). While the first optical axis was put in the light beam of the spectrometer, the second axis was used for illumination. Both optical axis had round holes with a diameter of 9 mm, which equals the size of the beam for illumination. To

avoid bleaching of the sample during the experiments, the sample was stirred by adding a stir bar to the cuvette and putting a magnetic stirrer (Variomag, H+P Labortechnik GmbH) below the cubic cuvette holder. The applied power of illumination was measured with a calibrated optometer sensor MD-37-SU100-2 (Gigahertz Optik, Türkenfeld). A lens was screwed on top of the LED, to ensure that most of the photons are directed onto the sample. Depending on whether UV/vis- or IR-spectra were recorded, different lenses were utilized.

For the experiments on BIST-cages, an LED with a central wavelength of 455 nm and a bandwidth (full width at half maximum (FWHM)) of 18 nm was used (M455L3, Thorlabs).

In case of the experiments on ceCAM, different sets of LEDs were used, to investigate the wavelength-dependence of the reaction quantum yield ( $\varphi_{\text{rqy}}$ ). For the *cis*-to-*trans*-isomerization, the solution was illuminated using a LED with a central wavelength of 385 nm or 405 nm and a bandwidth of 10 nm or 20 nm, respectively (M385L2, M405L3). In case of *trans*/*cis*-isomerization, the sample was excited using a LED with a central wavelength of 470 nm or 530 nm with a bandwidth of 25 nm or 33 nm, respectively (M470L3, M530L3). In any of these cases, ceCAM was illuminated until a so-called *pss* was reached, meaning that no changes absorbance spectra was observed by repetitive measured UV/vis-spectra. This implies, that the ratio of the *trans*- and the *cis*-isomer does not change anymore. As the composition of the *pss* is wavelength-dependent, the applied illumination wavelength is used as an index hereafter (e.g. *pss*<sub>405</sub>).

For some of the experiments, in which the isomerization reaction quantum yield of ceCAM was determined, the light of the LED was directed via an optical fiber from a self-built, enclosed, optical setup on top of the cuvette. This enabled the possibility of using the additional optical filters (Schott), to narrow down the excitation light even further. The filters were put in a filter holder between the LED and the optical fiber. For the *cis*/*trans*-isomerization, the LEDs with a central wavelength of 385 nm and 405 nm were combined with an interference (BG3) and a longpass filter (OG400, both SCHOTT). The LED used for the *trans*/*cis*-isomerization (530 nm) was combined with a OG530 and interference filter (IF528, both from Edmund Optics, York, UK), respectively.

For the fatigue-resistance measurements on ceCAM, cyclic measurements of the isomerization was achieved via alternating LED illumination. The duration of illumination was set as such that nearly a *pss* was achieved. The LEDs were operated via a LabVIEW routine (National Instruments, Austin, TX, USA) called Two-LED-Loop, which was written by Dr. S. Wahl (Wachtveitl lab, Goethe University Frankfurt)

## 4.4 TIME-RESOLVED EXPERIMENTS

Before and after every time-resolved experiment, absorption spectra in UV- and visible wavelength range were recorded to detect any possible photodegradation or changes in the composition of the sample in general.

Investigations on photodynamics can be divided into two time domains, firstly the region from femtoseconds (fs) to lower nanoseconds (ns) and secondly the region covering ns to milliseconds (ms) or even higher. The experimental setup covering the first time range is described in [Section 4.4.3](#), whereas the second region is described in [Section 4.4.1](#) (UV-vis) and [Section 5.6](#) (IR).

### 4.4.1 TRANSIENT FLASH-PHOTOLYSIS SETUP

The kinetics in the time region from ns to ms in the UV/vis were determined by performing (transient) flash photolysis experiments. The used setup is described elsewhere.<sup>[168]</sup> Excitation of the sample was achieved with a neodymium-doped yttrium aluminum garnet (Nd:YAG)-laser (Spitfire 600, InnoLas Laser, Krailing) which operates at a central wavelength of 1064 nm, a pulse width of 10 ns and a repetition rate of 10 Hz. The second harmonic generation (SHG) of this beam is generated (532 nm) and then passed to the optical parametric oscillator (OPO) (GWU Lasertechnik, Ertstadt) which is used to generate the desired wavelength for the experiment. The experiments BIST-cages were excited at 445 nm with a spot size of ca. 1 cm<sup>2</sup> and a pulse energy of 9.6 mJ·cm<sup>-2</sup>.

Probing of the absorbance changes in the visible was achieved by using a cw-light source (LIGHTNINGCURE LC8 L9588, type-4, Hamamatsu, Hamamatsu, Japan). The light was directed via an optical fiber onto the optical setup and then a monochromator (PTI, Photon Technologies International, Birmingham, NJ, USA), in which the desired probing wavelength can be manually selected. After passing through the sample, the light passes through another monochromator (identical in construction) to remove any stray light from the excitation pulse. A PMT (H6780-02, Hamamatsu) was used in combination with a self-built amplifier (J. Feldhaar, Heilemann lab, Goethe University Frankfurt) and sent to the digital oscilloscope (DPO5204B, Tektronix, Beaverton, OR, USA), at which the data can be saved on a USB-drive.

To record the time-zero point of the light-induced reaction, another photodiode (DET10A/M, Thorlabs) is placed in close proximity to the investigated sample, which is also connected to the oscilloscope and serves as the electronic trigger. The uncaging of BIST-NHnBu in DMSO with 20% H<sub>2</sub>O (or 100% CHCl<sub>3</sub>) were recorded with a sampling rate of 20 GS/s (100 MS/s) and a temporal resolution of 20 μs/div (10 ms/div).

The measurements were carried out in a quartz glass fluorescence cuvette (10.4 mm), while the longer path was used for the probing occurring absorbance changes. The sample was excited every 10 s and in total of 10 excitation events

were recorded, averaged and saved. As the file size of raw data is quite high (ca. 2-4 GB), the data was binned with the MATLAB program *OszDataReduction* 1.6 (P. Eberhardt, Wachtveitl lab). For the measurements of BIST-NHnBu in 20% H<sub>2</sub>O (or CHCl<sub>3</sub>), binning was performed firstly with a linear step size of 500 ns (100 ns) until 5 μs (10 μs), followed by 50 (150) logarithmic steps.

#### 4.4.2 TIME-RESOLVED IR-SPECTROSCOPY

As already described in [Section 2.1.2](#), IR-spectroscopy is a powerful tool to investigate the vibrations of molecules. To obtain further insights on how fast a vibration or chemical bond changes, time-resolved IR-spectroscopy can be used. Ideally, this allows one to understand the course of a reaction, as it would be possible to determine, e.g. in which order chemical bonds are being broken and subsequently reformed again.

If the reactions occur on a ps-ns time range, this can be realized by a UV/vis-pump IR-probe experiment, which is variation of the setup described later on. One major difference to that setup is the fact, that laser pulses with a frequency in the IR range need to be generated, which can be challenging. Chemical reactions which occur on a time scale above nanoseconds can be investigated by an IR-flash-photolysis setup, which works in analogy to the similarly named described above, as it simply requires a cw-IR light source for probing. This setup has been established just recently within the Wachtveitl lab.[\[169\]](#)

A simpler approach is achieved with the FTIR, which allows two techniques to record time-resolved spectra, which function differently.

**STEP-SCAN FTIR** To obtain information on the reaction dynamics in the upper range of nanoseconds to microseconds, step-scan FTIR can be used. This method is very similar to that of the transient flash-photolysis. The movable mirror is set to a fixed position and the investigated reaction is initiated, e.g. by a laser pulse. The transient course of the absorbance at that specific mirror position is recorded and, if necessary, measured multiple time and averaged. Then, the mirror is moved step-wise to another position and after a stabilization time, the reaction is initiated again.[\[170\]](#) The temporal limit is given by the electronics, which are used and is within the range of 10 μs for common devices, however, lower limits of 10 ns have been reported.[\[171\]](#)

One of the main disadvantages of step-scan is the lengthy experimental time, as multiple transients must be recorded at several mirror positions. As a consequence, only photostable compounds can be investigated with this method because e.g. the uncaging reaction of a photolabile compound would already be completed after a single scan.

**RAPID-SCAN FTIR** To investigate the vibrational changes on a time scale of milliseconds or above, rapid-scan FTIR can be utilized, which is less complex and easier to handle. Upon initiation of the reaction, multiple spectra are recorded

in rapid succession. The temporal limit of this method is therefore given by the speed of the moving mirror. Moreover, the time-resolution also depends on the spectral resolution, as a higher SNR in the spectrum requires a slower movement of the mirror. As with the step-scan technique, multiple cycles can lead to a higher quality of the data. However, photolabile compounds can be investigated with this method nevertheless, as in principle a single run is sufficient to yield a spectrum.

With currently available devices, measurements of up to 110 spectra per second can be achieved, which corresponds to a resolution of ca. 0.01 ms. However, when e.g. either a broader spectral range should be covered or a better SNR is necessary by recording more averages or a better spectral resolution is required, then the temporal resolution will decrease.

In this work, the uncaging dynamics of NPE-caged ATP was examined via a Rapid Scan-experiment. For this, NPE-ATP was dissolved in H<sub>2</sub>O and the concentration was set as such that the optical density was ca. 0.3 at the excitation wavelength ( $\lambda_{LED} = 365 \text{ nm}$ ,  $\lambda_{LED} = 365 \text{ nm}$ ,  $P = 3.5 \text{ mW}$ ). An IR-spectrum is recorded every 120 ms covering a range from 1550-900 cm<sup>-1</sup> was recorded over a time course of ca. 20 min (resulting in a total of 10,000 spectra).

#### 4.4.3 UV / VIS-PUMP UV / VIS-PROBE SETUP

This section can be divided into two parts: Firstly, the laser system is introduced, which was used for investigating the ultrafast dynamics, including some details about the occurring processes within beneath the cover. Hereafter, the elements of the setup are described. The setup, nicknamed ATAS (Advanced Transient Absorption Spectroscopy) was built by Dr. L. Dworak (Wachtveitl lab, Goethe University, Frankfurt) and is used to record transient absorption spectra in the UV/vis. The associated program ATAS\_Messprogramm\_V1.1 was used at this setup, to examine the stability of the white light, define the time zero point and ultimately record the transient data.

*Description of the used laser system*

For analysis of the ultrafast reaction dynamics in the fs to lower ns-range, a CPA iSeries (Clark-MXR, Dexter, MI, USA) laser system is used, which outputs laser pulses with a wavelength of 775 nm, a pulse width of ca. 150 fs and a power of ca. 1 W at a repetition rate of 1 kHz. A schematic illustration of the setup and its components is shown in Figure 4.1. The laser system is based on the principle of CPA and can be subdivided into four parts: the seed pulse, the pump pulse, the regenerative amplifier and the pulse compression.

*seed pulse*

For the generation of the **seed pulse** (shown in red) a laser diode (InGaAs<sup>1</sup>) is used as the pump source with a central wavelength of 980 nm and a power of 160 mW. The laser diode pumps the gain medium, which is an Er<sup>+</sup>-doped

<sup>1</sup> indium gallium arsenide



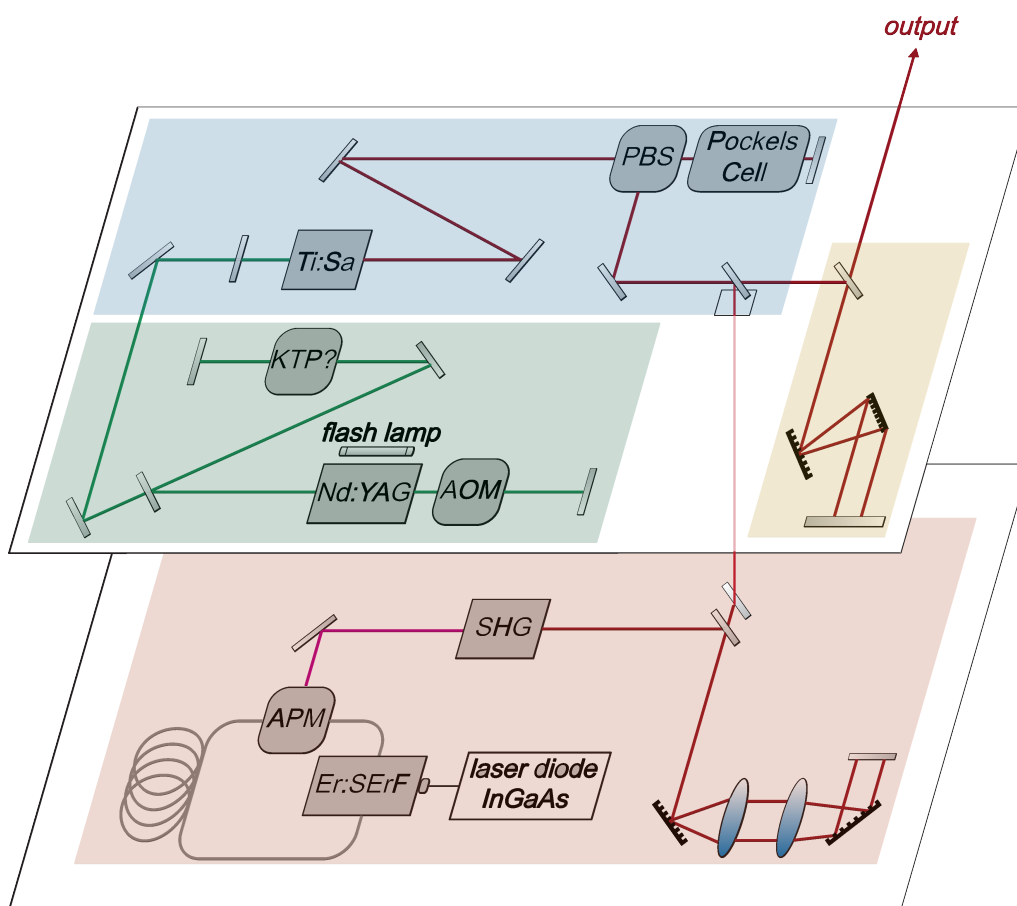


Figure 4.1: Schematical depiction of the used CLARK laser system. The generation of the seed pumpse (red), the pump pulse (green), the regenerative amplifier (blue) and the stretcher (yellow) illustrate the functionality of the used laser setup.

fiber oscillator (Er:SErF), yielding an emission wavelength of 1550 nm. Then, additive pulse mode-locking (APM) is used to generate short, optical pulses with high intensity. This process relies on utilizing waveplates ( $\lambda/2$ - and  $\lambda/4$ -plates) which non-linearly rotate polarization of the laser pulses, depending on their intensity-dependent. Thus, only the temporally central part of the pulse is amplified. Then, a PPLN<sup>2</sup> crystal is used to generate the second harmonic frequency, resulting in a seed pulse wavelength of 775 nm with a repetition rate of 35 MHz. Before entering the regenerative amplifier, the pulses are stretched temporally to avoid damages to the optical elements. The resulting pulse has a positive chirp with a pulse length of ca. 200 ps.

The **pump pulse** (shown in green) is generated by a Nd:YAG laser, consisting of a crystal with the same name which is pumped by a flash lamp resulting in a emission wavelength of 1064 nm. A KTP<sup>3</sup> within the resonator generates the

*pump pulse*

<sup>2</sup> periodically poled Lithium Niobate

<sup>3</sup> Potassium titanyl phosphate, KTiOPO<sub>4</sub>

second harmonic frequency. Moreover, an Q-switch is used (here an AOM) to generate short pulses of high intensity. A piezoelectric transducer attached to the AOM excites a sound (acoustic) wave, resulting in a periodic variation of the refractive index. The laser light passes the AOM and experiences a BRAGG diffraction, leading to a decrease of the optical frequency due to the sound frequency (state of low Q). As soon as the population inversion is achieved and the medium is *gain saturated* (high Q), the AOM is switched off and the high-intensity pulse can pass the resonator. This highly efficient process results in a pump pulse with a wavelength of 532 nm and an intensity of ca. 7 W at a repetition rate of 1 kHz.

*regenerative  
amplifier*

Both the seed and the pump pulse are directed into the **regenerative amplifier** (shown in blue) where the latter pumps a titanium-doped sapphire ( $\text{Al}_2\text{O}_3$ ) (Ti:Sa) crystal, leading to a emission in the wavelength range of 600-1000 nm. By optimally adjusting the temporal input of the seed pulse, its predetermined wavelength of 775 nm can be amplified by about a factor of  $10^6$ . For this, a Pockels cell in combination with a polarized beam splitter guarantee that only pulses which are adapted to the Nd:YAG laser are amplified. The pockels cell is operated at a repetition rate of 1 kHz and rotates the polarization of the transmitted light in a current-dependent matter. While the Ti:Sa is being pumped by the Nd:YAG laser, the Pockels prevents the seed pulse from being coupled into the crystal to avoid undesired stimulated emission. When the population inversion is established, the seed pulse is coupled in and the resonator closed. After 10-20 circulations in the resonator, the Pockels cell rotates the polarization again and the amplified stimulated emission is coupled out. The resulting pulse is then directed into the compressor (yellow), where it is temporally compressed to a final pulse length of ca. 150 fs.

*Description of the  
used setup (ATAS)*

The final output of the laser is directed to the measurement setup and split by a beam splitter (BS) into two parts: the pump and the probe branch. A schematic representation of the setup is given in several other works and is therefore omitted herein.[172, 173] The pump branch passes a variety of components before it is directed onto the motorized delay stage and then into the sample: Firstly, in a two-stage NOPA-process, the desired wavelength is generated (420-900 nm). The process is generated in a 0.5 mm-thick BBO crystal ( $\vartheta = 29^\circ$ , type II), which requires a supercontinuum, generated by focusing the fundamental into a sapphire crystal, and a pumping of the parametric process, which is generated in a 0.1 mm-thick BBO crystal ( $\vartheta = 30^\circ$ , type I[174]). Due to the fact that the pulse disperses between the two stages of the NOPA, it is directed onto a prism compressor, which compresses the NOPA-pulse to have a preferably short pulse width at the location of the sample. After passing the second stage of the NOPA for amplification of the pulse intensity, it can be directed into another crystal for SFG with the fundamental pulse. Hereafter, the pulse is is directed onto the delay stage, which is controlled externally by the measurement software. For detection of the absorbance changes, the probe branch is used. A supercon-

tinuum is generated in a calcium fluoride ( $\text{CaF}_2$ ) window, which is an alternative to using a sapphire crystal. Although  $\text{CaF}_2$  is a less stable material than sapphire and therefore requires a permanent movement in the  $x,y$ -plane, it generates white-light in a spectral range of 300-700 nm (sapphire: 450-1200 nm).[175] Another (less trivial) possibility to cover the UV region is to either create a supercontinuum with e.g. the SHG of the fundamental, or use LiF-windows (270-700 nm).[176, 177] The probe pulse is divided by a BS and directed to two separate detectors which record the absorbance of the sample with and without excitation of the pump pulse.

One of the splitted probe pulse and the pump pulse are focused in the same spot of the sample, whilst making sure that the diameter of the pump pulse is ca. 1.5 times larger to ensure that only the absorbance changes of the excited sample are detected. All measurements are carried out under magic angle polarization geometry, by placing a  $\lambda/2$ -plate in the pathway of the pump pulse after the delay stage. It is set to rotate polarization of the pump pulse to  $54.7^\circ$  relatively to the probe pulse, to reduce anisotropy effects.

In all experiments, the difference absorption spectra is recorded. For this, the absorption spectra of both the excited and non-excited spectra were taken. To overall improve the SNR the stray light of the excitation pulse is recorded in a third measurement. To realize this measurement scheme, one chopper wheel each (MC1F10, Thorlabs) rotating at a frequency of ca. 333 Hz (a third of the repetition rate of the laser) was placed in both the pump and probe branch of the setup, resulting in three events: The sample is only probed ( $I_{non-excited}$ ), both excited and probed ( $I_{excited}$ ), only excited ( $I_{straylight}$ ). As two detectors are used, this chopping scheme leads to a total of six signals, which are to be considered for the calculation of the difference absorbance.[173, 178]

In this work, a variety of pump pulses with distinct wavelengths were generated, based on different non-linear optical processes, which are described in detail in Section 2.2.1. The pump pulses with a central wavelength of 430, 440, 470 and 530 nm were all generated by a NOPA-process. For pump pulses of 362 nm, a NOPA-pulse and a subsequent sum frequency mixing (SFM) process was used. A NOPA-pulse with a central wavelength of 680 nm was used and focused ( $f = 250$  mm) into a BBO crystal ( $\vartheta = 32.4^\circ$ ), where it was spatially and temporally overlapped with the focused ( $f = 500$  mm) fundamental pulse with a wavelength of 775 nm.

The BIST-cages were excited at 430 nm, 440 nm and 470 nm. In case of the photoswitch the *cis*- and *trans*-isomer of cecAM was excited at 362 and 530 nm, respectively. The concentration of all investigated samples was set to exhibit an optical density of 0.3-0.6 at the excitation wavelength. To ensure comparable photostationary composition throughout all recorded scans in case of the photoswitch, the sample was constantly illuminated with LEDs with a central wavelength of 530 and 385 nm (M530L3 and M385L3, both Thorlabs).

The resulting transient data were processed with OPTIMUS 3.02, which were analyzed by GLA.[66] For every investigated photodynamics, a measurement containing the solvent was performed under nearly identical conditions to be able to fit the coherent artifact and apply it to the sample's measurements. The data which are shown in this work, were all corrected both the chirp of the white light and the coherent artifact.

Part III  
RESULTS



## RESULTS - HELICASE

---

The DEAD-box helicase RhlB is part of the multiprotein complex, called degradosome, which is found in *Escherichia coli*. The degradosome is primarily responsible for the processing of ribosomal RNA (rRNA) and the degradation of messenger RNA (mRNA), [179, 180] whereas the helicase RhlB is in charge of unwinding double-stranded (ds)-RNA. Understanding the general functionality and the unwinding reaction of helicases is one of the many domains in biochemical research. To be able to investigate the underlying reactions by means of optical spectroscopy, labels must be introduced into the structure of the samples, such as the fluorescence label 2-aminopurine (2AP) which is also used in this work. [181] However, monitoring the duplex unwinding by fluorescence spectroscopy requires sample concentrations, which are higher than those used in well-established biochemical methods, such as EMSA-based assays. [182]

These methods, however, are usually limited by the missing temporal resolution, at which data points can be recorded. They are usually applied to determine binding affinities and obtain information about the stoichiometry of complexes. [183] As a consequence, unwinding reactions with fast rate constants cannot be examined, and therefore require other spectroscopy-based methods. Stopped-flow fluorescence has been proven to be a reliable technique in this regard and was used to investigate both RNA and DNA helicases. [184–187] Despite the fact that larger amounts of samples are required, the key steps in unwinding are only accessible with time-resolved methods. Thus, steady-state, time-resolved and stopped-flow fluorescence spectroscopy were utilized, to obtain further insights into the functionality of the RNA helicase RhlB.

### 5.1 THE RNA-DUPLEX JM2H

The model RNA duplex, which is used in this work to investigate the helicase, is shown in Figure 5.1. It consists of a 46-mer single-stranded (ss)-RNA called J2h and a 21-mer named M2. If the duplex is investigated, the ds-RNA is named JM2h. This RNA duplex was thoroughly investigated by H. Zetzsche (Fürtig lab, University of Frankfurt) during her diploma thesis. Therefore, any relevant information regarding ideal concentrations, buffers, etc. are already well-known and can be applied to optical or nuclear magnetic resonance (NMR) spectroscopy. [188]

The design of this RNA-strand was chosen, to meet the requirements of the helicase for an ideal RNA-protein interaction. Thus, a stem-loop was implemented in the single-stranded J2h (nucleosides 30-35 with 40-45) which was known to serve as a loading platform for another DEAD-box protein CsdA. [189] For the

analysis with RhlB, this was included as well, independent of whether it would be needed later on. The length of the duplex was specifically chosen as such, because DEAD-box helicases typically unwind 1-2 helical turns (ca. 20 base-pairs). Moreover, in the duplexed form, the J2h-part has a 5'-overhang of two nucleobases, which might further facilitate the recognition by the protein and the subsequent formation of the RNA-protein complex. However, current research could already show that especially DEAD-box helicases prefer to have either a relatively long 5'- or a 3'-overhang to yield high efficiencies in unwinding, which does not necessarily have to be a loading platform.[190–192] In another approach, other model strands were investigated regarding the recognition and unwinding efficiency and currently require further optimization concerning the aforementioned sample conditions (e.g. buffer, concentration). Therefore, any measurements concerning protein-RNA interactions were performed on the established JM2h duplex and the results described in this chapter can then serve as a reference for future applications with other strands, which might exhibit improved characteristics.

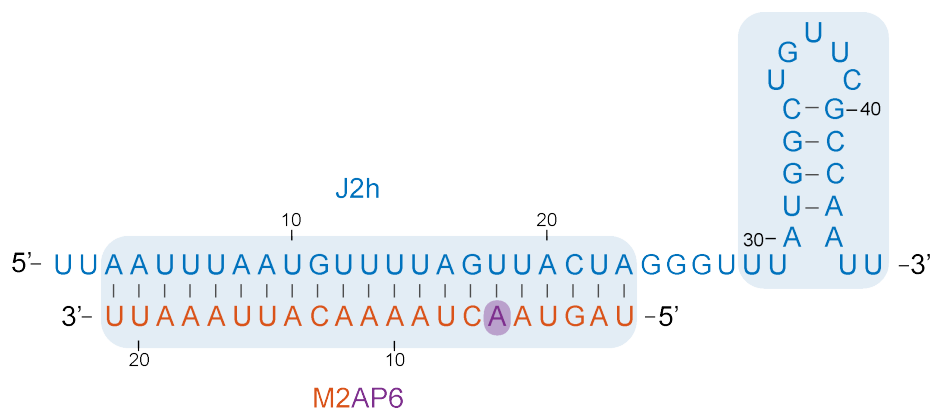


Figure 5.1: Sequence of test-duplex strand JM2h. The single-strand J2h (blue) is a 46-mer, which can form a stemloop. The 21-mer M2 is the corresponding counter-strand (red). In this work, 2AP was substituted at the 6<sup>th</sup> position (purple) to enable further investigations with fluorescence spectroscopy.

The helicase RhlB unwinds the RNA duplex by utilizing adenosine triphosphate (ATP) as an energy resource. Thus, the unwinding reaction can be examined from different perspectives, or even externally triggered, when using appropriate tools. The general core structure of ATP is shown in Figure 5.2 (black). It consists of the nucleobase adenine which is attached to a ribose sugar molecule (becoming a nucleoside called adenosine), as well as the triphosphate (nucleotide). Various applications of modified ATP are known to the literature,[193] some of which play a role in this chapter, as different modifications of it were used to address different aspects of the unwinding reaction. The generally proposed reaction mechanism is shortly described in Section 3.1.

In energy-converting reactions, ATP is normally hydrolyzed between the  $\beta$ - and the  $\gamma$ -phosphate groups.[193] In one of the modifications used in this work,



1-(2-Nitrophenyl)ethyl (NPE) was attached to the  $\gamma$ -phosphate group, rendering the whole molecule non-hydrolyzable and therefore halting any ATP-dependent reaction (red). The concept of photocages is described in detail in [Section 3.2](#). In fact, the characterization of photocages is one of the main projects described in this work within [Chapter 6](#). NPE-ATP is a special case, as it was one of the first photocages to be described in the literature.[194] The investigations on caged-ATP are described later in [Section 5.6](#).

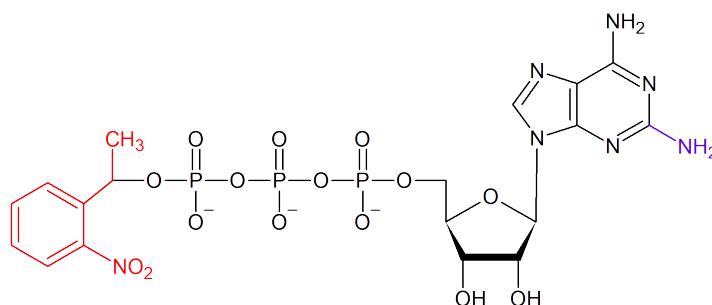


Figure 5.2: Chemical structure of ATP and differential modifications, which were used in this work. A modification at the phosphate moiety with a (2-Nitrophenyl)Ethyl-group gives NPE-caged ATP (red). To obtain the ATP analogue 2-aminopurine (2AP), the amino group is moved from position 6 to position 2 (purple).

Another modification of ATP, or rather adenosine, is 2-aminopurine (2AP). This molecule bears the amino group at the position 2 instead of position 6 (purple, [Figure 5.2](#)) and exhibits strong fluorescence compared to the naturally occurring adenosine. It could be shown for many applications that the incorporation of 2AP into RNA strands enables the possibility to perform fluorescence spectroscopy with the RNA, without changing the native RNA conformation.[181] When incorporated into both the single-strand and the double-strand, 2AP can still form WATSON-CRICK-pairs, which makes it a noninvasive tool to investigate base-pairing by fluorescence spectroscopy.

The general approach of this chapter is to investigate whether the DEAD-box helicase Rh1B exhibits a correct functionality and can unwind the model strand JM2AP. An assay for the investigations of duplex unwinding by RNA helicases, which is based on fluorescence spectroscopy, was already published by Putnam and Jankowsky just recently.[183] Therein, they used 2AP as a fluorescence label for their RNA model strands.

In this work, 2AP was incorporated into the single-stranded M2 at the 6<sup>th</sup> position. In case the 2AP-labeled strand is investigated, it is then renamed to M2AP6, whereas the duplexed form is now called JM2AP.

## 5.2 PRELIMINARY FLUORESCENCE MEASUREMENTS OF RNA SINGLE-STRANDS J2H AND M2AP6

First, the functionality of the 2AP-labeled strands is verified in steady-state and time-resolved fluorescence experiments. The results are summarized in this section.

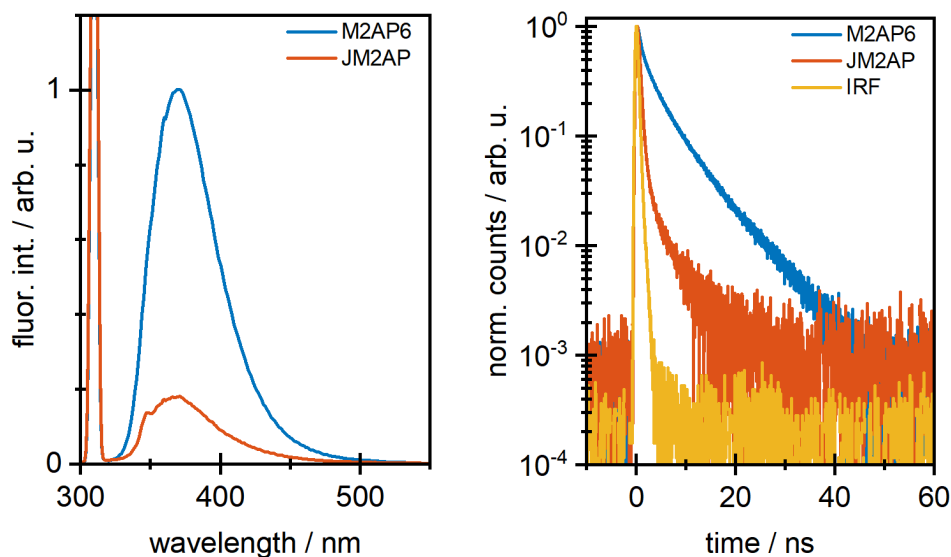
### 5.2.1 STEADY-STATE FLUORESCENCE

The steady-state fluorescence spectra of 2AP-labeled M2AP6 (blue), as well as JM2AP (red) are shown in [Figure 5.3a](#). Steady-state fluorescence spectra of J2h and M2 were recorded as well, but did not exhibit any significant fluorescence intensity and are therefore omitted in this figure. After photoexcitation at 310 nm, a single fluorescence band is detected with an emission maximum at 368 nm which does not change upon duplexation. In fact, the spectral shape stays the same, but the overall intensity decreases by a factor of ca. 2, due to base-pairing. As this observation is already known and well described, the absolute change of intensity can be used as a verification for a successful unwinding by the helicase. Alternatively, the duplexed sample and an excess of unlabeled M2 can be heated to 90 °C and cooled hereafter (analogous to the preparation of RNA solutions described in [Section 4.1.1](#)). During the cooling process, the so-called scavenger M2 will form the JM2h duplex and the solution would then have its initial increased fluorescence intensity again, resulting from the free, single-stranded M2AP6. This procedure is applied in later measurements involving the helicase RhlB, to actually confirm the functionality of the protein.

### 5.2.2 TIME-RESOLVED FLUORESCENCE

Next, time-correlated single photon counting (TCSPC) was conducted to investigate whether the free and duplexed M2AP6 and JM2AP would differ regarding their fluorescence lifetime as well. The results of the experiments are shown in [Figure 5.3b](#), depicting the normalized histogram of single-stranded, labeled M2AP6 (blue), duplexed JM2AP (red) and the instrument response function (IRF) of the setup (yellow).

The results from the time-resolved fluorescence measurements of M2AP6 are similar to the findings from the steady-state fluorescence measurements ([Figure 5.3b](#)). The overall fluorescence lifetime of single-stranded M2AP6 is relatively long ( $\tau = 3.85$  ns, fit not shown here), in which the residual offset at the temporal end of the experiment is barely fully recorded. The comparison of the transient courses unambiguously indicates that the lifetime of the excited state of the duplex is tremendously shortened ( $\tau = 0.6$  ns, fit omitted). The IRF is additionally shown, to emphasize the fact that the fluorescence lifetime of JM2AP is very low



(a) Steady-state fluorescence of M2AP6 and JM2AP6

(b) TCSPC measurements of M2AP6 and JM2AP6

Figure 5.3: Steady-state and time-resolved fluorescence measurements 2AP-labeled M2 (blue) and the duplexed form (red) after photoexcitation at 310 nm. Both experiments show that the overall fluorescence intensity and lifetime of free M2AP6 is larger than in the duplexed form.

and only marginally larger than the highest achievable temporal resolution of the used setup.

This proves that the modified RNA strands exhibit convenient spectroscopic properties and are suitable for the investigation of RNA-protein interactions by means of fluorescence spectroscopy. However, the focus for the investigation of certain steps of the unwinding reaction of the helicase RhlB will be set on steady-state and stopped-flow fluorescence experiments. The experimental details of the latter will be described in a later section.

In the first place, the recorded steady-state fluorescence spectra must undergo a number of spectral and instrumental corrections. These steps are absolutely necessary because of several reasons. Without some specific correction steps, certain spectral bands might be indiscernible otherwise. Moreover, if fluorescence spectra should be compared, which are recorded at different excitation wavelengths, the wavelength-dependent excitation intensity of the lamp must be considered. Thus, if particular physical processes are known to happen, they should be considered when recording the fluorescence spectra.

### 5.3 FLUCY - A MATLAB PROGRAM

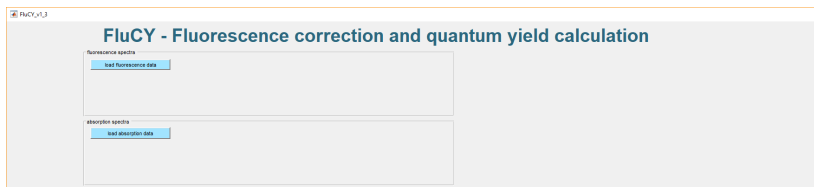
The various correction steps for fluorescence data are listed in this section and take up a bigger part of this chapter, as the experiments mainly revolve around the fluorescence-labeled M2AP6-strand. Typically, the different correction steps are done manually and must be renewed, whenever a new set of fluorescence spectra is recorded. For some of the correction steps, the absorbance spectra which correspond to the fluorescence spectra are compulsory, which adds up to a large total experimental time. The executed processes barely change, when e.g. investigating different samples or different excitation wavelengths in a comparable concentration or absorbance range, but the corrections must be performed anew.

Therefore, a MATLAB-program was written, which facilitates and, more importantly, accelerates the overall process. In the following, the graphical user interface (GUI) of this self-written program called FluCY is presented, which depicts all the underlying corrections. Although the necessary corrections are already described in detail in many other works,<sup>[163]</sup> their necessities are shortly introduced together with the equations which are used by the program. Thus, the following section can be understood as a manual for the operation of FluCY.

#### 5.3.1 INTRODUCING FLUCY

FluCY is an acronym for Fluorescence Correction and quantum Yield, which already indicates the possibilities of the program. The part concerning the corrections of the fluorescence spectra will be described in this chapter, whereas the determination of the fluorescence quantum yield ( $\Phi_{\text{QY}}$ ) will be described in [Section 7.2.5.2](#). This section will contain a nearly step-by-step manual with screenshots from version 1.3 of FluCY. The version history as well as the saving location of the most up-to-date version are summarized in the appendix of this work ([Section A.1](#)).

After the initial start of FluCY a GUI appears, containing only few buttons, as shown in [Figure 5.4a](#). In comparison to that, a view of the fully opened program is depicted in [Figure 5.4](#). The intention behind the programming was to keep it as simple as possible, hence most of the windows are only visible after pressing certain buttons. Whenever a certain order is required, this will be mentioned specifically in the following and described accordingly. This preview of the fully opened program allows the introduction to the possibilities of the program: (I) Importing the fluorescence and absorbance spectra, (II) performing excitation and emission corrections for the recorded fluorescence spectra and (III) calculating the fluorescence quantum yield, which requires a dilution series of the investigated sample and the corresponding fluorescence and absorbance spectra.



(a) View of FluCY, upon initial starting.

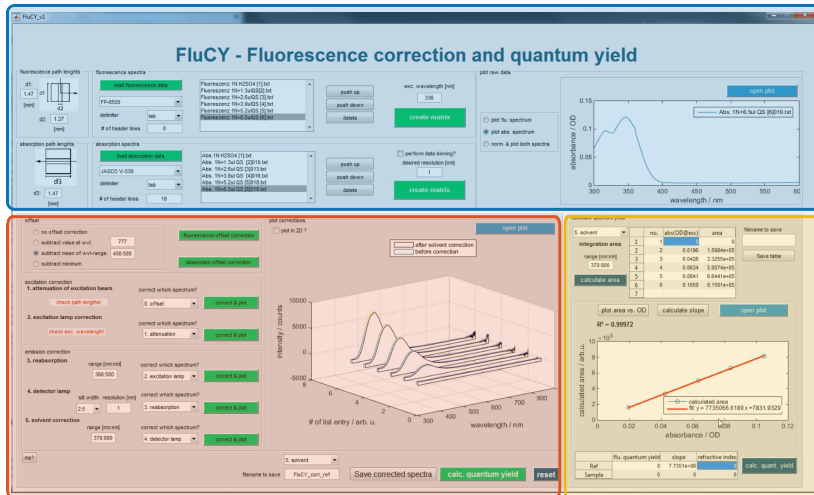
(b) Full view of the FluCY after completion of all the correction steps and calculation of the  $fQY$ .

Figure 5.4: Full view of the self-written MATLAB-program FluCY. The GUI can be divided into three parts, which are highlighted in a specific color: Importing the data (blue), correcting the spectra (red) and calculating the fluorescence quantum yield (green).

### 5.3.2 IMPORT THE RECORDED SPECTRA

The import of the sets of fluorescence and their corresponding absorbance spectra are shown in the first step (A). Figure 5.5 shows the corresponding windows in the GUI. It is of utmost necessity, that the files containing the recorded spectra are saved in the American Standard Code for Information Interchange (ASCII)-format, because otherwise FluCY will not be able to process and correct the recorded spectra. This would have been a requirement as well, when working with other data-handling software (e.g. Originlab).

(A<sub>1</sub>) **Load fluorescence spectra** By clicking on **load fluorescence data** a pop-up window appears, in which the fluorescence spectra can be selected. Multiple selection is allowed and even required, as by pressing the button again, all previously selected will disappear. Hereafter, additional windows appear, which will be explained in detail. Starting on the left side, the path lengths of the cuvette are entered, which was used for the fluorescence measurement. Both the excitation ( $d_1$ ) and emission path ( $d_2$ ) should be entered in millimeters.

When inspecting the exported .txt-file in which the spectra was saved, the

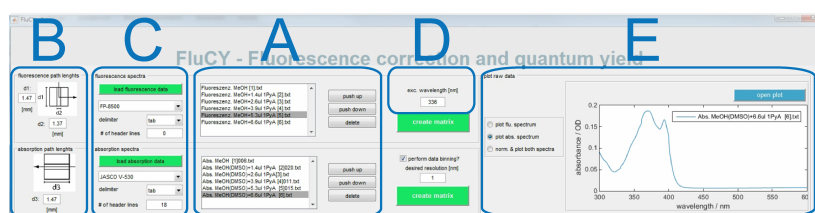


Figure 5.5: FluCY - Importing the data. The recorded fluorescence and corresponding absorbance spectra are imported separately in a batch (A). Information regarding the cuvette (B), the format of the files (C) and the excitation wavelength (D) are entered subsequently. A preview of the uncorrected spectrum is available as well (E).

necessary information on the delimiters (e.g. tab, space, comma, semicolon, etc.) and number of header lines can be retrieved. These information are entered into the corresponding fields. If available, the fluorimeter (e.g. FP-8500) can be chosen from a drop-down list above, which will automatically fill the fields with pre-selected settings according to the standard format of the exported file. It is important that all imported spectra are formatted in the same way and with the same number of header lines, otherwise further processing is impossible.

Next, the imported spectra can be sorted or deleted. By selecting a single one, the appropriate buttons (move up, move down, delete) can be used to rearrange the spectra. Although sorting is not a necessity, it facilitates the illustration later on. While doing so, a plot on the right hand side will show a preview of the raw data. This plot helps the user to identify whether the import of the data and the selection of delimiter and header lines was done correctly, as both an audio alert and an absent spectrum would be the error indication. The plot can be opened in an external window and inspected further by pressing the button **open plot**

In the second to last step, the excitation wavelength is set in the corresponding field. Lastly, by pressing **create matrix**, a matrix is created, containing the imported data which will be saved in the program's memory. Another part of the program will open, which enables the correction of the spectra.

- (A<sub>2</sub>) **Load absorbance spectra** By clicking on **load absorption data**, a window will open which is very similar to the one from the data import of the fluorescence spectra. Therefore, the particular steps until the creation of the absorbance matrix are almost identical to the ones described above. The path lengths of the cuvette with which the absorbance spectra were recorded might be different, which is why an additional path length ( $d_3$ ) must be entered (left site). Then, as the delimiters and number of header lines will most likely differ from the fluorescence spectra, these information are entered as well. As the number of accessible spectrophotometers

is larger, the drop-down list contains more options to choose from. Nevertheless, it is suggested that the users of this program look at the exported .txt-file themselves.

In the next step, the spectra are sorted. This is achieved in an analogous manner, but it is highly important that the order of the absorbance spectra matches that of the fluorescence spectra, as the following corrections are depending on each other. To change the preview of the spectra, the corresponding radio button on the left side of the plot is selected accordingly. Moreover, it is possible to have one fluorescence and absorbance spectrum selected and plotted together. For this, both spectra will be normalized.

Lastly, pressing the button `create matrix` will create a matrix, analogous to the matrix of the fluorescence data, which will be stored separately in the background of the program. An additional button is available, if the absorbance spectra were not recorded in equidistant steps of wavelengths (e.g. SPECORD© S100). Then, an interpolation of the data can be performed, which is achieved by activating the checkbox `perform data binning?` and entering the desired spectral resolution to match that of the fluorescence spectra. This whole procedure is only possible for the absorbance spectra and requires the fluorescence spectra to be recorded equidistantly.

Hereafter, the next steps of the program are described together with the necessary corrections. The focus is firstly set on the phenomena which makes the correction necessary including the underlying equations, followed by the corresponding steps in the program.

### 5.3.3 OFFSET CORRECTION

(B<sub>1</sub>) **Three possible offset corrections** To correct the offset of the spectra, there are three ways, which are commonly used. A fourth option is included in the program, if no offset correction is desired. Depending on which option is selected (by clicking on the corresponding radio button on the left side), the following types of offset-correction (and equations) are performed: No offset correction should be performed (no Equation); Subtract the fluorescence/absorbance at a specific wavelength  $\lambda_i$  from the whole spectrum (Eq. (5.1)); Subtract the mean of a specific wavelength range  $\lambda_j - \lambda_k$  from the whole spectrum (Eq. (5.2)); Subtract the minimum value  $F_{min}/A_{min}$  from the whole spectrum (Eq. (5.3)). In the second or third case, the wavelength or wavelength range (in form of  $\lambda_j : \lambda_k$ ) must be typed in.

The previously saved matrix is then corrected by clicking both the buttons `fluorescence offset correction` and `absorption offset correction`. If the correction of the offset is not desired, then this option must be actively selected nevertheless, followed by clicking the button. From this point on and for any further corrections, the matrix will be plotted in a

new layer on the right side. The data set is typically plotted as a three-dimensional waterfall plot with the wavelength and intensity (absorbance) as the x- and y-axis, and the number of list entry as the z-axis, but this can be changed by clicking on the checkbox  plot in 2D? on the right hand side of the window (not shown in figure). Moreover, the plot can be opened in an external window to retrieve further insights. This is achieved by the clicking on the button `open plot` in the top, right corner of the layer.

$$F_{offset,2}(\lambda) = F(\lambda) - F(\lambda_i) \quad (5.1)$$

$$F_{offset,4}(\lambda) = F(\lambda) - \frac{1}{n} \left( \sum_{j=1}^n F_i(\lambda_i) \right) \quad (5.2)$$

$$F_{offset,3}(\lambda) = F(\lambda) - F_{min}(\lambda_{min}) \quad (5.3)$$

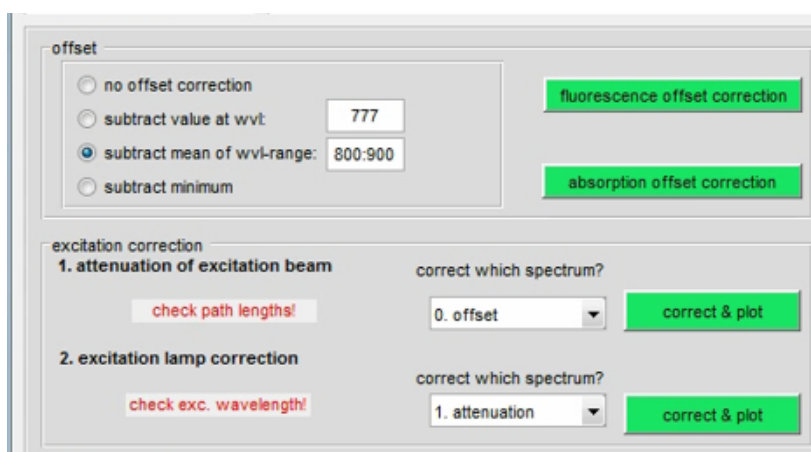


Figure 5.6: FluCY - Offset and excitation correction of the recorded spectra. Four different options are available for the offset correction of both the fluorescence and absorbance spectra. The corrections for the attenuation of the excitation beam and the excitation lamp are described in the paragraph.

### 5.3.4 EXCITATION CORRECTION

Starting from here, the order of corrections is irrelevant, as they are independent from each other. The order can therefore be adjusted by the user, although it is important to note, that the proper correction matrix, which the subsequent correction should be based on, must be selected from the drop-down menu prior to correction. Only then, the program will know on which matrix the correction shall be executed on. The following five correction steps are based on the reading correction within the program and are grouped into the excitation correction and the emission correction.

(C<sub>1</sub>) **Attenuation of excitation beam** The first step of the excitation correction is about the excitation beam. It is assumed that the emitted photons



have their origin in the center of the cuvette. For the excitation beam to reach that center, it first needs to pass a certain path length of the cuvette in which it will be partly absorbed by the sample and therefore attenuated. The actual fluorescence signal should therefore be higher than the recorded one. After consideration of the BEER-LAMBERT-law (Eq. (2.6)), and assuming that the intensity after ( $I$ ) and before ( $I_0$ ) passing the sample correspond to the fluorescence intensity ( $F, F_{att}$ ), Eq. (5.4) is obtained. Only half of the recorded absorbance is factored in, as the absorbance at the center of the cuvette is considered which correlates to half of the path length. This equation requires information on the path lengths of both the excitation beam in the fluorescence spectrum ( $d1$ ) and the probing beam in the absorbance spectrum ( $d3$ ), as the ratio of both is used to scale the measured absorbance.

$$\epsilon \cdot c \cdot d1 \cdot 0.5 = \log\left(\frac{I_0}{I}\right) = \log\left(\frac{F_{att}}{F}\right)$$

$$F_{att}(\lambda) = F(\lambda) \cdot 10^{A(\lambda_{exc}) \cdot 0.5 \cdot x_1}, \text{ with } x_1 = \frac{d1}{d3} \quad (5.4)$$

In FluCY, the correction is executed very easily. As mentioned above, the proper correction matrix must be selected from the drop-down menu, and a note reminds the user to control the path lengths. The correction is performed by clicking on the button `correct & plot`. If no errors occur, then the plot on the right hand side will change, and this button will change to a green background color.

- (C<sub>2</sub>) **Excitation lamp correction** The light intensity of the excitation lamp within the fluorimeter is not identical for all wavelengths. Because this is a device-specific parameter, a spectrum of the lamp can be recorded, which is then typically normalized to its maximum. The fluorescence spectrum is then multiplied with this correction value at the excitation wavelength of the spectrum ( $k(\lambda_{exc})$ ) according to Eq. (5.5).

In general, if the excitation wavelength is not changed throughout a set of experiments, then this effect is neglectable and this correction can be skipped. On the other hand, if an excitation spectrum or a three-dimensional fluorescence spectrum is recorded, then this correction is absolutely necessary, due to the wavelength-dependence of the lamp's intensity.

$$F_{exc}(\lambda) = F(\lambda) \cdot k(\lambda_{exc}) \quad (5.5)$$

Analogous to the other excitation corrections, the one for the excitation lamp is performed by choosing the proper correction matrix and verifying the excitation wavelength, as the latter value is required for FluCY to look for the correct value. The correction is then executed by pressing the button `correct & plot`.

Although FluCY is a (mostly) stand-alone program, some external data are inevitable for it to function properly, such as the lamp spectrum mentioned above. Typically the newest version of the lamp spectrum of the FP-8500 is used, because this is the most commonly used fluorimeter in the Wachtveitl lab. However, other spectra can be added by replacing the file `anregkorrrkurve.txt` which is located in the subfolder `/necessary files` of the program.

### 5.3.5 EMISSION CORRECTION

The emission correction is slightly more extensive as it allows the user to individually adjust the settings to their needs. Nevertheless, the structure of the program is relatively straight-forward and will be explained in detail hereafter.

The screenshot shows a dialog box titled "emission correction" with three sections:

- 3. reabsorption:** A text input field for "range [nm:nm]" contains "400:700". A dropdown menu for "correct which spectrum?" is set to "0. offset". A blue "correct & plot" button is to the right.
- 4. detector sensitivity:** A checkbox for "norm. spectrum?" is unchecked. A dropdown for "slit width" is set to "2.5". A text input for "resolution [nm]" contains "1". A dropdown for "correct which spectrum?" is set to "3. reabsorption". A blue "correct & plot" button is to the right.
- 5. solvent correction:** A text input field for "range [nm:nm]" contains "350:800". A dropdown for "correct which spectrum?" is set to "4. detector sensi...". A blue "correct & plot" button is to the right.

Figure 5.7: FluCY - Emission correction. The corrections for reabsorption by non-excited molecules and the wavelength-dependent detector sensitivity are described in the paragraph together with the solvent correction.

#### (D<sub>1</sub>) Reabsorption correction

Not all the emitted photons are necessarily detected. If a sample fluoresces and emits light, other non-excited molecules in the cuvette might absorb the energy of the photon. This process is called reabsorption and can occur, when there is a spectral overlap of the absorbance and fluorescence spectrum. As a consequence, the fluorescence in this wavelength range will decrease and should therefore be corrected. This effect is dependent on the path length of the cuvette, as the emitted photons will travel a certain distance from the center of the cuvette to the detector and other non-excited molecules are able to absorb the emitted photons.

To correct this phenomenon, the BEER-LAMBERT-law is consulted again. In this case, though, the fluorescence spectra is not divided by a distinct value, but by the (scaled) absorbance spectrum in a wavelength-dependent manner, which then results in Eq. (5.6). The wavelength range ( $\lambda_j - \lambda_m$ )

depends on the investigated sample and should be inspected by the user prior to the correction.

$$F_{reabs}(\lambda_{l-m}) = \frac{F(\lambda_{l-m})}{10^{-A(\lambda_{l-m}) \cdot 0.5 \cdot x_2}}, \text{ with } x_2 = \frac{d_2}{d_3} \quad (5.6)$$

In the program FluCY, an input field is available in which the wavelength range is entered, for which the reabsorption correction will be executed. The format of this input field must be  $\lambda_l : \lambda_m$ , like for one of the corrections of the offset. Again, the proper correction matrix is selected and by pressing the button `correct & plot`, the correction is executed and the plot of the matrix on the right hand side will change accordingly, together with the legend description.

#### (D<sub>2</sub>) Detector sensitivity

Similar to the correction of the excitation lamp, this correction considers the wavelength-dependent sensitivity of the used detector. For the resulting spectral shape of the final fluorescence spectrum, this correction probably has the biggest impact, which is why it should not be skipped. In principal, when a low intensity is recorded at a specific wavelength, this normally means that the investigated sample barely fluoresces at that wavelength. But if the detector is not quite sensitive in that specific wavelength, then even efficient fluorophores are erroneously recorded with a low intensity. This effect is corrected by dividing the fluorescence spectrum by the device-specific spectrum of detector sensitivity, according to Eq. (5.7). In case of the FP-8500, the spectra were recorded by H. Gustmann (Wachtveitl lab, Goethe University Frankfurt).

$$F_{det}(\lambda) = \frac{F(\lambda)}{F_{sensitivity}(\lambda)} \quad (5.7)$$

Before executing this correction in FluCY, two parameters must be set first. The correct spectrum for the detector sensitivity must be chosen from the drop-down menu, named SLIT WIDTH. As the spectrum differs, depending on the chosen slit width, it is necessary that the user knows about the details of the experiment. So far, FluCY only supports sensitivity spectra which were recorded with identical slit widths for the excitation and emission path. As for the excitation lamp spectrum, the files can be exchanged and renewed, by substituting the `emikorrkurve_5.txt` - (slit width of 5 nm) or `emikorrkurve_25.txt` -file (slit width of 2.5 nm) in the corresponding subfolder `/necessary files`. Then, the spectral resolution of this spectrum must be adjusted, to match that of the fluorescence spectrum of the sample. Because the available sensitivity spectra are all recorded with the highest possible resolution of 0.1 nm, the program needs to do a so-called downsampling of the spectra. This is quite different from the data interpolation described above, as it only takes every  $n^{\text{th}}$  intensity column and therefore does not alter the data. Moreover, the

user can choose, whether the absolute or normalized sensitivity spectrum should be applied. The correction is then initiated by pressing the button **correct & plot**, after which the plot on the right hand side will change, together with the legend description.

- (D<sub>3</sub>) **Solvent correction** The last of the five corrections described in this work factors in any fluorescence from either the solvent or RAMAN-scattering effects. The latter is sometimes observed in fluorescence measurement containing solvents with an hydrogen atom.[195] The scattering appears red-shifted to the excitation wavelength and can typically already be observed, when recording a spectrum of the solvent, which is why they are grouped together in the program.

The correction of the fluorescence spectra is relatively simple, as the solvent spectrum recorded under identical conditions will be subtracted, which is described in Eq. (5.8). Ideally, any flanks occurring from RAMAN-scattering will vanish hereafter. If any of the effects only appear within a certain part of the spectrum, then the correction is only performed for this specific wavelength range ( $\lambda_{n-o}$ ).

$$F_{\text{solv-corr}}(\lambda_{n-o}) = F(\lambda_{n-o}) - F_{\text{solv}}(\lambda_{n-o}) \quad (5.8)$$

In FluCY, this correction is achieved by entering the wavelength range, from which the solvent spectrum will be subtracted. The format is identical to the ones described above ( $\lambda_n : \lambda_o$ ). After selecting the proper correction matrix from the drop-down menu, pressing the button **correct & plot** will execute the correction, followed by an update of the plot and its legend on the right.

### 5.3.6 SAVING THE CORRECTED DATA

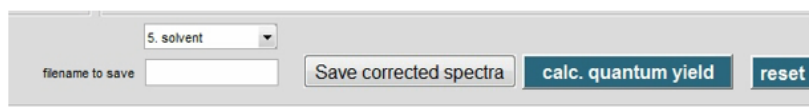


Figure 5.8: FluCY - Saving the data. The corrected fluorescence spectra are saved by selecting the latest correction step from the drop-down menu, entering a filename and clicking the proper button.

#### (E) Saving

From the drop-down list, the correction matrix is chosen which will be saved. The pre-selected choice is 5. solvent, assuming e.g. that the suggested order was chosen by the user. In the input field below, a file name needs to be put in. The button **Save corrected spectra** will save the matrix in the same folder, in which the raw fluorescence data was imported from. The file will be saved in an ASCII-formatted .txt-file, which contains

the wavelength information in the first column. The various spectra with the corrected intensities are saved in the following columns in the order, in which they are listed in the import window. The exported file will only contain numbers and values but not any information regarding the executed corrections.

This concludes the first and second part of FluCY. There are only two buttons left, which were not addressed, yet. First is the `reset`-button. This clears the (background) workspace in MATLAB and resets all windows to the point of the first start of the program. E.g. the background color the import and correction buttons are reset, enabling the user to start over again and/or correct the next set of fluorescence spectra. The button `calc. quantum yield` is for the calculation of the fluorescence quantum yield which will be described later in [Section 7.2.5.2](#).

The necessity of correcting recorded fluorescence spectra is illustrated in [Figure 5.9](#), which shows six corrections step on a fluorescence spectrum of the photoswitch ceCAM, whose photophysical characterization is one of the main projects in this thesis and thoroughly described in [Chapter 7](#). The plot shows the (raw) fluorescence spectrum (purple) and the fluorescence spectra after each correction step, in the order described above. The correction of the detector sensitivity was performed with the normalized sensitivity spectrum.

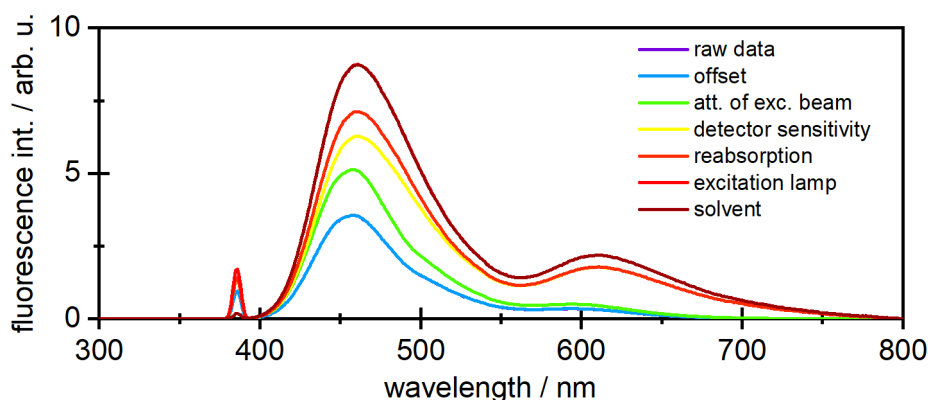


Figure 5.9: Effect of the conducted fluorescence corrections on the steady-state fluorescence spectrum of the photoswitch ceCAM. The fluorescence spectra were corrected with the MATLAB-program FluCY, revealing distinct spectral features.

The correction for both the attenuation of the excitation beam and the excitation lamp only increase the overall intensity, which is expected due to the fact that the corresponding equations scale the intensity spectrum by a factor which depends on the absorbance or the lamp intensity. Regarding the emission corrections, the reabsorption correction especially affects the intensity of the fluorescence band hinted at 461 nm which is attributed to the fact that reabsorption can only occur in this specific wavelength range (see absorbance spectrum of ceCAM in [Figure 7.2](#)). The following correction for the sensitivity of the detector

has a tremendous effect on the spectral shape of the fluorescence spectrum. As hinted above, an underlying fluorescence band around 611 nm becomes visible only after correction, as the detector is not quite sensitive in this wavelength region. Lastly, the solvent and correction of RAMAN-scattering decreases the intensity of the excitation peak.

One might argue that most of the corrections are redundant, except for the correction of the detector sensitivity, because this has actually influenced the resulting shape of the spectrum. It is still suggested to perform at least the emission corrections, as one can never predict, e.g. if reabsorption effects are negligible or the solvent exhibits either fluorescence or RAMAN-scattering. And even if the excitation corrections only scale the fluorescence spectra by a factor, this allows for further comparison of differentially excited samples. In the end, it is up to the user, whether and which corrections are applied, although as a general rule of thumb, it is always better to closely inspect the recorded data.

The third part of FluCY, in which the fluorescence quantum yield (fQY) of a sample can be calculated, will be described in [Section 7.2.5.2](#). FluCY allows the determination of the fQY via the comparative, but not the absolute method, which are both explained in [Section 4.2.3](#). Typically, if the devices are available, the determination via the absolute method is relatively straightforward and requires very little effort of data-handling. Moreover, this possibility of determining the fQY via e.g. the Ulbricht sphere has become available in the Wachtveitl lab just recently and is described in detail elsewhere.<sup>[161]</sup> Nevertheless, this and other options might be added in future versions of FluCY, together with some optimization steps.

So far, only a set of emission spectra for one excitation wavelength can be corrected. However, if samples are investigated, for which the most ideal excitation wavelength is not known yet, it is necessary to find out the most ideal excitation wavelength, for which so-called three-dimensional (3D)-spectra are recorded. These plots combine the emission and excitation spectra of a sample. In other words, the emission spectra at different excitation wavelengths are combined into a larger three-dimensional matrix. With this experiment, one can find out which excitation wavelength will yield the highest fluorescence intensity, give rise to distinct spectral features of the fluorescence bands, etc. Instead of correcting the emission spectrum separately for each excitation wavelength, which would take up more time and even requires other approaches, the correction of the excitation wavelength simply needs to be done throughout the matrix within FluCY.

Apart from this feature, only few optimizations are planned, such as the capability of adding more correction files, e.g. when working with a different spectrofluorometer on in other labs in general. Moreover, the correction of the detector sensitivity currently requires the fluorescence spectra to be recorded with the same slit width. A stand-alone version of FluCY, which has an executable file (.exe), should be also be available, so that the user will only require the (freely available) MATLAB runtime and becomes independent from the (pricy) MATLAB program.

## 5.4 STEADY-STATE AND STOPPED-FLOW FLUORESCENCE MEASUREMENTS OF JM2AP

In this section, steady-state and stopped-flow fluorescence measurements are carried out on the double strand (JM2AP) with varying concentrations of unlabeled J2h, to describe the effect of fluorescence quenching in greater detail, which was observed earlier in Figure 5.3. The steady-state fluorescence spectra were recorded to investigate the effect of an absolute decrease of fluorescence intensity at different ratios of J2h and M2AP6. Then, the operating principle of stopped-flow measurements are briefly introduced followed by a characterization of the annealing rate, depending on the different ratios of strands.

### 5.4.1 CONCENTRATION-DEPENDENT STEADY-STATE FLUORESCENCE OF JM2AP

In analogy to the experiment depicted in Figure 5.3a, the fluorescence spectra were recorded for different concentrations of the unlabeled counter-strand J2h. For this, fluorescence spectra with a fixed concentration of labeled M2AP6 were recorded, after adding J2h and subsequent mixing. The fluorescence intensity at the emission wavelength of 370 nm was then recorded and plotted against the ratio of J2h to M2AP6, which is shown in Figure 5.10. The fluorescence spectra were corrected with FluCY and the concentration ratios were corrected by the dilution effect as well.

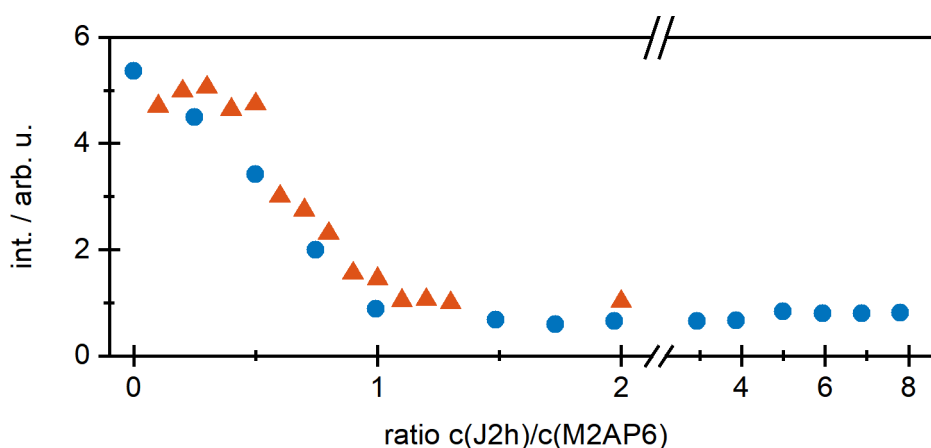


Figure 5.10: Fluorescence intensity of titration of J2h to M2AP. The emission intensity at 370 nm for two sets of experiments is plotted against the ratios of counter-strand to labeled M2AP6 and show a quenching of the fluorescence with increased concentration of J2h. The decrease follows a sigmoidal behaviour (red), whereas the intensity minimum is reached at a equimolar ratio. Residual luorescence can be still be observed at high concentrations of counter-strand (blue). The intensity from both experiments were scaled to each other.

In a first approach for this measurement (blue), the fluorescence intensity has its peak at low concentrations of J2h and is gradually quenched, the more counter-strand is added. Any further effects which might occur at higher ratios can be excluded, because many data points were recorded for high ratios of counter strand (up to a ratio of 8:1). The minimal fluorescence intensity is already reached at equimolar concentrations of both strands, although a residual fluorescence can still be detected, which extends the findings from the preliminary experiments shown in [Figure 5.3](#). A sigmoidal behaviour can be surmised from the data, but this was verified in a second approach (red), in which more data points at lower ratios are recorded as well, whereas the measurements at higher ratios are omitted. Although some data points from both sets of measurements do overlap and indicate an accordance of the data and therefore their comparability, few points at the lower range of ratio differ from each other. The intensities from both experiments were scaled to each other, for a better visualization of the underlying effects.

#### 5.4.2 CONCENTRATION-DEPENDENT STOPPED-FLOW FLUORESCENCE OF JM2AP

The necessity of stopped-flow measurements derives from the fact that the functionality of the DEAD-box helicase is to be verified according to a fluorescence assay from Putnam *et al.* which is based on the aforementioned method.[183] This assay grants access to the investigation of fast rate constants which are likely to prevail for the unwinding reaction. Initially, the annealing rate of JM2AP is investigated to confirm on the one hand, that the stopped-flow apparatus functions properly and detects a decrease in fluorescence upon mixing and on the other hand, whether the annealing rate would coincide with the time window of the unwinding reaction. The latter can be prevented with the aforementioned method, in which a scavenger strand of unlabeled M2 is added to the solution.

It could already be shown in the preliminary experiment that the lifetime of the excited state would decrease in the presence of the unlabeled counter-strand. However, this section focuses on the investigation on how fast the both RNA single-strands would form the duplex, depending on the concentration of unlabeled counter-strand J2h. This annealing rate was investigated by stopped-flow fluorescence spectroscopy, in which one syringe contained the 2AP-labeled strand and the other would have varying amounts of the corresponding counter-strand. The results are shown in [Figure 5.11](#) and resemble the findings from the titration experiments in the steady-state. The experimental conditions are listed in [Section 4.2.4](#).

Although the concentration of the counter-strand J2h is significantly larger than the one of M2AP6, the duplexation can still be detected with a high resolution. The two most apparent observations are that the annealing fol-



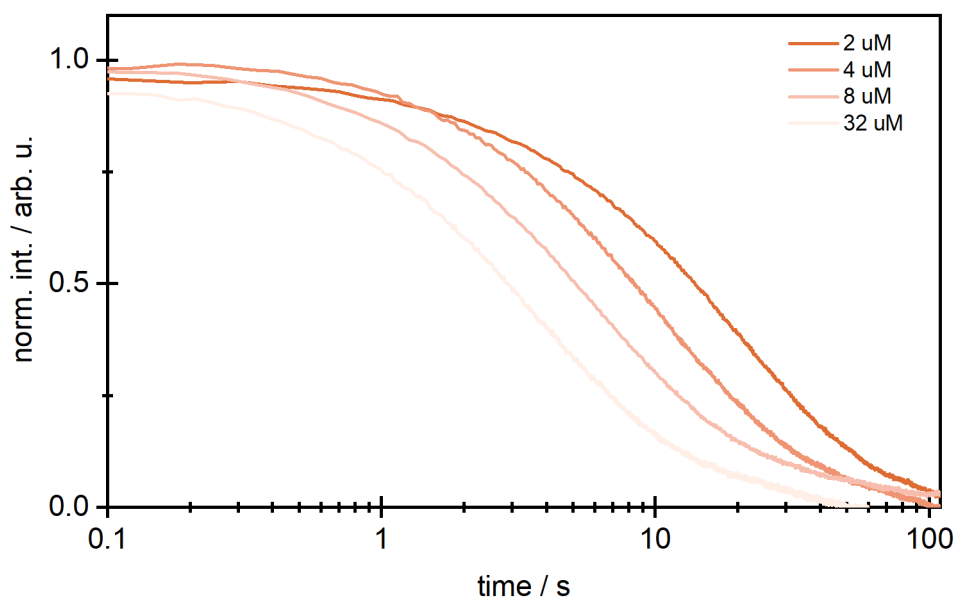


Figure 5.11: Stopped-flow measurements in which J2h and M2AP6 are mixed, verified that the fluorescence is quenched more rapidly with increasing concentration of the counter strand J2h. The concentration of M2AP6 was set to  $c_0 = 1 \mu M$  throughout all four mixing experiments.

lows a sigmoidal behaviour and that it is increased, when higher amounts of counter-strand is available in the solution. The latter observation can simply be explained by diffusion effects and the fact that the probability of duplex formation is tremendously increased, when the concentration of J2h is increased. In other words, the process of fluorescence quenching of 2AP-labeled M2 is accelerated with an increased concentration of J2h. Compared to the titration experiment in the steady-state, fewer data points were collected, as the overall consumption of sample is larger. This concludes the preliminary measures for the experiments involving the DEAD-box helicase RhlB, as the prevailing trend is already observable.

## 5.5 FLUORESCENCE MEASUREMENTS INVOLVING JM2AP AND RHLB

In this section the functionality of the helicase RhlB will be shown, as it is now investigated together with the previously described samples. To examine the unwinding mechanism of DEAD-box helicases, two types of approaches are viable, the single cycle or multiple cycle regime, which were shortly introduced in [Section 3.1](#). Here, the approach via the single cycle regime was taken, as it requires smaller concentrations of RhlB at the cost of higher amounts of scavenger, which on the other hand were accessible from previous experiments.

Compared to the stopped-flow measurements, in which only the single-strands were mixed, the experiments in which the helicase is to be included are more elaborate, as a greater number of different combinations is possible and must be considered before measuring. Moreover, as already mentioned previously, scavenger M2 is added to the number of investigated samples to trap the unwound J2h. Otherwise, the increase of fluorescence resulting from free M2AP6 would not have been detected. At first, steady-state fluorescence experiments with the different combinations were carried out, to have a reference, on when an increase of fluorescence will be observed. The used combinations are listed in Table 4.2. Thereafter, the actual stopped-flow fluorescence measurement would ideally verify the findings and provide further information on the unwinding reaction. The used combinations for this set of experiments are listed in Table 4.3, including the legend which was used in the following analysis.

The steady-state fluorescence measurements for the different compositions of helicase Rh1B, the 2AP-labeled duplex JM2AP, ATP and scavenger M2 are shown in Figure 5.12a. Interestingly, the helicase Rh1B exhibits its own fluorescence as well, which is an unfortunate property as it complicates the data (green). Although this has not been reported for other DEAD-box helicases yet, nor mentioned in the previously described fluorescence assay,[183] the emission maximum is significantly blue-shifted ( $\lambda_{em} = 347\text{ nm}$ ) compared to that of 2AP. Moreover, as a comparative study is carried out here, the relative intensity changes would allow one to deduce whether the fluorescence results from actual unwinding or from some other interaction. Thus, the difference of the fluorescence intensity of labeled JM2AP before (red) and after it has been reheated (pink) is used as a reference. It is important to highlight that the identical solution was investigated in any cases, to exclude any external effect onto the fluorescence spectrum. Lastly, a solution containing all the samples is investigated (blue) and another one, where solely ATP was omitted (light blue). The emission maximum of both experiments is at 367 nm and therefore located between that of the duplex RNA and the helicase. The overall fluorescence intensity is increased compared to that of the single counterpart, which is justified, as both samples fluoresce and are present in the solution. The intensity difference of the spectrum with and without ATP matches that of the RNA duplex before and after heating, resulting in the conclusion, that in presence of ATP, the unwinding reaction by the helicase Rh1B indeed takes place. Superimposition of the fluorescence spectra of Rh1B and the RNA duplex (before heating) gives the full spectrum with ATP (omitted in the plot), although one would expect to yield the spectrum with lower intensity, which would be without ATP. However, it is possible that the helicase Rh1B forms an ATP-independent protein-RNA interaction with either J2h, scavenger M2 or even M2AP6. In case of the latter, this would also lead to a decrease of fluorescence intensity. But as a signal increase is actually observed, which is in fact identical to that of the (reheated) RNA duplex, the assumption can be made that the helicase exhibits unwinding functionality.

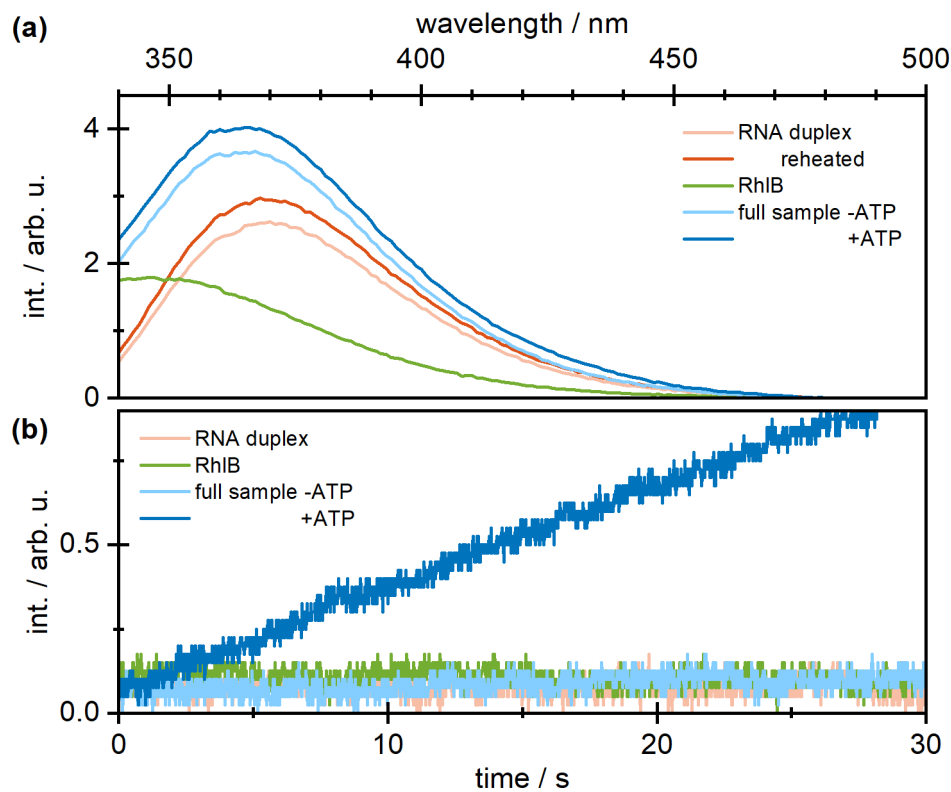


Figure 5.12: Unwinding of the duplexed RNA by the helicase RhIB is detected in both steady-state and stopped-flow fluorescence measurements. The increase in fluorescence intensity is observed by steady-state fluorescence (a) only when the duplexed RNA, the helicase and ATP are present in the solution. The detected intensity increase matches that of the reheated RNA duplex. This finding is verified by stopped-flow fluorescence measurements (b). Only when ATP is mixed to the solutions, an increase of fluorescence is observed over time, which is caused by unwound M2AP6.

The stopped-flow measurements are shown in Figure 5.12b and contain one measurement less than the corresponding steady-state experiments, as the reheated sample is excluded herein. Out of the four remaining samples, only the measurement named "full sample +ATP" would show a transient change of fluorescence. In other words, only in the presence of ATP an increase of fluorescence is observed upon mixing of the samples, which is most likely caused by free M2AP6. Although this partially confirms the findings from the steady-state experiment, that ATP can increase the efficiency of unwound RNA, this does not necessarily mean that the optimal parameters are determined yet. On the one hand, the expected increase in fluorescence is expected to reach an asymptotical value at which no further JM2AP duplex can be unwound. On the other hand, the rate with which the free M2AP6 is formed in this experiment, is extremely slow, as an expected residual maximum of fluorescence could not be detected in the applied experimental time window and therefore was not fitted. Under nearly identical conditions, other DEAD-box helicases, such as

Ded1p exhibit unwinding rates in the range of 2-10 min<sup>-1</sup>, depending on the investigated dsRNA.[196]

As of now, there are merely hints for the functionality of the helicase RhlB. Too many factors regarding the optimization remain undetermined, but need to be addressed before further investigations on the unwinding reaction can be carried out. Possible factors, such as other auxiliary proteins, the length of the duplex, etc. are listed and addressed below in [Section 5.7](#).

## 5.6 RAPID-SCAN MEASUREMENTS ON NPE-CAGED ATP

The unwinding reaction by the helicase is ATP-driven, which means that ATP hydrolysis will occur at some point of the reaction at which energy is required. Although it is theoretically possible that the event could either happen during (i) the formation of the protein-RNA complex, (ii) the unwinding reaction or (iii) the release of the unwound ssRNA, several indications were found that hydrolysis occurs during the last step.[196, 197]

Trapping of this specific reaction step can now be achieved, by using non-hydrolyzable ATP analogues. In biochemical sciences, adenylyl-imidodiphosphate (**AMP-PNP**) is typically used as an ATP replacement, as its chemical structure resembles ATP to some degree that it will be recognized by the protein. However, the subsequent hydrolyzation is completely hindered. When using a caged variation of ATP, such as NPE-ATP, the protein-ATP complex will ideally still be formed and will additionally allow one to monitor the following reaction, when applying light to trigger the uncaging reaction. Apart from this, there are several other advantages of photocaged compounds, which are extensively described in [Section 3.2](#).

As the experimental effort is larger when working with cages, especially along with biochemical compounds, it is necessary to find out, how fast the uncaging reaction occurs and moreover, whether the additional application of light would influence either the biochemical environment or the reaction. Therefore, only the uncaging reaction of NPE-ATP was investigated at first, by rapid-scan FTIR. So far, in the **IR** wavelength range only steady-state and time-resolved measurements covering the time ranges from ps-ns can be executed, although the technical requirements and preliminary data, which were obtained with step-scan and rapid-scan are available.[198] Rapid-scan **FTIR** would enable a new time window, as measurements recorded with this method would allow one to detect vibrational changes in the ms-s time frame.

Furthermore, examination of the uncaging reaction of NPE-ATP by rapid-scan would allow one to review the proper settings of the used setup. Since this reaction is well-known and has been thoroughly described by others,[199] the literature values can be used to verify the findings from the experiment at hand and establish this time-resolved method in the lab. The applied measurement

conditions and device settings are described in Section 4.4.2. The resulting measurement is shown in Figure 5.13. The experimental data were binned (factor of 40), because the amount of data would be too large to be plotted otherwise.

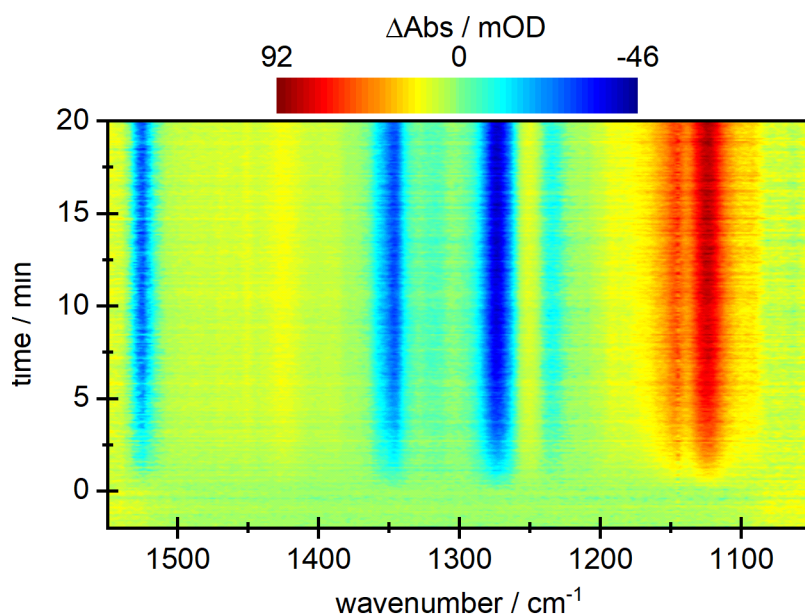


Figure 5.13: Rapid-scan measurement of NPE-caged ATP after LED illumination at 365 nm. Negative absorbance changes at 1523  $\text{cm}^{-1}$ , 1346  $\text{cm}^{-1}$  and 1272  $\text{cm}^{-1}$  indicate the loss of various vibrations due to uncaging, whereas the strong absorbance increase at 1125  $\text{cm}^{-1}$  show the appearance of an occurring  $\gamma\text{-PO}_3^{2-}$  bond.

Whereas negative difference signals (blue) indicate a loss of vibration, which occurs because of broken bonds in case of an uncaging reaction, positive absorbance bands (yellow, red) point to a newly formed bond. The IR-absorbance spectrum before photoexcitation is subtracted from the data to highlight any spectral changes. Upon turning on the LED ( $\lambda_{exc} = 365 \text{ nm}$ ) for photoexcitation, a variety of difference signals appear. The negative signals, centered around 1523  $\text{cm}^{-1}$ , 1346  $\text{cm}^{-1}$  and 1272  $\text{cm}^{-1}$  indicate loss of vibrations and decay with nearly the same rate (fits not shown). The latter signal could also be positioned at higher wavenumbers, and correspond to a broader signal, as the positive signal at ca. 1250  $\text{cm}^{-1}$  partially cancels out the signal. Other than that, only a broad positive absorbance change at 1125  $\text{cm}^{-1}$  is observed.

The evaluation of the data is then compared to the experiments described by Barth *et al.*[199] However, this can only be done for the spectral changes and not for the rates, because the experiment in this work was performed with LED illumination. In general, photoexcitation with a laser is not always necessary and LED is a viable alternative as well, as the handling of the latter is easier. Another

advantage of LEDs, is that the evolving absorbance changes appear more slowly, so that the spectra can be recorded with an improved signal-to-noise ratio (SNR). As a downside, the yielded temporal resolution of the experiment is lost and cannot be used to assign any formation rates. The uncaging mechanism of *o*-NB and NPE-caged compounds as well as the names of the involved intermediate species are described shortly in Figure 3.2. After photoexcitation, the *aci*-nitro intermediate will form via different possible pathways.[105, 106] The negative absorbance signals at  $1523\text{ cm}^{-1}$  (literature:  $1527\text{ cm}^{-1}$ ) and  $1346\text{ cm}^{-1}$  ( $1347\text{ cm}^{-1}$ ) are assigned to the antisymmetric and symmetric stretching modes of the disappearing nitro group. The third and intense negative signal at  $1272\text{ cm}^{-1}$  ( $1251\text{ cm}^{-1}$ ) is assigned to the antisymmetric  $\gamma\text{-PO}_2^-$  vibration of caged ATP, whereas the appearing positive band at  $1125\text{ cm}^{-1}$  ( $1119\text{ cm}^{-1}$ ) is caused by the appearance of the free  $\gamma\text{-PO}_3^{2-}$  group, upon release of ATP. The slight differences between the experimental values found in this work and the literature are most probably caused by the different chemical environment, as Barth *et al.* did their experiments in a buffered, aqueous solution at pH7, whereas this experiment was carried out in water. There are several reports on photocages being investigated in the IR wavelength range in which it could be shown, that the choice of solvents, as well as the buffer affects the spectral location of the signals.[103] Although the measurement was not redone with laser excitation to additionally confirm the rates, the successful implementation of rapid-scan FTIR is still given, nonetheless and the method is deemed established.

## 5.7 CONCLUDING REMARKS

Thus, incorporation of caged-ATP into the unwinding reaction of helicase RhlB would be next. However, this experiment was not done as the focus of the investigation was changed to gather further information on the helicase and its corresponding RNA-protein interactions, as well as other protein-protein interactions. This required a more detailed study on RhlB and the multistep reaction as whole, which are described by H. Zetsche.[200] The findings are summarized in the following and give the opportunity for future studies on this specific helicase.

Several pieces of evidence exist, that DEAD-box proteins require an overhang of the RNA to function properly.[190, 191, 201] Further studies approached this requirement in more detail and investigated a correlation between the number of nucleotides in the overhang and the unwinding efficiency.[192]

A preference of overhang could already be shown for the helicase RhlB, by investigation of different duplex strands than the ones described in this work. The M2 strand was kept unchanged, to enable future experiments with the fluorescence-label 2AP, whereas different variations of the J2h strand were investigated, including both a variation with a 5' and a 3' overhang. The binding affinity of RhlB to these RNA substrates was experimentally determined to yield the dissociation constant  $K_D$ . However, relatively weak RNA-protein interactions

are found, which are explained by the sequence unspecificity which these remodeling enzymes exhibit. Nevertheless, it could be shown that the DEAD-box helicase RhlB exhibits a binding preference towards RNA substrates which have a 5' single-stranded overhang. The common finding in all studies regarding DEAD-box RNA helicases is that they do not have a common preference regarding either a 3'- or 5'-overhang, as both types of preferences could be found.

This work studies the helicase's unwinding in the absence of any other proteins. The large degradosome, of which the helicase RhlB is part of, consists of several other protein subunits, though, such as the Polynucleotide Phosphorylase (PNPase) and Ribonuclease E (RNase E). The latter was shown to contain binding sites for the RNA helicase RhlB and other components of the degradosome.[81, 84, 202, 203] In her studies, H. Zetzsche could already verify with a truncated version of this subunit RNase E, that the binding affinity between the helicase RhlB and the RNA increases even further. It is however likely, that the RNase E has its own role in the unwinding mechanism and might be responsible for e.g. passing on the unwound RNA, which would explain the found decreased dissociation constant  $K_D$ .

The results of this work could be extended with the recent findings from H. Zetzsche for the eventual characterization of the unwinding reaction of the helicase RhlB. The experimental foundation are described thoroughly in this chapter and contain various findings. First and foremost, the steady-state and stopped-flow fluorescence characterization containing the 2AP-labeled single-strand M2AP6 and its counter-strand J2h. Therein, it could be shown that the fluorescence intensity of the free single-strand is the highest, when no counter-strand is present. The counter-strand was then added in a titration experiment, revealing that the intensity decreases in a sigmoidal behaviour until equimolar concentrations prevail. The corresponding stopped-flow experiment complemented the result and showed that this decrease of intensity goes along with a faster annealing rate. The results can now be used as a reference for measurements involving other variants of J2h with different lengths. Stopped-flow measurements would be able to not only verify the obtained information on the different binding affinities of the J2h-variations, but to also determine annealing rates of the different duplexes.

The steady-state fluorescence data were corrected with a self-written MATLAB-program called FluCY, which is able to perform usually time-consuming fluorescence corrections, such as the offset-, excitation- and emission-correction, in a short time. The program is also able to determine fluorescence quantum yields from the recorded spectra, but currently lack some features as e.g. the correction of excitation spectra.

Lastly, the general functionality of the helicase could be proven in preliminary fluorescence measurements. Only when ATP was present, the supposedly

ATP-dependent unwinding process occurred, leading to a slight increase of fluorescence intensity. A repetition of the measurements after the addition of RNase E would provide further information on a possible necessity of this subunit of the degradosome and might even enhance the unwinding efficiency of the reaction. If more ideal conditions are found hereafter, NPE-caged ATP or other (caged) analogues of ATP can then be used to halt the reaction and trap the protein-RNA complex for a characterization of the structure.



## RESULTS - BIST-CAGES

---

The numerous advantages for the application of photocages could already be shown in multiple cases but continue to be subject of current research. This is mostly due to the diversity with which they can be applied, but also the diversity of photochemistry in general. If a photocage is to be used for the investigations of a biochemical reaction of interest, it should fulfill a multitude of requirements. Among others, it should absorb light from the visible part of the spectrum, have a high molar extinction coefficient and be soluble in water.<sup>[91]</sup> These expectations are usually met by chemically modifying some of the well-established photocages, which might even lead to an improvement of their photophysical properties. One new class of molecules which was recently discovered are the BIST-cages, which were synthesized in the Ellis-Davies lab (see [Section 4.1.2](#)). Four variations of these BIST-cages were thoroughly characterized in this work and are summarized in this chapter.

At first, the steady-state properties of the chromophore and the different BIST-cages are analyzed, including illumination experiments, in which the absorbance changes upon uncaging are looked upon. Hereafter, the ultrafast dynamics in the ps-ns time range after photoexcitation is investigated by means of transient absorption measurements. Transient flash-photolysis measurements in the  $\mu$ s-ms regime complement the full time range. In an additional study, the water-dependence of the different stages of the reaction are presented.

### 6.1 THE BIST-CHROMOPHORE

The structures of the cages have a common chromophoric core, namely the dinitro derivative of bisstyrylthiophene (BIST) (see [Figure 6.1](#)). The planar structure of the molecule allows delocalization of the  $\pi$ -electrons, which leads to an absorption maximum in the visible. Attaching different leaving groups in *ortho*-position to the nitro-substituent results in the very well-known class of *ortho*-nitroveratryl (also called 1-(2-Nitrophenyl)ethyl (NPE)) protecting groups.

The first compound, BIST-amine is a tertiary amine and releases a secondary amine carrying two ethyl acetate residues. The leaving group is connected via a nitrogen atom and results in a secondary amine upon uncaging. Both BIST-ester and -ether are connected by an oxygen atom, but it was suspected that the different leaving group might affect the overall reaction and its dynamics. BIST-ester resembles the chemical structure of gamma-aminobutyric acid (GABA) and will yield this molecule after uncaging, except for the fact that the amine is still

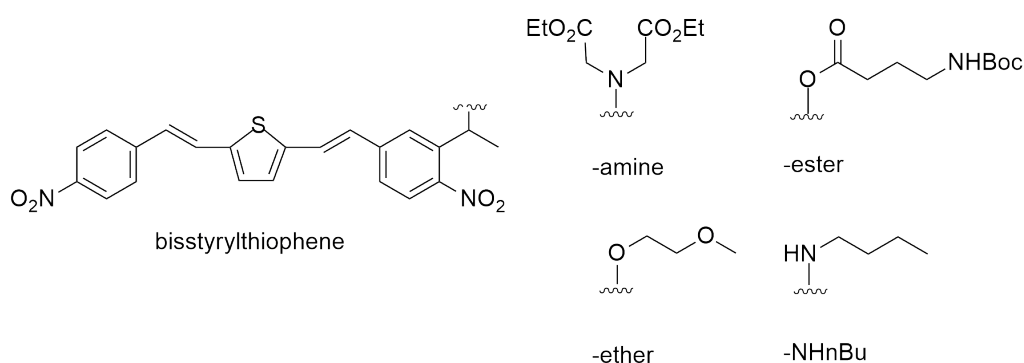


Figure 6.1: Lewis-Structure of investigated BIST-cages. The core chromophore consists of a dinitro derivative of bisstyrylthiophene which absorbs visible light very efficiently. Based on this chromophore four compounds were investigated, which have a methyl-group at the  $\text{C}_\alpha$  in common. The investigated compounds are named after the molecular bridge connecting the leaving group and the chromophore, BIST-amine, -ester, -ether and -NHnBu.

chemically protected with *tert*-Butyloxycarbonyl (Boc). Uncaging of BIST-ether will result in ethylene glycol. BIST-NHnBu is a secondary amine and compared to BIST-amine it cages *n*-butylamine instead (which is a primary amine). It stands out from this list, because it was synthesized at a later point of time, which is why the focus of its characterization is slightly different, as shown later in this chapter.

In recent studies, this chromophore was attached to a calcium chelator (ethylene glycol-bis( $\beta$ -aminoethyl ether)-*N,N,N',N'*-tetraacetic acid (EGTA)), resulting in a “caged calcium” molecule.[21] Therein, Agarwal *et al.* showed the promising photophysical properties of the BIST-chromophore, such as the one-photon (1P) absorbance maximum in the visible at 440 nm, the high molar extinction coefficient ( $66,000 \text{ M}^{-1}\text{cm}^{-1}$ ) and especially the high two-photon (2P) absorption cross section ( $350 \text{ GM}$  at 775 nm) allowing very efficient uncaging (quantum yield of 0.23) in the 720-830 nm range of the spectrum. Moreover, they could show that uncaging of  $\text{Ca}^{2+}$  triggered cell-wide (1P) and local (2P) physiological signaling events.

Following up on these studies, several other molecules, e.g. GABA were to be caged with BIST, requiring a different synthesis route. For this the different BIST-cages were investigated, bearing in mind, that they should be applied to a wide variety of molecules. The investigation of possible key steps within the uncaging dynamics and mechanism will facilitate the decision on the most suitable precursor for further BIST-cages.

## 6.2 STEADY-STATE CHARACTERIZATION

As part of the extensive characterization of the BIST-cages, steady-state absorption spectra of the differently caged BIST-compounds were recorded. As shown in Figure 6.2 the absorption spectra of the first three compounds in DMSO are very similar. They all have a single absorbance band in the visible with its maximum around 445 nm. All compounds absorb light very efficiently, as the molar extinction coefficients in DMSO can go up to ca.  $55,700 \text{ M}^{-1}\text{cm}^{-1}$ .

### 6.2.1 STEADY-STATE ABSORBANCE

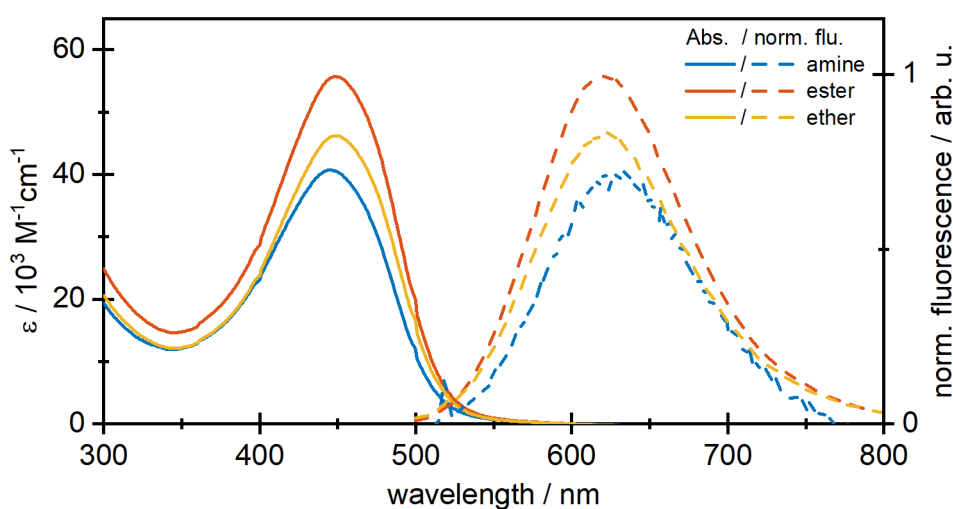


Figure 6.2: Molar extinction coefficients and scaled fluorescence spectra of three of the investigated model compounds BIST-amine, -ether and -ester in DMSO. Due to the BIST-scaffold, the molar absorptivity of the compounds are very high and the absorption maximum is located in the visible part of the spectrum (straight lines). Weak fluorescence could be detected (dashed), with a large STOKES-shift of ca. 185 nm.

Typically, if photocages are to be used for biological applications, they must fulfill certain photophysical and chemical properties, out of which three important ones have to be stressed in particular. Firstly, they should not only absorb UV light, as light from this wavelength range can lead to photodamage of the biological cells. As BIST-cages have their absorbance band in the visible, they meet this condition. Moreover, they should only require small doses of light for the uncaging reaction, meaning that they either have a high uncaging quantum yield and/or a high molar extinction coefficient. The product of both is called the efficiency, which should ideally have high values. When solely comparing the molar extinction coefficients of the BIST-cages to other well-known, established cages such as *o*-NB- ( $5,500 \text{ M}^{-1}\text{cm}^{-1}$ )[16] or DEACM-based compounds

(20,900 M<sup>-1</sup>cm<sup>-1</sup>)[204] the photocage investigated in this work surpasses them by a factor of at least 2.5. Lastly, the ideal photocage should have a high water-solubility and not decompose under hydrophilic conditions within the cell. Although the BIST-compounds investigated in this work are not completely soluble in water and still require the presence of an organic solvent such as DMSO, the attachment of water-soluble enhancing groups has already been achieved within the Ellis-Davies lab (yet unpublished results). The aforementioned characteristics are summed up in Table 6.1 for all four compounds and show that the investigated molecules at hand exhibit promising photophysical properties for further biological application. The molar extinction coefficient of BIST-NHnBu was not determined in this work, but is expected to be in a similar range than the other BIST-cages.

The uncaging quantum yield (uQY) of the different BIST-cages, as determined by Dr. M. T. Richers (Ellis-Davies lab), indicate very low uncaging efficiencies for all compounds. Compared to BIST-EGTA, the uQY dropped significantly.[21] Possible explanations for this findings will be discussed in the following sections.

Table 6.1: Absorption maxima ( $\lambda$ ) and molar extinction coefficients ( $\epsilon_{max}$ ) of the investigated BIST-cages in DMSO. The uncaging yield ( $\phi_u$ ) of selected cages were determined.

BIST-	$\lambda_{max}$	$\epsilon(\lambda_{max}) / \text{M}^{-1}\text{cm}^{-1}$	$\phi_u^1 / \%$
-amine	445	40,700	6.5
-ester	449	55,700	not determined
-ether	449	46,200	n.d.
-NHnBu	446	n.d.	2.7

## 6.2.2 STEADY-STATE FLUORESCENCE

The fluorescence spectra of the BIST-cages are depicted in Figure 6.2 and are scaled to the maximum of its corresponding absorbance spectrum. However, harsh experimental conditions (high concentrations and high PMT voltage) had to be met to yield the depicted fluorescence spectra, indicating a low fluorescence quantum yield (fQY), which is surmisable from the low SNR of the data. All the fluorescence spectra exhibit only a single fluorescence band with an emission maximum in the wavelength range around 627-634 nm. Almost no spectral overlap was found, in which reabsorption could take place. Due to its poor fluorescence properties, it is assumed that other deactivation pathways, which are more efficient than the fluorescence channel, exist for BIST. Although the fQY was not quantitatively characterized for the BIST-cages, it is assumed to be <1%, due to the aforementioned hurdles in recording the spectra.

<sup>1</sup> determined in Ellis-Davies lab

### 6.2.3 DFT-CALCULATIONS OF BIST-NHNBU

To fully characterize the electronic states of BIST-caged compounds, theoretical calculations were performed to obtain information about the ground-state geometry of the molecules. For this, density functional theory (DFT)-computations were performed on a theory level of B<sub>3</sub>LYP[205, 206] using the basis function cc-pVDZ[207] with Gaussian09.[208] The calculations were done exemplarily for BIST-NHnBu, as it was assumed that there will be no huge differences regarding the calculated results for the other BIST-cages. An implicit solvent function was applied in form of DMSO, as most of the actual experiments were carried out in this solvent.

As shown in Figure 6.3, the optimized geometry of the ground-state consists of a very long, planar structure, which would explain the highly red-shifted absorbance maximum of the BIST-chromophors. This would most likely not be affected by changing the investigated compound or the leaving group. E.g. in case of BIST-NHnBu the leaving group is electronically decoupled and it is assumed that this would hold true for the other cages as well. Vertical photoexcitation would lead to a population of the lowest excited state and requires an energy equivalent to 685 nm. The molecular orbitals involved in this  $S_0 \rightarrow S_1$ -transition are shown in Figure 6.3 and exhibit a  $\pi$ - $\pi^*$  character, with an oscillator strength of 2.051. Both, the highest occupied molecular orbital (HOMO) and lowest unoccupied molecular orbital (LUMO), indicate that the system does not become decoupled, as the electronic delocalization can still be observed.

Other excited-state transitions are found in the DFT-calculations as well, but with much smaller oscillator strengths ( $<0.02$ ) and are therefore not discussed here. Despite the fact that the calculated absorbance maximum does not exactly match the experimental value due to a small red-shift, the overall theoretical spectrum nicely resembles the actual spectrum. Hence, the results from the DFT-calculation most likely describe the actual transition upon photoexcitation.

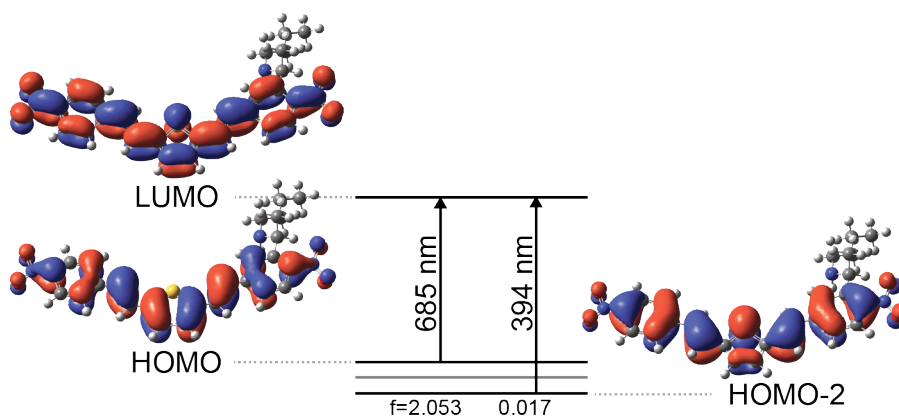


Figure 6.3: Electronic transitions and associated molecular orbitals for BIST-NHnBu found in DFT-calculations. The highest oscillator strength is found for the  $S_0 \rightarrow S_1$ -transition, involving the HOMO and LUMO. Other transitions were found to be too low ( $f < 0.02$ ) and are therefore neglected.

## 6.2.4 ILLUMINATION OF BIST-CAGES

Illumination of the BIST-cages at  $\lambda_{LED} = 455 \text{ nm}$  shows a variety of absorbance differences. [Figure 6.4](#) summarizes the absorbance spectra and the contour plots of the absorbance changes for all four BIST-compounds. Because some of the occurring features do not appear at the same time, a contour plot was chosen to depict the absorbance changes, in which positive and negative absorbance changes are depicted in yellow/red and blue, respectively. In some cases, the illumination experiments were measured separately and merged in the shown contour plots afterwards. As a result, few faint horizontal lines appear in some of these plots.

The illumination of **BIST-amine** ([Figure 6.4a](#)) exhibits a variety of spectral features over several time ranges. At first, a decrease at 445 nm, which corresponds to the ground-state absorbance, is observed. At the same time an increase around 500 nm can be observed. Both absorbance changes gradually intensify and moreover shift to higher wavelengths. The negative band stops shifting and decreasing when centered around 488 nm, whereas the positive absorbance keeps shifting until it reaches an intensity maximum at 523 nm. Hereafter, this band starts to decrease until it almost vanishes, while at the same time a new, broad absorbance band around 300-433 nm arises. Further illumination of BIST-amine does not affect both the negative and positive band at 488 and 580 nm, while the new positive band in the UV region continues to increase.

The negative band at 445 nm can be clearly assigned to the loss of ground-state absorbance, which does not recover. This is an unambiguous indicator for a successful uncaging reaction. The red-shifted positive band indicates the formation of either the *aci*-nitro intermediate or the nitroso-photoproduct, which are both known to exhibit a red-shifted absorbance.[\[103, 177\]](#) However, no isosbestic point can be found, which would have indicated a clean unimolecular reaction. This can be explained by the fact that the photoproduct itself can undergo a secondary photoreaction ( $A \rightarrow B \rightarrow C$ ).[\[209, 210\]](#) It is assumed that the absorbance band in the UV is derived hereafter. Its absorbance in the early stages of illumination is rather weak due to the fact that the primary photoproduct must be accumulated first. Only when the uncaging reaction is quantitatively completed - in this case at  $10^4 \text{ s}$  - then the secondary photoproduct can be formed and observed.

The absorbance spectra and the corresponding contour plot for the illumination of **BIST-ester** are shown in [Figure 6.4b](#). In comparison to BIST-amine, the relative absorbance changes are weaker, especially for the first few recorded spectra. The negative absorbance band close to the absorbance maximum of BIST-ester is very weak and the red-shifted positive band is missing, although the uQY of BIST-ester and BIST-amine should be comparable. Even though the negative band gradually intensifies, just like in case of BIST-amine, it shifts towards higher energies instead. At the same time a slight decrease of absorption centered around 300 nm is observed. A corresponding ground-state absorbance

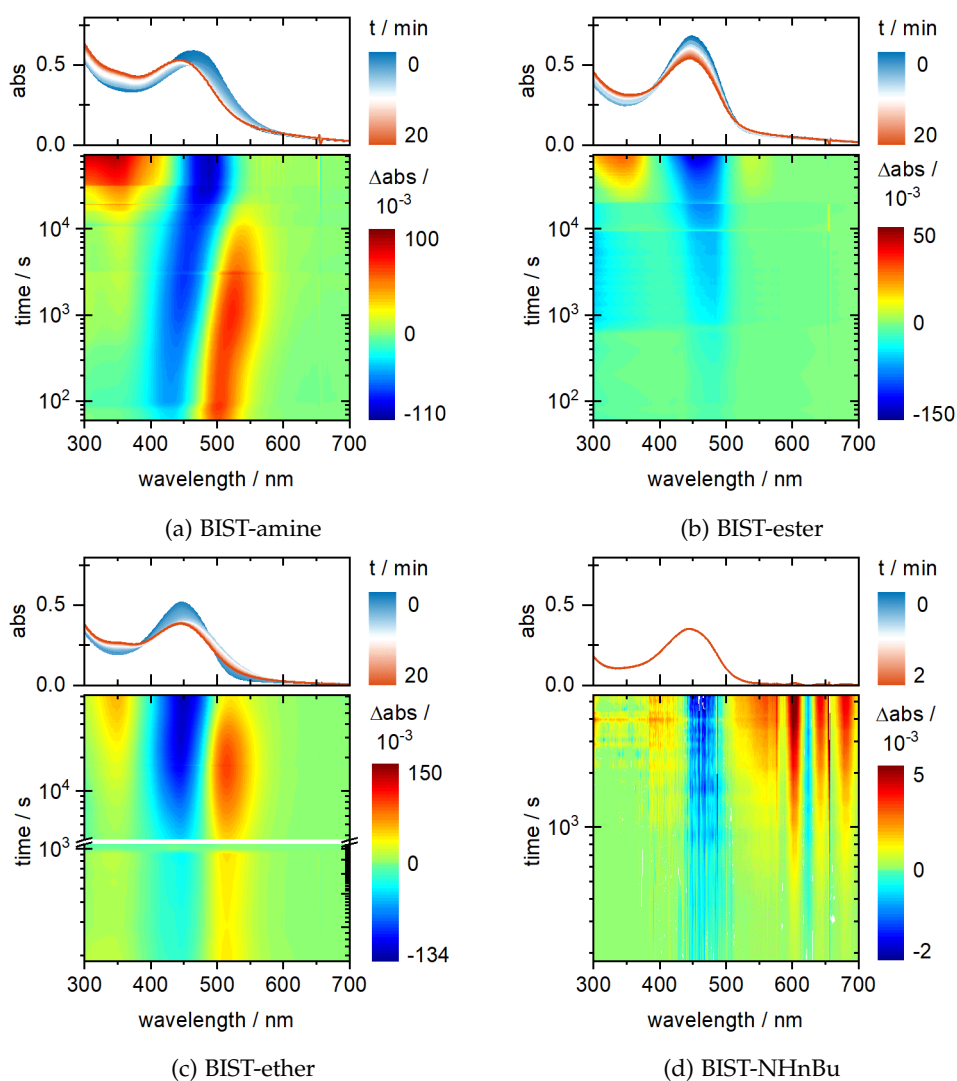


Figure 6.4: LED illumination experiments of the investigated BIST-cages in DMSO. Difference absorbance spectra of the four investigated BIST-compounds were recorded after LED-illumination ( $\lambda_{exc} = 455$  nm). The loss of ground-state absorbance around 455 nm indicates a successful uncaging reaction, whereas the arising red-shifted absorbance is assigned to the formed *aci*-nitro intermediate and nitroso-ketone photoproduct of the reaction.

band is missing in this spectral region and effects from stimulated emission or fluorescence can be excluded here. It is possible that the loss of ground-state absorbance and the (supposedly) missing absorbance band in the UV compensate each other.

Until the end of the illumination experiment, two positive absorbance changes are observed, a strong one ranging from 300-387 nm and a weak one centered around 535 nm. In contrast to BIST-amine, all three absorbance changes do not seem to be finished by the end of the experiment, indicating an incomplete uncaging reaction.

It is possible that the absorbance spectrum of the intermediate and photoproduct are overlapping with that of the BIST-ester. This would explain why the bands indicating a loss of absorbance and the formation of the photoproduct are missing. This assumption is justified, due to the fact, that at later delay times the absorbance in the UV increases, which matches the findings for BIST-amine.

The illumination of **BIST-ether**, as shown in [Figure 6.4c](#), contains features from both BIST-amine and -ester. The positive absorbance change around 350 nm appears initially within the first recorded spectra, accompanied by a negative and a positive absorbance change at 445 nm and 512 nm, respectively. The latter is a relatively strong positive absorbance change which shifts only slightly to higher wavelengths and reaches its intensity maximum at 514 nm. Similarly to BIST-amine, this absorbance band then decreases, followed up by a further increase of the absorbance band in the UV region. The negative band around the ground-state absorption maximum shifts to higher wavelengths as well and reaches its intensity minimum at 449 nm. Although the uncaging reaction for BIST-ether does not seem to be finished yet, the initial reaction steps are likely to be finished by the end of the experiment.

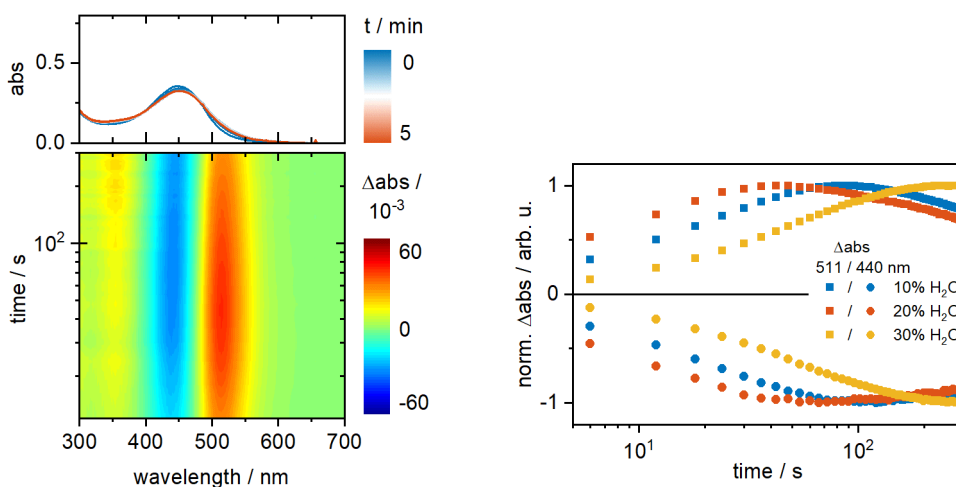
The assumptions which were made for BIST-amine can be applied to BIST-ether as well. A red-shifted intermediate or photoproduct appears at early illumination times and undergoes a subsequent, secondary photoreaction. In accordance to the other findings, the absorbance band in the UV appears with a delay.

As mentioned before, the case of **BIST-NHnBu** is outstanding, as it was investigated at a later time point and therefore with slightly different settings (regarding the concentration, illumination power, etc.). As seen in [Figure 6.4d](#) uncaging can barely be observed, however, the sample was illuminated for a shorter amount of time and a lower power. Apart from the noise in the spectral region above 600 nm, some features, which are observed for the other BIST-cages can be recognized. Firstly, the absorbance around the ground-state absorption maximum (446 nm) decreases, which hints towards an uncaging reaction, although the changes of optical density are very small. Moreover, two positive absorbance changes, red- and blue-shifted to the negative change, are observed, although the absolute change of the latter one is too small and could also be easily neglected.

Apparently, other measures were necessary to increase the uncaging efficiency of BIST-NHnBu. Therefore, a subset of experiments were performed separately for BIST-NHnBu to investigate the overall effect of water on the uncaging dynamics and efficiency.

**ILLUMINATION OF BIST-NHNBU IN A MIXTURE OF H<sub>2</sub>O/DMSO** The measurement for BIST-NHnBu was repeated under identical experimental conditions, but with a solvent mixture of 20% H<sub>2</sub>O in DMSO. The resulting absorbance spectra and contour plot in [Figure 6.5a](#) show that, although the same and relatively weak illumination power was applied, the changes of optical density are at least





(a) Difference absorbance spectra of BIST-NHnBu in DMSO + 20% H<sub>2</sub>O (b) Selected transient courses of BIST-NHnBu in DMSO with different contents of water.

Figure 6.5: Absorption spectra of BIST-NHnBu in DMSO with 20% H<sub>2</sub>O after LED illumination at 455 nm. (a) The contour plot shows absorbance changes at 439–445 nm (negative) and 415 nm (positive) which indicate the loss of ground-state absorbance due to uncaging and the formation of an intermediate or photoproduct, respectively. (b) The corresponding time courses with various amounts of water suggest a water-dependent reaction rate of the uncaging reaction.

10-fold increased. This also facilitates the description and assignment of the spectral features, as compared to the measurement without water. The overall contour plot resembles that of BIST-ether very much. Initially after illumination, a negative absorbance band at 445 nm arises, which is assigned to the ground state bleach and therefore indicates a successful uncaging reaction. Additionally, two positive bands at 355 and 511 nm appear, whereas the latter exhibits stronger changes overall, both of which have been observed for other BIST-cages. The positive absorbance change in the visible range shifts to higher wavelengths and reaches its intensity maximum at 514 nm. Interestingly, the maximum and priorly described minimum are reached at the same time, indicating a correlation between the assigned reaction. Analogous to the previously described BIST-compounds, the positive absorbance change at 511 nm hints towards the formation of the *aci*-nitro intermediate and the nitroso-photoproduct. The subsequent decrease of these bands is then accompanied by the absorbance increase at 355 nm, which so far has been assigned to a secondary photoproduct. Moreover, it is possible that the presence of water would also affect the secondary photoreaction, namely the decomposition of the nitroso-ketone, as its water-solubility is expected to be even worse than that of the BIST-compound prior to uncaging.

The steady-state experiments were repeated for different contents (10% and 30%) of water in DMSO. Due to a generally poor water solubility, BIST-NHnBu (as well as the other BIST-cages) can barely be dissolved in higher contents of

water. The difference absorbance spectra and corresponding contour plots (both not shown) barely differ from the one described above for a water content of 20% H<sub>2</sub>O, regarding its spectral features. [Figure 6.5b](#) shows the time course of the absorbance change at 440 and 511 nm, which were chosen to represent the changes of the absorbance maximum of the cage and the intermediate. The results suggest that the rate, with which the minimum and temporal maximum are reached, could be affected by the exact amount of water. Due to the fact that these steady-state experiments are highly dependent on the concentration of the sample, the illumination power, the sample volume, etc. - factors which are typically considered in the determination of the uQY - the observed effects on the uncaging rate were not further assigned.

Concluding this subset of experiments, the addition of water generally increases the uncaging yield (indicated by the relatively large absorbance loss around the ground-state maximum) as the comparison of the illumination experiments of BIST-NHnBu in DMSO with and without water could prove. A direct correlation between the uncaging rate or yield and the amount of water in solution is yet to be determined within the limits of the BIST-cages' solubility in water and its effects on the intermediates.

### 6.2.5 FTIR SPECTROSCOPY ON ILLUMINATED BIST-NHNBU

BIST-NHnBu in DMSO + 20% H<sub>2</sub>O was exemplarily investigated by recording [FTIR](#) absorbance spectra after LED illumination. Moreover, [DFT](#) calculations were performed to provide further insights on the involved vibrations and their corresponding spectral locations on both the BIST-cage and the nitroso-photoproduct. The DFT-computations were performed on a theory level of [BP86](#),[\[211, 212\]](#) using the basis function [SVP](#)[\[213\]](#) with Gaussian09 including an implicit solvent function in form of DMSO.[\[208\]](#) In general, the advantage of IR-spectroscopy is to get insights onto the changes of chemical bonds upon photoexcitation. In combination with DFT-calculations, one is able to precisely assign the spectral features to the vibrations. In contrast to the rapid-scan experiment of NPE-ATP described in [Section 5.6](#), here steady-state absorbance spectra were recorded in succession.

[Figure 6.6a](#) shows the result of the experiment, which depicts the difference FTIR-absorbance spectra, overlaid with the calculated vibrations of the BIST-NHnBu (blue) and the photoproduct nitroso-ketone (red), whereas the latter is represented as a positive signal. Several of the detected absorbance changes are consistent with the predicted vibrations. As a result, the following assignment of the vibrational changes could be based on the calculated vibrations. Three spectral regions are covered due to a total absorbance caused by the solvent (greyed areas).

Three positive absorbance changes at 1586 cm<sup>-1</sup>, 1290 cm<sup>-1</sup> and 1141 cm<sup>-1</sup> were detected. The transient changes of selected wavenumbers are shown in [Figure 6.6b](#)

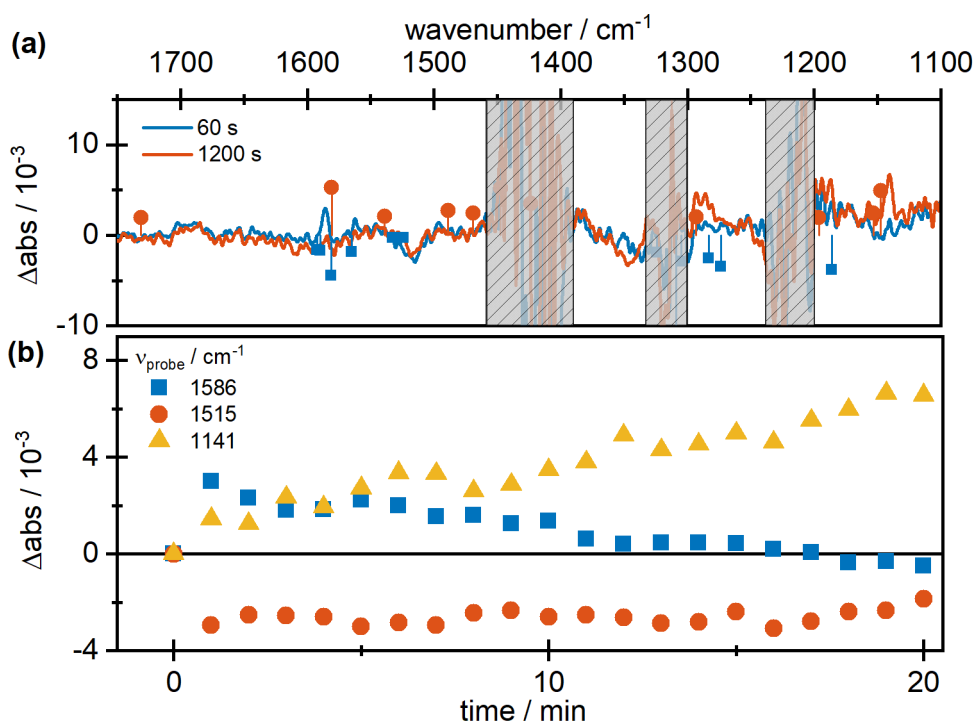


Figure 6.6: FTIR absorbance spectra of BIST-NHnBu after LED illumination. (a) Difference FTIR-absorbance spectra of BIST-NHnBu in 20% D<sub>2</sub>O after LED illumination (455 nm; 150 mW), overlaid with calculated vibrations of the reactant (blue) and photoproduct (red). (b) Transient courses of selected wavenumbers. The signals are assigned to vibrations of the *aci*-nitro intermediate (blue), nitroso-ringmodes (yellow) and nitro-stretches (red).

for a better representation of the course of the reaction. Instantaneously after illumination, the absorbance at 1586 cm<sup>-1</sup> increases and then decreases during continuous illumination. The calculations assign this vibration to the nitro-group of the BIST-cage. However, as a similar behaviour was found in the UV/vis, it is most likely that the vibration is rather assigned to the *aci*-nitro intermediate. Due to the structural similarity of the nitro- and the *aci*-nitro-group, it is possible that both calculated vibrations are not distinguishable. The positive changes at 1290 cm<sup>-1</sup> and 1141 cm<sup>-1</sup> are both assigned to ring-vibrations of the nitroso-group of the photoproduct and exhibit a constant increase of absorbance. Negative absorbances are found at 1515 cm<sup>-1</sup> and 1345 cm<sup>-1</sup>, both of which are assigned to vibrations of the nitro-group of BIST-NHnBu, which will be lost upon uncaging. Interestingly, the predicted vibration of the carbonyl-group of the photoproduct at 1713 cm<sup>-1</sup> was not detected in the experimental spectrum, which would have been an unambiguous indicator for the successful uncaging reaction. Due to the low  $\mu_{\text{QY}}$  of BIST-cages, the resulting signal changes aggravate a proper assignment of the involved vibrations. It is therefore necessary to repeat the experiment with optimized parameters regarding the setup and the sample conditions, in order to verify the hypotheses. Then, even time-resolved IR-experiments in

the ns-ms time range would be a possible way to confirm the actual results regarding the uncaging mechanism.

### 6.3 ULTRAFAST DYNAMICS IN THE PS-NS RANGE

To investigate the ultrafast dynamics in the ps-ns time range, transient absorption spectra of the BIST-cages are measured. The photocages BIST-amine, -ester and -ether were excited at both 430 and 470 nm (exemplarily shown in Figure 6.7).

Photoexcitation into two different flanks of the absorbance band provide information on whether a wavelength-dependent uncaging in the excited state prevails. If the excitation in the red flank of the absorbance does not or only barely affect the ultrafast dynamics, biological applications would be accessible more easily, as less harmful light can be used for uncaging. As BIST-NHnBu was investigated at a later point of time, it was only excited around the absorbance maximum at 440 nm. In return, the effect of water onto the ultrafast dynamics was investigated exemplarily for this compound. The reaction mechanism and the pathways after photoexcitation are summarized at the end of this chapter in Figure 6.8.

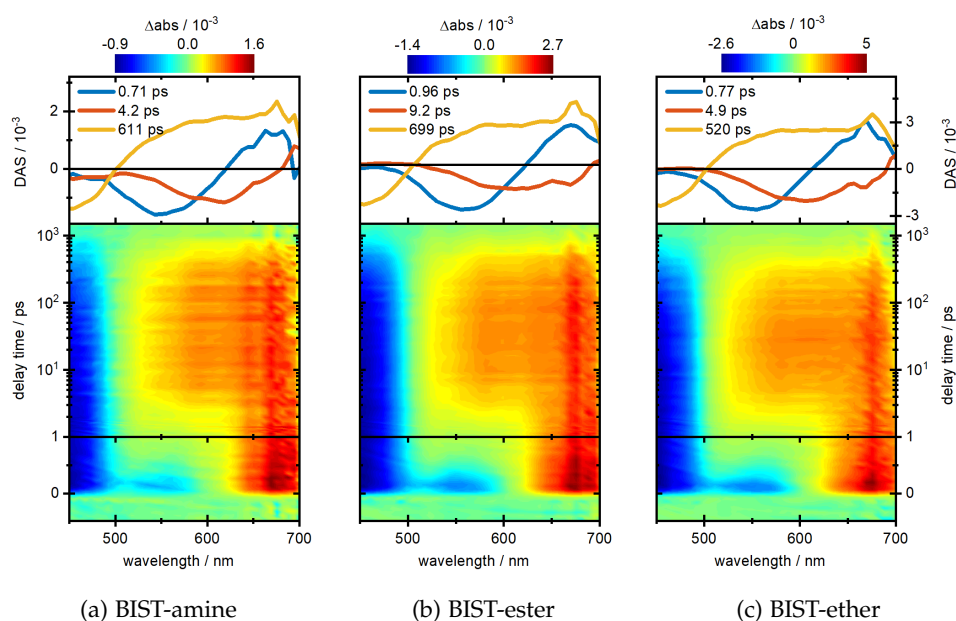


Figure 6.7: Transient maps and corresponding decay-associated spectra of BIST-amine, -ester and -ether after photoexcitation at 430 nm. The spectral shape of the maps resemble each other, indicating similar ultrafast dynamics. The broad positive absorbance band indicate that the BIST-cages undergo deactivation via the triplet pathway.

First, the BIST-cages -amine, -ester and -ether after photoexcitation at 430 nm are described. The resulting transient map for all three cages barely differ from each other regarding its spectral features, which is why only the transient absorption measurements for BIST-amine and -ester are shown (Figure 6.7a and Figure 6.7b). Instantaneously after photoexcitation, two strong signals can be observed: A strong GSB around 450 nm, and an ESA band ranging from 600-700 nm with a strong absorbance maximum around 675 nm. Moreover at early delay times, a weak negative absorbance change around 550 nm is observed, which is assigned to SE of the system. To describe the ultrafast relaxation processes after excitation, global lifetime analysis was performed,[66] and three exponential functions are necessary to describe the data set. The found lifetimes are summarized in Table 6.2.

The relatively weak SE seems to vanish after a few ps along with the strong ESA at 675 nm which is described with the lifetime  $\tau_1$  of 0.71 ps (0.96 ps and 0.77 ps for BIST-ester and -ether, respectively). After photoexcitation into the FRANCK-CONDON-region, the system relaxes to the vibrational ground state of the  $S_1$ -state, while radiating. This is described by the rate  $k_1$ , which, in this case, equals the inverse of lifetime  $\tau_1$  (s. Eq. (6.1)).

The steady-state fluorescence spectrum already suggested a weak fluorescence quantum yield and/or a short fluorescence lifetime. Nevertheless, an attempt has been made to directly validate the very short fluorescence lifetimes via a KERR-shutter measurement. The resulting measurement is far from being satisfactory, due to several restrictions regarding the sample's condition and the apparatus. This includes large amounts of sample at high concentrations and - depending on the KERR-medium - a fluorescence lifetimes, which is longer than 1 ps. Therefore, the resulting measurement is not considered for the evaluation of the ultrafast dynamics and thus omitted in this work. Another attempt with the help of TCSPC was not executed, as the assumed fluorescence lifetime is too short to be reliably detected.

Interestingly, the maximum of the SE is located at 550 nm, whereas the steady-state emission maximum is determined to be at 625 nm. This large wavelength-shift is probably caused by compensation due to the strong ESA at higher wavelengths leading to a presumable lower maximum of the SE. After the SE vanishes, a broad ESA band appears, ranging from 500-700 nm, which is described with the lifetime  $\tau_2$  of 4.2 ps. This lifetime is assigned to the relaxed  $S_1$  state and describes the buildup of the broad ESA band, as indicated by the corresponding DAS, which has a negative contribution ranging from 500-700 nm. This ESA band is assigned to the triplet state  $T_1$ , as described later on. Towards later delay times, the decay of the  $T_1$ -state is observed, which is described with the third lifetime  $\tau_3$  of 611 ps. The DAS of lifetime  $\tau_3$  shows a negative contribution from 450-500 nm, which describes the repopulation of the ground-state and a broad positive contribution from 500-700 nm, which describes the decay of the ESA band.

The ultrafast dynamics of nitro-benzylic compounds are well described in the literature, stating that from the relaxed  $S_1$ -state, a multitude of relaxation pathways are possible.[214–216, 103, 217–219] In this case, they lead to the formation of the *aci*-nitro intermediate, which is the first step in the uncaging reaction.

From the  $S_1$ -state, a singlet or triplet pathway is viable, which means that the  $S_1$ -lifetime  $\tau_2$  describes two different processes:[107] the reaction from the  $S_1$  via a barrier to the  $S_0$  ground-state of the *aci*-nitro intermediate through the CI (singlet pathway, which is described with the rate  $k_{2,a}$ ) and the ISC from the  $S_1$  excited-state to the triplet-state  $T_1$  (triplet pathway;  $k_{2,b}$ ). Unlike  $\tau_1$ , this second lifetime equals the inverse of the sum of both rates, as described in (6.2). Due to several reasons, it is suggested that  $k_{2,a} \ll k_{2,b}$ :

For *o*-NB compounds, the barrier within the singlet pathway is often described as the excited-state hydrogen transfer (ESHT)- or excited-state intermolecular proton transfer (ESIPT)-barrier, as it is responsible for the primary hydrogen transfer step.[220, 107] Šolomek *et al.* could show in quantum chemical calculations and by applying the BELL-EVANS-POLANYI principle to the photoreaction,[221, 222] that different leaving groups have an influence on this specific barrier. As a result, this affects the (non-)radiative processes on the excited singlet- and triplet surface and consequently changes not only the quantum yield but also the reaction rates of the different pathways.[107] In case of the BIST-cages, the  $u_{QY}$  is relatively low which suggests a high ESHT-barrier for the primary reaction step and therefore a low  $k_{2,a}$ .

Furthermore, a broad positive absorbance is typically assigned to a triplet state,[177] and its intense difference signals indicate that this process is very efficient. Normally, an ISC involves a change of the spin state and is formally forbidden in non-relativistic quantum theory.[223] If such a process occurs and can be observed, then it is typically very slow. On the other hand, if certain vibrational states in the  $S_1$ - and  $T_1$ -states are energetically degenerated, this process can happen very fast and within a few ps,[224] which apparently is the case for the BIST-cages.

Lastly, if both reaction channels would occur with similar rates, then the depletion of the  $S_1$ -state would lead to the population of a  $T_1$ -state and a  $S_0$ -state of the *aci*-nitro intermediate, which would have their own lifetime in either case. As only another third lifetime is observed, which is assigned to the decay and therefore the lifetime of the  $T_1$ -state, this unambiguously means that the formation of the triplet-state is the major relaxation channel.

$$\tau_1 = \frac{1}{k_1} \quad (6.1)$$

$$\tau_2 = \frac{1}{k_{2,a} + k_{2,b}} \quad (6.2)$$

$$k_{2,a} \ll k_{2,b} \Rightarrow \tau_2 \approx \frac{1}{k_{2,b}}$$

$$\tau_3 = \frac{1}{k_3} \quad (6.3)$$

The transient map suggests that by the end of the experiment, the ultrafast dynamics is finished and the excited-state signals have completely decayed to the ground-state, which does not coincide with the steady-state experiments, indicating the formation of an positive absorbance band around 510 nm. Upon closer inspection of the time slices at the latest delay times, a very weak absorbance change can be detected, indicating a reaction to the *aci*-nitro intermediate. Due to the fact that the  $\mu_{QY}$  is very low, the weak residual signals are reasonable. Apparently, the subsequent steps of the uncaging reaction happen on a later timescale, which requires a different measurement, as shown in [Section 6.4.1](#).

COMPARISON OF BIST-AMINE, BIST-ESTER AND -ETHER The transient absorption measurements of BIST-ester ([Figure 6.7b](#)) and -ether after photoexcitation at 430 nm resemble that of BIST-amine very strongly. Given the fact that the chromophore is the same for all three cages and the ultrafast reaction dynamics mainly revolve around the *aci*-nitro tautomer (which is only slightly different for the various leaving groups) this observation is comprehensible. Therefore, the following focus is set onto the resulting global lifetime analysis for BIST-ester and -ether and the differences hereof.

The data set of BIST-ester and -ether after photoexcitation at 430 nm are satisfactorily described with three exponential functions, just as for BIST-amine. [Table 6.2](#) summarizes the fitted lifetimes of all three compounds. The fitted lifetimes, as well as the spectral features of the corresponding [DAS](#) suggest that the same photoinduced processes occur in all three BIST-compounds. Upon closer comparison of the lifetimes, the differences of both  $\tau_1$  and  $\tau_2$  are within the error margin of the fit and therefore insignificant. BIST-ester stands out, as the formation of the triplet is slower compared to the other cages. This is most likely caused by the different chemical nature of the leaving groups and the related ESHT-barrier. The main contribution to this barrier is the radical stabilization energy (RSE) of the leaving group, which will decrease the height of the barrier, depending on the stabilization energy. In case of the BIST-cages, the RSE of the investigated leaving groups can be arranged in this order: esters (-24 kJ/mol) > tertiary amine (-20 kJ/mol)  $\simeq$  secondary amine (-19 kJ/mol)  $\simeq$  ether (-18 kJ/mol).<sup>[225]</sup> The comparably higher RSE of the ester group will decrease the ESHT-barrier and accelerate the reaction rate  $k_{2,a}$  to the  $S_0$ -state via the CI. As a result, the competing ISC ( $k_{2,b}$ ) to the  $T_1$ -state is decelerated, as actually observed for BIST-ester.

PHOTOEXCITATION AT 470 NM Next, the dependence of the ultrafast dynamics of the BIST-cages on the excitation wavelength is investigated. For this, the BIST-cages are excited at 470 nm. Although both the photoexcitation at 430 nm and 470 nm will lead to a population of the  $S_1$ -state, the amount of excess energy imparted onto the chromophore could make a difference in the reaction rate and mechanism. Excitation of the BIST-cages at 470 nm results in a lower excess energy in the excited state, which should make the triplet pathway more favorable. The excess energy might affect the ESHT-barrier and favor the reaction

*ultrafast dynamics of  
BIST-ester and  
-ether after  
photoexcitation at  
430 nm*

Table 6.2: Fitted lifetimes after global lifetime analysis of the BIST-cages after photoexcitation at 430 and 470 nm

lifetime	$\lambda_{exc} = 430 \text{ nm}$			$\lambda_{exc} = 470 \text{ nm}$		
	-amine	BIST- -ester	-ether	-amine	BIST- -ester	-ether
$\tau_1 / \text{ps}$	0.71	0.96	0.77	0.89	0.87	0.80
$\tau_2 / \text{ps}$	4.2	9.2	4.9	6.8	7.1	5.9
$\tau_3 / \text{ps}$	611	699	520	556	229	374

rate via the singlet pathway. Subsequently, the uQY for the formation of the *aci*-nitro intermediate will then mainly depend on the branching ratio at the **CI**. More importantly, if the excitation wavelength does not influence the ultrafast dynamics (or only slightly), then the uncaging reaction can also be initiated with wavelengths of lower energy, which are less harmful for any biological application. Moreover, modern confocal microscopes have a limited number of emission wavelengths (e.g. 430 nm is not covered, yet). A successful initiation of the photodynamics at 470 nm would allow the utilization of microscopes with similar wavelengths for future in-cell applications.[226, 227]

The transient map of BIST-amine after photoexcitation at 470 nm barely differs from the the previously described transient maps after photoexcitation at 430 nm (not shown). Initially after excitation, two negative signals centered around 455 nm and 575 nm, which are assigned to the **GSB** and **SE**, respectively, and a strong **ESA** band at 600 nm appears. Global lifetime analysis is performed and three exponential functions are necessary to satisfactorily describe the data set. As for the excitation of the BIST-cages at 430 nm, the first lifetime  $\tau_1$  of 0.80 ps describes both, the lifetime of the stimulated emission as well as the decay of the strong ESA around 700 nm, as the corresponding **DAS** has contributions for these specific wavelength ranges. The rate  $k_1$  describes the relaxation to the relaxed  $S_1$ -state. The second lifetime  $\tau_2$  of 6.8 ps describes the buildup of a broad positive band ranging from 500-700 nm, which is assigned to the formation of the triplet. As shown in Eq. (6.2), this lifetime describes the inverse of the sum of the reaction rates via the singlet and triplet pathway. The final lifetime  $\tau_3$  describes the repopulation of the GSB and the decay of the ESA and thus assigned to the lifetime of the  $T_1$  state, which is 556 ps in case of BIST-amine. Compared to the lifetimes after photoexcitation at 430 nm,  $\tau_1$  is (within the range of error) not affected by the excitation wavelength, whereas  $\tau_2$  is slightly higher (but possibly within the range of error as well) and  $\tau_3$  significantly lower. The proposed reaction mechanism suggests that the lifetimes  $\tau_2$  and  $\tau_3$  describe the buildup and decay of the triplet state, respectively. Although the second lifetime is short enough to be actually affected by the choice of excitation wavelength, the third lifetime is too large to be influenced by the ultrafast excitation pulse. So far, a well-founded explanation for these findings is not found yet.



Figure 6.8 illustrates and summarizes the proposed assignment of the determined lifetimes for the ultrafast dynamics of the BIST-cages. After photoexcitation (blue vertical line) into the FRANCK-CONDON region, the system relaxes into the vibrational ground-state. Hereafter, the singlet or triplet reaction path can be taken, whereas in the first case, the ESHT-barrier must be crossed to reach the CI and then the ground-state of the *aci*-nitro intermediate. Due to the low  $uQY$ , the barrier is assumed to be quite high, leading to the conclusion that this pathway is less likely. Instead, the triplet is formed, which is indicated by the broad positive absorbance band. Although the triplet state of the *aci*-nitro intermediate and then the singlet ground-state can be reached after another ISC, the system preferably decays to its former ground-state.

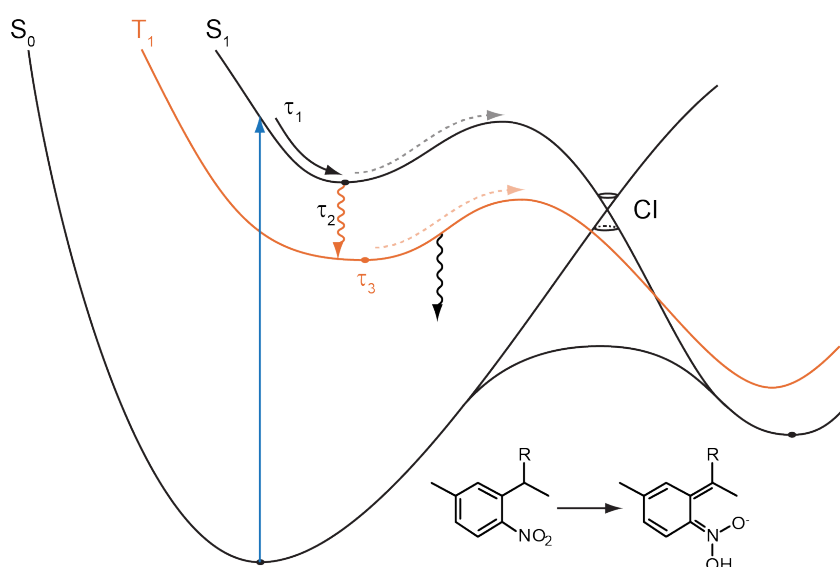


Figure 6.8: Suggested mechanism of the first steps for the BIST-uncaging reaction. After photoexcitation into the FRANCK-CONDON-region, the system relaxes to its vibrationally lowest state in the  $S_1$ . The ESHT-barrier for singlet pathway is relatively high, which results in a low  $uQY$ . The triplet pathway is taken instead which leads to an ISC, described with  $\tau_2$ . The decay of the long-lived triplet-state ( $\tau_3$ ) leads to the repopulation of the ground-state.

## 6.4 INFLUENCE OF WATER ON THE EXCITED DYNAMICS OF BIST-NHNBU

The steady-state experiments indicate that water plays a crucial role for the uncaging reaction of the BIST-cages (see Section 6.4). Therefore, water-dependent transient absorption measurements are performed to investigate possible aqueous solvent effects on the ultrafast dynamics. In the experiments shown above, BIST-NHnBu was not considered, yet. This cage has been chosen as the reference system for the water-dependent studies. BIST-NHnBu bears a secondary amine as a leaving group which is known to have a similar RSE as tertiary amines (like

BIST-amine) The resulting dynamics of BIST-NHnBu should therefore barely differ from the ones already described.

Firstly, the transient absorption spectroscopy of BIST-NHnBu in DMSO (without water) was performed to be able to compare the results to the other BIST-cages. Thereafter, increasing amounts of water (10, 20 and 30% H<sub>2</sub>O) were added to the solution to investigate any effects on the spectral shape and fitted lifetimes. The outcome of the experiment is summarized in [Figure 6.9](#), which depicts the transient maps for the measurement without and with 20% H<sub>2</sub>O. All experiments involving BIST-NHnBu were excited at 440 nm.

[Figure 6.9a](#) shows the transient map and the corresponding [DAS](#) of BIST-NHnBu in DMSO without water, which resemble those of the other BIST-cages. Initially after photoexcitation, two negative signals appear, a [GSB](#) at 450 nm and a [SE](#) ranging from 500-600 nm, as well as a positive band at 600-700 nm which is assigned to the [ESA](#). Global lifetime analysis is performed and three exponential functions are necessary to describe the data set. In a direct comparison to the tertiary amine BIST-amine, the lifetime for the buildup of the triplet-state is almost identical, with the difference lying only within the error margin. This finding confirms the fact that in the literature very similar RSE for both leaving groups are reported.[225] Interestingly, the lifetime of the triplet-state which is described by  $\tau_3$  is less than half for BIST-NHnBu, compared to the other BIST-cages, independent of their excitation wavelength. Unlike the wavelength-dependent investigations at 470 nm and 430 nm, the difference for the third lifetime of BIST-NHnBu compared to the other BIST-cages is assumed to be resulting from the difference of the leaving group and therefore a sample-specific characteristic.

Then, small amounts of water are added to the solution, ranging from 10-30% H<sub>2</sub>O, to examine the overall influence of the aqueous solvent and a potential acceleration and facilitation of the uncaging reaction, as it has been observed in the steady-state experiments. The transient absorption measurement of BIST-NHnBu in DMSO with 20% H<sub>2</sub>O is shown in [Figure 6.9b](#). As for the other BIST-cages, global lifetime analysis was performed and three exponential functions are necessary to describe the ultrafast dynamics. The resulting transient maps are, regarding the spectral features and the [DAS](#), nearly identical to the ones previously described. [Table 6.3](#) summarizes the results from the global lifetime analysis for the transient absorption measurements of BIST-NHnBu for the various contents of water in DMSO.

By comparing the measurements with different water content, the first lifetime describing the relaxation process from the [FRANCK-CONDON](#) region to the relaxed [S<sub>1</sub>](#)-state is not influenced i.e. the changes are within the error margin. The second lifetime  $\tau_2$  describing the formation of the triplet-state is only slightly affected, when a ratio of at least 30% water is present. It seems that this minimum amount of water is required, to affect the [ESHT](#)-barrier and possibly decrease it to an

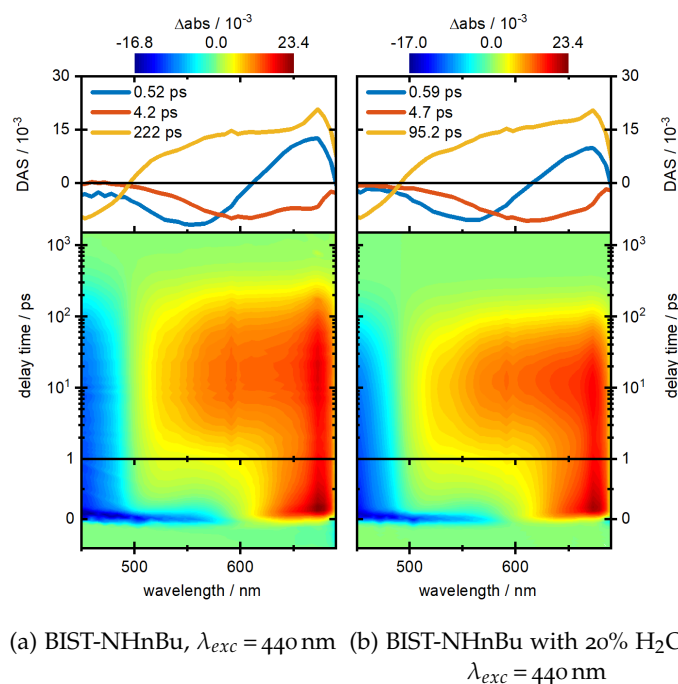


Figure 6.9: Transient maps of BIST-NHnBu without (a) and with 20% H<sub>2</sub>O (b) after photoexcitation at  $\lambda_{exc} = 440 \text{ nm}$ . Although the spectral similarity is given, the triplet lifetime is significantly decreased in the presence of water.

extent, that the competing process via the singlet pathway actually becomes viable enough, to lower the overall lifetime  $\tau_2$ .

Table 6.3: Global lifetime analysis of BIST-NHnBu in different contents of water after photoexcitation at 440 nm

	DMSO + [% H <sub>2</sub> O]			
	0	10	20	30
$\tau_1 / \text{ps}$	0.55	0.61	0.60	0.41
$\tau_2 / \text{ps}$	4.3	4.7	4.6	3.0
$\tau_3 / \text{ps}$	222	206	95.6	45.2

The first reaction step in the photoreaction of *o*-NB and NPE-cages is the formation of the *aci*-nitro intermediate which requires the re-arrangement of a proton. If water is therefore added to the solution, this step is facilitated, leading to a higher reaction rate and therefore a lowered lifetime. As the ESHT-barrier of the T<sub>1</sub>-state is lowered as well, this consequently leads to a shorter lifetime  $\tau_3$ . However, the overall lifetime of the triplet-state is already affected by low amounts of water. Although 10% H<sub>2</sub>O decreases the lifetime  $\tau_3$  only slightly (206 ps), this lifetime is less than half with double the amount of water. It is observed that this lifetime becomes even shorter at 30%. The transient courses at 465 and 629 nm are shown in Figure 6.10 and highlight the effect of water very

well. It seems that water also decreases the ESHT-barrier of the triplet pathway, and does so at even low water contents. This can be explained by correlating the absolute lifetime of the excited-states with concentration-dependent diffusion of water. As the lifetime of the  $S_1$ -state is too short and the excited molecules react very fast, the water molecules are only able to affect the excited state barriers when their concentration is comparably high. The triplet state is formed at a later time and lives longer, which then allows the diffusion-controlled interaction between water molecules and the barrier to take place. In conclusion, a higher amount of water decreases the ESHT-barrier and increases the rate of formation of the *aci*-nitro intermediate. So in contrast to the observation in the steady-state experiments, higher amounts of water accelerate the *aci*-nitro formation, which is one of the key steps of the uncaging mechanism. Although the rate-limiting step in the reaction of *o*-NB cages is supposed to be the lifetime of the formed *aci*-nitro intermediate, this effect will also influence the choice of precursors for further BIST-cages or *o*-NB cages in general.

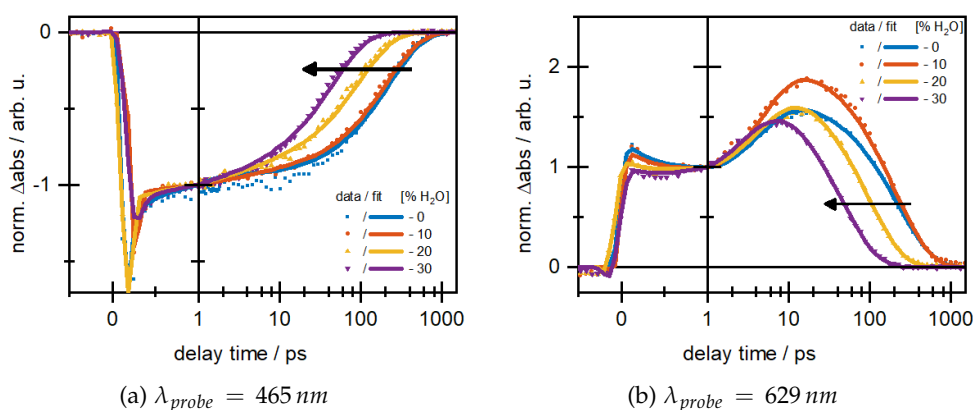


Figure 6.10: Influence of water to the ultrafast dynamics of (selected transients) BIST-NHnBu after excitation at  $\lambda_{exc} = 440 \text{ nm}$ . The depicted transients correspond to a water content of 0/10/20/30% (blue/red/yellow/purple) in DMSO solution and were normalized to the difference absorbance at 1 ps.

This set of measurements concludes the section, in which the ultrafast dynamics of the BIST-cages are investigated. So far, the most suitable precursor for the next generation of BIST-cages cannot be pointed out. The transient absorption measurements revealed that BIST-NHnBu (in a mixture with water) has the shortest excited-state lifetime and the corresponding *aci*-nitro intermediate is formed the fastest. Although this does not necessarily imply an actual acceleration of the overall uncaging reaction, it helps to understand the nature of BIST-caged compounds. The effect of water is not necessarily present for all cages, as the opposite effect has been reported for DEACM-caged azide.[228] Van Wilderen *et al.* could show that the addition of water slows the uncaging mechanism down, as the formation of the azide ion is hindered with an increased amount of water. Although the authors used heavy water ( $D_2O$ ) the kinetic isotope effect (KIE) can be neglected,[229] as a proportionality was observed between

the amounts of D<sub>2</sub>O and the effect of deceleration should also exist for H<sub>2</sub>O. It is therefore of utmost importance to characterize and understand the influence of the chromophore, the leaving group and any additional external influences such as the additional water content to optimize the reaction mechanism.

#### 6.4.1 REACTION DYNAMICS IN THE $\mu$ S-MS RANGE

As part of the full time-resolved characterization for the BIST-cages, this section covers the dynamics in the  $\mu$ s - ms time range. By the end of the transient absorption measurements, a very weak residual difference absorbance is detected, and most of the excited molecules have returned to the ground-state. This residual signal is assigned to the *aci*-nitro intermediate. As the lifetime of the *aci*-nitro intermediate is longer than the possible time window in the transient absorption setup, this section investigates the decay in the  $\mu$ s-ns time range by flash-photolysis measurements. It is important to note that the absolute absorbance changes in the different types of measurements are not necessarily comparable, as different experimental settings were applied (laser system, excitation pulse, etc.). The intermediate reacts to a cyclic isoxazol-analogue and subsequently forms a hemiketal/hemiaminal-analogue and then the nitroso-photoproduct in a concerted and irreversible reaction.

The general opinion suggests that the uncaging of molecules protected with *o*-NB does not have an unambiguous rate-limiting reaction step. In many cases (shown for phosphates, carboxylates, etc.) it is the *aci*-nitro decay which determines the uncaging rate, however examples are known where another part of the reaction is rate-limiting.[87] So far, the *aci*-nitro intermediate of the BIST-compounds could be spectrally identified, which allows to determine its lifetime and possibly the rate-limiting step of the uncaging reaction.

As discussed in [Section 6.2](#), the positive absorbance change around 510 nm is assigned to both the *aci*-nitro intermediate and the subsequently formed nitroso-product. A residual positive absorbance change is also observed in the ps time range, so transient flash-photolysis measurements were conducted with that probe wavelength. The measurements were carried out on BIST-NHnBu, with a major focus on the water-dependence. The result of this experiment is shown in [Figure 6.11](#). Instantaneously after photoexcitation, a positive signal is present, which decays in the range of a few hundred  $\mu$ s and then reaches a plateau at longer time scales. These findings are in accordance with the results from the steady-state experiment, indicating the reaction from the *aci*-nitro to the nitroso-photoproduct. As this reaction is supposed to be concerted, a first-order reaction is assumed and a monoexponential fit of the decay is performed. For the measurement without water, the fit yields a time constant of 310  $\mu$ s, which directly corresponds to the lifetime of the *aci*-nitro intermediate (see [Figure 6.11a](#)). This decay is much slower, compared to other *o*-NB based cages, such as NVOC-puromycin (32  $\mu$ s).[22] As already mentioned, the different

leaving groups are a possible explanation for the big difference. Moreover, BIST-NHnBu carries an additional methyl group in  $\alpha$ -position to the leaving group, while NVOC-puromycin only contains a hydrogen atom at that position, which is why the slightly different types of cages and their respective photoproducts (nitroso-ketone and -aldehyde) can influence the speed of the reaction as well.

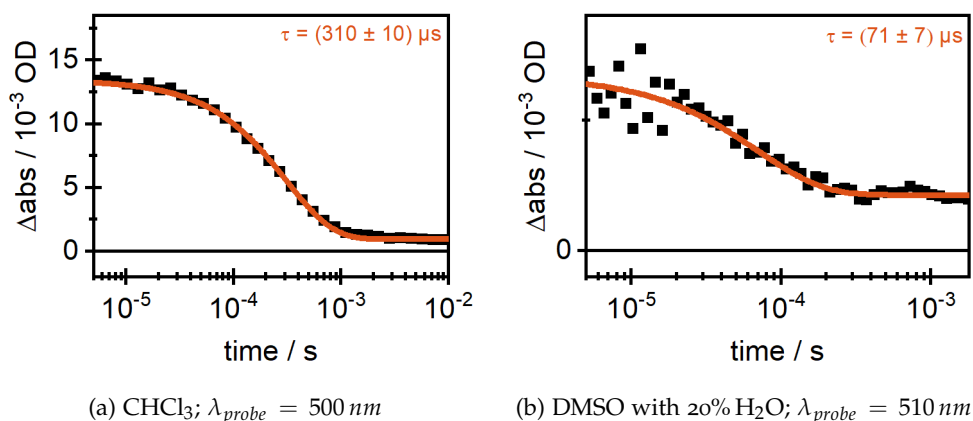


Figure 6.11: Flash-photolysis experiments of BIST-NHnBu after photoexcitation at  $\lambda_{\text{exc}} = 455 \text{ nm}$ .

The measurement of BIST-NHnBu is repeated with an additional content of 20%  $\text{H}_2\text{O}$ . This was done to investigate whether water not only lowers the lifetime of either the singlet or triplet excited state but also influences the subsequent reaction from the *aci*-nitro intermediate to the nitroso-product. The resulting measurement is shown in Figure 6.11b. The experimental settings were adapted to suit the detected time window.

As for the measurement without water, the positive absorbance appears initially after photoexcitation. This band decays in  $\mu\text{s}$  range and results in a residual positive absorbance. The monoexponential fit of the decay gives a lifetime of 71  $\mu\text{s}$ . When comparing the lifetimes, the one from the measurement with water is less than four times smaller, indicating a tremendous acceleration of the reaction in water.

In contrast to ultrashort time measurements, no extensive water-dependence was measured for the dynamics in the  $\mu\text{s}$ -ms range. Due to the fact that the measurements in this time-regime require larger amounts of sample and ideal settings of the used setup, the shown measurement has to be understood as a proof of principle.

## 6.5 CONCLUDING REMARKS

In this chapter, four different photolabile compounds, which carried the same chromophore bisstyrylthiophene (BIST) as its core, were investigated. Steady-state characterizations were performed and showed that the implementation of BIST leads to several favorable photophysical properties such as an absorbance

maximum in the visible wavelength range around 445 nm and a large molar extinction coefficient of up to  $55,700 \text{ M}^{-1} \text{ cm}^{-1}$ . Despite the low emission intensities fluorescence spectra were measured, leading to the conclusion that this deactivation channel is not favored. However, the fluorescence quantum yield of the BIST-cages should be obtained in future experiments, to reliably verify this hypothesis.

Steady-state absorbance spectra of BIST-cages in the UV/vis and under constant illumination revealed useful information about the reaction course of BIST, which helped in identifying the occurring species in the proposed reaction mechanism, shown in Figure 6.12. The *aci*-nitro intermediate exhibits an absorbance maximum which is red-shifted to that of the BIST-cage and located around 510 nm. Upon LED-illumination, its absorbance increases until a point is reached where it starts to decrease again, accompanied by an absorbance increase in the UV. This is assumed to describe a secondary photoreaction of the nitroso-photoproduct, which is known to be photolabile as well.[209] In the specific case of the illumination of BIST-NHnBu it was observed that the addition of water to the solvent facilitates the uncaging reaction. This can be explained by the fact, that the reactions from the *aci*-nitro intermediate through the isoxazol and the hemiketal/hemiaminal to the nitroso-ketone mainly consists of proton migrations and are therefore possibly accelerated by water.

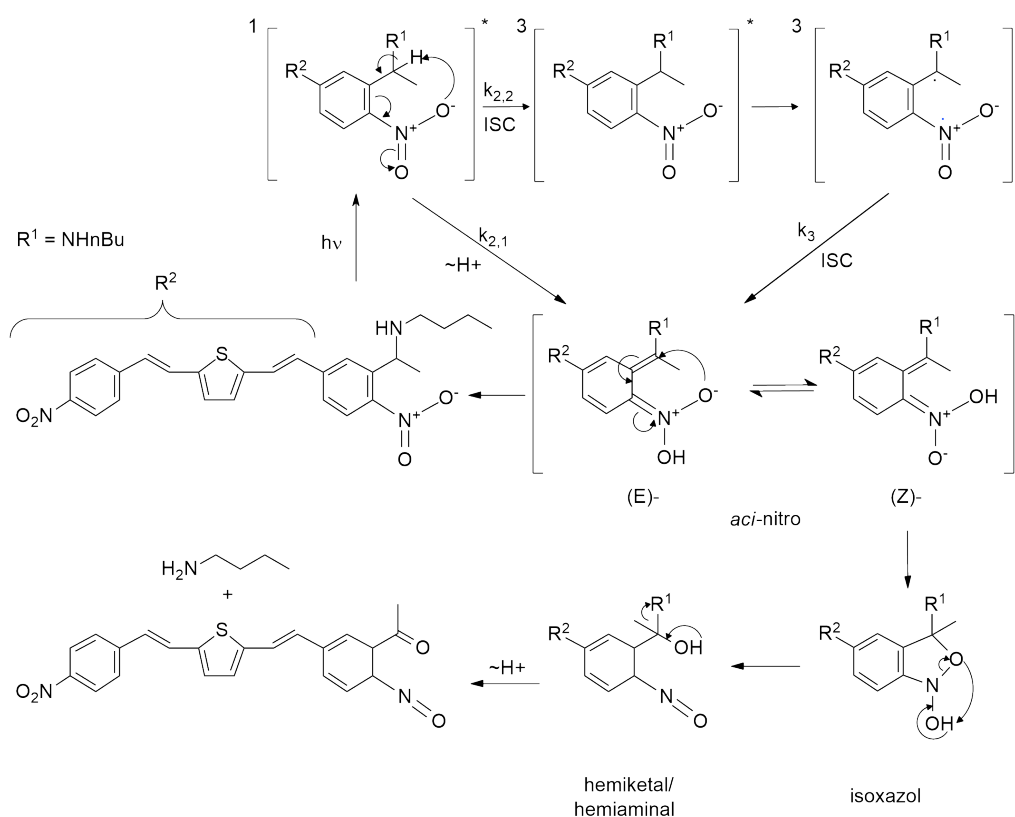


Figure 6.12: Proposed mechanism for the uncaging reaction of BIST-cages

Hereafter, ultrafast transient absorption measurements provide clear evidence that the BIST-cages follow the triplet-pathway after photoexcitation. This also explains the unfortunate low uncaging quantum yields of BIST-cages which are in the range of ca. 5%. GLA was performed and three lifetimes are found to describe the data set. The third lifetime  $\tau_3$  is assigned to the previously mentioned triplet-state and is in the range of 230-700 ps, depending on the investigated BIST-cage and the excitation wavelength. In an additional study, the water-dependence of the excited-state lifetimes is investigated exemplarily for BIST-NHnBu. It was observed that the triplet-lifetime decreases significantly with increasing amounts of water. A lifetime of 45.2 ps was found at a water content of 30%.

Although the majority of the excited molecules repopulates the ground-state by the end of the experiment, residual absorbance changes suggest that the actual uncaging reaction is not finished, which is further underlined by missing absorbance of the *aci*-nitro-intermediate around 510 nm. Thus, flash-photolysis experiments were carried out, in which the probe wavelength was set to 510 nm to determine the lifetime of the intermediate. The positive absorbance change after photoexcitation confirms that lifetime of the *aci*-nitro-intermediate is longer than the experimentally accessible time range of the transient absorption setup. The lifetime of the intermediate was found to be 310  $\mu$ s, which was accelerated by a factor of four in the presence of water to 71  $\mu$ s. Due to the fact that the other intermediates are not detectable in the visible wavelength range, this reaction is assigned to be the rate-limiting step in the uncaging reaction of the BIST-cages. These results are within a reasonable time range comparable to other *o*-NB- or NPE-cages.

Despite the fact that most of the findings for the characterization of the BIST-cages described in this chapter follow the general pattern of *o*-NB uncaging, further confirmation could be obtained in elaborate time-resolved IR-experiments. If the lifetime of the vibration resulting from the nitro-group, as well as nitroso-ketone vibration, would be unambiguously determined, the results could be used to verify the *aci*-nitro lifetime obtained from transient flash-photolysis. Moreover, if the BIST-cages are to be applied in a biochemical environment, the influence of water onto the various reaction steps should be inspected more closely. So far, the combination of the results of both, the steady-state and ultrafast measurements of BIST-NHnBu in the presence of water, leads to the assumption that the various steps in the reaction mechanism are affected by water in different ways.

Lastly, it was shown for multiple cases that along the triplet pathway the quantum yield of the uncaging process is low. If one would be able to predict which molecular parameters determine the preference for the different pathways will be taken, this would provide a tremendous progress for the synthesis of photocages based on *o*-NB or NPE.



## RESULTS - CECAM

---

One of the approaches to understand biochemical processes, is the ability to photochemically control the underlying reaction. Usually, this can be achieved by two alternative strategies, which are both described within this work. The previous chapter contains the characterization of a photocage, whereas this chapter will focus on a photoswitch. Also known as photochromic compounds, a wide variety of switchable molecules is already known in the literature, each with their own sets of advantages, which are summarized in [Section 3.3](#). Most of the investigated photoswitches are simply chemical modifications of the major classes, out of which many examples are part of a broader domain of current research, such as azobenzenes, spiropyrans or fulgides.[\[53, 135, 230–232\]](#).

The compound investigated in this thesis and presented in this chapter is an alkene (allylidene) photoswitch, in which one end is chemically substituted by [DEACM](#) to optimize many photophysical properties, such as the absorbance maximum or the molar extinction coefficient. Due to this chromophoric core, this set of photoswitches is named coumarin allylidene malonate ([CAM](#)) compounds. The other end of the alkene is substituted with electron-pushing groups, such as nitriles or *tert*-butylester. Two lowercase letters are put before the name indicating what functional groups are substituted to the allylidene (dicyano: dc, cyanoester: ce). In this work, the focus is solely put onto ceCAM. As part of the thorough characterization of this photoswitch, different properties are necessary to be identified first. After the characterization of the thermal stability of either isomer, fatigue-resistance measurements are carried out to identify the numbers of switching cycles, which the compound can undergo before photodegradation takes place. This is followed by the determination of the reaction quantum yield ([rQY](#)) for either isomerization direction. Then, the fluorescence of ceCAM is investigated. As coumarins are not only widely used as laser dyes but also as fluorophores,[\[121–123\]](#) the identification and characterization of this radiative deactivation channel is necessary and the fluorescence quantum yield ([fQY](#))  $\phi_f$  is determined. After the aforementioned steady-state characterization, the ultrafast reaction dynamics in the ps-time range is investigated to identify the rates of the isomerization reaction.

### 7.1 GENERAL STEADY-STATE PROPERTIES OF CECAM

The chemical structure of the investigated photoswitch ceCAM is shown in [Figure 7.1](#), depicting the *trans*- (left) and *cis*-isomer (right). According to The International Union of Pure and Applied Chemistry ([IUPAC](#)), the *E/Z*-convention

is the preferred description for the isomerization, to avoid a wrong assignment in cases of three or more substituents at the alkene moiety. Due to the fact that the allylidene of ceCAM is only doubly substituted, the *trans/cis*-convention is unambiguous here and therefore used throughout the entire work.

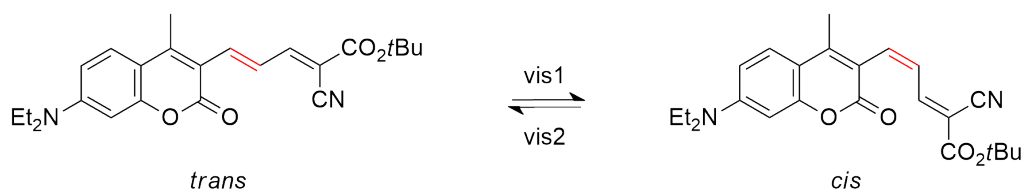


Figure 7.1: Photochromism of the investigated photoswitch ceCAM. The *trans*- and *cis*-isomer are depicted on the left and right, respectively. Isomerization occurs around the internal double bond, shown in red.

Both isomers already exhibit very promising photophysical properties from their respective absorbance spectra, which is depicted in Figure 7.2. The *trans*-isomer (blue) has a relatively weak absorbance band around 330 nm and a single, strong band centered around 489 nm. Visible light is absorbed very efficiently, with a molar extinction coefficient of up to 50,300 M<sup>-1</sup> cm<sup>-1</sup> in MeCN. The *cis*-isomer has a broad absorbance band ranging from 350-500 nm which is made up of two overlapping absorbance bands, with maxima at 365 nm and 437 nm. From the calculated pure spectrum, the molar extinction coefficient is determined to be 18,600 M<sup>-1</sup> cm<sup>-1</sup> at 437 nm in MeCN.[160] An isosbestic point is found at 432 nm which does not change upon illumination. The absorbance at the isosbestic point can therefore be used, to follow any undesirable side reaction, such as photodegradation.

The absorbance spectrum of the *trans*-isomer was recorded in various solvents, such as ethyl acetate, toluene, *i*-PrOH, acetone, MeOH, MeCN and DMSO and a strong solvatochromism was observed for ceCAM. The absorbance maximum ranges from 476 nm (toluene) to 505 nm (DMSO) as well. In this work, all the measurements are carried out in MeCN.

The double bond, which is undergoing the isomerization reaction is the internal double bond, closest to the coumarin and highlighted in red (Figure 7.1). This was shown by Richers *et al.*, who synthesized the dicyano analog dcCAM with two terminal nitriles.[160] If the outer double bond isomerized, then the absorbance spectra would not change for this derivative, because the resulting molecule would be identical, due to the identical nitrile residues. However, the found spectra of *trans*- and *cis*-dcCAM are very similar to those of ceCAM. This can only be the case, when the isomerization occurs around the internal bond. The observed small red-shift for the absorbance maximum of dcCAM ( $\epsilon_{513}(\text{dcCAM}) = 59,100 \text{ M}^{-1} \text{ cm}^{-1}$ ) was explained by the stronger electron-withdrawing properties of malononitrile.[233]

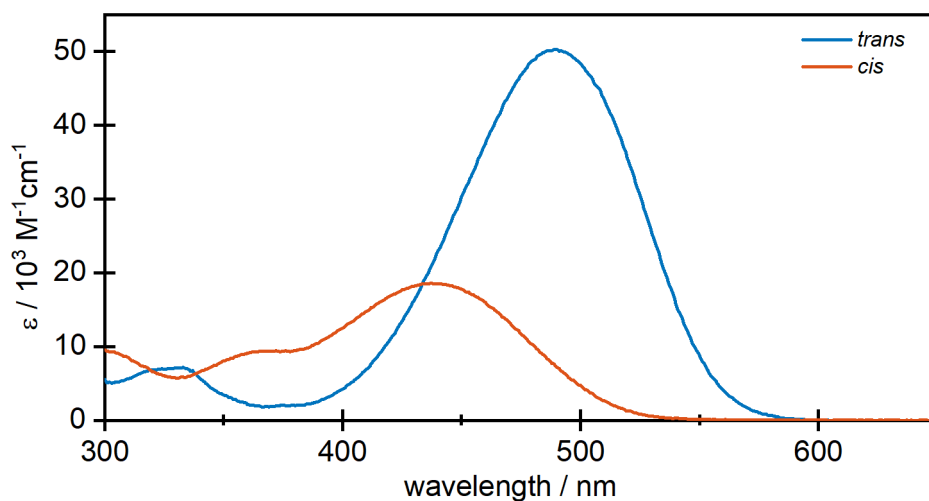


Figure 7.2: The absorbance spectra of *trans*-cecAM (blue,  $\epsilon_{489} = 50,300 \text{ M}^{-1} \text{ cm}^{-1}$ ) and calculated absorbance spectrum of *cis*-ceCAM in MeCN (red,  $\epsilon_{437} = 18,600 \text{ M}^{-1} \text{ cm}^{-1}$ ) show that both isomers absorb visible light very efficiently.

### 7.1.1 DFT-CALCULATIONS OF CECAM

Calculating the ground-state optimized structures of the *trans*- and *cis*-isomer and comparing them to their corresponding spectra (Figure 7.2) could give a possible explanation for the spectral differences regarding both the wavelength-shift and decrease of absorbance maximum. The chemical structure of the *cis*-isomer suggests a twisted conformation, which could lead to an inhibition of delocalization of  $\pi$ -electrons, shifting the absorbance maximum to higher energies. Then, the spectrum would resemble that of its coumarin-core DEACM, which has similar photophysical properties ( $\epsilon_{375} = 20,800 \text{ M}^{-1} \text{ cm}^{-1}$ ).[24]

Similar to the DFT-calculations of the BIST-compounds, DFT-computations were performed on a theory level of  $B_3LYP$  using the basis function cc-pVDZ with Gaussian09.[208] Pre-optimized geometries of *trans*- and *cis*-ceCAM were obtained from Avogadro,[234] and used as the initial structure. Without this step, the optimization would have lead to the *trans*-isomer in any case. An implicit solvent function was applied in form of acetonitrile, which was also the solvent of choice in the practical experiments.

The resulting ground-state optimization of *trans*-ceCAM confirms the suggested planar structure. Photoexcitation was found to be most efficient for a  $S_0 \rightarrow S_1$ -transition, with a wavelength of 488.55 nm (2.538 eV) and an oscillator strength of 1.623. The involved molecular orbitals in the transition, HOMO and LUMO, are shown in Figure 7.3 and indicate a transition with  $\pi$ - $\pi^*$  character. The other transitions that were found, exhibited low oscillator strengths ( $<0.2$ )

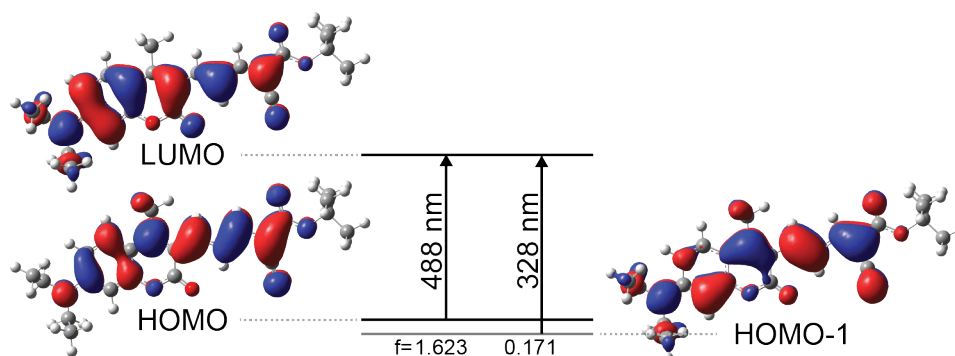


Figure 7.3: DFT calculations for the ground-state geometry and MOs involved in photoexcitation of *trans*-ceCAM

and are therefore neglected. Both the value for the absorbance maximum and the fact that only a single bright state was found, are in accordance with the spectrum of *trans*-ceCAM. Therefore, the DFT-calculations are assumed to reflect experimental results.

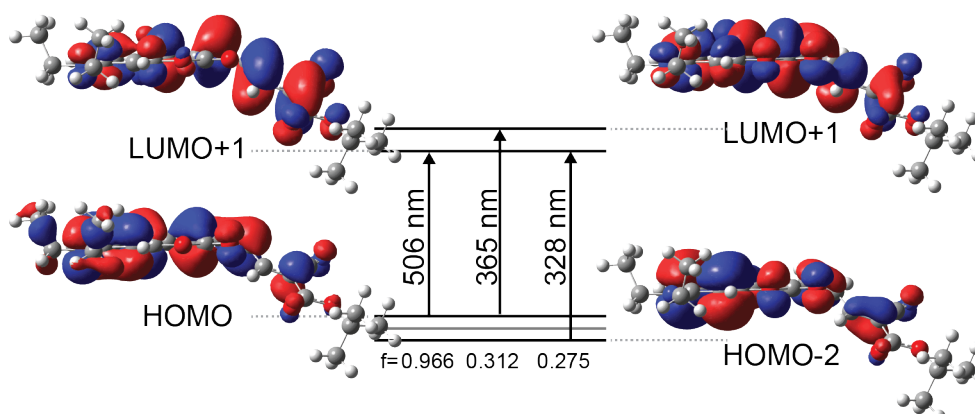


Figure 7.4: DFT calculations for the ground-state geometry and MOs involved in photoexcitation of *cis*-ceCAM

The electronic transitions for the ground-state of *cis*-ceCAM are shown in [Figure 7.4](#) which comprises the involved molecular orbitals. In this representation, the slightly distorted structure can be observed. The DFT-calculations could show that at least three bright states can be found. The most probable transition to the excited state  $S_1$  was found with an oscillator strength of 0.966 at a wavelength of 506 nm (2.447 eV), corresponding to a HOMO→LUMO transition with a  $\pi$ - $\pi^*$  character. In the LUMO, the electron density is slightly shifted towards the exocyclic part of ceCAM.

Two other likely transitions are found at 365 nm (3.394 eV) and 328 nm (3.775 eV), with an oscillator strength of 0.312 and 0.275 and correspond to HOMO→LUMO+1 and HOMO-2→LUMO, respectively, both of which have a  $\pi$ - $\pi^*$  character. Unfortunately, a clear assignment regarding the shift of electron density is not possible

and requires further studies. However, the found spectral shape of the calculated spectrum matches that of the experimental spectrum and the associated absorbance maxima are only slightly shifted. Although the experimental findings could be verified by DFT-calculations, it is yet unclear, whether excitation of both bands of *cis*-ceCAM would lead to an isomerization of the photoswitch in either case. This will be investigated in the following. However, the absorbance bands of *cis*-ceCAM exhibit a large overlap, which makes the excitation into isolated bands (or transitions) quite challenging.

### 7.1.2 ACTINIC EFFECT OF THE SPECTROMETER

During the preliminary measurements on the ceCAM photoswitch, an interesting feature was identified, namely the actinic effect of the used spectrophotometers. In general, actinism describes the property, that radiation causes a photochemical reaction of a molecule.[235] Although this is required for the photoswitch ceCAM to function, even the weak probing light of the UV/vis spectrophotometer (described in Section 4.1.3) already initiates the isomerization reaction of ceCAM. This effect was mainly dependent on the chosen integration time within the program, but interestingly also on the time window between each measurement.

Starting from the photostationary state (pss) of either isomer, an absorbance spectrum is recorded every 10 s over the course of 12 min. The resulting absorbance spectra are shown in Figure 7.5 (top, left). It is evident to see that the absorbance spectra change and approach the one of the respective other isomer. E.g. the spectrum, which is dominated by the *trans*-isomer starts to decrease in intensity and shift to lower wavelengths, while the opposite is observed for the other isomer. This clearly indicates that the light of the spectrophotometer triggers the photochemical reaction of ceCAM. The same procedure is repeated with the same sample, but a spectrum is recorded every 180 s instead. The resulting absorbance spectrum is shown in Figure 7.5 (bottom, left) and shows barely any sign of photoinduced isomerization. This set of experiments is repeated with different time windows but with the same overall time frame and the transient change of the difference absorbance is plotted in Figure 7.5 (right). The absorbance change at 489 nm is monitored, whereas the top and bottom half show the transient change starting from *cis* (pss<sub>385</sub>) and *trans* (pss<sub>530</sub>), respectively. As expected, a lower time window causes a bigger effect on the investigated reaction and this needs to be kept in mind for future steady-state investigations using this spectrophotometer. On the contrary, there is no optimal setting in which the reaction is not triggered at all, although at time windows of 120 s or higher, the observed changes between the varied time windows are negligibly small. Therefore, any of the following steady-state experiments are carried out with this specific experimental setting and/or the resulting measurements are additionally corrected by the actinic effect of the spectrophotometer.

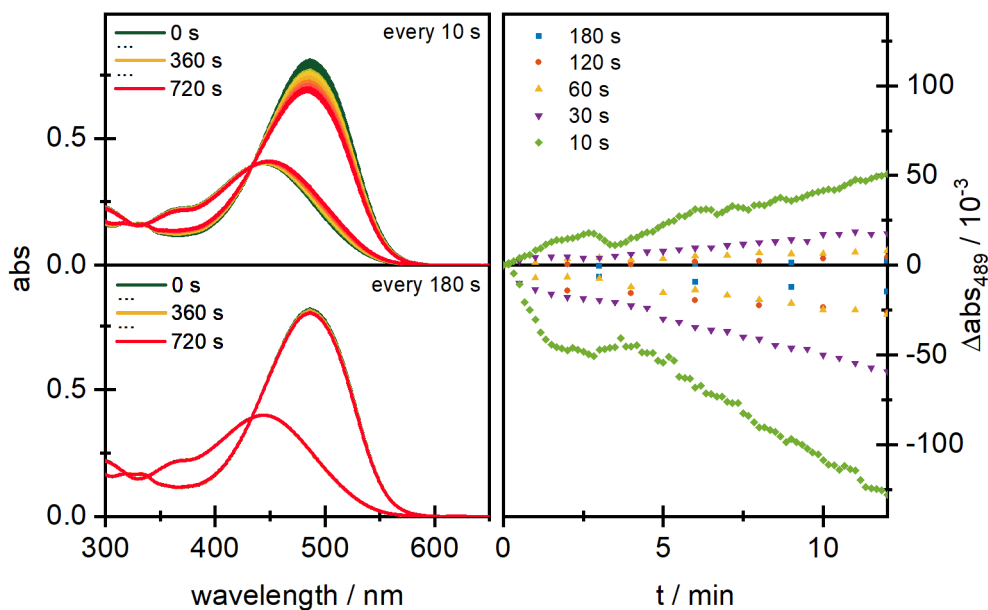


Figure 7.5: Actinic effect of the spectrophotometer on ceCAM isomerization. Left: Absorbance spectra for the  $pss_{385}$  and  $pss_{530}$  are recorded every 10 s (top layer) and 180 s (bottom) and indicate that the lamp of the spectrophotometer induces the isomerization reaction. Right: The transient course of the difference absorbance at 489 nm for the different time windows are shown. Frequent recording of the absorbance spectrum leads to a faster photoswitching. At a time window below 120 s, the switching is kept to a minimum.

## 7.2 DETERMINATION OF THE PHOTOPHYSICAL PARAMETERS

This section summarizes the results for the steady-state characterization of ceCAM. First, the  $pss$  upon LED-illumination at different wavelengths are characterized. The photoconversion efficiencies at the  $pss$  are determined and compared with each other. Then, the thermal back-reaction of either isomer is investigated, followed by a study on the photodegradation, for which fatigue-resistance measurements were carried out. The steady-state characterization is concluded with the determination of both the reaction and fluorescence quantum yield.

### 7.2.1 PHOTOCONVERSION EFFICIENCY

*Correlation between  
 $pss$  and  $rQY$*

When discussing the efficiency of a photoswitch, one typically consults the  $rQY$  of a reaction, which will be determined for ceCAM in a later section. On the other hand, the photostationary state is normally not considered, although both terms (or values) in a way describe how “good” the isomerization takes place. Although there is a correlation between the  $rQY$  and the  $pss$ , it is necessary to cleanly separate the two parameters. Therefore, the reaction quantum yield

can be ascribed to the microscopic and the pss to a macroscopic quantity. Upon irradiation of the sample, e.g. with one photon, the rQY gives the probability for the isomerization to take place. Increasing either the illumination power or the duration will not affect this probability, as shown from the equation for the rQY (Eq. (7.9), derived in detail at a later point). From a macroscopic point of view, the pss represents the overall amount of molecules in a specific state. Here, a continuous illumination will (with some restrictions) lead to a higher amount of the desired isomer. As such, this might lead to confusions regarding the efficiency of a photoswitch. Ideally, both the rQY and the pss for either reaction direction are high enough to ultimately declare the photoswitch to be efficient.

Photoswitching is mainly initiated with different LEDs comprised of the following central wavelengths: 385 nm to initiate *cis/trans*-isomerization and 530 nm for the reversed *trans/cis*-isomerization, represented by vertical bars in Figure 7.6. Typically, photochemical reactions are induced by illumination at the absorbance maximum. This was deliberately avoided in this work, because the absorbance bands of the different isomers overlap with each other. Instead, such LEDs were chosen, in which the other isomer hardly absorbs at the aforementioned wavelengths. As a presumed drawback, the isomerization reaction might be less effective, but because the compounds generally exhibit high molar extinction coefficients and therefore absorb light efficiently, this decision is justifiable. For example, illumination at 530 nm to induce the *trans/cis*-isomerization is reasonable, because the absorbance of the opposed *cis*-isomer at that wavelength drops to ca. 3% compared to its maximum value. On the other hand, the molar extinction coefficient of *trans* at that wavelength is still large enough with  $\epsilon_{530} = 25,400 \text{ M}^{-1} \text{ cm}^{-1}$ .

Moreover, ceCAM is also illuminated by LEDs with a central wavelength of 405 nm and 470 nm. On the one hand, illumination at 405 nm possibly addresses the alternative HOMO $\rightarrow$ LUMO+1 transition of the *cis*-isomer (see Section 7.1.1) and on the other hand, the *trans*-isomer exhibits relatively weak absorbance at that wavelength. Moreover, these wavelengths have been chosen as many confocal microscopes are operated at these wavelengths, among others. As the biological application is one future aspect for this photoswitch, photophysical characterization at these wavelengths regarding the effectiveness of the switching process are to be determined as well. The vertical bars representing these two wavelengths are also depicted in Figure 7.6, and already suggest that a slightly less effective photoreaction might occur. Additionally, photoexcitation at 385 nm and 405 nm for the *cis/trans*-isomerization might address the two types of transitions, as suggested from the DFT-calculations.

The samples are illuminated until the photochemical equilibrium is reached (pss). The corresponding final spectra, which are reached with the aforementioned LEDs are shown in Figure 7.6. When comparing these experimental spectra to the ones of the pure compounds in Figure 7.2, it is obvious that the

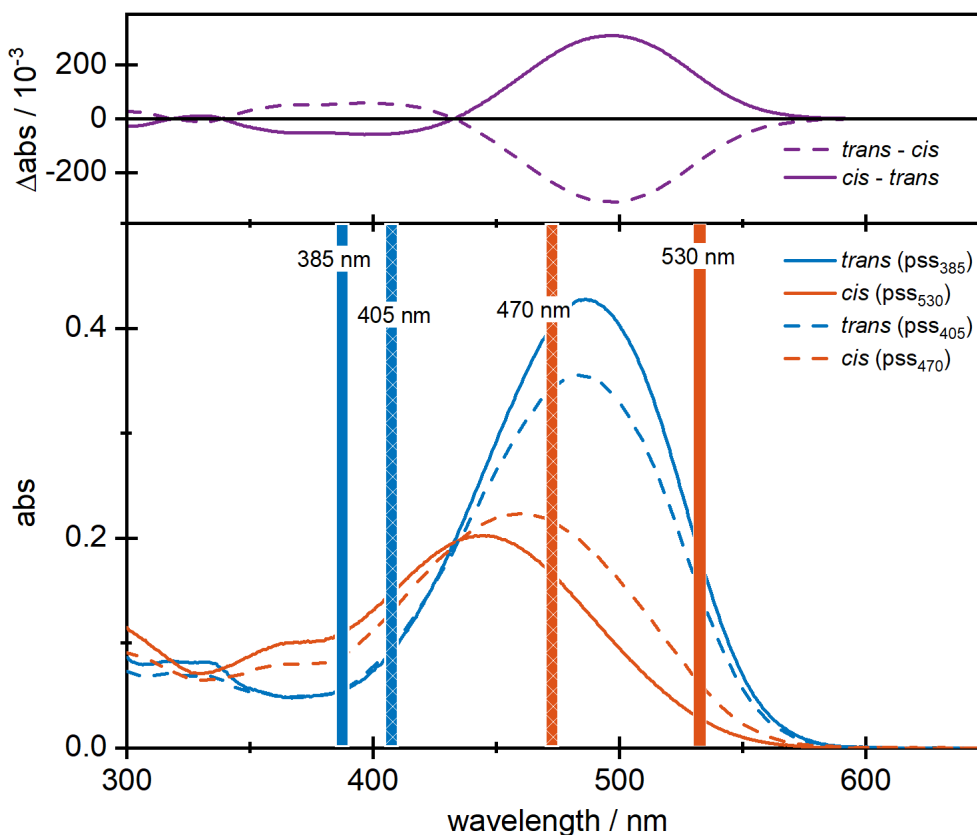


Figure 7.6: UV/vis absorbance spectra of the pss of ceCAM. Bottom: pss for the *cis/trans*-illumination are shown in blue (straight: pss<sub>385</sub>, dashed: pss<sub>405</sub>) and pss for the reversed *trans/cis*-isomerization are shown in red (straight: pss<sub>530</sub>, dashed: pss<sub>470</sub>). The corresponding illumination wavelengths are depicted with vertical lines. Top: Difference spectrum of *cis/trans* and *vice versa*. The difference spectra do not change, when other pss are used.

LEDs cannot fully convert the solution to either isomeric state. Moreover, as already assumed, the conversion efficiencies obtained from the 405 nm- and 470 nm-LEDs are not as large as those from the 385 nm- and 530 nm-LEDs, respectively.

For any experimentally obtained spectrum of the pss, the composition of the isomers within the solution is a result of the combination of the pure *trans*- and *cis*-spectrum and can be calculated as such, as shown in Eq. (7.1). The pure spectra is scaled with a factor  $c$ , which corresponds to the concentration of the sample and can be easily done via the isosbestic point of the sample.

$$A_{exp}(\lambda) = x \cdot (A_{trans}(\lambda) \cdot c) + (1 - x) \cdot (A_{cis}(\lambda) \cdot c) \quad (7.1)$$

This rather simple equation only requires the absorbance spectra  $A_{trans}$  and  $A_{cis}$  of the pure isomers and the experimental spectrum  $A_{exp}$  to determine the amount of the isomers, but assumes that the recorded spectrum consists of only the two isomers. A perfect photoconversion would be reached, if the parameter



$x$  reaches values of 0% and 100%. Photoswitches, for which the isomers have a spectral overlap, can hardly reach this. So if these kinds of photoswitches are to be used for a biological application, in which either isomer initiates the biological activity, they are inferior to photocages, as the latter exhibit a clean ON/OFF-property. To quantitatively characterize this photoconversion, the percentage  $x$  is calculated via Eq. (7.2) from the experimental spectrum.

$$x = \frac{A_{exp}(\lambda) - A_{trans}(\lambda)}{A_{cis}(\lambda) - A_{exp}(\lambda)} \quad (7.2)$$

The isomeric composition within the solution at the pss is summarized in Table 7.1 and compared to those after illumination with a cw-laser ( $\lambda_{laser} = 405 \text{ nm}$  &  $533 \text{ nm}$ , determined by Dr. M. Richers, Ellis-Davies lab). As expected, illumination at  $385 \text{ nm}$  results in a higher conversion than the illumination at  $405 \text{ nm}$ . The overall difference between the conversion efficiencies of *trans*-isomer is relatively high (80% to 62%) but reasonable: The contribution of *trans* at  $405 \text{ nm}$  is larger and therefore results in a photoinduced back-reaction. Analogously for the *trans/cis*-isomerization, the illumination at  $530 \text{ nm}$  yields a higher efficiency than that at  $470 \text{ nm}$  (90% vs. 76%). Generally, the photoconversion efficiencies for all wavelengths are quite high, considering the fact that there are no isolated absorbance bands for either isomer.

Table 7.1: Photoconversion efficiency for the isomerization of ceCAM after LED- and laser illumination at different wavelengths. *cis/trans*-isomerization is triggered by illumination at  $385 \text{ nm}$ ,  $405 \text{ nm}$  (both LED) and  $405 \text{ nm}$  (laser), whereas the reversed reaction is initiated by photoexcitation at  $470 \text{ nm}$ ,  $530 \text{ nm}$  (both LED) and  $533 \text{ nm}$  (laser).

	$\lambda_{LED} / \text{nm}$				$\lambda_{laser}$	
	<i>cis</i>	<i>trans</i>	<i>cis</i>	<i>trans</i>	<i>cis</i>	<i>trans</i>
	385	405	470	530	405	533
[%] of <i>trans/cis</i>	80/20	62/38	24/76	10/90	71/29	4/96

As mentioned earlier, the photoconversion efficiency is dependent on the choice of illumination wavelength. Moreover, it can also be influenced by the type of light source, or rather the FWHM thereof. High-power cw-lasers have a narrower bandwidth than LEDs, which is why the photoconversion efficiency at the pss is improved even further. Although the direct comparison of the pss at  $405 \text{ nm}$  show that the amount of *trans* can be significantly increased, full conversion is still far from being reached for the *cis/trans*-isomerization. On the other hand, the *cis*-isomer can be efficiently acquired with a  $533 \text{ nm}$ -laser (96% *cis*).

Generally, photoconversion at wavelengths, which are readily accessible in labs with confocal microscopes, such as  $405 \text{ nm}$  and  $470 \text{ nm}$  can be sufficient enough. However, this heavily depends on the further applications and the investigated reaction. In conclusion, the conversion efficiencies of ceCAM are very high, making it an attractive alternative to other commonly investigated photoswitches.

## 7.2.2 THERMAL STABILITY

Depending on the application, thermal bistability is a desirable aspect, which photoswitches should exhibit.[236] This feature describes the fact that both isomeric states are thermally stable and do not react to the energetically preferred isomer or only very slowly. In a reaction coordinate diagram, the two compounds are separated by a barrier which could be crossed by depositing the so-called activation energy into the system. The alternative pathway to reach the other ground-state isomer is via photoexcitation which is thoroughly described in the other sections.

For the investigations of the thermal stability of ceCAM, two different solutions were prepared, in which the *trans*- (pss<sub>385</sub>) and *cis*-isomer (pss<sub>530</sub>) were enriched. Then, the solutions were kept in dark and an absorbance spectrum was recorded every 6 h (in case of *trans*: every 24 h) over the course of ca. 6 days (*trans*: 9 days) at room temperature, to monitor any absorbance changes. The result is shown Figure 7.7. Additionally, the absorbance at the maximum (486 nm, in black squares) and the isosbestic point (432 nm, in red dots) are taken and plotted over time to facilitate the detection of any thermal reaction. The absorbance at the isosbestic in all measurements only changes within the sensitivity of the spectrometer and proves that the sample is still intact and does not e.g. decompose.

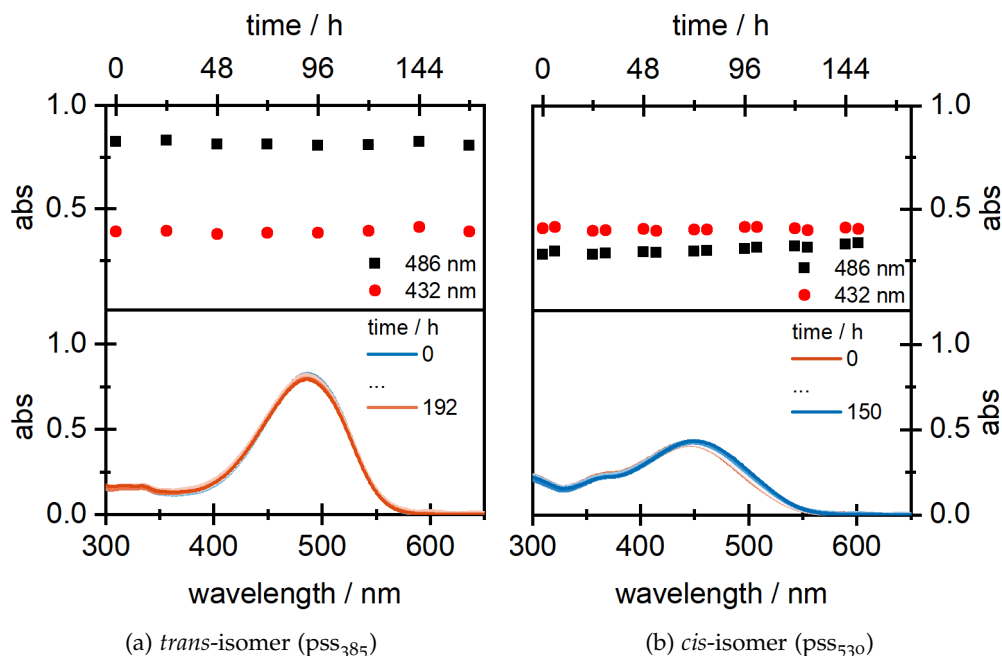


Figure 7.7: Thermal stability of ceCAM. Solutions containing accumulated *trans*- (pss<sub>385</sub>; (a)) and *cis*-isomer (pss<sub>530</sub>; (b)) are investigated. The top layer depicts the transient change at the absorbance maximum (486 nm, black squares) and isosbestic point (432 nm, red dots).

Although the *trans*-isomer (Figure 7.7a) is investigated over a longer time period, the absolute change of the optical density is very small and hardly visible from the absorbance spectrum ( $\Delta Abs_{486} < 0.03$  OD). The isomeric ratio is calculated with Eq. (7.2) and it is found that only ca. 3% of the *trans*-isomer is actually thermally converted to its corresponding *cis*-isomer over the course of 9 days. When starting with the *cis*-isomer (pss<sub>530</sub>), the overall absorbance change is also very small, but larger than for the previously described *trans*-isomer ( $\Delta Abs_{486} < 0.05$  OD), which can be explained by the fact that *trans* absorbs light more efficiently (Figure 7.7b). The changes from the thermal conversion of *cis*-ceCAM are determined to be ca. 5% (in 6 days).

Ideally, the available data can be used to determine the thermal isomerization half-life. This was not done for this data, as the absolute changes are too small to be actually considered for a determination. Richers *et al.* were able to determine this half-life time by utilizing high-performance liquid chromatography (HPLC) to monitor the *cis*-conformer. They assessed that over the course of one week, less than 3% (in this work: 5%) convert to the *trans*-isomer, which is equivalent to a half-life time of 175 days.[160] This means that the thermal back-reaction of ceCAM is negligible for either isomerization direction and both reaction directions can be initiated with light. At this point ceCAM can already be described as a so-called bistable photoswitch.

Further characterization on ceCAM regarding its thermodynamical behavior could include temperature-dependent investigations and measurements in different solvents. Following ARRHENIUS' equation and plotting  $\ln k$  (calculated via the half-life time) *vs.* the inverse temperature, the activation energy can be derived from the slope of the linear fit.[237] However, at room temperature the reaction rates are too slow to be determined with high certainty. This could drastically change at higher temperatures. The temperature can be increased up to 82 °C, which would be the boiling point of MeCN. However, many other aspects must be examined in advance, as at such high temperatures, the compound could decompose and/or other effects could be observed, which then complicate the measurement again. In a first attempt, the experiment was redone at 75 °C (not shown here), but failed, as the monitored absorbance at the isosbestic point decreased over time, indicating a degradation of ceCAM. Even so, the absolute change was still too small to be reliably determined. This leads to the conclusion that the activation barrier of ceCAM is too high to be experimentally determined.

### 7.2.3 FATIGUE-RESISTANCE

Apart from the thermal stability, ideal photoswitches should be photostable as well and exhibit resistance to photodegradation. Typically this is examined in an experiment, where many cycles of photoinduced switching are performed repeatedly. The absorbance spectrum is monitored over the course of the experiment to detect any signs of fatigue. For this, ceCAM in MeCN is illuminated with

the LEDs mentioned above. By alternate switching with the 385 and 530 nm-LED, the fatigue-resistance can be verified. The investigated sample is illuminated until the corresponding *pss* of either isomer is reached. An absorbance spectrum is recorded and the percentage of the *trans*-isomer in the solution is calculated from that. In total, more than 265 switching cycles have been performed, which took ca. 44 h. To keep the overall experimental duration as short as possible and to avoid and minimize external instrumental influence, the illumination power of both LEDs was set to high values. The result of the experiment is shown in Figure 7.8. For reasons of a better overview, some time frames are omitted. The

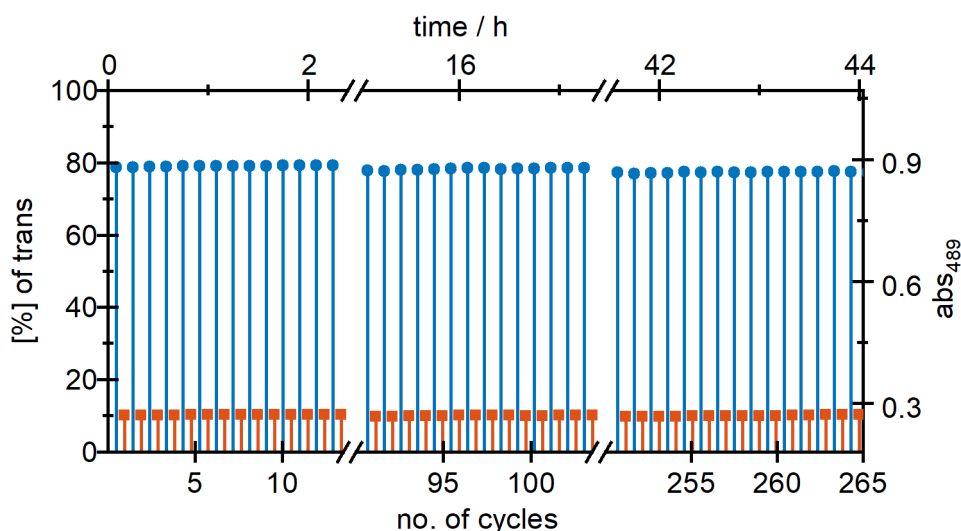


Figure 7.8: Fatigue resistance of ceCAM after alternate photoswitching at 385 and 530 nm. More than 265 switching cycles are performed, leading to almost no detectable photodegradation of ceCAM, as the amount of *trans* in the solution bare decreases.

red dots represent switching the *pss*<sub>530</sub>, in which *cis*-isomer is accumulated in the solution, whereas the blue squares depict the *pss*<sub>385</sub>, which corresponds to the *trans*-isomer. Within the first shown time frame, 14 switching cycles are performed and no significant photodegradation is found. The representative dots for the *trans* (*pss*<sub>385</sub>) appear a little bit more “shaky”, which is explained by the fact that a non-referencing spectrophotometer was used in this experiment. So if there are any fluctuations e.g. regarding the lamp or the background throughout the measurement, they could not have been considered in the measurement. The same observation can be found in the other time frames, whereas the skip between the second and third is considerably larger. Nevertheless, significant photodecomposition cannot be found after 265 cycles of photoinduced switching. This shows that ceCAM exhibits excellent fatigue resistance.

The fatigue-resistance after illumination at 405 and 470 nm was measured as well and gave the same results (not shown here). As the deposited energy for the *cis/trans*-isomerization is lower, compared to photoexcitation at 385 nm, any

in-cell application with high amounts of switching cycles would not only keep the photoswitch but also the cells intact. The number of switching cycles were lowered in this experiment (25), however, the results are the same as no obvious photodegradation is detected. Expectedly, ceCAM is resistant to photodamage at these wavelengths as well, but the outcome of this experiments enables a wider variety of possibilities. The advantage of this set of wavelengths is mainly focused on the illumination wavelength for the *cis/trans*-isomerization.

#### 7.2.4 DETERMINATION OF THE REACTION QUANTUM YIELDS OF CECAM

This section summarizes the extensive investigations on the reaction quantum yield (rQY) of ceCAM for both isomerization directions. In general, the reaction quantum yield is defined as the number of reactions  $n_{react}$  per absorbed photons  $n_{abs}$ , as shown in Eq. (7.3).[54]

$$\phi_r = \frac{n_{react}}{n_{abs}} \quad (7.3)$$

There are different approaches to determine both numbers, which highly depend on the observed chemical reaction. Moreover, additional correction factors might be necessary to include, to accurately determine the rQY. With the methods of optical spectroscopy, typically only low absorption regimes are covered, where the fraction of photons actually absorbed by the available isomers need to be determined first.[238] The derivation for the rQY in this regime is summarized hereafter: The number of reacting molecules is calculated via the sample volume (V), concentration (c) and the AVOGADRO constant ( $N_A$ ), which are then combined with the BEER-LAMBERT-law (Eq. (2.6)), containing the aforementioned parameters  $\Delta A(\lambda_{probe})$  (change of absorbance),  $\epsilon_{prod}(\lambda_{probe})$  (molar extinction coefficient of the product) and d (path length of the cuvette).[22, 133, 172] As a result of the isomerization, the absorbance spectrum will change, which is why it is considered in the equation as well. This results in Eq. (7.4).

*Derivation of the rQY*

$$n_{react} = c \cdot V \cdot N_A = \frac{\Delta A_{prod}(\lambda_{probe}) \cdot V \cdot N_A}{\epsilon_{prod}(\lambda_{probe}) \cdot d} \quad (7.4)$$

For the number of absorbed photons, it is necessary to determine the number of photons first, which are emitted from the light source over a certain amount of time  $t$ . This can be calculated via the illumination power  $P_0$  and wavelength  $\lambda_{exc}$ , as done in Eq. (7.5). The energy of a single photon can be calculated via the PLANCK constant ( $h$ ), the speed of light ( $c$ ) and its wavelength ( $\lambda_{exc}$ ). The

reaction quantum yield is then calculated via Eq. (7.6).

$$n_{abs} = \frac{P_0}{h \cdot \frac{c}{\lambda_{exc}}} \cdot t \quad (7.5)$$

$$\phi_r = \frac{\Delta A_{prod}(\lambda_{exc}) V \cdot N_A}{\epsilon_{prod} \cdot d} \cdot \frac{h \cdot c}{P_0 \cdot t \cdot \lambda_{exc}} \quad (7.6)$$

For the experimental determination of the reaction quantum yield with this equation, the sample is illuminated and consecutive absorbance spectra are recorded. For a monitored wavelength, the absorbance is plotted against the illumination duration.

However, several prerequisites on the sample must be given, which makes the method error-prone: The molar extinction coefficient must be determined with high accuracy and isolated absorbance bands are necessary, to reliably determine the change of absorbance ( $\Delta A$ ). In case of overlapping absorbance, both isomers will contribute to the monitored value after a short duration of illumination. This aspect will affect the difference of absorbance, which is considered in the number of absorbed molecules. Moreover, if the isomerization product absorbs at the excitation wavelength as well, this photoinduced back-reaction will affect the rQY as well.

In a variation of this approach, only the first data points are considered, which are supposed to behave linearly. This is due to the fact that within the first time frames only the isomer of interest absorbs the photons, because the overall number of product molecules is too small to significantly contribute to the absorbance. Therefore, the problems which were previously addressed can be minimized to some extent. In case of the isomerization of the ceCAM, this linear approach is used to determine its reaction quantum yield.

The resulting equations change only slightly. The illumination time  $t$  and the change of absorbance  $\Delta A_{prod}(t)$  will result in the factor  $m$ , which corresponds the slope of the linear fit (Eq. (7.7)). Moreover, a correction factor is introduced to the illumination power, to consider the absorbed fraction of the illumination. This is realized by factoring in the transmittance of the sample ( $1 - 10^{-A_0(\lambda_{exc})}$ ).

$$m = \frac{\Delta A_{prod}(\lambda_{exc})}{t} \quad (7.7)$$

If the solution contains not a pure isomer but an isomeric mixture at the beginning of the experiment, then the incoming light at the illumination wavelength will be absorbed by both reactants. Therefore, the actual  $A_0$  is smaller and the resulting rQY will always be underestimated. To take this into account, a correction factor is added to the final equation which utilizes the deconvolution of the spectra. If the isomeric ratio is known, then the initial absorbance is an additive composition of the initial absorbance of either isomer. This enables the calculation of the absorbance ratio  $x$ , which is shown in Eq. (7.8) and used for the correction of the rQY, with  $A_0 = A_{0,reactant} + A_{0,product}$ . [239]

$$x = \frac{A_{0,reactant}(\lambda_{exc})}{A_{0,reactant}(\lambda_{exc}) + A_{0,product}(\lambda_{exc})} \quad (7.8)$$

Analogously for the linear approach in general, this correction factor requires that only small amounts of the isomerization product are present in solution. Otherwise, at high amounts of that isomer will compete for the absorption of photons and the rQY for the actual reaction will be underestimated. Insertion of the slope  $m$  and the correction factor  $x$  gives the final equation, which is ultimately applied in this work:

$$\phi_r = m \cdot \frac{V \cdot N_A}{\epsilon_{prod}(\lambda_{probe}) \cdot d} \cdot \frac{h \cdot c}{P_0 \cdot \lambda_{exc} \cdot (1 - 10^{-A_0(\lambda_{exc})})} \cdot x \quad (7.9)$$

For the actual experimental determination of the rQY, the sample was illuminated as described in Section 4.3. The absorbance at  $\lambda_{probe} = 550 \text{ nm}$  was monitored, because at this wavelength the contribution of *cis* is very small and the detected absorbance change will predominantly come from the *trans*-isomer. A very low illumination power of the LED was applied to the sample, in order to achieve as many linear data points as possible and facilitate the following linear fit. The measurement for determining the rQY of the *cis/trans*-isomerization after illumination at 405 nm is shown in Figure 7.9, with an inset showing the transient change at 550 nm. The inset shows very nicely that at first a linear increase is observed, followed by an exponential behaviour leading to a nearly asymptotic value, which corresponds to the photostationary state (see Section 7.2.1).

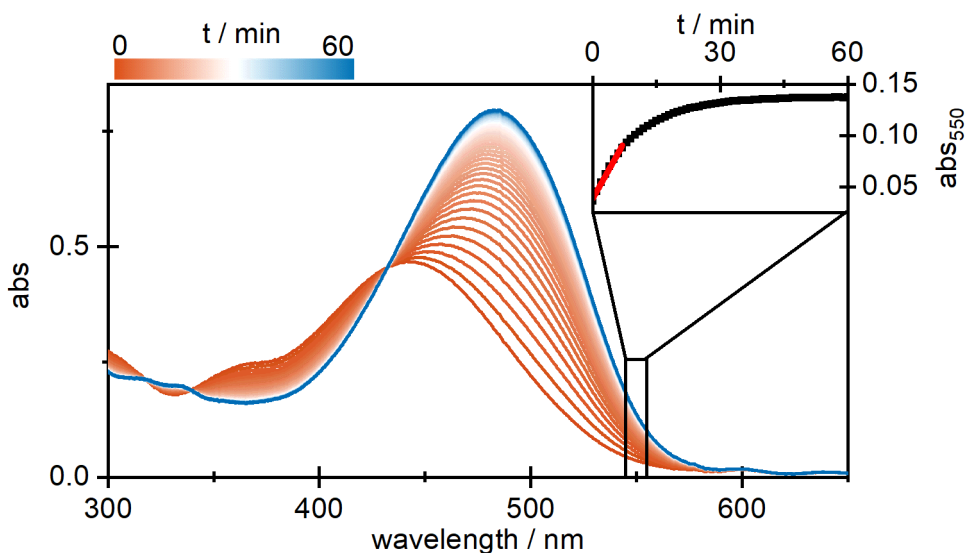


Figure 7.9: UV/vis spectra for the determination of the reaction quantum yield of the *cis/trans*-isomerization of ceCAM (red to blue) in MeCN after LED-illumination at 405 nm. The spectra are recorded over a time of 60 min. The inset shows the absorbance change at 550 nm (black squares) and the linear fit of the first eight points, resulting in a slope of  $m = 1.23 \cdot 10^{-4} \frac{OD}{s}$ .

The rQY at 405 nm is then calculated from the following values, which are taken from that measurement: slope of the linear fit  $m = 1.24 \cdot 10^{-4} \frac{OD}{s}$ , sample volume  $V = 2 \text{ mL}$ , molar extinction coefficient  $\epsilon_{550} = 8,775 \text{ M}^{-1} \text{ cm}^{-1}$ , path length  $d = 1 \text{ cm}$ , PLANCK constant  $h = 6.626 \cdot 10^{-34} \text{ J} \cdot \text{s}$ , speed of light  $c = 3 \cdot 10^8 \text{ ms}^{-1}$ , illumination power  $P_0 = 0.037 \text{ mW}$ , illumination wavelength  $\lambda_{exc} = 405 \text{ nm}$ , initial absorbance  $A_0(405) = 0.345 \text{ OD}$  and initial absorbance of the *cis*-isomer  $A_{cis,0}(405) = 0.307 \text{ OD}$ . This results in a  $\phi_r(405)$  of 43%.

The experiment was redone for the *trans/cis*-isomerization and the previously described alternative sets of wavelength. The evaluation of the data is performed in analogy to the reversed isomerization, including the monitored wavelength of 550 nm. As there is neither an isolated absorbance band for the *cis*-isomer, nor a wavelength at which the *cis/trans*-ratio of the molar extinction coefficient is large enough, the wavelength is kept unchanged. For that reason, the assumption is made that the negative slope caused by the decrease of *trans*-isomers correlates to the direct formation of *cis*-ceCAM.

Additional reaction quantum yields were determined, in which optical filters were used to narrow down the bandwidth of the LED. The emission and absorption spectra of the LEDs and selected filters, respectively are shown in Figure 7.10. The broad emission spectra of the LED indicate, that the determined rQY might be distorted. As the utilized LEDs are not perfectly monochromatic, the additional usage of filters will lead to a more precise value of the rQY.

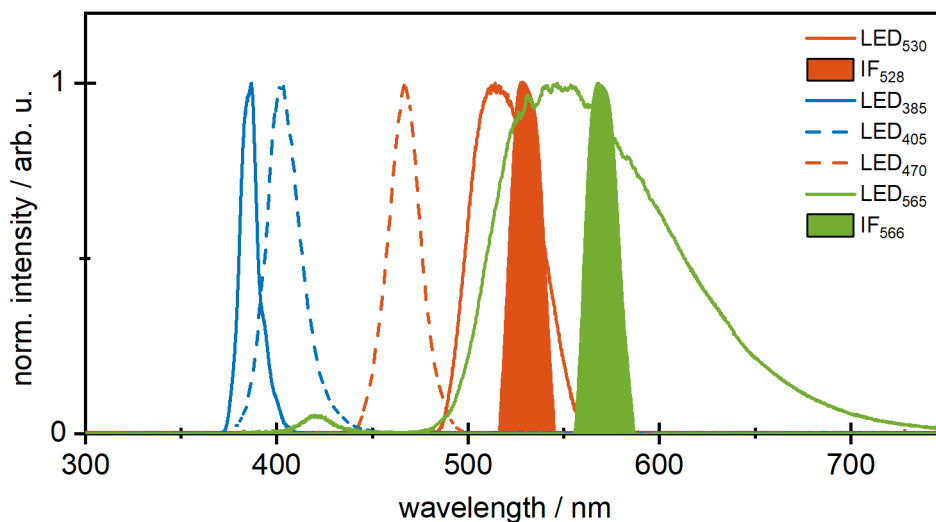


Figure 7.10: Normalized emission and absorbance spectra of selected LEDs and optical filters, respectively, which were used for the determination of the rQY of ceCAM. As the LEDs partly have a big FWHM, optical filters were placed in front of the LED to narrow down the emission spectra and obtain a more precise rQY.



Moreover, the rQY for the *trans/cis*-isomerization are compared with the results from the Ellis-Davies lab. There, pure *trans*-ceCAM was irradiated with a monochromatic light source, 533 nm-laser and the reaction monitored via HPLC-measurement. The isomerization quantum yields were determined using photon counting methods.[160, 238, 240] The values and reaction quantum yields are summarized in Table 7.2. It should be noted that the rQYs in both cases are calculated from a multitude of linear fits, for which a different amount of data points is considered. This was done to reliably determine the rQY, while considering that the other isomer could have competitively absorbed the incoming photons. Therefore, the correction factor  $x$  was always newly calculated depending on the number of considered linear data points. In Table 7.2, the average values and standard deviation of the rQYs are given.

Table 7.2: Reaction quantum yields for isomerization of ceCAM at different excitation wavelengths and with various optical filters.

	LED / nm	$P_0 / \mu W$	$\phi_r / \%$
<i>cis/trans</i>	385	16.5	$42.1 \pm 1.0$
with BG3-filter		7.52	$41 \pm 5$
<i>cis/trans</i>	405	72.4	$45 \pm 4$
with IF404-filter		47.8	$48 \pm 3$
with OG400-filter		37.3	$45 \pm 3$
<i>trans/cis</i>	530	15.9	$34.1 \pm 0.6$
with OG530-filter		10.9	$23.5 \pm 0.3$
with IF528-filter		16.5	$23.9 \pm 0.6$
<i>trans/cis</i> with IF566-filter	565	25.0	$67 \pm 3$
<i>trans/cis</i> <sup>1</sup>	533	$2 \cdot 10^5$	50

For the *cis/trans*-isomerization, rQYs are found to be in the range from 0.41 to 0.48. For the reverse isomerization direction, the rQY ranges from 0.23 to 0.67, which is a huge span for a single possible reaction. Possible sources of errors are the experimentally determined values in Eq. (7.9). The errors for the sample volume ( $V$ ), initial absorbance ( $A_0$ ), molar extinction coefficient ( $\epsilon_{prod}$ ) and path length ( $d$ ) are estimated to be ca. 1-10%, which would only affect the determined rQY by <4,5%. The effect of the number of data points considered for the linear fit is already considered and given in the overview table. Therefore, the error source with the most likely largest effect is the determination of the illumination power  $P_0$ . As mentioned previously, very low powers are applied to the sample which leads to a error-prone power measurement, as such low intensities are difficult to be reliably determined by the power meter. The error for  $P_0$  can be estimated with 10% as well, but unlike the other parameters, this causes a change of the rQY of up to ca. 20%, which is tremendously huge. If

<sup>1</sup> determined in Ellis-Davies lab with a 533 nm-laser: 10 W Verdi, Coherent, Palo Alto, CA, USA

this error is assumed for the determined rQYs, then the values for the *trans/cis*-isomerization determined in this work, match the one which were identified via monochromatic excitation and HPLC-analysis.

Ultimately, the spectral bandwidth of the LEDs are still too large and will definitely induce a back-reaction. Especially the photoinduced isomerization at 530 nm is problematic, as the overlapping absorbance bands of *cis*- and *trans*-ceCAM prevent an unambiguous determination of the rQY for this wavelength. However, indications for a wavelength-dependency are observed when comparing the *trans/cis*-isomerization at 530 nm and 565 nm, which contradicts KASHA-VASILOV's rule stating that any photoinduced reaction can only occur from the lowest excited state and is therefore independent of the excitation wavelength.[241] Generally, this is only applicable for photoluminescence (fluorescence and phosphorescence), but this rule has been extended to a broader range of photochemical reactions. Several exceptions have also been reported, which includes photoswitches as well.[52, 242–245] For the *cis/trans*-isomerization, the determined values of the rQY are very similar and the differences within the margin of error. Therefore, to either validate or disprove the indications for a non-KASHA behavior, an extensive and more sophisticated study is required. However, this is ultimately challenging, as the overlapping absorbance bands do not permit an unambiguous assignment.

Generally, the determination of the reaction quantum yield via the approach of the linear fit is still error-prone, especially when working with photoswitches which have isomers with overlapping absorbance bands. Influences on the rQY were carefully considered and even partially investigated. The determined values state that probability for a successful isomerization is high in both cases. Compared to other commonly investigated photoswitches, once again, the quantum yields of ceCAM are relatively large, which makes it a viable class of photoswitches for future applications.

## 7.2.5 FLUORESCENCE SPECTRA AND QUANTUM YIELDS OF CECAM

### 7.2.5.1 Stationary spectra

The following section investigates the fluorescence properties of the ceCAM-photoswitch. Coumarins are known in the literature to exhibit high fluorescence quantum yields and hence are used as fluorescent dyes.[122, 123] Meanwhile, coumarins are starting to get widely used for other photoactivatable applications, such as photocages or photoswitches like ceCAM. However, if a molecule is photoexcited and then undergoes deactivation e.g. either via a (non-)radiative process or a CI to another isomer, the various processes will affect each other and reduce the efficiency of a desired pathway. In case of ceCAM, this would be the isomerization reaction. Therefore, steady-state investigations on its fluorescence properties are carried out, on the one hand to examine whether the

coumarin-core still fluoresces and on the other hand, how efficient this process is. This is done by determination of the fluorescence quantum yield ( $fQY$ ) of both ceCAM-isomers, followed by the comparison to the respective reaction quantum yield ( $rQY$ ).

As for the spectrophotometer, an actinic effect has been observed for the fluorimeter as well. Unfortunately, the intensity of the excitation path of the fluorimeter cannot be adjusted. Though, a compartment exists within the device, which can be used to insert neutral-density (ND)-filters to attenuate the excitation beam and reduce the actinic effect of the fluorimeter. Absorbance spectra of the solution were recorded and compared before and after the acquisition of a fluorescence spectrum. Ultimately, a 1 OD-ND-filter was used, as the utilization of filters with this and higher optical densities largely prevented photoswitching. The steady-state fluorescence investigations were carried out on solutions containing a pss. To maintain this pss, the solution was illuminated from the top during the acquisition of the fluorescence spectrum. For the solution containing *cis* (pss<sub>530</sub>), this proved to be counterproductive, as the stray light of the external illumination covered the whole fluorescence spectrum. In case of *trans* (pss<sub>385</sub>), no improvements were detected compared to the method which utilizes ND-filter, which is why this approach was applied herein.

Generally, the detected fluorescence is very weak, as high PMT-voltages had to be applied to achieve a good SNR of the spectra. The resulting fluorescence spectra of the *cis*-(pss<sub>530</sub>) and *trans*-isomer (pss<sub>385</sub>) are shown in Figure 7.11 together with the pure absorbance spectra. For the fluorescence spectrum of *trans* (pss<sub>385</sub>) after photoexcitation at 385 nm, a single band is found at 610 nm, which does not exhibit any fine structures. As this fluorescence band is symmetrical to the absorbance band of *trans*, it is assigned to *trans*-isomer. Moreover, this means that there is no fluorescent contribution from *cis*-isomer, although this might have been overlapped by the fluorescence of *trans*. The investigated isomer has a relatively large STOKES-shift of  $\Delta_{\text{STOKES}} = 121\text{nm}$ .

For the fluorescence spectrum of *cis* (pss<sub>530</sub>) which was excited at 530 nm, two maxima are observed at 461 nm and 611 nm. The latter band directly corresponds to the fluorescence maximum of *trans*, which is most likely caused by a residual amount of that isomer in the solution, which is able to fluoresce after photoexcitation at 385 nm, due to excitation to a higher excited state. This observation is in accordance with KASHA's rule. To actually confirm this hypothesis, a fluorescence spectrum of pure *cis*-ceCAM must be recorded, which, however, is not obtainable. But as both the fluorescence maxima (nearly) match each other, this assumption is justified. The fluorescence spectrum does not exhibit any fine structure as well, but compared to the other isomer, the observed STOKES-shift of *cis* is relatively small ( $\Delta\lambda_{\text{STOKES}} = 24\text{nm}$ ). An explanation for the small red-shift could be a weak dipole moment of the fluorescing state.[163]

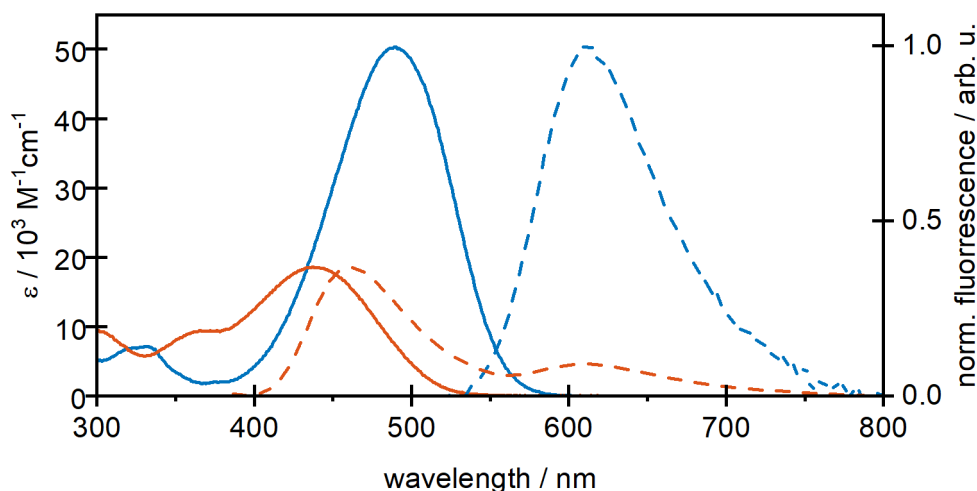


Figure 7.11: Steady-state absorbance and normalized fluorescence spectra of ceCAM. The normalized fluorescence spectra of *trans*-ceCAM exhibits only a single fluorescence band with its emission maximum located at 610 nm which a small reabsorption range. *cis*-ceCAM only has a single fluorescence band at  $\lambda_{em} = 461 \text{ nm}$ . The other, red-shifted band is results from residual *trans*-isomer in the solution.

The fQY of both ceCAM-isomers are determined with the comparative method (see Section 4.2.3), for which a dilution series was prepared according to Section 4.2.3. For the *trans*-isomer, the fQY after photoexcitation at 530 nm was determined, whereas for the opposed *cis*-isomer, two excitation wavelengths were used, to investigate a possible influence of the second, blue-shifted absorbance band. Therefore, the solution was excited at 362 nm and 385 nm. As a reference compound for the *cis*- and *trans*-isomer, coumarin 153 (C153) and rhodamin 6G (R6G) were used, respectively.[164, 246]. As the literature value was unknown for the fQY of C153 at the specific, aforementioned excitation wavelengths, an additional experiment was required to yield those fQY. This was realized, by exciting C153 at 362 nm (or 385 nm) and using its literature values at 400 nm (410 nm).[247]

#### 7.2.5.2 Determination of the fluorescence quantum yield with FluCY

For the determination of the fQY, the self-written program Fluorescence Correction & Quantum Yield (**FluCY**) was used, whose first part is described in Section 5.3. In the following section, the operation of the second part is described, with an emphasis on the graphical user interface (GUI). Most of the calculations which are performed in the background have already been described above.

The GUI of the second part of FluCY will open, after pressing the button **calc. quant. yield** (located on the bottom, center). An area on the right hand side of the GUI becomes visible, where a variety of settings can be made. The

corresponding window is shown in Figure 7.12. The individual steps for the calculation of the fQY are explained in the following. If a specific order must be kept, this will be pointed out in the appropriate part.

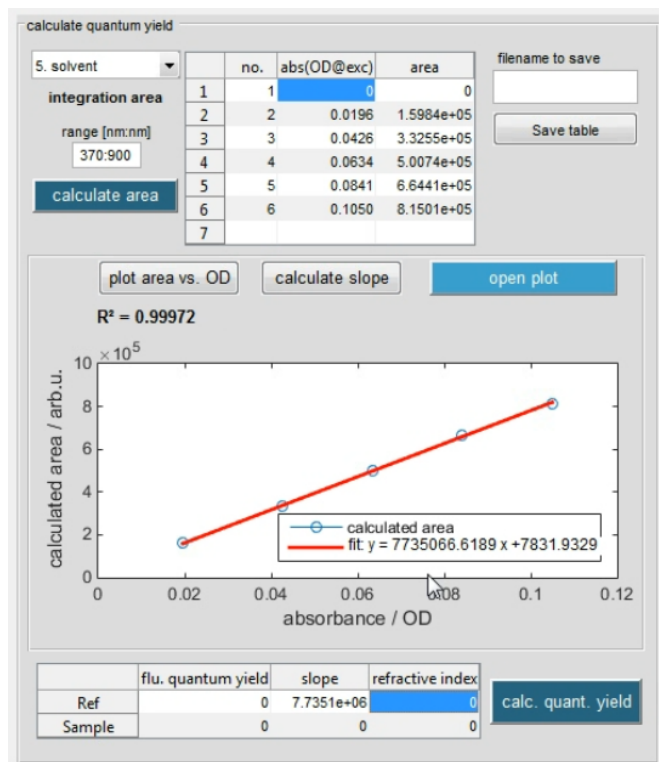


Figure 7.12: FluCY - GUI for the determination of the fQY.

(F<sub>1</sub>) **Calculate the integration area** The proper correction matrix is chosen from the drop-down menu. If the user executes the corrections in the suggested order, then the pre-selected choice 5. solvent is the proper matrix to continue the calculation for the fQY. The current version of FluCY does not allow the import of externally corrected matrices. Hereafter, the wavelength range is set, for which the integrated area will be calculated. The input field only allows the format known from the previous correction steps, which were described in Section 5.3 ( $\lambda_p : \lambda_q$ ). A click on the button **calculate area** will calculate the integration areas for the set wavelength range for all fluorescence spectra listed in the import window, and then insert the values into the table in the center. In this table, the first column simply states the number of order of the spectrum, whereas the second column represents the absorbance at the excitation wavelength. As already mentioned above, it is important that the listing order of the absorbance and fluorescence spectra match each other. This table can be saved in an ASCII-format as a .txt-file by entering a filename in the corresponding input field and clicking the button **Save table**.

(F<sub>2</sub>) **Calculate the slope** In the next step, the integrated area is plotted against the absorbance, for which the data will be retrieved from the table above. It is even possible to change or add values to this table, so that the following plot and subsequent fit can consider these changes or additions. The main reasoning to implement this feature was to allow the addition of a zero point, which might be desired by the user, as described in [Section 4.2.3](#). The current version of FluCY does not have the possibility to force the linear fit to have no y-intercept, so the editing of the table is an approach to suffice the requirement.

Pressing the button `plot area vs. OD` will plot the values in the table as dots, which will be shown in the window below. If the user updates the values in the table, the changes will not happen on-the-fly, but require a refresh of the plot, with an anew click on the button. The linear fit is executed by clicking on `calculate slope`.

The fit will be shown as a red line, with the two data points, which are the furthest away from each other, as its boundary. Another window will pop up in the window plot, which shows the calculated fit function in the format  $y = mx + b$ , with the values of the slope ( $m$ ) and the y-intercept ( $b$ ). As in case of the refresh function of the plot-button, updating the values in the table will require an anew click on the buttons for plotting and calculating the slope. Lastly, like in the previously described parts of FluCY, the button `open plot` allows for further inspection of the plot and the fit.

(F<sub>3</sub>) **Calculate the fluorescence quantum yield** A double-click on the fit window allows the user to copy the slope from the fit function and then paste it into the corresponding cell of the table below. This must be done manually, because in the current version of FluCY, the program cannot inherit the value from the fit into the correct cell in the table, as it is not defined, whether it just calculated the slope of the reference or the sample. Then, the measured refractive index of the solvent is entered manually into the table as well. Depending on whether the user just corrected the fluorescence spectra and calculated the slope for the sample or reference compound, the whole process can now be repeated for the other one. The resulting slope and the corresponding refractive index, which are needed for the calculation, are then entered into the table leaving only one cell empty. Clicking on the button `calc. quant. yield` will calculate the yield and the output will be shown in the table in the cell for the sample's fQY. If the values are not entered into the correct cells, then the program FluCY is not able to calculate the quantum yield.

This concludes the description of the self-written MATLAB-program FluCY.

### 7.2.5.3 Evaluation of the determined fluorescence quantum yield

The fluorescence spectra and the fQY were corrected and determined with FluCY, respectively and verified by doing the manual spectral corrections, the

calculation of the integrated area and fitting of slope via another program. Both values match each other, which proves that there are no obvious errors in the code of the program. The resulting quantum yields are listed in Table 7.3. As mentioned above, the fQY after photoexcitation at 362 nm and 385 nm were cross-referenced with two literature values (400 and 410 nm), which are both listed in the table to be able to compare the differentially obtained values.

Table 7.3: Fluorescence quantum yield of *cis*- and *trans*- ceCAM. The fQY were determined from the pss

	$\lambda_{exc}$	Ref( $\lambda_{exc}/nm$ )	$\phi_f / \%$
<i>cis</i> -ceCAM	362	C153(400)	(0.5 $\pm$ 0.4)
	362	C153(410)	(0.5 $\pm$ 0.4)
	385	C153(400)	(2.10 $\pm$ 0.13)
	385	C153(410)	(2.20 $\pm$ 0.13)
<i>trans</i> -ceCAM	530	R6G(530)	(17.6 $\pm$ 1.1)

At first, the unambiguously determined fQY of the *trans*-isomer is evaluated. When comparing this quantum yield to that of other fluorophores, such as C153, which also contain a coumarin core, then this value is relatively low. However, this emphasizes the fact that ceCAM has another very efficient deactivation channel from the excited state, which was already determined to be the reaction quantum yield (rQY). From a chemist's point of view, who wants to design an efficient photoswitch, this fQY is still too high, and should ideally be decreased or even become non-existent.

As two deactivation channels are addressed and both quantum yields identified, this allows the determination of the rate for the non-radiating decay. If the rate of the excited-state decay is known, then the non-radiating rate can be calculated via Eq. (4.1).

For the *trans*-isomer, the fQY was not investigated after photoexcitation at 470 nm. Due to the fact, that the determined rQY hinted of a violation of the KASHA-VASILOV's rule, three-dimensional fluorescence spectra were recorded (not shown in this work) to possibly get further insights onto a possible wavelength-dependency of the fluorescence spectrum. These 3D-spectra showed that by applying different excitation wavelengths, only a change of fluorescence intensity is observed, whereas the spectral shape and the location of the fluorescence are not affected. Therefore, the fQY at other wavelengths were not determined in this work.

In case of *cis*-ceCAM, the quality of the cross-referencing is examined first. The values found for the fQY of C153 after photoexcitation at 362 nm or 385 nm are the same, independent of the reference wavelength (400 nm or 410 nm). In either case of the excitation wavelength, the difference of the resulting fQY were below 5%, and when including the calculated error, they are even identical, which

proves the quality of the found results for the cross-referencing. The absolute values which were found for the fQY of the *cis*-isomer are very low, with the fQY at 362 nm being even below 1%. The fQY of *cis*-ceCAM after photoexcitation at 385 nm is slightly higher, but still very small, compared to coumarins in general or the opposed *trans*-isomer.

Depending on the application, fluorescence could be an unwanted photo-physical property, as it competes with the mainly desired switching efficiency. However, it is important to recognize and investigate the effect of this rivaling process. Although the findings of this section show that both ceCAM-isomers exhibit fluorescence, which was expected due to its coumarin-core, the fluorescence quantum yield of both isomers are very low to actually compete with the isomerization reaction. The *cis*-isomer exhibits very low fluorescence at the stronger absorbance band at 385 nm resulting in a yield of ca. 2.1%, whereas the lower absorbance band at 362 nm *de facto* does not fluoresce at all ( $\phi_f = 0.5\%$ ). On the contrary, the *trans*-isomer has a fluorescence quantum yield of 17.6%, which is too high to be neglected, but still lower than its reaction quantum yield. As the fluorescence is not expected to dramatically increase after excitation into different flanks of the absorbance bands, other excitation wavelengths (e.g. 405 nm, 470 nm, etc) should be addressed in future studies.

## 7.2.6 CHARACTERIZATION OF THE ULTRAFAST ISOMERIZATION REACTION DYNAMICS IN THE PS-NS RANGE

To get further insights into the excited-state dynamics and to understand the different deactivation processes which can occur, the last section will focus on the ultrafast photodynamics of both ceCAM-isomers in the ps-ns time regime to conclude the extensive photophysical characterization of this photoswitch. The sample was constantly illuminated with an LED to ensure high concentrations of the isomer of interest. The specifics of this illumination, as well as the experimental setup are described in [Section 4.3](#) and [4.4](#).

The *cis/trans*- and *trans/cis*-isomerization reactions were initiated by setting the excitation wavelength to 362 nm and 530 nm, respectively. Whereas the latter wavelength is identical to the one used in the steady-state characterization so far, the excitation wavelength for *cis/trans*-isomerization was slightly blue-shifted to avoid excitation of the back-reaction. The resulting transient maps for both isomerization reactions are shown in [Figure 7.13](#). GLA was performed<sup>[66]</sup> and the resulting lifetimes are listed in [Table 7.4](#).

*ultrafast dynamics of  
the trans/cis-  
isomerization*

In the case of the transient map of the *trans* to *cis* reaction, directly after photoexcitation two broad excited-state absorption (ESA) bands at 390-490 nm and 525 nm and a stimulated emission (SE) band at 625 nm appears. The latter resembles the spectral shape of the steady-state fluorescence spectrum, which



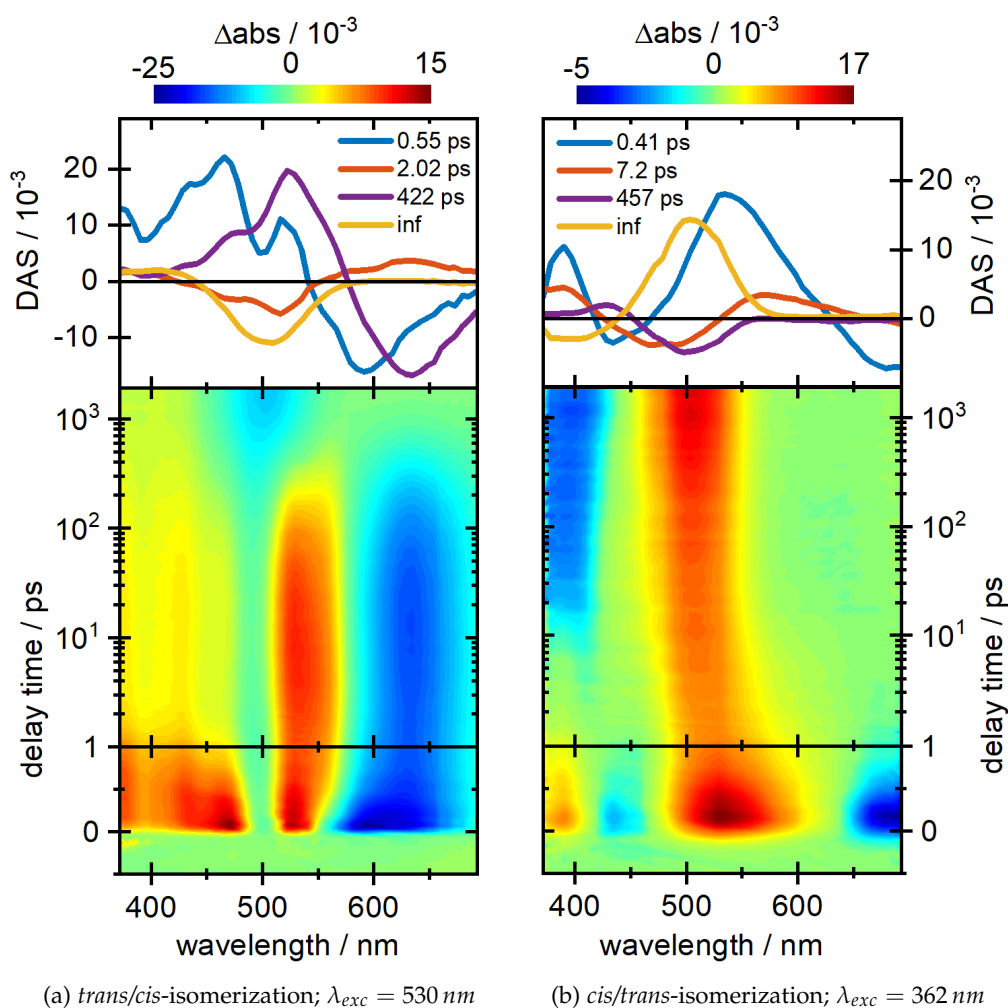


Figure 7.13: Transient maps (bottom panels) and corresponding DAS (upper panels) of the *trans/cis*- (a) and *cis/trans*- (b) isomerization of ceCAM. The samples were constantly illuminated with an LED to accumulate the isomer of interest.

facilitates the assignment for this negative band. Moreover, a ground-state bleach (GSB) (which would also evoke a negative absorbance change) is expected to appear around 487 nm, but is overlapped by the strong ESA in this wavelength region. GLA was performed and three exponential functions and an infinite lifetime are necessary to satisfyingly describe the experimental data and the residual signal at around 2 ns, respectively. The decay-associated spectra (DAS), which correspond to the fitted lifetimes, are shown in the top layer.

The first lifetime  $\tau_1$  of 0.55 ps describes the movement from the FRANCK-CONDON region to the relaxed  $S_1$ -state, accompanied by a red- and blue-shift of the positive and negative signals on this time range, respectively. This STOKES-shift is more pronounced later on and the wavelength-shift is described with the second lifetime  $\tau_2$  of 2.02 ps. The shifting is relatively fast and therefore ascribed to be caused by a solvent-assisted relaxation. The third lifetime  $\tau_3$  of 422 ps describes the lifetime of the ESA centered around 525 nm and the SE at 635 nm, which

are associated to the  $S_1$ -excited state. For photoswitches like cecAM, the decay of this state typically proceeds via a conical intersection (CI) and populates the ground state of either the *cis*- or *trans*-isomer. The branching ratio of the CI then determines the efficiency of the reaction, which in this case is the reaction quantum yield of the *trans/cis*-isomerization. The positive signal around 400 nm did not completely decay at the latest delay times, and moreover a distinct negative signal is observed at 500 nm. Both observations indicate the successful formation of the photoproduct. This assumption is further verified by the DAS of the infinite lifetime which matches the steady-state difference spectrum of the pure isomers (see Figure 7.6), leading to the conclusion that the isomerization is ultimately finished within the measurement time of 1.5 ns.

Table 7.4: Fitted lifetimes of the ultrafast photodynamics of ceCAM after GLA. The *trans/cis*- and *cis/trans*-isomerization are initiated with photoexcitation at 530 nm and 362 nm, respectively.

	<i>trans/cis</i>	<i>cis/trans</i>
$\tau_1$ / ps	0.55	0.41
$\tau_2$ / ps	2.02	7.2
$\tau_3$ / ps	422	457
$\tau_4$ / ps	inf.	inf

The transient data for the reversed *cis/trans*-isomerization is noticeably different (Figure 7.13) and will be described in the following. Instantaneously after photoexcitation, four signals appear: At first, two positive absorbance changes which are assigned to ESA-bands centered around 385 nm and 525 nm. Then, a negative signal around 445 nm is assigned to the ground-state bleach (GSB), because its spectral location matches the ground-state absorbance. Lastly, another negative absorbance change around 696 nm can be observed, which is assumed to be a band resulting from SE. This SE might be a contribution from residual *trans*-isomers in the solution, as it resembles the ground-state fluorescence spectrum of *trans*.

The first lifetime  $\tau_1 = 0.41$  ps describes the motion away from the FRANCK-CONDON region, similar to the reversed isomerization and, more importantly, the decay of the SE at 670 nm, which is indicative for  $S_1$ -state. As for the reverse reaction, the decay of the  $S_1$  implies that the isomerization reaction is completed, which is further verified by the time slices in this time region, which resemble the steady-state difference spectrum (Figure 7.6). The second lifetime  $\tau_2$  of 7.2 ps describes a subsequent wavelength shift, which is assigned to vibrational cooling. However, another third lifetime  $\tau_3$  of 457 ps is found, which describes a spectral shift as well and the buildup of the residual absorbance signals. This lifetime is assigned to the conformational folding to obtain the correct geometric structure.

Interestingly, the found isomerization lifetime is tremendously shorter (factor of 1000) than the one for the *trans/cis*-isomerization. A possible explanation for this different ultrafast behaviour may be found in the geometry of the isomers. As explained in Section 7.1.1, the spectral characteristics of *cis* are mainly dominated by its coumarin-core DEACM. Therefore, it is assumed that the spectra during the transition from the *cis*- to *trans*-isomer (or *vice-versa*) will also be mainly composed of the coumarin core. As soon as the basic scaffold of the *trans*-isomer is obtained, which would allow a delocalization of the  $\pi$ -electrons, the resulting absorbance spectrum will immediately change accordingly, which is why  $\tau_1$  indicates a finished reaction. After vibrational cooling ( $\tau_2$ ), the correct geometry of the *trans*-isomer requires a multitude of atoms to be arranged in a specific position. Thus, the third lifetime  $\tau_3$  describes a ground-state rearrangement of the isomerized chain.

*the cis/trans-isomerization appears to be so much faster*

When trying to understand the data which were collected so far from the time-resolved and steady-state experiments, it is possible to grasp the chemical nature of this photoswitch ceCAM. In fact, with both the ultrafast dynamics of *trans*- and *cis*-ceCAM and the findings in the steady-state regarding the reaction and fluorescence quantum yield, many important excited-state (deactivation) processes are already determined. Assuming that the  $S_1$ -state is the only excited state, then its lifetime would describe all deactivation processes. Then, the general equation  $\tau = \frac{1}{k}$  must consider the sum of all rates in the denominator (Eq. (7.10)). Insertion of this equation into the equation for the fQY, which considers the rates  $k_i$  (Eq. (4.1)), allows for a calculation of the fluorescence rate. The reaction rate is calculated analogously with the reaction quantum yield (Eq. (7.12)).

$$\tau_{S_1} = \frac{1}{k_r + k_f + k_{nr}} \quad (7.10)$$

$$\phi_f = \frac{k_f}{k_f + k_r + k_{nr}} = k_f \cdot \tau_{S_1} \quad (7.11)$$

$$\phi_r = \frac{k_r}{k_r + k_f + k_{nr}} = k_r \cdot \tau_{S_1} \quad (7.12)$$

Exemplarily for *trans*-ceCAM, the values found above for the  $S_1$ -lifetime and the reaction quantum yield ( $\phi_r = 0.5$ ) are inserted to get the reaction rate  $k_r$  of the *trans/cis*-isomerization.

$$\begin{aligned} \tau_{S_1} &= \frac{1}{k_f + k_r + k_{nr}} = \tau_3 = 422 \text{ ps} \\ \phi_r &= k_r \cdot \tau_3 = k_r \cdot 422 \text{ ps} = 0.50 \\ \implies k_r &= \frac{\phi_r}{\tau_3} = \frac{0.5}{422 \text{ ps}} = 1.19 \cdot 10^9 \text{ s}^{-1} \end{aligned} \quad (7.13)$$

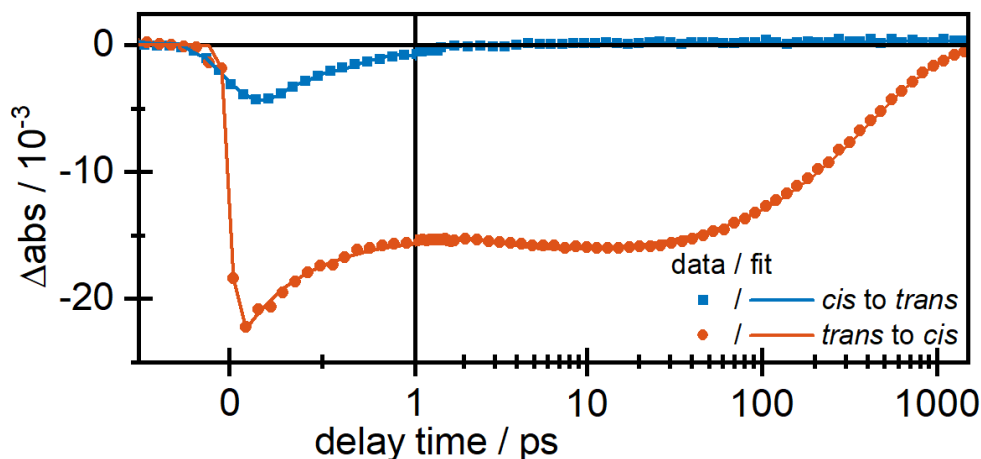
The rate for the fluorescence quantum yield is calculated analogous to Eq. (7.13). The  $S_1$ -lifetimes and the corresponding rates are summarized in Table 7.5.

Table 7.5: Summary of the excited-state lifetimes ( $S_1$ ), reaction rates ( $k_r$ ), fluorescence rates ( $k_f$ ) and rates of the non-radiating processes ( $k_{nr}$ ) of ceCAM

	$\tau_{S_1} / \text{ps}$	$k_r / 10^9 \text{ s}^{-1}$	$k_f / 10^9 \text{ s}^{-1}$	$k_{nr} / 10^9 \text{ s}^{-1}$
<i>trans</i>	422	1.18	0.41	0.78
<i>cis</i>	0.41	1097.5	48.8	1292.7

The reaction and fluorescence quantum yields of *trans*-ceCAM differ by a factor of ca. 3, which is reflected by the corresponding reaction rates. Moreover, the rate for the radiationless decay is slightly higher than that of the fluorescence rate. The initial assumption made in Section 7.2.5.3, that the fluorescence process might be too efficient and also induces unwanted reactions, is mitigated. Ideally, the *trans/cis*-isomerization is not only more efficient but also tremendously faster, so that unwanted side reactions are unlikely to occur.

In case of *cis*-ceCAM the same observation can be found, but with an even stronger emphasis on the isomerization reaction. The first lifetime  $\tau_1$  is inserted into the equation, resulting in a reaction rate which, compared to the opposed isomerization, is larger by a factor of  $10^3$ , which was already indicated by the lifetimes. The fluorescence lifetime is too small to have a significant contribution and therefore cannot compete with the desired isomerization reaction. To emphasize the difference regarding the isomerization rates, Figure 7.14 depicts the transient courses at 630 nm and 670 nm, for the *trans/cis*- and *cis/trans*-isomerization, respectively. These wavelengths represent the course of the SE and show the large difference regarding the  $S_1$ -lifetimes very nicely.

Figure 7.14: Transient courses of the SE for the *trans/cis*- (630 nm) and *cis/trans*-isomerization (670 nm).

Concluding the evaluation and comparison of the photophysical parameters, ceCAM exhibits promising and fast isomerization reactions, with minor contributions from other unwanted reactions. The reaction quantum yields for both isomerization directions are very efficient and similar, although the rate of the

*cis/trans*-reaction is slightly faster.

Unlike the steady-state investigations, different excitation wavelengths for the ultrafast reaction of ceCAM were not applied. For both isomerization directions, future studies should contain in each case two more excitation wavelengths (e.g. 405 nm and 385/388 nm for the *cis/trans*- and 470 nm and 565 nm for the *trans/cis*-isomerization). Then, a direct correlation between the reaction rates and quantum yields can be obtained. Although there were subtle hints during the determination of the  $\tau_{QY}$ , that any form of excess energy in the excited-state of *trans*-ceCAM could influence the efficiency of isomerization, detailed transient-absorption spectroscopy would definitely provide more insights into the reaction dynamics.

Overall, the ultrafast data show that the lifetimes, which are associated to the isomerization reactions in both directions, are faster than 1.5 ns. In general, if photoswitches are to be used in biological environments, e.g. initiate biological processes, underlying photochemical reactions must be fast. One requirement regarding the speed of the reaction is that it is faster than the induced biological process. Although *cis*- and *trans*-isomerization happen on different timescales, they are both sufficiently fast enough for any possible biological applications, which are typically occurring in the  $\mu$ -ms time region.

### 7.3 CONCLUDING REMARKS

The assignment of the ultrafast dynamics concludes the extensive spectroscopic characterization of the bistable photoswitch ceCAM. This chapter summarized the investigations on a newly designed alkene photoswitch, which is linked to a coumarin moiety on the one side and electron-donating groups (cyano and *tert*-butylester) with an ethene bridge on the other side. By doing so, the basic overall photophysical properties could be improved, as the absorbance maximum of the *trans*-isomer is in the visible wavelength range, with a large molar extinction coefficient of  $\epsilon_{489} = 50,300 \text{ M}^{-1} \text{ cm}^{-1}$ . The corresponding *cis*-isomer has a blue-shifted absorbance maximum ( $\epsilon_{437} = 18,600 \text{ M}^{-1} \text{ cm}^{-1}$ ), due to a loss of planarity upon isomerization. Both isomeric states could be obtained by LED-illumination with different sets of wavelengths, leading to very high conversion efficiencies at the  $\text{pss}$  of up to 80 % of *trans*- and even 96 % of *cis*-ceCAM.

The thermal stability of both isomers could be shown, as no significant conversion was detected after a whole week. Due to the fact that illumination of either isomer would accumulate an isomer which does not undergo thermal back-reaction, ceCAM is also proven to be a bistable photoswitch. Additionally, photostability could be shown in fatigue-resistance measurements, in which over 250 cycles of photoswitching barely lead to any detectable degradation. The reaction and fluorescence quantum yields were then determined for both

reactions and isomers, respectively, showing that the reactive pathway is the more efficient pathway in either case. Upon photoexcitation of the *cis*-isomer, it is more than 20 times more likely to undergo an isomerization reaction ( $\phi_r = 0.42$ ) than to deactivate via the fluorescence channel. On the other hand, *trans*-ceCAM also exhibits relatively high reaction quantum yields of ca. 39%, but is also likely to fluoresce ( $\phi_f = 17.6\%$ ).

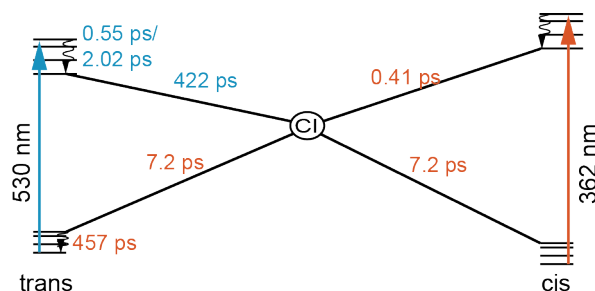


Figure 7.15: Summary of the steady-state and kinetic parameters found for the photophysical characterization of ceCAM.

Lastly, the ultrafast dynamics of both isomers were investigated in transient absorption measurements. Despite the fact, that the transient maps barely resemble each other, the isomerization reaction could be assigned to occur within 1 ns, whereas the found lifetimes are summarized in Figure 7.15. In case of *trans*-ceCAM, the third lifetime  $\tau_3$  of 422 ns describes the lifetime of the excited state  $S_1$ , whereas in case of *cis*-ceCAM,  $\tau_1$  describes the isomerization to the corresponding *trans*-isomer, as the time slices in that time region resemble the steady-state difference absorbance spectrum. The Although the isomerization lifetime for *trans*-isomer is relatively high, the photoinduced isomerization of *cis*-ceCAM occurs within a comparable time range.[248, 134] Ultimately, the photophysical properties found in the steady-state and time-resolved measurements make ceCAM a competitive photoswitch in all regards.

Part IV

CONCLUSION





## CONCLUSION AND OUTLOOK

---

The regulation of biochemical processes or improvement of materials, e.g. for energy storage demand a keen understanding of the underlying systems. For the investigation of those processes or systems, light is ideally suited as a tool, as it is able to obtain useful information about the chemical structure, its properties and a possibly fast course of the reaction. To aid the analysis on the biochemical reactions, small chemical compounds can be incorporated, which because those are easier to be synthesized, analyzed and improved than e.g. a large biomolecule. These compounds can be fluorescence labels, photolabile protecting groups or photoswitchable compounds, just to give a few examples.

In this work, the results of three different projects are summarized. The thesis comprises fluorescence measurements on an RNA helicase and a 2AP-labeled RNA model strand (Chapter 5), the investigations on the uncaging reaction of four different compounds carrying the chromophore BIST (Chapter 6) and the photophysical characterization of a new alkene photoswitch and its corresponding isomerization reaction (Chapter 7).

The many functions of RNA are important and complex, which makes them indispensable for life within a small cell or in larger organisms. Hence, to fulfill their many roles, a correct three-dimensional structure must be obtained. To guarantee that, many biochemical processes are involved, out of which one step is responsible for the unwinding of the helical structure. Regardless of the subsequent aim of single-stranded RNA, this is typically achieved by an RNA helicase, of which many representatives exist.

Within this work, the scarcely investigated RNA helicase RhIB is inspected, which belongs to the family of DEAD-box proteins. Many members of that group have been thoroughly described, providing knowledge about their structural characteristics, recognition pattern and ultimately their unwinding mechanism. Many common features are known for several other DEAD-box helicases, which then had to be verified for RhIB and a model RNA strand. To study the unwinding reaction and the associated RNA-protein interactions, double-stranded JM2h was used as an RNA model strand. The introduction of the label 2AP to one of the single-strands (M2AP6) enabled fluorescence measurements in the steady-state and by means of the stopped-flow technique.

Initially, RhIB was omitted from the studies to solely focus on the RNA duplex. Whereas the labeled single-strand exhibits strong fluorescence, the addition of the complementary strand leads to a significant decrease of the fluorescence intensity, where the minimum is reached at an equimolar ratio. In the stopped-flow

*helicase RhIB and  
dsRNA JM2AP*

measurement, this annealing reaction was found to be accelerated, when higher concentrations of the counter-strand are present within the solution, resulting in an expected second-order kinetics. This information can be useful in further studies, when other RNA model strands are to be investigated in combination with the helicase.

Subsequently, the helicase was added to the solution, expected to unwind the RNA duplex. However, this did not lead to a renewed increase of fluorescence intensity, unless ATP was added. This observation verified the ATP-dependence of the unwinding reaction, which is commonly found in other helicases as well. The observed increase in intensity was identical to another sample containing the RNA duplex (at the same concentration), which was reheated in order to separate the strands.

Despite the fact that the unwinding reaction was not resolved temporally, both the unwinding functionality, as well as the ATP-dependency could be proven. Future studies on the time-resolved unwinding mechanism will comprise investigations of other RNA model strands, with an improved RNA-protein binding affinity. A higher affinity could already be shown in a protein-protein interplay with another subunit of the protein degradosome (RNase E), which will facilitate the investigations on RhlB even further. The foundations for a characterization by fluorescence spectroscopy have been successfully laid by this work.

#### *Uncaging dynamics of BIST-cages*

An alternative approach to observe biological or (bio-)chemical reactions, is by incorporation of small, light-sensitive molecules. One of these concepts is realized with so-called photocages, which deactivates a biomolecule by chemical modification. Upon excitation with a light pulse, the molecule is released and the (bio-)chemical reaction will be triggered. In order to enable an application in cells, several requirements regarding the (photo-)chemical properties of such a photolabile compound are necessary. Many of those were found in an *o*-NB derivative, called **BIST**, which was introduced just recently.

Within this work, four different cages comprising the BIST-scaffold were investigated. For a biological application, low doses of visible light should be applied, to induce the cleavage of the photolabile chemical bond. The investigated BIST-cages fulfill both requirements, as they absorb visible light very efficiently with an extinction coefficient of up to  $\epsilon_{445} = 55,700 \text{ M}^{-1} \text{ cm}^{-1}$ , which is explained by the long and planar structure. In order to identify the key reaction steps of the uncaging reaction, the absorption changes upon illumination were investigated. In the steady-state, two main spectral changes were observed. The loss of absorbance around the ground-state maximum indicated a successful uncaging reaction, whereas a signal increase at higher wavelengths around 510 nm was assigned to the formation of the *aci*-nitro intermediate. An additional of water lead to a stronger signal, indicating a more efficient uncaging reaction. This finding is an advantageous property for cages with regards to a possible biological application where hydrophilic conditions prevail.

The ultrafast dynamics in the ps-ns time range exhibit a spectrally broad, positive band, indicating that in case of the BIST-cages the triplet pathway is favored.

This is in agreement with the findings of the relatively low uncaging yield. Although the uncaging reaction should be higher for a biological application, the efficiency of the uncaging reaction, which is the product of the uncaging yield and the extinction coefficient, is still within a reasonable range.

The rate-limiting step was determined to be the reaction of the *aci*-nitro intermediate around 510 nm. For BIST-NHnBu, this intermediate decayed with a lifetime of 71  $\mu\text{s}$ , which should be fast enough for the investigation of a subsequent biochemical reaction. In conclusion, BIST-cages are a viable option to other photocages, due to their many promising photochemical properties.

In some cases, it is desired to turn an activity on and off. This can be realized by incorporating a small organic molecule, which can be actively interconverted between two isomeric form by exciting it with light. One representative of a so-called photoswitch was investigated in this work, regarding its (photo-)chemical properties for a suitable application. The cyano-ester derivative of CAM was analyzed, which is an alkene photoswitch and undergoes *cis/trans*-isomerization upon illumination. It has electron-rich substituents on both sides of the double bond and thus absorbs visible light very efficiently, which is indicated by its large molar extinction coefficient of  $\epsilon_{489} = 50,300 \text{ M}^{-1} \text{ cm}^{-1}$ . In fact, both isomerizations can be induced by light from an innocuous wavelength range, which makes it a suitable candidate for medical applications.

At room temperature and without any external influences, a thermal isomerization could only be detected after weeks, which makes ceCAM thermally stable. In case the isomerization was in fact photochemically induced, high macroscopic switching efficiencies of up to 80% (*trans*) and 96% (*cis*) at their so-called photostationary states were observed, depending on the wavelength of illumination. Fortunately, ceCAM exhibited a high photostability. In a cyclic switching experiment, it was switched back and forth over 250 times without any major decrease of absorbance.

Moreover, the isomerization event could be triggered with a relatively high probability, as the determined reaction quantum yield for either reaction was in the ranges of 0.39 (*trans*) and 0.42 (*cis*), respectively. By multiplying these values with their respective molar extinction coefficients, the physical value  $E$ , which stands for the efficiency of a reaction, can be determined. Compared to the firstly introduced azobenzenes (3,150 for  $\pi - \pi^*$ -*trans*),<sup>[249]</sup> the efficiency of ceCAM (19,617) is over six times larger.

Lastly, time-resolved spectroscopy was utilized to investigate how fast this reaction occurs. Inspection of the ultrafast dynamics revealed that the isomerization is finished by the end of the experimentally accessible time, which is below 2 nanoseconds. Although the *trans/cis*-isomerization is slightly slower, both conformational changes are still faster than most of the biological processes.

Due to its many advantageous photophysical properties, a multitude of applications for ceCAM in medical or material sciences is imaginable. In particular its ultrafast isomerization reaction allows the specific and rapid regulation of a biomolecular activity.

*photophysical  
characterization of  
the photoswitch  
ceCAM*



## ZUSAMMENFASSUNG UND AUSBLICK

---

Für die Kontrolle biochemischer Prozesse oder die Verbesserung von Materialien, z.B. zur Energiespeicherung, ist ein detailliertes Verständnis der zugrunde liegenden Systeme notwendig. Zur Untersuchung dieser Systeme eignet sich Licht als ideales Werkzeug. Dadurch können nützliche Informationen über die chemische Struktur, ihre Eigenschaften und den damit zusammenhängenden, schnellen Reaktionsabläufen erhalten werden. Um die Aufklärung zu erleichtern, können kleine, chemische Verbindungen eingeführt werden, die einfach zu synthetisieren, analysieren und verbessern sind. Idealerweise beeinflussen die eingeführten Moleküle hierbei das System nur marginal. Diese Verbindungen können z.B. ein Fluoreszenzmarker, eine photolabile Schutzgruppe oder eine photoschaltbare Verbindung sein. In dieser Arbeit werden die Ergebnisse von drei verschiedenen Projekten zusammengefasst, die von den genannten Beispiele handeln.

Diese Arbeit umfasst Fluoreszenzmessungen an einer RNA Helikase und einem 2AP-markierten RNA-Modellstrang ([Kapitel 5](#)), die statischen und zeitaufgelösten Untersuchungen zur Freisetzungsreaktion von vier verschiedenen Verbindungen mit dem Chromophor BIST ([Kapitel 6](#)) sowie die Charakterisierung photophysikalischer Eigenschaften und der entsprechenden Isomerisierungsreaktion eines neuen Alken-Photoschalters ([Kapitel 7](#)).

Die Funktionen von RNA sind sehr vielfältig und sind für das Leben in einer kleinen Zelle sowie einem größeren Organismus unverzichtbar. Um die jeweiligen Funktionalitäten zu gewährleisten, muss die RNA daher in ihrer nativen Struktur vorliegen, um von anderen (Bio-)Makromolekülen korrekt identifiziert zu werden. Um dies zu gewährleisten, sind weitere biochemische Prozesse notwendig, u.a. um die helikale Struktur und die Basenpaare voneinander zu trennen. Das Entwinden dieser dreidimensionalen Struktur wird typischerweise durch eine RNA-Helikase realisiert, von der es viele Vertreter gibt.

In dieser Arbeit wird die RNA-Helikase Rh1B untersucht, die der Familie der DEAD-box Proteine zugeordnet wird. Viele Mitglieder dieser Familie wurden bereits gründlich beschrieben, sodass grundlegende Informationen über die strukturellen Eigenschaften, Erkennungsmuster und den Reaktionsmechanismus, mit dem der Doppelstrang aufgelöst wird, bekannt sind. Diese Informationen wurden genutzt, um Gemeinsamkeiten und etwaige Unterschiede zu Rh1B zu identifizieren. Um die Entwindung und die damit verbundene RNA-Proteininteraktion zu untersuchen, wurde ein doppelsträngiger RNA-Modellduplex (JM2h) verwendet. Die zusätzliche Einführung des Markers 2-Aminopurin (2AP) an einem der Einzelstränge (M2AP6) ermöglichte statische

*Helikase Rh1B und  
dsRNA JM2AP*

Fluoreszenzmessungen sowie Mischexperimente, die mit Hilfe der *stopped-flow*-Technik durchgeführt wurden.

Zunächst wurde die Helikase RhlB in den Studien weggelassen, um die Fluoreszenzeigenschaften des RNA-Duplexes zu analysieren. Während der markierte Einzelstrang eine starke Fluoreszenz aufweist, führt die Zugabe des komplementären Strangs zu einer deutlichen Abnahme der Intensität, deren Minimum bei einem äquimolaren Verhältnis beider Stränge erreicht wird. Dies ist auf die Hybridisierungsreaktion zurückzuführen, bei der die Einzelstränge den stabilen Duplex ausbilden. Bei einer analogen *stopped-flow* Messung wurde festgestellt, dass diese Hybridisierungsreaktion beschleunigt wird, sobald höhere Konzentrationen des Gegenstrangs in der Lösung vorhanden sind. Die aus beiden Experimenten gewonnenen Informationen sind für die folgenden Untersuchungen der RNA-Protein-Interaktion, aber auch für weiterführenden Studien von Relevanz, in denen andere RNA-Modellstränge, die auf M2AP6 aufbauen, untersucht würden.

Anschließend wurde die Helikase der Lösung hinzugefügt, wobei erwartet wurde, dass der frei gewordene M2AP6-Einzelstrang die Fluoreszenzintensität der Lösung erhöht. Dies konnte jedoch erst nach einer weiteren Zugabe von ATP beobachtet werden. Dieser Befund bestätigt die ATP-Abhängigkeit der Reaktion, die auch schon bei anderen DEAD-Box Helikasen beobachtet wurde. Um die korrekte und volle Funktionalität der Helikase zu verifizieren, wurde die Intensitätsdifferenz bestimmt. Diese war konsistent mit einer anderen Lösung, die die gleiche RNA-Konzentration aufwies und bei der die Stränge thermisch voneinander getrennt wurden.

Ebenso konnte der zeitliche Verlauf der Entwindung in *stopped-flow*-Messungen beobachtet werden, wobei die Entwindung langsamer verlief als bei anderen Helikasen. Die Vermutung liegt nahe, dass die RNA-Protein-Interaktion durch die Zugabe weiterer Makromoleküle verbessert werden könne, da die Helikase RhlB Teil eines größeren Multiprotein-Komplexes ist. In weiterführenden Studien soll dann untersucht werden, wie sich beispielsweise die Protein-Protein-Bindung auf die Bindungsaffinität zwischen RNA und Helikase sowie die darauffolgende Entwindungsaktivität auswirkt. Letztlich konnte für RhlB die allgemeine Funktionalität des Entwindens sowie die ATP-Abhängigkeit dieser Reaktion an einem RNA-Modellstrang gezeigt werden. Weitere Modellstränge, die sich auf die Effizienz dieser Reaktion auswirken könnten, sollen untersucht werden, wobei die Grundlagen für eine Charakterisierung mittels Fluoreszenzspektroskopie mit dieser Arbeit erfolgreich geschaffen wurden.

Sämtliche statische Fluoreszenzspektren wurden mit einem selbstgeschriebenen MATLAB-Programm namens FluCY korrigiert (engl.: *Fluorescence Correction & Quantum yield*). Bei der Aufnahme eines Fluoreszenzspektrums sind verschiedene spektrale Korrekturen hinsichtlich der Anregung und Emission notwendig. Die entsprechenden Maßnahmen sind relativ fehleranfällig und nehmen viel

Zeit in Anspruch. Das Programm, welches eine einfach zu bedienende Oberfläche hat, beschleunigt den Prozess der Korrektur und vermeidet überdies Fehler in der Datenverarbeitung.

Die zwei im folgenden beschriebenen Projekte handeln von photoaktivierbaren Molekülen. Diese stellen einen alternativen Ansatz dar, biologische oder (bio-)chemische Reaktionen zu untersuchen. Eines dieser Konzepte wird mit sogenannten lichtempfindlichen Verbindungen realisiert, die beispielsweise die Funktion eines Biomoleküls durch chemische Modifikation deaktivieren (sogenannte Käfig-Verbindungen oder engl.: *caged compounds*). Bei Anregung mit einem Lichtimpuls wird die Modifikation abgespalten, das Biomolekül freigesetzt und die Funktionalität des Biomoleküls wiederhergestellt. Für die mögliche Anwendung in Zellen sind mehrere Anforderungen an die photochemischen und -physikalischen Eigenschaften einer solchen photolabilen Schutzgruppe gegeben. Viele davon wurden für BIST gefunden, welches ein Derivat von *ortho*-Nitrobenzol darstellt und erst kürzlich entwickelt und vorgestellt wurde.

Im Rahmen dieser Arbeit wurden vier photolabile Verbindungen mit dem Chromophor BIST (*bis*styryl-*thi*ophen) untersucht. Für eine biologische Anwendung sollten niedrige Dosen von Licht aus dem sichtbaren Spektralbereich verwendet werden, um den Bindungsbruch zu induzieren. Die untersuchten BIST-Verbindungen erfüllen beide Anforderungen, da sie sichtbares Licht mit einem Extinktionskoeffizienten von  $\epsilon_{445} = 55.700 \text{ M}^{-1} \text{ cm}^{-1} \text{ cm}^{-1}$  sehr effizient absorbieren können. Dies lässt sich auf die planare Struktur zurückführen, die eine weitreichende Delokalisierung der Elektronen zulässt und somit die für eine Photoanregung notwendige Energie herabsetzt.

Um die wichtigsten Teilschritte der Freisetzungsreaktion zu identifizieren, wurden die Absorptionsänderungen im sichtbaren Wellenlängenbereich nach Photoanregung untersucht. In den statischen Messungen wurden zwei dominante Signale beobachtet. Der Verlust der Absorption am Grundzustandsmaximum deutete auf eine erfolgreiche Freisetzungsreaktion hin, wohingegen der Signalanstieg bei höheren Wellenlängen um 510 nm der Bildung des *aci*-Nitro zugeordnet wurde, was ein bekanntes Intermediat dieser Reaktion ist. Das Experiment wurde mit einer zusätzlichen Menge an Wasser (20%) wiederholt, was zu einer stärkeren Signaländerung führte, die wiederum auf eine effizientere Reaktion hinweist. Dieser Befund ist eine vorteilhafte Eigenschaft für die untersuchten Verbindungen hinsichtlich einer möglichen biologischen Anwendung, bei der hydrophile Bedingungen vorherrschen.

Die ultraschnelle Dynamik im ps-ns-Zeitbereich war durch eine spektral breite, positive Absorptionsänderung dominiert. Diese impliziert, dass nach Photoanregung der BIST-Moleküle die anschließende Deaktivierung bevorzugt über den Triplettpfad abläuft. Dieser Pfad hat normalerweise zur Folge, dass die Quantenausbeute der Freisetzung vergleichsweise gering ausfällt, was hier bestätigt wurde ( $\phi_u \leq 5\%$ ). Obwohl die Quantenausbeute der Freisetzungsreaktion für eine biologische Anwendung idealerweise höher sein sollte, liegt die so-

*Freisetzungs-  
Dynamik von  
BIST-geschützten  
photolabilen  
Verbindungen*

genannte Effizienz der Reaktion noch in einem angemessenen Bereich. Die Effizienz ist definiert über das Produkt aus der Quantenausbeute und dem Extinktionskoeffizienten und sollte üblicherweise hoch ausfallen, sodass bereits kleine Mengen an Licht die Reaktion initiieren können. Im vorliegenden Fall der BIST-Verbindungen können die geringen Quantenausbeuten durch die hohen Extinktionskoeffizienten kompensiert werden.

Der geschwindigkeitsbestimmende Schritt der Freisetzungsreaktion wurde anhand der Lebensdauer des angeregten Zustands von *aci*-Nitro bestimmt. Mit Hilfe der Blitzlicht-Photolyse wurde der transiente Verlauf bei 510 nm untersucht und eine Lebensdauer von 71  $\mu\text{s}$  für BIST-NHnBu gefunden. Idealerweise ist die Freisetzung der geschützten Verbindung schneller als die von ihr zu initiiierende Reaktion. Da dies jedoch vom Anwendungsbereich der photolabilen Moleküle abhängt und viele biochemische Prozesse deutlich langsamer ablaufen, ist die für BIST-Verbindungen gefundene Lebensdauer in einem geeigneten Zeitbereich. Insgesamt wurden für die BIST-geschützten Verbindungen weitere gute photochemische und -physikalische Eigenschaften gefunden. Dadurch sind sie als eine geeignete Alternative zu den bisher bekannten photolabilen Schutzgruppen anzusehen.

In einigen Fällen ist es erwünscht, eine vorliegende Aktivität nicht nur ein-, sondern auch ausschalten zu können. Dies kann durch die Integration eines Moleküls realisiert werden, welches lichtinduziert zwischen zwei isomeren Formen wechseln kann. Diese photochromen Verbindungen stellen die Alternative zu den photolabilen Schutzgruppen dar. Ein Vertreter der Photoschalter wird in dieser Arbeit hinsichtlich seiner photophysikalischen Eigenschaften für eine geeignete Anwendung untersucht.

Charakterisierung  
des Photoschalters  
ceCAM

ceCAM ist ein Alken-Photoschalter und vollführt bei der Bestrahlung mit Licht eine *cis/trans*-Isomerisierung. Auf der einen Seite der Doppelbindung wurde es mit einem Cumarin-Derivat verknüpft, während die andere Seite elektronenreiche Substituenten in Form eines Nitril- und *tert*-Butylesterrests trägt. Dadurch absorbiert ceCAM effizient sichtbares Licht, was sich durch den großen molaren Extinktionskoeffizienten des *trans*-Isomers von  $\epsilon_{489} = 50.300 \text{ M}^{-1}\text{cm}^{-1}$  bemerkbar macht. Beim zugehörigen *cis*-Isomer ist die Struktur verdrillt, sodass eine Delokalisation der Elektronen nicht mehr über das gesamte Molekül möglich ist. Dies hat zur Folge, dass sich das Absorptionsmaximum zu höheren Energien verschiebt ( $\epsilon_{437} = 18.600 \text{ M}^{-1}\text{cm}^{-1}$ ).

Beide Reaktionsrichtungen können durch Photoanregung im sichtbaren Wellenlängenbereich induziert werden. Bei Raumtemperatur und ohne äußere Einflüsse konnte eine eigenständige Isomerisierung erst nach Wochen festgestellt werden, d.h. ceCAM weist eine hohe thermische Stabilität auf. Idealerweise konnte für ceCAM auch eine hohe Photostabilität gezeigt werden. In einem Experiment wurde alternierend zwischen den beiden Isomeren hin- und hergeschaltet und auch bei über 250 Zyklen konnte nur eine geringe Abnahme der



Absorption beobachtet werden. Im Falle einer solchen photochemisch induzierten Reaktion wurden je nach Wellenlänge der Belichtung hohe makroskopische Schalteffizienzen von bis zu 80% (*trans*) und 96% (*cis*) im photostationären Gleichgewicht beobachtet.

Darüber hinaus wurde gezeigt, dass die Isomerisierung mit einer relativ hohen Wahrscheinlichkeit induziert werden konnte. Dafür wurden die Reaktionsquantenausbeuten  $\phi_r$  beider Isomerisierungen bestimmt, wofür Werte im Bereich von 39% (*trans*) und 42% (*cis*) ermittelt wurden. Analog zu den photolabilen Verbindungen lässt sich die Effizienz dieser Reaktion bestimmen. Dadurch, dass für ceCAM beide Faktoren hoch sind, ist auch bspw. die *trans/cis*-Isomerisierung sehr effizient (ca. 19.600) und über sechsmal größer als die des erstmalig vorgestellten Azobenzols (3.150 für  $\pi\pi^*$ -*trans*-Isomerisierung).[249]

Als weiterer Aspekt der photophysikalischen Charakterisierung wurden die Fluoreszenzquantenausbeuten  $\phi_f$  von ceCAM bestimmt. Viele Derivate von Cumarin sind als Fluorophore in der Literatur bekannt. Aufgrund der Eingliederung von Cumarin in die Struktur von ceCAM wurde erwartet, dass auch der Photoschalter Fluoreszenzeigenschaften aufweist. Die Bestimmung der Quantenausbeuten erfolgte über die relative Methode und wurde mit Hilfe des selbst geschriebenen Programms FluCY ausgewertet. Die erhaltenen Fluoreszenzquantenausbeuten sind sehr gering und liegen im Bereich von 1% (*cis*) und 17,6% (*trans*). Obwohl die beobachtete Fluoreszenz eine unerwünschte Eigenschaft von ceCAM bzw. allgemein von Photoschaltern ist, so ist der konkurrierende Prozess der Isomerisierung deutlich wahrscheinlicher.

Letztlich wurde mit Hilfe der Ultrakurzzeit-Spektroskopie untersucht, wie schnell die Isomerisierung aus beiden Richtungen abläuft. Die Untersuchung der Dynamik im ps–ns ergab, dass die Isomerisierung in beiden Fällen innerhalb von 2 ns abgeschlossen ist. Als Indikator wurde das statische Differenzspektrum herangezogen, was einen Hinweis auf die Änderungen der Absorptionsbanden gibt. Interessanterweise ist die *trans/cis*-Isomerisierung deutlich langsamer, da der angeregte Zustand erst mit einer Lebensdauer von 422 ps zerfällt. Jedoch findet die Konformationsänderung deutlich schneller statt als die meisten biologischen Prozesse, die damit untersucht werden können, was ebenso für die umgekehrte, schnellere *cis/trans*-Isomerisierung gilt. Die daraus erhaltenen Reaktionsraten stehen im Einklang zu den gefunden niedrigen Fluoreszenzquantenausbeuten von ceCAM. Da die schnelle Isomerisierung eine effektive Depopulierung des angeregten Zustands impliziert, ist die Deaktivierung dieses Zustands über den Fluoreszenzpfad nur bedingt möglich.

Aufgrund seiner vielen vorteilhaften photophysikalischen Eigenschaften sind zahlreiche Anwendungen für ceCAM denkbar. Die hohe thermische und photochemische Stabilität sowie ein effizientes und schnelles Schalten ermöglichen die gezielte und schnelle Regulation einer gezielten Aktivität, bspw. in der Medizin oder in den Materialwissenschaften.



Part V

APPENDIX





## APPENDIX

---

### A.1 FLUCY - VERSION HISTORY AND SAVING LOCATION

#### A.1.1 LOCATION OF FILES AND FOLDERS

The most up-to-date version of the matlab-program Fluorescence Correction & Quantum Yield (FluCY) is located on the Server marge, which is administered by the Burghardt-lab.

Within the subfolder /data/femtochem/Software/FluCY the following files are included:

- 20150505\_groupseminar\_Dinh\_introduction\_FluCY.pptx contains a powerpoint-presentation which was given in the internal group seminar of the Wachtveitl lab. Therein, the program was firstly introduced. Apart from this work, that presentation can assist new users, as it contains video material on the program as well
- changelog.txt provides a version history of the program
- The subfolder matlab versions contains a FluCY\_vx\_y.m and a .fig file, which are both needed for running FluCY.
- Two other folders called necessary files and Temp-Files are included, which contain the files for the sensitivity of detector, a spectrum of the excitation lamp and pictures which are necessary for the program. The other folder could be empty, but is still necessary for the program to function, as the intermediary files are saved therein.
- Future versions will include a batch of exemplary fluorescence and absorbance spectra.

#### A.1.2 VERSION HISTORY

1. Creating FluCY
  - 1.1. implement possibility to use normalized/non-normalized detector correction curve
  - 1.2. correct wrong codeforthe normalization of detector correction curve rearrange code of solvent correction (line 936ff.)

## A.2 AMINO ACID SEQUENCE OF RHLB

Protein: ATP-dependent RNA helicase RhlB  
 Size: 420 AA  
 Weight: 47 kDa  
 Gene: rhlb  
 Organism: *Escherichia coli* (strain K12)  
 Proteomic database: PoA8J8.

```

      10      20      30      40      50
MSKTHLTEQKFSDFALHPKVVEALEKKGFFHNCTPIQALALPLTLAGRVDVAGQAQT

      60      70      80      90     100     110
GTGKTMAFLLTSTFHILLSHPAIADRKVNQPRALIMAPTRELAVQIHADAEPLEAA

      120     130     140     150     160
TGLKLGLAYGGDGYDKQLKVLESGVDILIGTTGRLIDYAKQNHINLGAIQVVLD

      170     180     190     200     210     220
EADRMVDLGFIKDIRWLFRRMPPANQRLNMLFSATLSYRVRELAFEQMNAEYIE

      230     240     250     260     270
VEPEQKTGHRIKEELFYPSNEEKMRLLQTLIEEWPDRAIIFANTKHRCEEIUGH

      280     290     300     310     320     330
LAADGHRVGLLTGDVAQKKRLRILDEFTRGDLIDLVAATDVAARGLHIPAVTHVFN

      340     350     360     370     380
YDLPDDCEDYVHRIGRTGRAGASGHSISLACEEYALNLP AIETYIGHSIPVSKYN

      390     400     410     420
PDALMTDLPKPLRLTRPRTGNGPRRTGAPRNRRRSG

```

## BIBLIOGRAPHY

---

- [1] Hugo, V. *William Shakespeare* (Librairie internationale (A. Lacroix, Verboeckhoven et Ce), 1864).
- [2] Schawlow, A. L. & Townes, C. H. Infrared and Optical Masers. *Physical Review* **112**, 1940–1949 (1958).
- [3] Maiman, T. H. Stimulated Optical Radiation in Ruby. *Nature* **187**, 493–494 (1960).
- [4] Townes, C. H., Basov, N. G. & Prokhorov, A. M. Fundamental work in the field of quantum electronics, which has led to the construction of oscillators and amplifiers based on the maser-laser principle. *The Nobel Prize in Physics 1964*.
- [5] Gabor, D. Invention and development of the holographic method. *The Nobel Prize in Physics 1971*.
- [6] Bloembergen, N. & Schawlow, A. L. Contribution to the development of laser spectroscopy. *The Nobel Prize in Physics 1981*.
- [7] Ramsey, N. F. Invention of the separated oscillatory fields method and its use in the hydrogen maser and other atomic clocks. *The Nobel Prize in Physics 1989*.
- [8] Chu, S., Cohen-Tannoudji, C. & Phillips, W. D. Development of methods to cool and trap atoms with laser light. *The Nobel Prize in Physics 1997*.
- [9] Cornell, E. A., Ketterle, W. & Wieman, C. E. Achievement of Bose-Einstein condensation in dilute gases of alkali atoms, and for early fundamental studies of the properties of the condensates. *The Nobel Prize in Physics 2001*.
- [10] Hall, J. L. & Hänsch, T. W. Contributions to the development of laser-based precision spectroscopy, including the optical frequency comb technique. *The Nobel Prize in Physics 2005*.
- [11] Mather, J. C. & Smoot, G. F. Discovery of the blackbody form and anisotropy of the cosmic microwave background radiation. *The Nobel Prize in Physics 2006*.
- [12] Eigen, M., Norrish, R. G. W. & Porter, G. Studies of extremely fast chemical reactions, effected by disturbing the equilibrium by means of very short pulses of energy. *The Nobel Prize in Chemistry 1967*.
- [13] Ashkin, A., Mourou, G. & Strickland, D. Groundbreaking inventions in the field of laser physics. *The Nobel Prize in Physics 2018*.
- [14] Mitchison, T., Sawin, K., Theriot, J., Gee, K & Mallavarapu, A. in *Methods in enzymology* 63–78 (1998).

- [15] Tsien, R. Y. & Zucker, R. S. Control of cytoplasmic calcium with photolabile tetracarboxylate 2-nitrobenzhydrol chelators. *Biophysical Journal* **50**, 843–853 (1986).
- [16] Adams, S. R., Kao, J. P. Y., Grynkiewicz, G., Minta, A. & Tsien, R. Y. Biologically useful chelators that release Ca<sup>2+</sup> upon illumination. *Journal of the American Chemical Society* **110**, 3212–3220 (1988).
- [17] Kaplan, J. H. & Ellis-Davies, G. C. Photolabile chelators for the rapid photorelease of divalent cations. *Proceedings of the National Academy of Sciences of the United States of America* **85**, 6571–6575 (1988).
- [18] Ellis-Davies, G. C. & Kaplan, J. H. Nitrophenyl-EGTA, a photolabile chelator that selectively binds Ca<sup>2+</sup> with high affinity and releases it rapidly upon photolysis. *Proceedings of the National Academy of Sciences of the United States of America* **91**, 187–191 (1994).
- [19] Adams, S. R., Lev-Ram, V. & Tsien, R. Y. A new caged Ca<sup>2+</sup>, azid-1, is far more photosensitive than nitrobenzyl-based chelators. *Chemistry and Biology* **4**, 867–878 (1997).
- [20] Ellis-Davies, G. C. & Barsotti, R. J. Tuning caged calcium: Photolabile analogues of EGTA with improved optical and chelation properties. *Cell Calcium* **39**, 75–83 (2006).
- [21] Agarwal, H. K., Janicek, R., Chi, S.-H., Perry, J. W., Niggli, E. & Ellis-Davies, G. C. R. Calcium Uncaging with Visible Light. *Journal of the American Chemical Society* **138**, 3687–3693 (2016).
- [22] Kohl-Landgraf, J., Buhr, F., Lefrancois, D., Mewes, J.-M., Schwalbe, H., Dreuw, A. & Wachtveitl, J. Mechanism of the Photoinduced Uncaging Reaction of Puromycin Protected by a 6-Nitroveratryloxycarbonyl Group. *Journal of the American Chemical Society* **136**, 3430–3438 (2014).
- [23] Buhr, F., Kohl-Landgraf, J., Tomdieck, S., Hanus, C., Chatterjee, D., Hegelein, A., Schuman, E. M., Wachtveitl, J. & Schwalbe, H. Design of photocaged puromycin for nascent polypeptide release and spatiotemporal monitoring of translation. *Angewandte Chemie - International Edition* **54**, 3717–3721 (2015).
- [24] Herzig, L.-M., Elamri, I., Schwalbe, H. & Wachtveitl, J. Light-induced antibiotic release from a coumarin-caged compound on the ultrafast timescale. *Physical Chemistry Chemical Physics* **19**, 14835–14844 (2017).
- [25] Schwalbe, H., Elamri, I., Heumüller, M., Herzig, L. M., Stirnal, E., Wachtveitl, J. & Schuman, E. A new photocaged puromycin for an efficient labelling of newly translated proteins in living neurons. *ChemBioChem*, accepted (2018).
- [26] Goswami, P. P., Syed, A., Beck, C. L., Albright, T. R., Mahoney, K. M., Unash, R., Smith, E. A. & Winter, A. H. BODIPY-Derived Photoremovable Protecting Groups Unmasked with Green Light. *Journal of the American Chemical Society* **137**, 3783–3786 (2015).



- [27] Carling, C. J., Olejniczak, J., Foucault-Collet, A., Collet, G., Viger, M. L., Nguyen Huu, V. A., Duggan, B. M. & Almutairi, A. Efficient red light photo-uncaging of active molecules in water upon assembly into nanoparticles. *Chemical Science* **7**, 2392–2398 (2016).
- [28] Lipp, P. & Niggli, E. Fundamental calcium release events revealed by two-photon excitation photolysis of caged calcium in guinea-pig cardiac myocytes. *Journal of Physiology* **508**, 801–809 (1998).
- [29] Furuta, T., Wang, S. S.-H., Dantzer, J. L., Dore, T. M., Bybee, W. J., Callaway, E. M., Denk, W. & Tsien, R. Y. Brominated 7-hydroxycoumarin-4-ylmethyls: Photolabile protecting groups with biologically useful cross-sections for two photon photolysis. *Proceedings of the National Academy of Sciences* **96**, 1193–1200 (1999).
- [30] Matsuzaki, M., Ellis-Davies, G. C., Nemoto, T., Miyashita, Y., Iino, M. & Kasai, H. Dendritic spine geometry is critical for AMPA receptor expression in hippocampal CA1 pyramidal neurons. *Nature Neuroscience* **4**, 1086–1092 (2001).
- [31] Noguchi, J., Nagaoka, A., Watanabe, S., Ellis-Davies, G. C. R., Kitamura, K., Kano, M., Matsuzaki, M. & Kasai, H. In vivo two-photon uncaging of glutamate revealing the structure-function relationships of dendritic spines in the neocortex of adult mice. *The Journal of Physiology* **589**, 2447–2457 (2011).
- [32] Bort, G., Gallavardin, T., Ogden, D. & Dalko, P. I. From one-photon to two-photon probes: "caged" compounds, actuators, and photoswitches. *Angewandte Chemie - International Edition* **52**, 4526–4537 (2013).
- [33] Hirshberg, Y. & Fischer, E. Photochromism and reversible multiple internal transitions in some spiropyrans at low temperatures. Part I. *Journal of the Chemical Society (Resumed)*, 297 (1954).
- [34] Irie, M. & Mohri, M. Thermally irreversible photochromic systems. Reversible photocyclization of diarylethene derivatives. *The Journal of Organic Chemistry* **53**, 803–808 (1988).
- [35] Campbell, N., Henderson, A. W. & Taylor, D. 257. Geometrical isomerism of azo-compounds. *Journal of the Chemical Society (Resumed)*, 1281–1285 (1953).
- [36] Ballard, D. A. & Dehn, W. M. Preparation of Certain Reduction Products of Benzoin. *Journal of the American Chemical Society* **54**, 3969–3971 (1932).
- [37] Fukaminato, T., Umemoto, T., Iwata, Y., Yokojima, S., Yoneyama, M., Nakamura, S. & Irie, M. Photochromism of diarylethene single molecules in polymer matrices. *Journal of the American Chemical Society* **129**, 5932–5938 (2007).
- [38] Velema, W. A., Szymanski, W. & Feringa, B. L. Photopharmacology: Beyond Proof of Principle. *Journal of the American Chemical Society* **136**, 2178–2191 (2014).

- [39] Blanco-Lomas, M., Samanta, S., Campos, P. J., Woolley, G. A. & Sampedro, D. Reversible Photocontrol of Peptide Conformation with a Rhodopsin-like Photoswitch. *Journal of the American Chemical Society* **134**, 6960–6963 (2012).
- [40] Poloni, C., Stuart, M. C., Van Der Meulen, P., Szymanski, W. & Feringa, B. L. Light and heat control over secondary structure and amyloid-like fiber formation in an overcrowded-alkene-modified Trp zipper. *Chemical Science* **6**, 7311–7318 (2015).
- [41] Panchbhai, A. Wilhelm Conrad Röntgen and the discovery of X-rays: Revisited after centennial. *Journal of Indian Academy of Oral Medicine and Radiology* **27**, 90 (2015).
- [42] Huheey, J. E., Keiter, E. A. & Keiter, R. L. *Inorganic Chemistry: Principles of Structure and Reactivity* 4th ed., 964 (Addison Wesley Pub Co Inc., 1993).
- [43] Laporte, O. & Meggers, W. F. Some Rules of Spectral Structure. *Journal of the Optical Society of America* **11**, 459 (1925).
- [44] Born, M. & Oppenheimer, R. Zur Quantentheorie der Molekeln. *Annalen der Physik* **389**, 457–484 (1927).
- [45] Stuart, B. H. *Infrared Spectroscopy: Fundamentals and Applications* 244 (John Wiley & Sons, Ltd, Chichester, UK, 2004).
- [46] Demtröder, W. *Molekülphysik: Theoretische Grundlagen und experimentelle Methoden* 487 (Oldenbourg Verlag, 2013).
- [47] Demtröder, W. *Atome, Moleküle und Festkörper* 617 (Springer-Verlag, 2005).
- [48] Hippler, H. *Vorlesungsskript: Physikalische Chemie II, Quantenmechanik und Spektroskopie* 51 (Universität Karlsruhe, 2002).
- [49] Hamm, P., Ohline, S. M. & Zinth, W. Vibrational cooling after ultrafast photoisomerization of azobenzene measured by femtosecond infrared spectroscopy. *The Journal of Chemical Physics* **106**, 519–529 (1997).
- [50] Hamm, P., Zurek, M., Röschinger, T., Patzelt, H., Oesterheld, D. & Zinth, W. Subpicosecond infrared spectroscopy on the photoisomerisation of the protonated Schiff base of all-trans retinal. *Chemical Physics Letters* **268**, 180–186 (1997).
- [51] Brust, T., Malkmus, S., Draxler, S., Ahmed, S. A., Rück-Braun, K., Zinth, W. & Braun, M. Photochemistry with thermal versus optical excess energy: Ultrafast cycloreversion of indolylfulgides and indolylfulgimides. *Journal of Photochemistry and Photobiology A: Chemistry* **207**, 209–216 (2009).
- [52] Cordes, T., Malkmus, S., DiGirolamo, J. A., Lees, W. J., Nenov, A., De Vivie-Riedle, R., Braun, M. & Zinth, W. Accelerated and efficient photochemistry from higher excited electronic states in fulgide molecules. *Journal of Physical Chemistry A* **112**, 13364–13371 (2008).

- [53] Slavov, C., Boumrifak, C., Hammer, C. A., Trojanowski, P., Chen, X., Lees, W. J., Wachtveitl, J. & Braun, M. The ultrafast reactions in the photochromic cycle of water-soluble fulgimide photoswitches. *Physical Chemistry Chemical Physics* **18**, 10289–10296 (2016).
- [54] Lakowicz, J. R. *Principles of Fluorescence Spectroscopy* 3rd ed. (Springer US, 2006).
- [55] Haken, H. & Wolf, H. C. *Molekülphysik und Quantenchemie* (Springer-Verlag, Berlin/Heidelberg, 2006).
- [56] Demtröder, W. *Laserspektroskopie* 5th ed., 726 (Springer Berlin Heidelberg, Berlin, Heidelberg, 2007).
- [57] Bass, M, Franken, P. a., Ward, J. F. & Weinreich, G. Optical Rectification. *Physical Review Letters* **9**, 446–448 (1962).
- [58] Franken, P. A., Hill, A. E., Peters, C. W. & Weinreich, G. Generation of optical harmonics. *Physical Review Letters* **7**, 118–119 (1961).
- [59] Weinberger, P. John Kerr and his effects found in 1877 and 1878. *Philosophical Magazine Letters* **88**, 897–907 (2008).
- [60] Alfano, R. R. & Shapiro, S. L. Observation of Self-Phase Modulation and Small-Scale Filaments in Crystals and Glasses. *Physical Review Letters* **24**, 592–594 (1970).
- [61] Steinwand, S. Conformational control of organic molecules by azobenzene-based photoswitches – a spectroscopic study. *PhD thesis*, Goethe University Frankfurt (2016).
- [62] Heisenberg, W. Über den anschaulichen Inhalt der quantentheoretischen Kinematik und Mechanik. *Zeitschrift für Physik* **43**, 172–198 (1927).
- [63] Hargrove, L. E., Fork, R. L. & Pollack, M. A. Locking of hene laser modes induced by synchronous intracavity modulation. *Applied Physics Letters* **5**, 4–5 (1964).
- [64] Mocker, H. W. & Collins, R. J. Mode competition and self-locking effects in a q-switched ruby laser. *Applied Physics Letters* **7**, 270–273 (1965).
- [65] Strickland, D. & Mourou, G. Compression of Ampified Chirped Optical Pulses. *Optics Communications* **55**, 447–449 (1985).
- [66] Slavov, C., Hartmann, H. & Wachtveitl, J. Implementation and Evaluation of Data Analysis Strategies for Time-Resolved Optical Spectroscopy. *Analytical Chemistry* **87**, 2328–2336 (2015).
- [67] Berg, J. M., Tymoczko, J. L. & Stryer, L. *Stryer Biochemie* (Springer Spektrum; Auflage: 7. Aufl. 2013, 2012).
- [68] Lehninger, A., Nelson, D. & Cox, M. *Lehninger Principles of Biochemistry* (W. H. Freeman, 2008).
- [69] Crick, F. Central Dogma of Molecular Biology. *Nature* **227**, 561–563 (1970).

- [70] Shine, J. & Dalgarno, L. The 3'-Terminal Sequence of Escherichia coli 16S Ribosomal RNA: Complementarity to Nonsense Triplets and Ribosome Binding Sites. *Proceedings of the National Academy of Sciences* **71**, 1342–1346 (1974).
- [71] Traub, P. & Nomura, M. Structure and function of E. coli ribosomes. V. Reconstitution of functionally active 30S ribosomal particles from RNA and proteins. *Proceedings of the National Academy of Sciences* **59**, 777–784 (1968).
- [72] Winkler, W. C., Nahvi, A., Roth, A., Collins, J. A. & Breaker, R. R. Control of gene expression by a natural metabolite-responsive ribozyme. *Nature* **428**, 281–286 (2004).
- [73] Caruthers, J. M. & McKay, D. B. Helicase structure and mechanism. *Current Opinion in Structural Biology* **12**, 123–133 (2002).
- [74] Subramanya, H. S., Bird, L. E., Brannigan, J. A. & Wigley, D. B. Crystal structure of a DExx box DNA helicase. *Nature* **384**, 379–383 (1996).
- [75] Rudra, S & Skibbens, R. Chl1 DNA helicase regulates Scc2 deposition specifically during DNA-replication in *Saccharomyces cerevisiae*. *PLoS one* **8**, e75435 (2013).
- [76] Rogers, G., Richter, N. & Merrick, W. Biochemical and Kinetic Characterization of the RNA Helicase Activity of Eukaryotic Initiation Factor 4A. *Journal of Biological Chemistry* **274**, 12236–12244 (1999).
- [77] Py, B, Higgins, C., Krisch, H. & Carpousis, A. A DEAD-box RNA helicase in the Escherichia coli RNA degradosome. *Nature* **381**, 169–72 (1996).
- [78] Pan, C. & Russell, R. Roles of DEAD-box proteins in RNA and RNP Folding. *RNA biology* **7**, 667–676 (2010).
- [79] Pyle, A. M. Translocation and Unwinding Mechanisms of RNA and DNA Helicases. *Annual Review of Biophysics* **37**, 317–336 (2008).
- [80] Jain, C. The E. coli RhlE RNA helicase regulates the function of related RNA helicases during ribosome assembly. *RNA* **14**, 381–389 (2007).
- [81] Iost, I. & Dreyfus, M. DEAD-box RNA helicases in Escherichia coli. *Nucleic acids research* **34**, 4189–97 (2006).
- [82] Linder, P, Lasko, P., Ashburner, M, Leroy, P, Nielsen, P, Nishi, K, Schnier, J & Stonimski, P. Birth of the D-E-A-D box. *Nature* **337**, 121–2 (1989).
- [83] Tseng, Y.-T., Chiou, N.-T., Gogiraju, R. & Lin-Chao, S. The Protein Interaction of RNA Helicase B (RhlB) and Polynucleotide Phosphorylase (PN-Pase) Contributes to the Homeostatic Control of Cysteine in Escherichia coli. *Journal of Biological Chemistry* **290**, 29953–29963 (2015).

- [84] Chandran, V., Poljak, L., Vanzo, N. F., Leroy, A., Miguel, R. N., Fernandez-Recio, J., Parkinson, J., Burns, C., Carpousis, A. J. & Luisi, B. F. Recognition and Cooperation Between the ATP-dependent RNA Helicase RhlB and Ribonuclease RNase E. *Journal of Molecular Biology* **367**, 113–132 (2007).
- [85] Tamai, N. & Miyasaka, H. Ultrafast Dynamics of Photochromic Systems. *Chemical Reviews* **100**, 1875–1890 (2000).
- [86] Goeldner, M. & Givens, R. *Dynamic Studies in Biology: Phototriggered, Photoswitches and Caged Biomolecules* 1st ed. (Wiley VCH, New York, 2005).
- [87] Ellis-Davies, G. C. R. Caged compounds: photorelease technology for control of cellular chemistry and physiology. *Nature methods* **4**, 619–628 (2007).
- [88] Brieke, C., Rohrbach, F., Gottschalk, A., Mayer, G. & Heckel, A. Light-controlled tools. *Angewandte Chemie - International Edition* **51**, 8446–8476 (2012).
- [89] Klán, P., Šolomek, T., Bochet, C. G., Blanc, A., Givens, R., Rubina, M., Popik, V., Kostikov, A. & Wirz, J. Photoremovable Protecting Groups in Chemistry and Biology: Reaction Mechanisms and Efficacy. *Chemical Reviews* **113**, 119–191 (2013).
- [90] Kumpulainen, T., Lang, B., Rosspointner, A. & Vauthey, E. Ultrafast Elementary Photochemical Processes of Organic Molecules in Liquid Solution. *Chemical Reviews* **117**, 10826–10939 (2017).
- [91] Mayer, G. & Heckel, A. Biologically Active Molecules with a “Light Switch”. *Angewandte Chemie International Edition* **45**, 4900–4921 (2006).
- [92] Fournier, L., Aujard, I., Le Saux, T., Maurin, S., Beaupierre, S., Baudin, J. B. & Jullien, L. Coumarinylmethyl caging groups with redshifted absorption. *Chemistry - A European Journal* **19**, 17494–17507 (2013).
- [93] Curcio, J. A. & Petty, C. C. The Near Infrared Absorption Spectrum of Liquid Water. *Journal of the Optical Society of America* **41**, 302–304 (1951).
- [94] Göppert-Mayer, M. Über Elementarakte mit zwei Quantensprüngen. *Annalen der Physik* **401**, 273–294 (1931).
- [95] Olson, J. P., Kwon, H. B., Takasaki, K. T., Chiu, C. Q., Higley, M. J., Sabatini, B. L. & Ellis-Davies, G. C. Optically selective two-photon uncaging of glutamate at 900 nm. *Journal of the American Chemical Society* **135**, 5954–5957 (2013).
- [96] Aujard, I., Benbrahim, C., Gouget, M., Ruel, O., Baudin, J. B., Neveu, P. & Jullien, L. O-nitrobenzyl photolabile protecting groups with red-shifted absorption: Syntheses and uncaging cross-sections for one- And two-photon excitation. *Chemistry - A European Journal* **12**, 6865–6879 (2006).

- [97] Gug, S., Bolze, F., Specht, A., Bourgogne, C., Goeldner, M. & Nicoud, J. F. Molecular engineering of photoremovable protecting groups for two-photon uncaging. *Angewandte Chemie - International Edition* **47**, 9525–9529 (2008).
- [98] Pelliccioli, A. P. & Wirz, J. Photoremovable protecting groups: reaction mechanisms and applications. *Photochemical & Photobiological Sciences* **1**, 441–458 (2002).
- [99] Hammer, C. A. Spectroscopic Characterization of Photoresponsive Systems: from Chromoproteins to Switchable and Caged Compounds. *PhD thesis*, Goethe University Frankfurt (2018).
- [100] Engels, J. & Schlaeger, E. J. Synthesis, structure, and reactivity of adenosine cyclic 3',5'-phosphate-benzyltriesters. *Journal of Medicinal Chemistry* **20**, 907–911 (1977).
- [101] Wong, P. T., Tang, S., Mukherjee, J., Tang, K., Gam, K., Isham, D., Murat, C., Sun, R., Baker, J. R. & Choi, S. K. Light-controlled active release of photocaged ciprofloxacin for lipopolysaccharide-targeted drug delivery using dendrimer conjugates. *Chemical Communications* **52**, 10357–10360 (2016).
- [102] Kumari, P., Kulkarni, A., Sharma, A. K. & Chakrapani, H. Visible-Light Controlled Release of a Fluoroquinolone Antibiotic for Antimicrobial Photopharmacology. *ACS Omega* **3**, 2155–2160 (2018).
- [103] Il'ichev, Y. V., Schwörer, M. A. & Wirz, J. Photochemical Reaction Mechanisms of 2-Nitrobenzyl Compounds: Methyl Ethers and Caged ATP. *Journal of the American Chemical Society* **126**, 4581–4595 (2004).
- [104] Corrie, J. E., Barth, A., Munasinghe, V. R. N., Trentham, D. R. & Hutter, M. C. Photolytic cleavage of 1-(2-nitrophenyl)ethyl ethers involves two parallel pathways and product release is rate-limited by decomposition of a common hemiacetal intermediate. *Journal of the American Chemical Society* **125**, 8546–8554 (2003).
- [105] Yip, R. W., Sharma, D. K., Giasson, R & Gravel, D. Photochemistry of the o-Nitrobenzyl System in Solution: Evidence for Singlet State Intramolecular Hydrogen Abstraction. *J. Phys. Chem* **89**, 5328–5330 (1985).
- [106] Yip, R. W., Sharma, D. K., Giasson, R. & Gravel, D. Picosecond excited-state absorption of alkyl nitrobenzenes in solution. *Journal of Physical Chemistry* **88**, 5770–5772 (1984).
- [107] Šolomek, T., Bochet, C. G. & Bally, T. The primary steps in excited-state hydrogen transfer: The phototautomerization of o-nitrobenzyl derivatives. *Chemistry - A European Journal* **20**, 8062–8067 (2014).
- [108] Schmierer, T, Laimgruber, S, Haiser, K, Kiewisch, K, Neugebauer, J & Gilch, P. Femtosecond spectroscopy on the photochemistry of ortho-nitrotoluene. *Physical Chemistry Chemical Physics* **12**, 15653–15664 (2010).

- [109] Givens, R. S. & Park, C.-h. p-Hydroxyphenacyl ATP<sub>1</sub>: A new phototrigger. *Tetrahedron Letters* **37**, 6259–6262 (1996).
- [110] Park, C. H. & Givens, R. S. New photoactivated protecting groups. 6. p-Hydroxyphenacyl: A phototrigger for chemical and biochemical probes. *Journal of the American Chemical Society* **119**, 2453–2463 (1997).
- [111] Umeda, N., Takahashi, H., Kamiya, M., Ueno, T., Komatsu, T., Terai, T., Hanaoka, K., Nagano, T. & Urano, Y. Boron dipyrromethene as a fluorescent caging group for single-photon uncaging with long-wavelength visible light. *ACS Chemical Biology* **9**, 2242–2246 (2014).
- [112] Givens, R. S. & Matuszewski, B. Photochemistry of phosphate esters: an efficient method for the generation of electrophiles. *Journal of the American Chemical Society* **106**, 6860–6861 (1984).
- [113] Corden, J. L. & Tollervey, D. in *Cell Biology* (eds Pollard, T. D., Earnshaw, W. C. & Johnson, G. T.) 3rd ed., 443–462 (Elsevier, 2017).
- [114] Zucker, R. S. The calcium concentration clamp: spikes and reversible pulses using the photolabile chelator DM-nitrophen. *Cell Calcium* **14**, 87–100 (1993).
- [115] Kasai, H., Takagi, H., Ninomiya, Y., Kishimoto, T., Ito, K., Yoshida, A., Yoshioka, T. & Miyashita, Y. Two components of exocytosis and endocytosis in pheochromocytoma cells studied using caged Ca<sup>2+</sup> compounds. *Journal of Physiology* **494**, 53–65 (1996).
- [116] Kasai, H. Comparative biology of Ca<sup>2+</sup>-dependent exocytosis: Implications of kinetic diversity for secretory function. *Trends in Neurosciences* **22**, 88–93 (1999).
- [117] Amatrudo, J. M., Olson, J. P., Agarwal, H. K. & Ellis-Davies, G. C. R. Caged compounds for multichromic optical interrogation of neural systems. *European Journal of Neuroscience* **41**, 5–16 (2015).
- [118] Awapara, J., Landua, A. J., Fuerst, R. & Seale, B. Free gamma-aminobutyric acid in brain. *The Journal of biological chemistry* **187**, 35–9 (1950).
- [119] Roberts, E. & Frankel, S. gamma-Aminobutyric Acid in Brain: Its Formation from Glutamic Acid. *Journal of Biological Chemistry* **187**, 55–63 (1950).
- [120] Hammer, C. A., Falahati, K., Jakob, A., Klimek, R., Burghardt, I., Heckel, A. & Wachtveitl, J. Sensitized Two-Photon Activation of Coumarin Photocages. *Journal of Physical Chemistry Letters* **9**, 1448–1453 (2018).
- [121] Brackmann, D. U. *Lambdachrome Laser Dyes* 3rd ed., 1–294 (Lambda Physik AG, Göttingen, 2000).
- [122] Wagner, B. D. The use of coumarins as environmentally-sensitive fluorescent probes of heterogeneous inclusion systems. *Molecules* **14**, 210–237 (2009).

- [123] Gonçalves, M. & Sameiro, T. in *Advanced Fluorescence Reporters in Chemistry and Biology I* (ed Demchenko, A. P.) 27–64 (Springer Berlin Heidelberg, Berlin, Heidelberg, 2010).
- [124] Feringa, B. L. & Browne, W. R. *Molecular Switches* 2nd ed. (eds Feringa, B. L. & Browne, W. R.) (Wiley-VCH Verlag GmbH & Co. KGaA, Weinheim, Germany, 2011).
- [125] Irie, M. Diarylethenes for Memories and Switches. *Chemical Reviews* **100**, 1685–1716 (2000).
- [126] Beharry, A. A. & Woolley, G. A. Azobenzene photoswitches for biomolecules. *Chemical Society Reviews* **40**, 4422–4437 (2011).
- [127] Szymański, W., Beierle, J. M., Kistemaker, H. A., Velema, W. A. & Feringa, B. L. Reversible photocontrol of biological systems by the incorporation of molecular photoswitches. *Chemical Reviews* **113**, 6114–6178 (2013).
- [128] Klajn, R. Spiropyran-based dynamic materials. *Chemical Society Reviews* **43**, 148–184 (2014).
- [129] Tochitsky, I., Kienzler, M. A., Isacoff, E. & Kramer, R. H. Restoring Vision to the Blind with Chemical Photoswitches. *Chemical Reviews*, accepted (2018).
- [130] Garcia-Amorós, J., Díaz-Lobo, M., Nonell, S. & Velasco, D. Fastest thermal isomerization of an azobenzene for nanosecond photoswitching applications under physiological conditions. *Angewandte Chemie - International Edition* **51**, 12820–12823 (2012).
- [131] Ochi, R., Perur, N., Yoshida, K. & Tamaoki, N. Fast thermal cis-trans isomerization depending on pH and metal ions of water-soluble azobenzene derivatives containing a phosphate group. *Tetrahedron* **71**, 3500–3506 (2015).
- [132] Steinwand, S., Halbritter, T., Rastädter, D., Ortiz-Sánchez, J. M., Burghardt, I., Heckel, A. & Wachtveitl, J. Ultrafast Spectroscopy of Hydroxy-Substituted Azobenzenes in Water. *Chemistry - A European Journal* **21**, 15720–15731 (2015).
- [133] Özçoban, C., Halbritter, T., Steinwand, S., Herzig, L. M., Kohl-Landgraf, J., Askari, N., Groher, F., Fürtig, B., Richter, C., Schwalbe, H., Suess, B., Wachtveitl, J. & Heckel, A. Water-soluble Py-BIPS spiropyran as photoswitches for biological applications. *Organic Letters* **17**, 1517–1520 (2015).
- [134] Kaiser, C., Halbritter, T., Heckel, A. & Wachtveitl, J. Thermal, Photochromic and Dynamic Properties of Water-Soluble Spiropyran. *ChemistrySelect* **2**, 4111–4123 (2017).
- [135] Halbritter, T., Kaiser, C., Wachtveitl, J. & Heckel, A. Pyridine-Spiropyran Derivative as a Persistent, Reversible Photoacid in Water. *Journal of Organic Chemistry* **82**, 8040–8047 (2017).



- [136] Leyssner, F., Hagen, S., Óvári, L., Dokić, J., Saalfrank, P., Peters, M. V., Hecht, S., Klamroth, T. & Tegeder, P. Photoisomerization ability of molecular switches adsorbed on Au(111): Comparison between azobenzene and stilbene derivatives. *Journal of Physical Chemistry C* **114**, 1231–1239 (2010).
- [137] Asano, T., Okada, T., Shinkai, S., Shigematsu, K., Kusano, Y. & Manabe, O. Temperature and Pressure Dependences of Thermal Cis-to-Trans Isomerization of Azobenzenes Which Evidence an Inversion Mechanism. *Journal of the American Chemical Society* **103**, 5161–5165 (1981).
- [138] Zimmerman, G., Chow, L.-Y. & Paik, U.-J. The Photochemical Isomerization of Azobenzene 1. *Journal of the American Chemical Society* **80**, 3528–3531 (1958).
- [139] Rau, H. & Lüddecke, E. On the Rotation-Inversion Controversy on Photoisomerization of Azobenzenes. Experimental Proof of Inversion. *Journal of the American Chemical Society* **104**, 1616–1620 (1982).
- [140] Waldeck, D. H. Photoisomerization dynamics of stilbenes. *Chemical Reviews* **91**, 415–436 (1991).
- [141] Moore, W. M., Morgan, D. D. & Stermitz, F. R. Cis Stilbene Intermediate. *Journal of the American Chemical Society* **85**, 829–830 (1963).
- [142] Srinivasan, R & Powers, J. C. Mechanism of the Photochemical Formation of Phenanthrene from cis-Stilbene in the Vapor Phase. *Journal of the American Chemical Society* **85**, 1355–1356 (1963).
- [143] Mallory, F. B. & Mallory, C. W. in *Organic Reactions* (John Wiley & Sons, Inc., Hoboken, NJ, USA, 1984).
- [144] Kwasniewski, S. P., Claes, L., François, J. P. & Deleuze, M. S. High level theoretical study of the structure and rotational barriers of trans-stilbene. *Journal of Chemical Physics* **118**, 7823–7836 (2003).
- [145] Meier, H. The Photochemistry of Stilbenoid Compounds and Their Role in Materials Technology. *Angewandte Chemie - International Edition* **31**, 1399–1420 (1992).
- [146] Fihey, A., Perrier, A., Browne, W. R. & Jacquemin, D. Multiphotochromic molecular systems. *Chemical Society Reviews* **44**, 3719–3759 (2015).
- [147] Schweighöfer, F., Dworak, L., Hammer, C. A., Gustmann, H., Zastrow, M., Rück-Braun, K. & Wachtveitl, J. Highly efficient modulation of FRET in an orthogonally arranged BODIPY–DTE dyad. *Scientific Reports* **6**, 1–9 (2016).
- [148] Heng, S., Reineck, P., Vidanapathirana, A. K., Pullen, B. J., Drumm, D. W., Ritter, L. J., Schwarz, N., Bonder, C. S., Psaltis, P. J., Thompson, J. G., Gibson, B. C., Nicholls, S. J. & Abell, A. D. Rationally Designed Probe for Reversible Sensing of Zinc and Application in Cells. *ACS Omega* **2**, 6201–6210 (2017).

- [149] Lennartson, A., Roffey, A. & Moth-Poulsen, K. Designing photoswitches for molecular solar thermal energy storage. *Tetrahedron Letters* **56**, 1457–1465 (2015).
- [150] Kolpak, A. M. & Grossman, J. C. Azobenzene-functionalized carbon nanotubes as high-energy density solar thermal fuels. *Nano Letters* **11**, 3156–3162 (2011).
- [151] Han, G. D., Park, S. S., Liu, Y., Zhitomirsky, D., Cho, E., Dincă, M. & Grossman, J. C. Photon energy storage materials with high energy densities based on diacetylene–azobenzene derivatives. *Journal of Materials Chemistry A* **4**, 16157–16165 (2016).
- [152] Olmsted, J., Lawrence, J. & Yee, G. G. Photochemical storage potential of azobenzenes. *Solar Energy* **30**, 271–274 (1983).
- [153] Giordano, L., Jovin, T. M., Irie, M. & Jares-Erijman, E. A. Diheteroarylethenes as thermally stable photoswitchable acceptors in photochromic fluorescence resonance energy transfer (pcFRET). *Journal of the American Chemical Society* **124**, 7481–7489 (2002).
- [154] Van Der Molen, S. J., Liao, J., Kudernac, T., Agustsson, J. S., Bernard, L., Calame, M., Van Wees, B. J., Feringa, B. L. & Schönenberger, C. Light-controlled conductance switching of ordered metal-molecule-metal devices. *Nano Letters* **9**, 76–80 (2009).
- [155] Wakayama, Y., Hayakawa, R. & Seo, H.-S. Recent progress in photoactive organic field-effect transistors. *Science and Technology of Advanced Materials* **15**, 1–19 (2014).
- [156] Frolova, L. A., Rezvanova, A. A., Lukyanov, B. S., Sanina, N. A., Troshin, P. A. & Aldoshin, S. M. Design of rewritable and read-only non-volatile optical memory elements using photochromic spiropyran-based salts as light-sensitive materials. *Journal of Materials Chemistry C* **3**, 11675–11680 (2015).
- [157] Dong, M., Babalhavaeji, A., Hansen, M. J., Kálmán, L. & Woolley, G. A. Red, far-red, and near infrared photoswitches based on azonium ions. *Chemical Communications* **51**, 12981–12984 (2015).
- [158] Broichhagen, J., Frank, J. A. & Trauner, D. A Roadmap to Success in Photopharmacology. *Accounts of Chemical Research* **48**, 1947–1960 (2015).
- [159] Borowiak, M., Nahaboo, W., Reynders, M., Nekolla, K., Jalinot, P., Hasserodt, J., Rehberg, M., Delattre, M., Zahler, S., Vollmar, A., Trauner, D. & Thorn-Seshold, O. Photoswitchable Inhibitors of Microtubule Dynamics Optically Control Mitosis and Cell Death. *Cell* **162**, 402–411 (2015).
- [160] Richers, M. T., Tran, D. D., Wachtveitl, J. & Ellis-Davies, G. C. Coumarindiene photoswitches for rapid and efficient isomerization with visible light. *Chemical Communications* **54**, 4983–4986 (2018).

- [161] Gustmann, H. Zeitaufgelöste Charakterisierung struktureller Änderungen von spezifisch modifizierter RNA. *PhD thesis*, Goethe University Frankfurt (2018).
- [162] Yvon, J. A Guide to Recording Fluorescence Quantum Yields. *HORIBA - Technical Guide* (2003).
- [163] Trojanowski, P. P. Breitbandige, zeitaufgelöste Spektroskopie als empfindliche Methode zur Beobachtung von biomolekularer Dynamik. *PhD thesis*, Goethe Universität Frankfurt (2014).
- [164] Würth, C., Grabolle, M., Pauli, J., Spieles, M. & Resch-Genger, U. Comparison of methods and achievable uncertainties for the relative and absolute measurement of photoluminescence quantum yields. *Analytical Chemistry* **83**, 3431–3439 (2011).
- [165] Ware, W. R. & Rothman, W. Relative fluorescence quantum yields using an integrating sphere. The quantum yield of 9,10-diphenylanthracene in cyclohexane. *Chemical Physics Letters* **39**, 449–453 (1976).
- [166] Porrès, L., Holland, A., Pålsson, L. O., Monkman, A. P., Kemp, C. & Beeby, A. Absolute measurements of photoluminescence quantum yields of solutions using an integrating sphere. *Journal of Fluorescence* **16**, 267–272 (2006).
- [167] Brissette, P., Ballou, D. P. & Massey, V. Determination of the dead time of a stopped-flow fluorometer. *Analytical Biochemistry* **181**, 234–238 (1989).
- [168] Scholz, F. G. Photozyklusstudien an mikrobiellen Retinalproteinen. *PhD thesis*, Goethe-Universität, Frankfurt (2013).
- [169] Asido, M. Time-Resolved Measurements on the Sodium Pump KR2 in the Infrared. *Master thesis*, Goethe University Frankfurt (2014).
- [170] Radu, I., Schleege, M., Bolwien, C. & Heberle, J. Time-resolved methods in biophysics. 10. Time-resolved FT-IR difference spectroscopy and the application to membrane proteins. *Photochemical & Photobiological Sciences* **8**, 1517 (2009).
- [171] Chen, P. & Palmer, R. A. Time-Resolved Spectroscopy : Applications to Excited States of Transition Metal Complexes. *Applied Spectroscopy* **51**, 580–583 (1997).
- [172] Herzig, L.-M. Molekulare Dynamik der Freisetzung eines photolabil geschützten Antibiotikums. *PhD thesis*, Goethe University Frankfurt (2018).
- [173] Eckert, C. E. Deaktivierungsdynamik von mikrobiellem und visuellem Rhodopsin. *PhD thesis*, Goethe University Frankfurt (2017).
- [174] Reuß, A. J. Functional Dynamics of Ribonucleic Acids. *PhD thesis*, Goethe University Frankfurt (2016).

- [175] Bradler, M. Bulk continuum generation: The ultimate tool for laser applications and spectroscopy - From new insights to ultrafast amplifiers and spectrometers. *PhD thesis*, Ludwig-Maximilians-Universität München (2014).
- [176] Kohl-Landgraf, J., Nimsch, J.-E. & Wachtveitl, J. LiF, an underestimated supercontinuum source in femtosecond transient absorption spectroscopy. *Optics Express* **21**, 17060–17065 (2013).
- [177] Kohl-Landgraf, J. Zeitaufgelöste Spektroskopie von lichtgesteuerten Prozessen: Photochromie und Photofreisetzung. *PhD thesis*, Goethe-Universität, Frankfurt (2013).
- [178] Schweighöfer, F. Dynamik von Energietransferprozessen in photoschaltbaren molekularen Dyaden-Untersuchungen mittels Ultrakurzzeitspektroskopie. *PhD thesis*, Goethe University Frankfurt (2017).
- [179] Carpousis, A. J. The RNA Degradosome of *Escherichia coli*: An mRNA-Degrading Machine Assembled on RNase E. *Annual Review of Microbiology* **61**, 71–87 (2007).
- [180] Bandyra, K. J., Bouvier, M., Carpousis, A. J. & Luisi, B. F. The social fabric of the RNA degradosome. *Biochimica et Biophysica Acta - Gene Regulatory Mechanisms* **1829**, 514–522 (2013).
- [181] Lee, H.-W., Briggs, K. T. & Marino, J. P. Dissecting structural transitions in the HIV-1 dimerization initiation site RNA using 2-aminopurine fluorescence. *Methods* **49**, 118–127 (2009).
- [182] Anderson, B. J., Larkin, C., Guja, K. & Schildbach, J. F. *Chapter 12 Using Fluorophore-Labeled Oligonucleotides to Measure Affinities of Protein-DNA Interactions* 1st ed. **08**, 253–272 (Elsevier Inc., 2008).
- [183] Putnam, A. & Jankowsky, E. *Analysis of duplex unwinding by RNA helicases using stopped-flow fluorescence spectroscopy* 1st ed., 1–27 (Elsevier Inc., 2012).
- [184] Jankowsky, E. & Putnam, A. in, 245–264 (Humana Press, Totowa, NJ, 2009).
- [185] Lucius, A. L., Jason Wong, C. & Lohman, T. M. Fluorescence Stopped-flow Studies of Single Turnover Kinetics of *E. coli* RecBCD Helicase-catalyzed DNA Unwinding. *Journal of Molecular Biology* **339**, 731–750 (2004).
- [186] Raney, K., Sowerst, L., Millar, D. & Benkovic, S. A fluorescence-based assay for monitoring helicase activity. *Proceedings of the National Academy of Sciences of the United States of America* **91**, 6644–6648 (1994).
- [187] Henn, A., Cao, W., Licciardello, N., Heitkamp, S. E., Hackney, D. D. & De La Cruz, E. M. Pathway of ATP utilization and duplex rRNA unwinding by the DEAD-box helicase, DbpA. *Proceedings of the National Academy of Sciences of the United States of America* **107**, 4046–4050 (2010).

- [188] Zetzsche, H. Investigation of RNA folding processes under the influence of helicases by NMR spectroscopy. *Diploma thesis*, Goethe University Frankfurt (2014).
- [189] Turner, A.-M. W., Love, C. F., Alexander, R. W. & Jones, P. G. Mutational Analysis of the Escherichia coli DEAD Box Protein CsdA. *Journal of Bacteriology* **189**, 2769–2776 (2007).
- [190] Del Campo, M., Mohr, S., Jiang, Y., Jia, H., Jankowsky, E. & Lambowitz, A. M. Unwinding by local strand separation is critical for the function of DEAD-box proteins as RNA chaperones. *Journal of molecular biology* **389**, 674–93 (2009).
- [191] Rajagopal, V., Park, E.-H., Hinnebusch, A. G. & Lorsch, J. R. Specific Domains in Yeast Translation Initiation Factor eIF4G Strongly Bias RNA Unwinding Activity of the eIF4F Complex toward Duplexes with 5'-Overhangs. *Journal of Biological Chemistry* **287**, 20301–20312 (2012).
- [192] Yang, Q., Del Campo, M., Lambowitz, A. M. & Jankowsky, E. DEAD-Box Proteins Unwind Duplexes by Local Strand Separation. *Molecular Cell* **28**, 253–263 (2007).
- [193] Bagshaw, C. R. ATP analogues at a glance. *Journal of Cell Science* **114**, 459–460 (2001).
- [194] Kaplan, J. H., Forbush, B. & Hoffman, J. F. Rapid photolytic release of adenosine 5'-triphosphate from a protected analog: utilization by the sodium:potassium pump of human red blood cell ghosts. *Biochemistry* **17**, 1929–1935 (1978).
- [195] Parker, C. A. Raman spectra in spectrofluorimetry. *The Analyst* **84**, 446–453 (1959).
- [196] Putnam, A. A., Gao, Z., Liu, F., Jia, H., Yang, Q. & Jankowsky, E. Division of Labor in an Oligomer of the DEAD-Box RNA Helicase Ded1p. *Molecular Cell* **59**, 541–552 (2015).
- [197] Chen, Y., Potratz, J. P., Tijerina, P., Del Campo, M., Lambowitz, A. M. & Russell, R. DEAD-box proteins can completely separate an RNA duplex using a single ATP. *Proceedings of the National Academy of Sciences* **105**, 20203–20208 (2008).
- [198] Tran, D. D. Schwingungsspektroskopische Untersuchungen biomolekularer Dynamiken. *Master thesis*, Goethe University Frankfurt (2014).
- [199] Barth, A., Hauser, K., Maentele, W., Corrie, J. E. T. & Trentham, D. R. Photochemical Release of ATP from "Caged ATP" Studied by Time-Resolved Infrared Spectroscopy. *Journal of the American Chemical Society* **117**, 10311–10316 (1995).
- [200] Zetzsche, H. Investigation of helicase promoted RNA unwinding reactions by static and time resolved NMR spectroscopy. *PhD thesis in preparation*, Goethe University Frankfurt (2018).

- [201] Pyle, A. M., Jankowsky, E., Gross, C. H. & Shuman, S. The DEXH protein NPH-II is a processive and directional motor for unwinding RNA. *Nature* **403**, 447–451 (2000).
- [202] Vanzo, N. F., Li, Y. S., Py, B., Blum, E., Higgins, C. F., Raynal, L. C., Krisch, H. M. & Carpousis, A. J. Ribonuclease E organizes the protein interactions in the Escherichia coli RNA degradosome. *Genes and Development* **12**, 2770–2781 (1998).
- [203] Callaghan, A. A. J., Aurikko, J. J. P., Ilag, L. L. L., Grossmann, G., Chandran, V., Kühnel, K., Poljak, L., Carpousis, A. A. J., Robinson, C. V. C., Symmons, M. M. F., Luisi, B. F. B., Günter Grossmann, J., Chandran, V., Kühnel, K., Poljak, L., Carpousis, A. A. J., Robinson, C. V. C., Symmons, M. M. F. & Luisi, B. F. B. Studies of the RNA Degradosome-organizing Domain of the Escherichia coli Ribonuclease RNase E. *Journal of Molecular Biology* **340**, 965–979 (2004).
- [204] Eckardt, T., Hagen, V., Schade, B., Schmidt, R., Schweitzer, C. & Bendig, J. Deactivation behavior and excited-state properties of (coumarin-4-yl)methyl derivatives. 2. Photocleavage of selected (coumarin-4-yl)methyl-caged adenosine cyclic 3',5'-monophosphates with fluorescence enhancement. *Journal of Organic Chemistry* **67**, 703–710 (2002).
- [205] Becke, A. D. Density-functional thermochemistry. III. The role of exact exchange. *The Journal of Chemical Physics* **98**, 5648–5652 (1993).
- [206] Stephens, P. J., Devlin, F. J., Chabalowski, C. F. & Frisch, M. J. Ab Initio Calculation of Vibrational Absorption and Circular Dichroism Spectra Using Density Functional Force Fields. *The Journal of Physical Chemistry* **98**, 11623–11627 (1994).
- [207] Dunning, T. H. Gaussian basis sets for use in correlated molecular calculations. I. The atoms boron through neon and hydrogen. *The Journal of Chemical Physics* **90**, 1007–1023 (1989).
- [208] Frisch, M. J., Trucks, G. W., Schlegel, H. B., Scuseria, G. E., Robb, M. A., Cheeseman, J. R., Scalmani, G., Barone, V., Petersson, G. A., Nakatsuji, H., Li, X., Caricato, M., Marenich, A. V., Bloino, J., Janesko, B. G., Gomperts, R., Mennucci, B., Hratchian, H. P., Ortiz, J. V., Izmaylov, A. F., Sonnenberg, J. L., Williams-Young, D., Ding, F., Lipparini, F., Egidi, F., Goings, J., Peng, B., Petrone, A., Henderson, T., Ranasinghe, D., Zakrzewski, V. G., Gao, J., Rega, N., Zheng, G., Liang, W., Hada, M., Ehara, M., Toyota, K., Fukuda, R., Hasegawa, J., Ishida, M., Nakajima, T., Honda, Y., Kitao, O., Nakai, H., Vreven, T., Throssell, K., Montgomery, J. A., J., Peralta, J. E., Ogliaro, F., Bearpark, M. J., Heyd, J. J., Brothers, E. N., Kudin, K. N., Staroverov, V. N., Keith, T. A., Kobayashi, R., Normand, J., Raghavachari, K., Rendell, A. P., Burant, J. C., Iyengar, S. S., Tomasi, J., Cossi, M., Millam, J. M., Klene, M., Adamo, C., Cammi, R., Ochterski, J. W., Martin, R. L., Morokuma, K., Farkas, O., Foresman, J. B. & Fox, D. J. Gaussian 16, Revision B.01. 2016.

- [209] Ayer, R. K. & Zucker, R. S. Magnesium binding to DM-nitrophen and its effect on the photorelease of calcium. *Biophysical journal* **77**, 3384–3393 (1999).
- [210] Walbert, S., Pfliederer, W. & Steiner, U. E. Photolabile Protecting Groups for Nucleosides: Mechanistic Studies of the 2-(2-Nitrophenyl)ethyl Group. *Helvetica Chimica Acta* **84**, 1601–1611 (2001).
- [211] Becke, A. D. Density functional calculations of molecular bond energies. *The Journal of Chemical Physics* **84**, 4524–4529 (1986).
- [212] Perdew, J. P. Errata. *Physical Review B* **34**, 7406 (1986).
- [213] Schäfer, A., Horn, H. & Ahlrichs, R. Fully optimized contracted Gaussian basis sets for atoms Li to Kr. *The Journal of Chemical Physics* **97**, 2571–2577 (1992).
- [214] Gaplovsky, M., Il'ichev, Y. V., Kamdzhilov, Y., Kombarova, S. V., Mac, M., Schwörer, M. A. & Wirz, J. Photochemical reaction mechanisms of 2-nitrobenzyl compounds: 2-Nitrobenzyl alcohols form 2-nitroso hydrates by dual proton transfer. *Photochemical & Photobiological Sciences* **4**, 33–42 (2005).
- [215] Zhu, Q. Q., Schnabel, W. & Schupp, H. Formation and decay of nitronic acid in the photorearrangement of o-nitrobenzyl esters. *Journal of Photochemistry* **39**, 317–332 (1987).
- [216] Schwörer, M. & Wirz, J. Photochemical Reaction Mechanisms of 2-Nitrobenzyl Compounds in Solution, I. 2-Nitrotoluene: Thermodynamic and Kinetic Parameters of the *anti*-Nitro Tautomer. *Helvetica Chimica Acta* **84**, 1441–1458 (2001).
- [217] Bley, F., Schaper, K. & Görner, H. Photoprocesses of Molecules with 2-Nitrobenzyl Protecting Groups and Caged Organic Acids. *Photochemistry and Photobiology* **84**, 162–171 (2007).
- [218] Laimgruber, S., Schmierer, T., Gilch, P., Kiewisch, K. & Neugebauer, J. The ketene intermediate in the photochemistry of ortho-nitrobenzaldehyde. *Physical Chemistry Chemical Physics* **10**, 3872–3882 (2008).
- [219] Mewes, J. M. & Dreuw, A. On the role of singlet versus triplet excited states in the uncaging of ortho-nitrobenzyl caged compounds. *Physical Chemistry Chemical Physics* **15**, 6691–6698 (2013).
- [220] Gudem, M. & Hazra, A. Intersystem Crossing Drives Photoisomerization in o-Nitrotoluene, a Model for Photolabile Caged Compounds. *Journal of Physical Chemistry A* **122**, 4845–4853 (2018).
- [221] Bell, R. P. The Theory of Reactions Involving Proton Transfers. *Proceedings of the Royal Society A: Mathematical, Physical and Engineering Sciences* **154**, 414–429 (1936).
- [222] Evans, M. G. & Polanyi, M. Inertia and driving force of chemical reactions. *Transactions of the Faraday Society* **34**, 11–24 (1938).

- [223] Shankar, R. *Principles of Quantum Mechanics* 2nd ed. (Springer US, Boston, MA, 1994).
- [224] Hollas, J. M.J. M. *Modern spectroscopy* 4th ed., 452 (John Wiley & Sons, Ltd, Chichester, UK, 2004).
- [225] Poutsma, M. L. The radical stabilization energy of a substituted carbon-centered free radical depends on both the functionality of the substituent and the ordinality of the radical. *Journal of Organic Chemistry* **76**, 270–276 (2011).
- [226] Wessels, J. T., Pliquet, U. & Wouters, F. S. Light-emitting diodes in modern microscopy-from David to Goliath? *Cytometry Part A* **81A**, 188–197 (2012).
- [227] Albeanu, D. F., Soucy, E., Sato, T. F., Meister, M. & Murthy, V. N. LED Arrays as Cost Effective and Efficient Light Sources for Widefield Microscopy. *PLoS ONE* **3** (ed Wong, R. O. L.) e2146 (2008).
- [228] Van Wilderen, L. J., Neumann, C., Rodrigues-Correia, A., Kern-Michler, D., Mielke, N., Reinfelds, M., Heckel, A. & Bredenbeck, J. Picosecond activation of the DEACM photocage unravelled by VIS-pump-IR-probe spectroscopy. *Physical Chemistry Chemical Physics* **19**, 6487–6496 (2017).
- [229] Blanc, A. & Bochet, C. G. Isotope Effects in Photochemistry. 1. o - Nitrobenzyl Alcohol Derivatives. *Journal of the American Chemical Society* **126**, 7174–7175 (2004).
- [230] Slavov, C., Yang, C., Heindl, A. H., Stauch, T., Wegner, H. A., Dreuw, A. & Wachtveitl, J. Twist and Return-Induced Ring Strain Triggers Quick Relaxation of a (Z)-Stabilized Cyclobisazobenzene. *The Journal of Physical Chemistry Letters* **9**, 4776–4781 (2018).
- [231] Jaumann, E. A., Steinwand, S. & Klenik, S. A combined optical and EPR spectroscopy study : azobenzene-based biradicals as reversible molecular photoswitches. *Physical Chemistry Chemical Physics* **19**, 17263–17269 (2017).
- [232] Schweighöfer, F., Moreno, J., Bobone, S., Chiantia, S., Herrmann, A., Hecht, S. & Wachtveitl, J. Connectivity pattern modifies excited state relaxation dynamics of fluorophore-photoswitch molecular dyads. *Physical Chemistry Chemical Physics* **19**, 4010–4018 (2017).
- [233] Hara, K., Sato, T., Katoh, R., Furube, A., Ohga, Y., Shinpo, A., Suga, S., Sayama, K., Sugihara, H. & Arakawa, H. Molecular Design of Coumarin Dyes for Efficient Dye-Sensitized Solar Cells. *The Journal of Physical Chemistry B* **107**, 597–606 (2003).
- [234] Hanwell, M. D., Curtis, D. E., Lonie, D. C., Vandermeersch, T., Zurek, E. & Hutchison, G. R. Avogadro: an advanced semantic chemical editor, visualization, and analysis platform. *Journal of Cheminformatics* **4**, 17 (2012).



- [235] Phipson, T. L. On a Curious Actinic Phenomenon. *Scientific American* **12**, 4677–4677 (1881).
- [236] Kathan, M. & Hecht, S. Photoswitchable molecules as key ingredients to drive systems away from the global thermodynamic minimum. *Chemical Society Reviews* **46**, 5536–5550 (2017).
- [237] Arrhenius, S. Über die Reaktionsgeschwindigkeit bei der Inversion von Rohrzucker durch Säuren. *Zeitschrift für Physikalische Chemie* **4U**, 226–248 (1889).
- [238] Stranius, K. & Börjesson, K. Determining the photoisomerization quantum yield of photoswitchable molecules in solution and in the solid state. *Scientific Reports* **7**, 1–9 (2017).
- [239] Köhler, T. unknown title. *PhD thesis in preparation*, Goethe University Frankfurt (2018).
- [240] Anstaett, P., Leonidova, A. & Gasser, G. Caged Phosphate and the Slips and Misses in Determination of Quantum Yields for Ultraviolet-A-Induced Photouncaging. *ChemPhysChem* **16**, 1857–1860 (2015).
- [241] Kasha, M. Characterization of Electronic Transitions in Complex Molecules. *Discussions of the Faraday Society* **9**, 14–19 (1950).
- [242] Tseng, H.-W., Shen, J.-Y., Kuo, T.-Y., Tu, T.-S., Chen, Y.-A., Demchenko, A. P. & Chou, P.-T. Excited-state intramolecular proton-transfer reaction demonstrating anti-Kasha behavior. *Chemical Science* **7**, 655–665 (2016).
- [243] Renth, F., Siewertsen, R. & Temps, F. Enhanced photoswitching and ultrafast dynamics in structurally modified photochromic fulgides. *International Reviews in Physical Chemistry* **32**, 1–38 (2013).
- [244] Altoè, P., Haraszkiwicz, N., Gatti, F. G., Wiering, P. G., Frochot, C., Brouwer, A. M., Balkowski, G., Shaw, D., Woutersen, S., Buma, W. J., Zerbetto, F., Orlandi, G., Leigh, D. A. & Garavelli, M. Multistate photo-induced relaxation and photoisomerization ability of fumaramide threads: A computational and experimental study. *Journal of the American Chemical Society* **131**, 104–117 (2009).
- [245] Cembran, A., Bernardi, F., Garavelli, M., Gagliardi, L. & Orlandi, G. On the Mechanism of the cis-trans Isomerization in the Lowest Electronic States of Azobenzene: S<sub>0</sub>, S<sub>1</sub>, and T<sub>1</sub>. *Journal of the American Chemical Society* **126**, 3234–3243 (2004).
- [246] Kim, D., Sambasivan, S., Nam, H., Hean Kim, K., Yong Kim, J., Joo, T., Lee, K.-H., Kim, K.-T. & Han Ahn, K. Reaction-based two-photon probes for in vitro analysis and cellular imaging of monoamine oxidase activity. *Chemical Communications* **48**, 6833–6835 (2012).
- [247] Sens, A. Statische Absorptions- und Fluoreszenzuntersuchungen an einem bistabilen Cumarin-Photoschalter. *Bachelor thesis*, Goethe University Frankfurt (2018).

- [248] Steinwand, S., Yu, Z., Hecht, S. & Wachtveitl, J. Ultrafast Dynamics of Photoisomerization and Subsequent Unfolding of an Oligoazobenzene Foldamer. *Journal of the American Chemical Society* **138**, 12997–13005 (2016).
- [249] Conti, I., Marchioni, F., Credi, A., Orlandi, G., Rosini, G. & Garavelli, M. Cyclohexenylphenyldiazene: A simple surrogate of the azobenzene photochromic unit. *Journal of the American Chemical Society* **129**, 3198–3210 (2007).

## SCIENTIFIC CONTRIBUTIONS

---

### PUBLICATIONS

- M. T. Richers,\* D. D. Tran,\* J. Wachtveitl and G. C. R. Ellis-Davies “*Coumarin-diene photoswitches for rapid and efficient isomerization with visible light*”, Chem. Commun. **2018**, 54, 4983-4986

\* These authors contributed equally

### ORAL CONTRIBUTIONS TO CONFERENCES

- “*A novel, bistable coumarin-photoswitch with enhanced extinction and low fatigue*”, Design and Light Control, **2017**, Niedernberg/Germany

### POSTER CONTRIBUTIONS TO CONFERENCES

- “*A novel, bistable coumarin-photoswitch with enhanced extinction and low fatigue*”, International Symposium on Photochemistry **2018** (27<sup>th</sup> PhotoIUPAC), Dublin/Ireland
- “*A novel, bistable coumarin-photoswitch with enhanced extinction and low fatigue*”, Design and Light Control **2017**, Niedernberg/Germany
- “*Investigation of RNA helicase unwinding mechanism via NMR and fluorescence spectroscopy*”, Joint meeting between GRK2039 and CLiC **2016**, Freudenstadt-Lauterbad/Germany

### ORAL PRESENTATIONS

- “*Wavelength-dependent characterization of a coumarin-based photoswitch*”, Internal group seminar **2018**, Frankfurt/Germany
- “*A novel, bistable coumarin-photoswitch with promising properties*”, CLiC summer school **2017**, Niedernberg/Germany
- “*Wavelength-dependent characterization of a coumarin-based photoswitch*”, Internal group seminar **2017**, Frankfurt/Germany
- “*A ‘visible’ cage*”, Annual seminar of the Institute of Physical and Theoretical Chemistry Goethe University, Hirschegg/Austria, **2017**

- *“a cage, a coumarin-photoswitch - a collaboration”*, Internal group seminar **2017**, Frankfurt/Germany
- *“RNA unwinding dynamics of a DEAD-box helicase”*, CLiC summer school **2016**, Lindau/Germany
- *“Basics of: (time-resolved) optical spectroscopy”*, CLiC Workshop: Elucidating talks for summer school **2016**, Frankfurt/Germany
- *“Measuring helicase unwinding”*, University internal mentoring comitee meeting **2016**, Frankfurt/Germany
- *“uncaging small molecules”*, CLiC summer school **2015**, Konstanz/Germany
- *“FLUorescence Correction & quantum Yield calculation - A tutorial for FluCY”*, Internal group seminar **2015**, Frankfurt/Germany
- *“Kinetic separation of folding and association dynamics triggered by differentially caged ATP ”*, CLiC kickoff: Project presentations **2014**, Frankfurt/Germany

DANKE!

---

Mein allergrößter Dank gilt meinem Betreuer und Doktorvater **Prof. Dr. Josef Wachtveitl**, der mir die Möglichkeit gab, meine Thesis in seinem Arbeitskreis durchzuführen und mir dabei ausreichend wissenschaftliche Freiheiten einräumte. Ich möchte mich auch insbesondere für seine Unterstützung und sein Vertrauen bedanken, unabhängig davon, ob es um die Arbeit selbst, E-Mail-Korrespondenzen oder auch die Kooperationen ging, ohne die ich diese Arbeit nicht hätte fertig stellen können. Insgesamt war das gesamte Arbeitsumfeld in der Gruppe war, dank ihm sehr angenehm.

...

In dieser elektronischen, zur Veröffentlichung vorgesehenen Fassung ist der restliche Teil der Danksagung mitsamt den personenbezogenen Daten entfernt worden.

...



## EIDESSTATTLICHE ERKLÄRUNG

---

Ich, Dinh Du TRAN, erkläre an Eides statt, dass ich die bei der promotionsführenden Fakultät der Goethe-Universität zur Promotionsprüfung vorgelegte Arbeit mit dem Titel:

„Spectroscopic Studies on Photosensitive Probes - Molecular Dynamics of RNA-Protein Complexes, Caged and Photoswitchable Compounds“

im Institute for Physical and Theoretical Chemistry unter der Anleitung und Betreuung durch Prof. Dr. Josef Wachtveitl ohne sonstige Hilfe erstellt und bei der Abfassung nur die angegebenen Hilfsmittel benutzt habe.

- Ich habe keine Organisation eingeschaltet, die gegen Entgelt Betreuerinnen und Betreuer für die Anfertigung von Dissertationen sucht, oder die mir obliegenden Pflichten hinsichtlich der Prüfungsleistungen für mich ganz oder teilweise erledigt.
- Ich habe die Dissertation in dieser oder ähnlicher Form in keinem anderen Prüfungsverfahren als Prüfungsleistung vorgelegt.
- Ich habe den angestrebten Doktorgrad noch nicht erworben und bin nicht in einem früheren Promotionsverfahren für den angestrebten Doktorgrad endgültig gescheitert.

Die öffentlich zugängliche Promotionsordnung der Goethe-Universität ist mir bekannt, insbesondere habe ich die Bedeutung von § 15 (Aberkennung des Doktorgrades) zur Kenntnis genommen. Ich bin mir der Konsequenzen einer falschen Eidesstattlichen Erklärung bewusst.

Frankfurt, den 29.10.2019

---

Unterschrift





# Dinh Du Tran

---

## Personal Information

Geburtsdatum 20. Dezember 1988  
Geburtsort Frankfurt a.M.  
Nationalität deutsch

---

## Promotion

11/2014 – 02/2019 **Promotion in der Physikalischen Chemie**, Institut für Physikalische und Theoretische Chemie, Goethe Universität, Frankfurt a.M.  
Titel Spectroscopic Studies on Photosensitive Probes - Molecular Dynamics of RNA-Protein Complexes, Caged and Photoswitchable Compounds  
Betreuer Prof. Dr. Josef Wachtveitl

---

## Studium

04/2013 – 09/2014 **Master of Science (Chemie)**, Goethe Universität, Frankfurt a.M.  
Titel Schwingungsspektroskopische Untersuchungen biomolekularer Dynamiken  
Betreuer Prof. Dr. Josef Wachtveitl

10/2009 – 03/2013 **Bachelor of Science (Chemie)**, Goethe Universität, Frankfurt a.M.  
Titel Analyse von photochemisch geschützter DNA mittels NMR-Spektroskopie  
Betreuer Prof. Dr. Harald Schwalbe

Akad. Lehrer Prof. Dr. H.-J. Bader, PD Dr. M. Braun, Prof. Dr. J. Bredenbeck, PD Dr. G. Bruls, Prof. Dr. I. Burghardt, Prof. Dr. E. Egert, Prof. Dr. M. Göbel, Prof. Dr. A. Heckel, PD Dr. R. Hegger, Prof. Dr. M. Holthausen, Prof. Dr. A. Lühken, Dr. E. Israr, Prof. Dr. T. Prisner, Prof. Dr. M. Rehahn, Prof. Dr. M. Schmidt, Prof. Dr. H. Schwalbe, Prof. Dr. A. Terfort, Prof. Dr. J. Wachtveitl, Prof. Dr. M. Wagner

---

## Schulische Ausbildung

1999 – 2008 **Abitur**, Ziehenschule, Frankfurt a.M.